UNIVERSITY OF Southampton

University of Southampton Research Repository

Copyright © and Moral Rights for this thesis and, where applicable, any accompanying data are retained by the author and/or other copyright owners. A copy can be downloaded for personal non-commercial research or study, without prior permission or charge. This thesis and the accompanying data cannot be reproduced or quoted extensively from without first obtaining permission in writing from the copyright holder/s. The content of the thesis and accompanying research data (where applicable) must not be changed in any way or sold commercially in any format or medium without the formal permission of the copyright holder/s.

When referring to this thesis and any accompanying data, full bibliographic details must be given, e.g.

Thesis: Author (Year of Submission) "Full thesis title", University of Southampton, name of the University Faculty or School or Department, PhD Thesis, pagination.

Data: Author (Year) Title. URI [dataset]

University of Southampton

Faculty of Engineering and Physical Sciences

Optoelectronics Research Centre

Low Power Optical Phase Shifter devices

by

Bharat Pant

Thesis for the degree of Doctor of Philosophy

July 2022

University of Southampton

<u>Abstract</u>

Faculty of Engineering and Physical Sciences

Optoelectronics Research Centre

Thesis for the degree of <u>Doctor of Philosophy</u>

Low Power Optical Phase Shifter Devices

by

Bharat Pant

Silicon photonics is a disruptive technology that is poised to revolutionize number of application areas such as data centres, high performance computing and sensing. The key driving force behind silicon photonics is its compatibility with CMOS fabrication, high volume production and low cost. The optical modulator is one of the key elements in the transmission of data in short and long reach optical interconnects. With ever increasing numbers of integrated components on a chip, the total power budget for modulation becomes more demanding.

This report outlines two promising approaches based on phase modulation of light for reducing the energy requirements which can be implemented in integrated optical communication systems in foreseeable future. The first involves light recycling through an MMI and utilizing the present thermal gradient/carriers to accumulate additional phase change. Another approach utilizes actuation of suspended slot waveguide-based structures to achieve the phase change by modifying the structure geometry when actuated electrically.

Table of Contents

Table of Contents i
Table of Tables v
Table of Figures vii
Research Thesis: Declaration of Authorship xix
Acknowledgements xxi
Definitions and Abbreviations xxiii
Chapter 1 Introduction 25
1.1 Optics and Photonics 25
1.2 Silicon Photonics 26
1.3 Thesis outline 30
Chapter 2 Fundamentals and literature review 31
2.1 Passive Devices 31
2.1.1 Waveguides, Grating couplers, Splitters/Combiners 31
2.2 Modulators 33
2.2.1 Group IV based optical modulators 33
2.2.1.1 Plasma Dispersion Effect 34
2.2.1.2 Franz- Keldysh Effect and Quantum Confined Stark effect 37
2.2.1.3 Pockels Effect and Kerr Effect 39
2.2.1.4 Thermo Optic effect 39
2.2.2 MEMS/NEMS photonic modulators 41
2.2.2.1 Electrostatic mechanism 42
Chapter 3 Modulator device configurations, Simulation and Experimental tools 46
3.1 Mach-Zehnder Interferometer (MZI) 46
3.1.1 MZI Free Spectral Range (FSR) 48
3.2 Ring Resonators 50
3.3 Standard Metrics 51
3.3.1 Modulation Efficiency 51

3.3.2 Insertion Loss (IL) and Extinction Ratio (ER) 51
3.3.3 Dynamic Extinction Ratio 51
3.3.4 Dark Current 52
3.4 Characterization setup 52
3.5 Cutback method 53
3.6 Device modelling and mask design tools and software 53
Chapter 4 Thermal optical modulators 55
4.1 Review of fundamental Science of an MMI 55
4.2 Thermo- optic phase shift modulator - 2x2 MMI (2 pass) 57
4.2.1 Simulation parameters 58
4.2.2 Simulated temperature and Δn_{eff} change 59
4.2.3 Simulated phase change 63
4.2.4 Device parameters 65
4.2.5 Mask design and device Fabrication 67
4.2.6 Experimental Results 70
4.3 Summary 74
Chapter 5 Carrier injection modulator 75
5.1 Simulation Analysis 76
5.1.1 Optical mode confinement and carrier density induced ΔN_{eff} 77
5.1.2 Design motivation for two pass 2x2 MMI injection phase modulator 79
5.2 Device design strategy 80
5.2.1 Simulation errors and multimode region length of fabricated devices 86
5.3 Layout and Fabrication 87
5.4 Experimental results 88
5.4.1 AC characterization 97
5.5 Summary 99
Chapter 6 Spread of heat from Thermo optic elements 100
6.1 Simulation and fabrication test structure 100
6.2 Fabrication 102

6.3 Simulation and experimental results 103
6.3.1 Type A structures (with heater element and waveguide displacement) 103
6.3.2 Type B structures (with separation between the MZI arms) 104
6.3.3 Other platforms 105
6.4 Summary 107

Chapter 7 MOEMS Phase modulator 108

7.1 Slot waveguide mode 108
7.2 Simulation Analysis 110
7.2.1 Effective index variation 110
7.2.2 Displacement of beam under electrostatic forces 111
7.3 Device configuration 112
7.4 Fabrication 115
7.5 Issues with Stiction 116
7.6 Stiction removal approach 117
7.6.1 HF vapour etch 117
7.6.1.1 Fabrication flow 118
7.6.2 Critical point drying (CPD) 120
7.6.2.1 Fabrication flow 123
7.7 Mode converter design 124
7.8 STRIP waveguide based platform for CPD 126
7.8.1 Strip to Slot mode converter 126
7.8.2 Fabrication 127
7.8.3 Simulation and experimental results 129
7.8.3.1 Length section 1 variation 129
7.8.4 Effect of section 2 length variation 130
7.8.5 1x2 MMI 131
7.8.6 2x2 MMI 133
7.8.7 Slot waveguide losses 137
7.9 RIB waveguide based platform for vapor phase HF 137

7.9.1 STRIP to STRIP-loaded SLOT mode converter ... 137
7.9.2 1x2 MMI ... 141
7.9.3 2x2 MMI ... 143
7.9.4 Fabrication ... 143
7.9.4.1 Imaging before the modulator under-etch ... 144
7.9.4.2 Imaging after HF vapour etching ... 146
7.10 Summary ... 148
Chapter 8 Conclusion ... 149
Appendix A 153
A.1 Data points selection and fitting ... 154
Bibliography ... 156

Table of Tables

Table 1 Typical performance for plasma dispersion based modulators (partially reproduced from [47]). 37

Table 2 Simulated modal area for modes of 2 μm and 6 μm width waveguide for applied heater power of 0 and 20 mW. 63

Table 3 Simulated phase change efficiencies for various waveguide widths for a heated section length of 86.67 μm. 64

Table 4 Fabricated devices with various heater geometries. 67

Table 5 Heater dimensions and efficiency results for fabricated thermo-optic devices. 73

Table 6 Simulated (highest) FDE power overlap for mode 1 and mode 2 for access waveguide dimensions (position and width) w.r.t. multimode region width. 80

Table 7 Real part of effective index of guided modes of a 1.76 μm wide waveguide. 81

Table 8 Simulated mode overlap and power coupling of access waveguide fundamental mode with multimode region (1.76 μm) guided modes. 81

Table 9 Simulated multimode region length and transmission for MMI defined by parameters in Table 6. 83

Table 10 Simulated device dimensions for tapered 2x2 MMI device. 86

Table 11 Fabricated device lengths (different than presented in simulation work). 87

Table 12 Minimum loss and wavelength for non-tapered 2x2 MMI device. 93

Table 13 Minimum loss and wavelength for tapered 2x2 MMI device. 93

Table 14: π phase shift current and power requirements for fabricated devices around 1.55 μm wavelength. 97

Table 15: Time response of the fabricated MZI devices at 1.55 μm wavelength. 98

Table 16 Common SOI platforms offered by CORNERSTONE MPW service. 100

Table 17 Guidelines for waveguide separation with minimal thermal crosstalk for various SOI platforms. 107

Table of Tables

Table 18 Change in effective index vs slot gap size. 110

Table 19 Slot waveguide device iterations fabricated. 144

Table of Figures

Figure 1-1 Optics related component and equipment (a) Production share, (b) Industry revenue. Recreated with data from [1]. 25

Figure 1-2 Silicon photonics milestones. Figure recreated from [5]. 26

Figure 1-3 Silicon photonics die market forecast by applications. Image reproduced from [14].27

Figure 1-4 Complexity scaling in silicon photonics integrated circuits. Image reproduced from [16]. 28

Figure 1-5 Silicon photonics chip cost per mm^2 (shared CMOS facilities). Data from members of ePIXfab, image reproduced from [5]. 29

Figure 2-1 STRIP and RIB waveguide geometries. Silicon substrate not shown in illustrations. .31

Figure 2-2 Schematic representation of various passive devices (top view). 1x2 MMI, Ring resonator and directional coupler. 32

Figure 2-3 Grating couplers used for coupling light between a single mode fibre and Si waveguide on photonics chip. (a) Out of plane coupling (top view), (b) Inverse taper grating coupler (Image reproduced from [42]). 33

Figure 2-4 Various modulation mechanisms compared w.r.t. their speed and magnitude of modulation. 34

Figure 2-5 P-i-N Modulators based on (a) Carrier accumulation, (b) Carrier Injection, and (c) Carrier depletion. Image reproduced from [46] 35

Figure 2-6 Diffusion capacitance (C_d) and depletion capacitance (C_j) of the p-n junction diode w.r.t. drive voltage V_D. Image reproduce from [52] 36

Figure 2-7 QCSE - Tilting of energy bands and wavefunction allowing photons with energy less than the band gap to be absorbed, in the presence of applied electric field. Image taken from [71]. 38

Figure 2-8 Typical implementations of TOPS (a) Metal bar on top of waveguide, (b) doped silicon on both sides of the waveguide 39

Figure 2-9 Thermal switch using (a) light recycling (Image reproduced from [85]), and densely packed waveguides using (b) 14 folded waveguides (Image reproduced from

[81]), and (c) folded waveguide in a spiral structure (Image reproduced from [80]). 40

Figure 2-10 (a) 2x2 micro machined bypass switch denoting motion of the mirror, (b) 2D MEMS Add-Drop optics switches. Image reproduced from [93] and [95]. 41

Figure 2-11 Parallel plate capacitor model for electrostatic forces. Image reproduced from [98]. 42

Figure 2-12 (a)Initial MOEMS devices proposed for optical modulation, (b)Light coupling based optical routing methods using MEMS/NEMS. Image reproduced from [2] and [102]. 43

Figure 2-13 (a)Deformable silicon wire phase modulator. Image reproduced form [92]. (b)Cross section of under-etched slot waveguide used as modulator. 44

Figure 2-14 Schematic of MEMS tuneable ring resonator. Actuation of free standing cantilever forming part of the slot waveguide ring resonator changes the refractive index, resulting in resonance wavelength shift. Image reproduced from [114] 45

Figure 3-1 Schematic diagram of a 1x2 balanced MZI. 47

Figure 3-2 Normalized intensity response of an ideal MZI with changing phase 48

Figure 3-3 Schematic layout of a ring resonator based modulator (waveguide cross section on the top left). Image reproduced from [120]. 50

Figure 3-4 GeSi electro absorption modulator based on Franz-Keldysh effect showing dark current pathways in the device [124]. Image reproduced from [125] 52

Figure 3-5 Lab setup for characterizing samples. 52

Figure 3-6 Illustration of cutback method to calculate the loss per device. 53

Figure 4-1 Modes of the multimode region [136]. W_e represents the effective width of the mode including the lateral penetration depth for each mode. Image recreated from [136] 56

Figure 4-2 Top view of the two pass 2x2 MMI device used as a phase modulator in the arms of an imbalanced MZI (not shown here). The regions drawn in blue and grey are implemented in 220 nm thick silicon on a 2000nm BOX. 57

Figure 4-3 Simulation model cross section for the study of heat gradient across various waveguides for a fixed heater width of 0.2 µm..58

Figure 4-4 Thermal profile across the centre of waveguide for varying waveguide widths. Applied heater power is 20 mW for a heater filament width of 2 µm and length 86.67 µm 59

Figure 4-5 Peak waveguide temperature at the centre of waveguide for various waveguide widths (0.45 to 9um) with constant heater dimensions of 0.2 x 2 μm^2 (height x width), length 86.67 µm and 20 mW applied power to the heating element............60

Figure 4-6 Change in the effective index of the fundamental mode for various waveguide widths with constant heater element dimensions (0.2 µm wide) and power 20 mW.60

Figure 4-7 Change in the effective index for modes 1 to 10 for various waveguide widths (0.45 to 9 µm). The heater filament dimensions are fixed at 2um, 0.2um, 86.67 µm width, height and length with 20 mW of applied power..61

Figure 4-8 Electric field intensity profile for the first five TE modes of 5.45 um width waveguide. 62

Figure 4-9 Electric field intensity profile of first five modes for wavguide width 5.45 um. 62

Figure 4-10 Simulated electric field intensity profile of a STRIP waveguide with width 6 µm, 220 nm height surrounded by silicon dioxide at the top and the bottom with no applied heater power. 62

Figure 4-11 Simulated thermal profile for STRIP waveguide of height 220 nm and width (a) 0.45 µm, (b) 1 µm, (c) 2 µm, (d) 4 µm (e) 6 µm. 64

Figure 4-12 Top view of the 2x2 MMI modulator device and dimensions. 65

Figure 4-13 Normalized transmission vs multimode region length for the simulated 6 µm 2x2 MMI modulator device using the EME solver. 66

Figure 4-14 Intensity profile for the simulated MMI phase shifter device with multimode region length 89.6 µm at 1.55 µm wavelength...66

Figure 4-15 Schematic top view of the 2x2 MMI thermal phase shifter with dimensions..........67

Figure 4-16 180 degree bend used for light recirculation in the 2x2 MMI................................68

Figure 4-17 L-edit mask layout for 2x2 MMI modulator in an imbalanced MZI. 69

Figure 4-18 Fabrication flow (top) and schematic cross section (below) of the fabricated thermo-optic device (0.45 µm waveguide width). 70

Figure 4-19 Normalized wavelength spectrum response of the MZI comprising 2x2 MMI phase shifter devices for various applied heater power. Filled blue dots represents wavelength spectrum when no voltage is applied. 71

Figure 4-20 Flow chart representation of the MATLAB code used to calculate phase shift. 72

Figure 4-21 Phase shift vs applied heater power for devices with a heater width of 2 µm and lengths of 80 µm (blue) and 160 µm (green). Normalization MZI are represented by circles, and MMI based MZI devices are represented by triangles. 73

Figure 5-1 Schematic top view of the PIN junction based injection current modulators (a) 2x2 multiple pass MMI modulator, (b) tapered 2x2 multiple pass MMI modulator.75

Figure 5-2 Device geometry used in Lumerical DEVICE with CHARGE solver to calculate the carrier concentration change. 76

Figure 5-3 Mode 1, 2, 3, 4 silicon confinement factor for waveguide widths from 0.4 µm to 2 µm. 77

Figure 5-4 Electron density for various waveguide widths with an applied power of 21.24 mW.78

Figure 5-5 Variation in Delta Neff vs waveguide geometry for the first 4 guided modes relating to injection modulators with power of 21.24 mW. 79

Figure 5-6 Simulated mode profiles of the multimode region with width 1.76 µm on 220 nm Silicon with 100 nm Silicon slab. 81

Figure 5-7 Simulated length sweep for non-tapered MMI (through port and cross port for single pass) usign EME solver. 82

Figure 5-8 Simulated intensity profile of the MMI defined by parametrs in Table 6 and Table 9.83

Figure 5-9 Linear adiabatic taper length sweep for mode conversion from 1.76 µm to 0.8 µm waveguide. 84

Figure 5-10 Simulation device parameters for tapered MMI device. 85

Figure 5-11 Simulated external MMI length (1.76 µm width) for tapered MMI device. 85

Figure 5-12 Intensity profile for simulated device dimensions as quoted in Table 10 86

Figure 5-13 Fabrication flow (top) and schematic cross section (below) of the fabricated carrier injection phase shift devices. 88

Figure 5-14 Transmission wavelength spectrum of the fabricated non tapered and tapered 2x2 MMI device with MMI length = 100 µm and external length = 106.53 µm repectively (wihtout MZI). 89

Figure 5-15 Transmission wavelength spectrum of the fabricated cutback type non- tapered 2x2 MMI devices with external MMI length = 100 um (1, 2, 4, 5 two pass MMI devices in series) and averaging function giving the 'filtered data' used for calculations. 91

Figure 5-16 Transmission wavelength spectrum of the cutback type fabricated tapered 2x2 MMI devices with external MMI length = 106.53 um (1, 2, 4, 5 two pass MMI devices in series) and averaging function giving the 'filtered data' used for calculations. 92

Figure 5-17 2x2 non-tapered MMI cross port output transmission as a function of multimode region length. 94

Figure 5-18 Normalized MZI response with 2x2 non-tapered MMI as phase shifter elements in both arms. 94

Figure 5-19 Wavelength spectrum shift with applied power for MZI with 2x2 non-tapered MMI as phase shifter element. 95

Figure 5-20 Wavelength spectrum shift with applied power for MZI with 2x2 tapered MMI as phase shifter element. 96

Figure 5-21 Phase shift vs applied power for fabricated normalization MZI and MZI with 2x2 MMI devices at 1.55 µm. 96

Figure 5-22 AC measurements for various devices (a) the input signal 31.25 MHz, (b) Normalization MZI, (c) 2x2 MMI MZI, (d) Tapered 2x2 MMI MZI. 98

Figure 6-1 Cross-section of the simulated structures with 220nm x 500 nm (height x width) STRIP waveguides. (a) Represent the study structure for change in heater offset (ΔS_{offset}) w.r.t. the waveguide centre. (b) Represents the study structure for thermal crosstalk between two waveguides separated by ΔS (c) Cross-section for two different waveguide separations (Type B), ΔS2>ΔS1. 101

Figure 6-2 Fabricated test structures for characterization of the lateral spread of heat. (a) Type A- Consists of multiple heating elements along one arm of MZI, each with a different positional offset from normal position (ΔS_{offset}=0, where centre of the waveguide and the centre of the heating element are placed on top of each other). (b) Type B - Consists of a set of MZI, each with a different waveguide arm separation to study the thermal crosstalk. 102

Figure 6-3 Microscope image (top view) of the fabricated devices (Type B). 102

Figure 6-4 (a) MZI normalised transmission against electrical drive power for the different heating element offset positions. (b) Electrical power required for switching (2π phase shift) with the heater off-set from the waveguide by different amounts. ... 103

Figure 6-5 Temperature change in the waveguide for different heater element position offsets (ΔS_{offset}) with the electrical power required for 2π switching in the zero offset case. 104

Figure 6-6 Simulated temperature line profile across the centre of waveguide cross section (as shown in Figure 6-1(b)) for different MZI arm separations. Red line (ΔS=0) represents the heated and reference waveguide without separation (i.e. they are the same waveguide), and blue, orange, green line represents heated waveguides at position -3, -6, -9um distance with reference waveguide placed at 0 µm. 104

Figure 6-7 (a)Normalised transmission against electrical drive power for the three MZI with waveguide arm separations of 2um, 4um and 6um. (b) Electrical power required for switching (2π phase shift) for the 3 different MZI with different arm separation. 105

Figure 6-8 Percentage temperature change in the reference waveguide for different waveguide separations (ΔS) in various SOI platforms. 106

Figure 7-1 Slot mode intensity profile (TE) for a waveguide cross section having beam width 250 nm, height 220 nm, and air gap of 70 nm. 109

Figure 7-2 Normalized Electric field profile of the slot mode (TE) for a beam width 250 nm, height 220 nm, and gap 70 nm. 109

Figure 7-3 Effective index variation of slot waveguide mode with air gap for different silicon beam widths and varying air gap between them. 110

Figure 7-4 Deformation of different lengths of silicon beams (width= 250 nm, height =220 nm) for an applied potential of 5 V between them. 112

Figure 7-5 Schematic layout of the phase modulators incorporated in an MZI. 113

Figure 7-6 Designs of modulators using (a) Single beam modulator, (b) Double beam modulator. 113

Figure 7-7 SEM images (top view) of the fabricated (a) Single beam and (b) double beam slot waveguide modulator devices in the initial run. 114

Figure 7-8 Proposed device with electrostatic forces causing attraction between the beams of slot waveguide. 115

Figure 7-9 Failed devices due to Stiction. Stiction due to (a) capillary forces while drying, (b) electrostatic charge. 116

Figure 7-10 L-Edit layout of fabricated test structures to get the maximum fabrication length of the freestanding slot waveguides. 118

Figure 7-11 Sample etched in vapour HF with ZEP as a mask. 70 nm gap and 250 nm beams of length 15, 25, 35, and 45 µm from bottom to top. 118

Figure 7-12 Pictorial representation of the modulator waveguide transition using HF vapour for release. 119

Figure 7-13 Fabrication flow using vapour HF for the freestanding slot waveguide modulators.120

Figure 7-14 CO_2 Pressure temperature phase diagram with process trajectory. Image reproduced from [153]. 121

Figure 7-15 Concentration of water and transitional fluid after etching. 121

Figure 7-16 CPD process flow. 122

Figure 7-17 Pictorial representation (top view) of the free standing slot waveguide modulator using CPD after etching of the BOX. 123

Figure 7-18 Fabrication layout for Strip and strip-loaded based designs. 124

Figure 7-19 Schematic diagram of the Y shaped strip to slot mode converter w=400 nm, d=60 nm, w2=100 nm, w3= 260 nm, h_s=250 nm. Image reproduced from ..125

Figure 7-20 Schematic of the strip to slot mode converter. Image reproduced from [159].125

Figure 7-21 Top view of the strip to slot mode converter with mode profiles (cross section) along the length of the converter as the mode is transformed............................126

Figure 7-22 SEM image (top view) of the fabricated Strip to slot converter with section 1 length 0.5 µm and section 2 length 20 µm. 127

Figure 7-23 Contamination after ICP etch. 128

Figure 7-24 Fabrication issues on chip 1 (a) Unexpected features due to ebeam writing and development (b) E-beam stitching error. 128

Figure 7-25 The sample contaminated from ICP (a) Before RCA clean (b) after RCA clean129

Figure 7-26 Experimental transmission data for pair of mode converters fabricated with variation in length section 1 compared to simulation results......................130

Figure 7-27 Experimental, simulated transmission and reflection data for a pair of mode converters fabricated with variations in length of section 2 compared to the simulation results. 131

Figure 7-28 Simulated 1x2 MMI intensity profile with a 32.04 µm MMI length using the EME solver in Lumerical...132

Figure 7-29 L-edit layout mask for array fabricated to characterize the 1x2 MMI loss. ..132

Figure 7-30 SEM image (top view) of fabricated 1x2 MMI of length 32.04 µm. 132

Figure 7-31 Experimental data for the fabricated 1x2 MMI lengths compared with the simulation results. 133

Figure 7-32 2x2 MMI simulated field profile. 134

Figure 7-33 SEM image of a fabricated 2x2 MMI with multimode region with a length of 42.56 µm. 134

Figure 7-34 L-Edit layout of the MMI array for the 2x2 MMI with the output from the lower port. 135

Figure 7-35 Experimental data for different fabricated 2x2 MMI lengths. 135

Figure 7-36 Wavelength scans for transmission through the lower port of the 2x2 MMI with a multimode region length of 42.56 µm. 136

Figure 7-37 SEM image of a fabricated slot waveguide with a 70nm gap and 250 nm beam width. 137

Figure 7-38 Shematic representation of STRIP to STRIP-loaded-SLOT waveguide mdoe converter. 138

Figure 7-39 Schematic representation of the STRIP to STRIP-loaded-SLOT wavegudie mode converter for 250 nm silicon rails and an air gap of 70 nm. 138

Figure 7-40 Top view of the STRIP to strip-loaded slot mode converter with mode profiles (cross section) along the length of the converter as the mode is transformed. A represents the under-etched STRIP waveguide mode, B represents the Strip-loaded-SLOT waveguide mode, and C represents fully etched SLOT waveguide mode. 139

Figure 7-41 Simulated transmission for RIB to under-etched STRIP waveguide using the FDTD solver. 140

Figure 7-42 Simulated transmission for under-etched STRIP waveguide to STRIP-loaded-SLOT waveguide using the FDTD solver. 140

Figure 7-43 Simulated transmission for the STRIP-loaded SLOT mode to fully suspended SLOT mode using FDTD. 141

Figure 7-44 Simulation results for 1x2 MMI for various MMI lengths. 142

Figure 7-45 Simulated 1x2 MMI intensity profile at 32.1 µm MMI length using the EME solver in Lumerical. 142

Figure 7-46 Simulation results for length of the multimode region of the 1x2 MMI. 143

Figure 7-47 Simulated 2x2 MMI intensity profile at 42.2 µm MMI length using EME solver in Lumerical. 143

Figure 7-48 Mask layout of the slot waveguide modulator MZI (beam width = 250 nm, gap width =70 nm) with 1, 3, 5 and 7 modulator segments in each MZ arm. 144

Figure 7-49 Fabricated RIB to STRIP mode converter before performing the under-etch. 145

Figure 7-50 Fabricated STRIP to STRIP-loaded-SLOT mode converter before performing the under-etch for a silicon beam width of 250nm and gap width 70 nm. 145

Figure 7-51 Fabricated modulator with a silicon beam width of 250nm, gap width of 70 nm and a length of 12.5 µm (before performing the underetch) 146

Figure 7-52 Sample with titanium as adhesion layer after being processed with vapour HF... 147

Figure 8-1 Freestanding SLOT waveguides as resonant wavelength tuning element in racetrack resonator. 152

Figure 8-2 Coupled ring structures consisting of freestanding SLOT waveguides as resonant wavelength tuning element in racetrack resonator. 153

Figure A-8-3 Experimental and fitted data points for Strip to slot mode converter with length section 1=0.5 µm and length section 2 = 20µm. 155

Research Thesis: Declaration of Authorship

Print name:	Bharat Pant
Title of thesis:	Low Power Optical Phase Shifter devices

I declare that this thesis and the work presented in it are my own and has been generated by me as the result of my own original research.

I confirm that:

1. This work was done wholly or mainly while in candidature for a research degree at this University;
2. Where any part of this thesis has previously been submitted for a degree or any other qualification at this University or any other institution, this has been clearly stated;
3. Where I have consulted the published work of others, this is always clearly attributed;
4. Where I have quoted from the work of others, the source is always given. With the exception of such quotations, this thesis is entirely my own work;
5. I have acknowledged all main sources of help;
6. Where the thesis is based on work done by myself jointly with others, I have made clear exactly what was done by others and what I have contributed myself;
7. Parts of this work have been published as:
   Journal Paper
   B. Pant, W. Zhang, M. Ebert, X. Yan, H. Du, M. Banakar, D. T. Tran, Y. Qi, D. Rowe, V. Jeyaselvan, C. G. Littlejohns, G. T. Reed, and D. J. Thomson, "Study into the spread of heat from thermo-optic silicon photonic elements," Opt. Express 29, 36461-36468 (2021)
   Conference Proceedings
   B. Pant, W. Zhang, M. Ebert, X. Yan, H. Du, M. Banakar, D. T. Tran, Y. Qi, D. Rowe, V. Jeyaselvan, C. G. Littlejohns, G. T. Reed, and D. J. Thomson "Enhanced efficiency thermo-optic phase-shifter using multi-mode-interference device," 2020 IEEE Photonics Conference (IPC), 2020, pp. 1-2, doi: 10.1109/IPC47351.2020.9252212.

Signature:		Date:	07/07/2022

Acknowledgements

I would like to express my sincere gratitude to my supervisor Prof. David J. Thomson for proving the initial ideas and guidance throughout my Ph.D studies. Without their immense knowledge and constant motivation, this work would not have been possible. They deserve special thanks for giving me the utmost freedom in exploring the ideas and their patience when things were not moving at a pace.

My sincere acknowledgement goes to Dr. Scott A. Reynolds, Dr. Zhibo Qu, Dr. Callum G. Littlejohns, Dr. Jordi S. Penadés, Dr. Milos Nedeljković, Dr. Milan Milosević, Dr. Mehdi Banakar, Dr. Kian S. Kiang, Dr. Xingzhao Yan, Dr. Weiwei Zhang, Ms. Lauren Reid, Dr. Ying Tran and Prof. Graham T. Reed for their help and support during this work.

My special appreciation goes to Dr. Panagiotis Galanis, Dr. Shuichiro Rikimi, Dr. Natsupa Taengnoi and Mr. Peng Li for continuing their studies alongside mine and the good times.

I would like to thank my friends, without them all the world would mean a bit hollow.

Above all I would like to thank my dad, mom and my brother for their eternal support through this distance, space , and time, some more than the others.

“Nothing but a hole, to live without a soul and nothing to be learned.” - CC

Definitions and Abbreviations

BOX	Buried Oxide
CAGR	Compound annual Growth Rate
MZI	Mach-Zehnder Interferometer
NOEMS	Nano Optical Electronic Mechanical Systems
MEMS	Micro Electrical Mechanical Systems
HF	Hydro Fluoric
CPD	Critical Point
SOI	Silicon on Insulator
GOI	Germanium on Insulator
GOS	Germanium on Silicon
SiN	Silicon Nitride on Insulator
EBL	Electron Beam Lithography
FIB	Focussed Ion Beam
UV	Ultra Violet
DUV	Deep Ultra Violet
Au	Gold
CVD	Chemical Vapor Deposition
PECVD	Plasma Enhanced Chemical Vapor Deposition
EME	Eigen Mode Expansion
PIC	Photonics Integrated Circuits

Chapter 1 Introduction

Light is all around us, playing a vital role in our lives by enabling plants to synthesize and produce basic food and oxygen which is crucial for human survival. Various phenomenon such as reflection, diffraction, scattering etc help us perceive objects as our eyes act as receptors and the brain decodes the information to helps us visualize. Similarly, light applications have integrated into our day to day lives leading from general activities like illumination, display devices to niche applications such as optical data communication, biomedical, automotive, aerospace, sensing, machining and artificial intelligence to name a few.

1.1 Optics and Photonics

In broad terms, light is defined to be made of quanta of particles known as 'Photons' which have an electric and magnetic field associated with them. The science of manipulating photons and their study fall under the umbrella term of 'Photonics'.

Figure 1-1 displays the market division and industrial revenue for optical components and equipment. The combined production of optics related components and equipment is estimated around USD 600 billion across major markets with compound annual growth rate (CAGR) of 6.4 % from 2016 to 2021 [1].

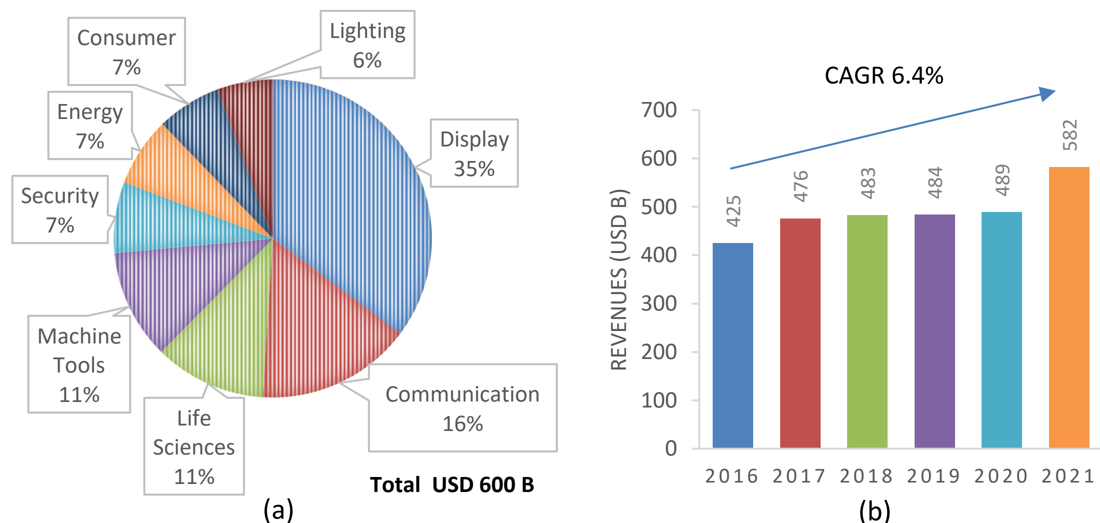

Figure 1-1 Optics related component and equipment (a) Production share, (b) Industry revenue. Recreated with data from [1].

1.2 Silicon Photonics

Early work on optical circuits involved working with ferroelectric materials and III-V semiconductors [2]. In the mid-1980s, Soref and Lorenzo [3] demonstrated that silicon waveguides can be used to guide light, followed by the first active device [4] attracting interest from companies such as INTEL, IBM. Since then, photonic integrated circuits (PIC) with high density and complex functionality have been fabricated utilizing the existing CMOS infrastructure leading to lower cost and power, small footprint and high yield, complexity, performance and ergonomics. Various material platforms such as Silicon-on-insulator (SOI), Germanium-on-insulator (GOI), Germanium-on-silicon (GOS), Silicon Nitride-on-Insulator (SiN) etc. all fall under the definition of silicon photonics and are pushing towards commercial volume production in various application fields. Figure 1-2 summarizes the major milestones in the field of silicon photonics.

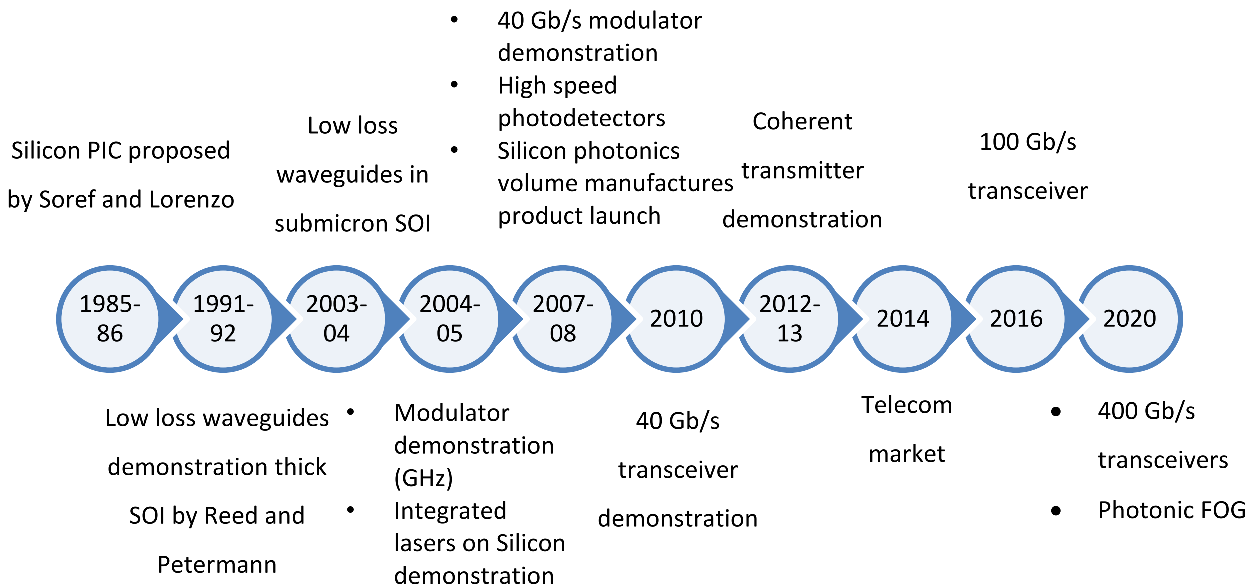

Figure 1-2 Silicon photonics milestones. Figure recreated from [5].

Silicon is a very versatile material which leverages the CMOS capabilities to deliver low cost, heigh yield, compact devices. However, due to the indirect bandgap, it is a poor light emitter. Great effort has been devoted in the past few years towards integrating III-V on Si lasers (as well as other devices) and maturing the technology for a cost effective solution with techniques like Flip-chip, micro transfer printing, epitaxial growth and heterogenous bonding [6-9].

Semiconductor electronics components have reached a high level of sophistication and can be produced industrially with high yield and low cost. Nowadays, hundreds of million transistor per mm^2 are volume produced using a 5 nm node [10] in commercial foundries. But still, the growth of electronic devices has seemingly reached a saturation due to parasitic capacitance, power

consumption and the operating speed which cannot be enhanced by conventional methods [11]. Compared to electronics, photonic systems offer inherent advantages such as orders of magnitude higher operation rate, low crosstalk between adjacent channels [12, 13], but owing to the large footprint of photonic components, the possibility of replacing critical computing components like CPU, memory etc are not feasible. However silicon photonics have found its niche in various other applications like optical transceivers, sensing and bio photonics, LiDAR, fiber-optic gyroscope, consumer healthcare, machine learning, quantum information processing etc as shown in Figure 1-3. The current market for silicon photonics is heavily dominated by optical transceivers for datacentres, but looks to be shifting towards consumer applications in the coming five years [14].

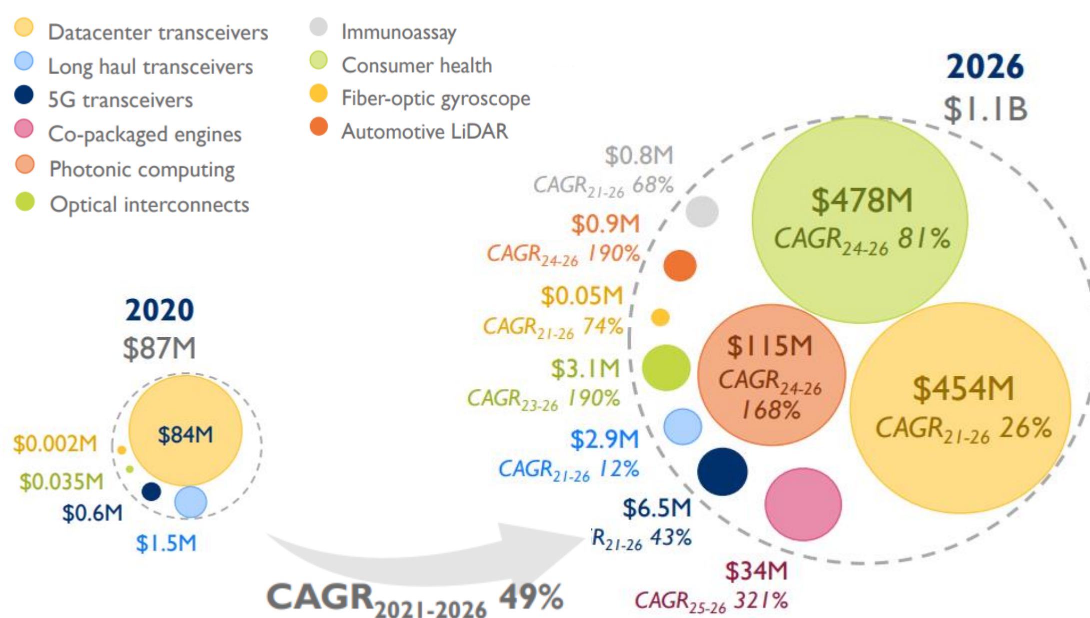

Figure 1-3 Silicon photonics die market forecast by applications. Image reproduced from [14].

The functionality of a photonic chip relies on various components such as light sources, filters, modulators and detectors connected via waveguides [15]. Owing to the large refractive index difference between the silicon and surrounding oxide, light can be confined in submicron waveguide structures which can be stacked closely together facilitating densely packed photonic chips with a large number of components. As shown in Figure 1-4, the number of components in a silicon photonics chip have doubled every 12 months for non-transceiver based optical chips from 2002 – 2016 [16] and continue to follow similar trends as more demanding applications are introduced.

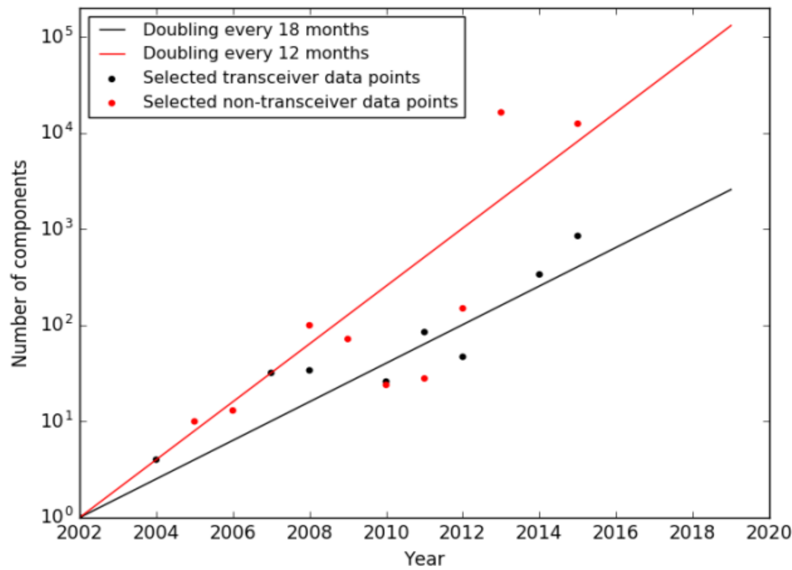

Figure 1-4 Complexity scaling in silicon photonics integrated circuits. Image reproduced from [16].

This has been made possible with an increase in infrastructure facilities over the years, offering production of silicon photonics chips at various scales. These can usually be classified into three categories. Firstly, the vertically integrated electronics manufacturers such as INTEL, IBM and ST Microelectronics which are devoted towards the company's own use exclusively and commercialized products. Secondly, the open access CMOS foundries such as TSMC, GlobalFoundries, Silterra, Advanced Micro foundry, TowerJazz which offer large volume PIC manufacturing services to external users. And lastly, the research fabrication facilities like IMEC, CEA LETI, AMF, IHP, CORNERSTONE which offer low volume manufacturing to external users via various Multi project wafer (MPW) runs for prototyping. Along with the major push in fabrication facilities, there has also been a huge effort to constantly improve the design and simulation tools with companies like Lumerical, Luceda Photonics, VLC photonics, RSOFT etc. Packaging and testing are equally required and organizations such as PIXAPP, Tyndall have emerged. Such an ecosystem has been crucial in fuelling the present and upcoming ventures in the field of PIC devices and applications [17-21].

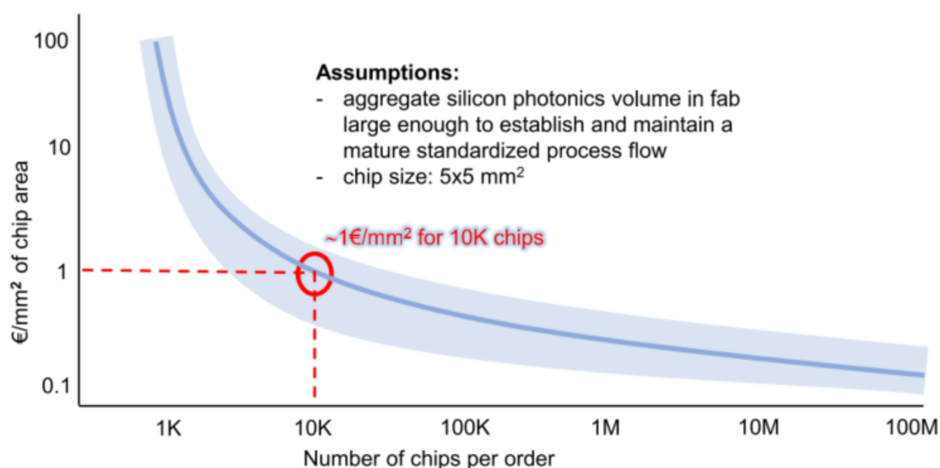

Figure 1-5 Silicon photonics chip cost per mm^2 (shared CMOS facilities). Data from members of ePIXfab, image reproduced from [5].

Figure 1-5 shows the estimated costs for standardized silicon photonics platforms comprising of both active and passive components, supporting monolithic or hybrid integration and does not include any packaging costs. For up to 1000 chips, the cost is calculated using MPW fabrication and for upto 10000 chips, using 25 200mm wafers [5].

Other than high speed optical transceivers for data centres, silicon photonics has been utilized in applications such as LiDAR and imaging [22-24], Optical quantum systems [25, 26], machine learning processors [27, 28], large scale optical switches [28, 29] and programmable PIC [30] which require a large number of optical components to be integrated. Following the trend of largescale PICs with ever growing number of optical components, low power consumption, small footprint and insertion loss have become essential ingredients to help keep the overall power budget and device cost in check while delivering complex functionality.

This project aims to lower the power consumption in optical phase shifters and switching devices based on conventional modulation mechanisms like thermal and carrier injection on SOI platforms operating around 1550 nm. The phase shifting element in these conventional modulators are usually implemented along a single mode waveguide having width of ~ 0.5 µm. We report a 29% (thermal) and 66% (carrier injection) reduction in power required to achieve π phase shift using a 2x2 multi-mode-interferometer (MMI) device. The multimode waveguide of the MMI is utilized as the modulation region through which the optical signal is circulated twice, hence increasing the efficiency. A nano-electro-mechanical-systems (NEMS) based approach involving free standing slot waveguides has also been investigated for low power phase modulation applications.

1.3 Thesis outline

The following work, described in this thesis focuses on low power phase modulation devices using 3 different optical modulation mechanisms i.e. Thermal phase shifters, Carrier injection phase shifters and free standing slot waveguides.

- Chapter 1 has introduced the impact and development of silicon photonics and the need for low power optical components.
- Chapter 2 lays down the fundamental modulation mechanisms used in group IV materials, and the theoretical concepts and their implementation.
- Chapter 3 highlights common configurations and simulation tools and techniques utilized commonly and in this work.
- Chapter 4 details the work on two-pass multi-mode interference devices, devised to increase the efficiency of thermal optical phase modulators. The design procedure, simulation tools, layout generation and experimental results to achieve power savings of 29.46% have been detailed.
- Chapter 5 extends the work on two pass multi-mode interference devices proposed in chapter 4 for the case of carrier injection based optical phase shifter devices and explains the design, and experimental results to achieve 66 % power savings compared to conventional single mode waveguide based modulators.
- Chapter 6 presents a side study giving design rules for fabricating compact thermal based devices for various standard SOI platforms using simulation and experimental study
- Chapter 7 introduces another approach undertaken during this work for achieving low power phase modulation using Nano-opto-electric-mechanical NOEMS devices utilizing slot waveguide structure to achieve phase modulation. The design strategy, device fabrication, and analysis have been detailed. In the later part, two fabrication approaches using vapour HF and critical point drying to reduce the effect of stiction commonly encountered in MEMS based devices is presented. The simulation, fabrication, and experimental results for the vapour phase HF etching and critical point drying are discussed.
- Chapter 8 provides a review, concluding remarks and future work suggestions for the work carried out during this thesis.

Chapter 2 Fundamentals and literature review

2.1 Passive Devices

Silicon photonics integrated circuits use a plethora of basic building components which enable routing of light within the photonic chip. Waveguides are the most basic component used to confine and guide optical signals to and from other passive optical components such as bends, splitters, directional couplers, star coupler, grating couplers, MMI etc.

2.1.1 Waveguides, Grating couplers, Splitters/Combiners

Refractive index contrast between the core and the cladding, required for waveguiding structures, can be achieved by doping silicon with III/V ions but the resulting structure require thick cladding layers and large waveguide spacings between waveguides due to the not so strong confinement of light in the waveguide structure[31, 32]. Silicon-on-insulator (SOI) offers an excellent platform for Si/SiO_2 waveguides with strong mode confinement owing to the large refractive index contrast between the refractive index of Si and SiO_2 i.e. 3.45 and 1.45 respectively in the vertical direction. Etching of the waveguide is performed using lithographic patterning to give confinement in horizontal plane producing two possible waveguide geometries as Figure 2-1.

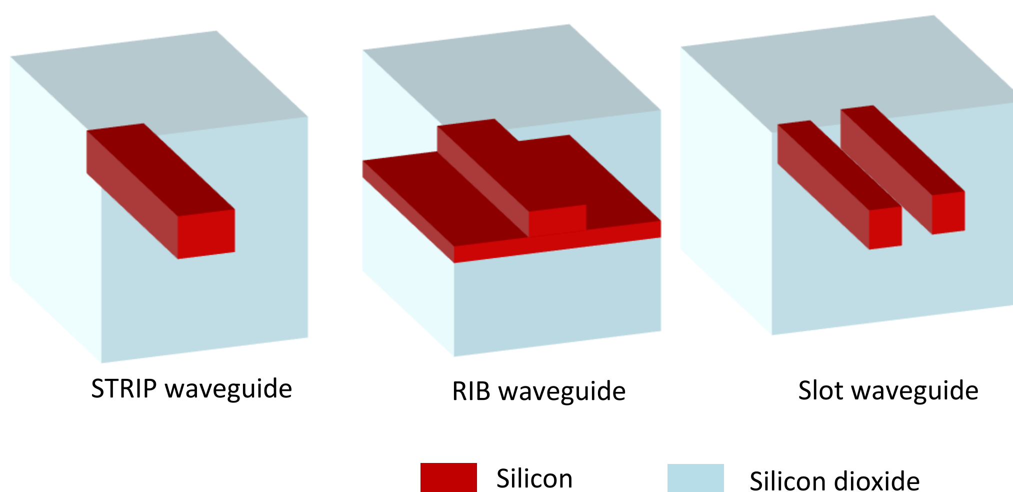

Figure 2-1 STRIP and RIB waveguide geometries. Silicon substrate not shown in illustrations.

STRIP waveguides are produced when all of the silicon layer is etched away from the sides of waveguide core. These provide high optical mode confinement and are beneficial in producing compact PIC’s with reduced footprint. RIB waveguides have a thin slab layer of silicon left unetched and are useful in providing contact areas for active doped devices. These can also be

designed in a way such that the higher order modes leak out through the slab while propagating, helping in single mode operation. Slot waveguides consist of two silicon rails and confine light in the gap between the two silicon rails and are also used for light guiding.

The causes of propagation loss in waveguides can be defined as intrinsic loss which are due to absorption within the waveguide, and extrinsic loss occurring due to the surface roughness or sidewall scattering and radiation into the substrate. With a reduction in waveguide cross-section, scattering loss becomes the larger contributor to the propagation loss which is studied to be 0.2 - 3.0 dB/cm [33].

Bends are utilized to change the direction of propagating light and allow dense integration and smaller die sizes. Splitting and combining of light from one or more waveguides is required in applications such as MZI, signal monitoring etc which utilize structures such as Y-splitter, directional couplers and MMI devices [34]. Other important type of devices performing as filters and multiplexers are arrayed waveguides [35], planar concave gratings (echelle gratings) [36], ring resonators [37], angled MMI [38], bragg gratings [39] etc. These are utilized for splitting and combining various wavelengths to and from a waveguide.

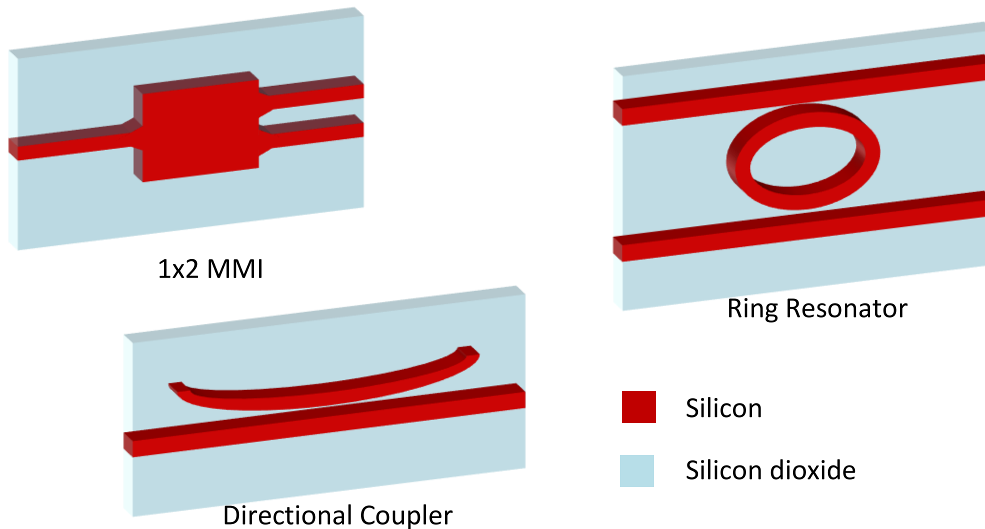

Figure 2-2 Schematic representation of various passive devices (top view). 1x2 MMI, Ring resonator and directional coupler.

The coupling of light between fibres and silicon waveguides is also challenging due to the mismatch in optical mode sizes in the two mediums. The commonly used solution involves using grating couplers [40], which offer great flexibility for light injection and extraction on the chip, and relatively large alignment tolerance leading to lower packaging costs [40] and limited bandwidth which is adequate for wide range of applications [41]. Other types of devices used for coupling light between a fibre and an on chip silicon waveguide include a Silicon inverse taper and a

medium contrast waveguide made by a polymer [42]. Both approaches have been demonstrated to show loss of well under 1 dB [43, 44].

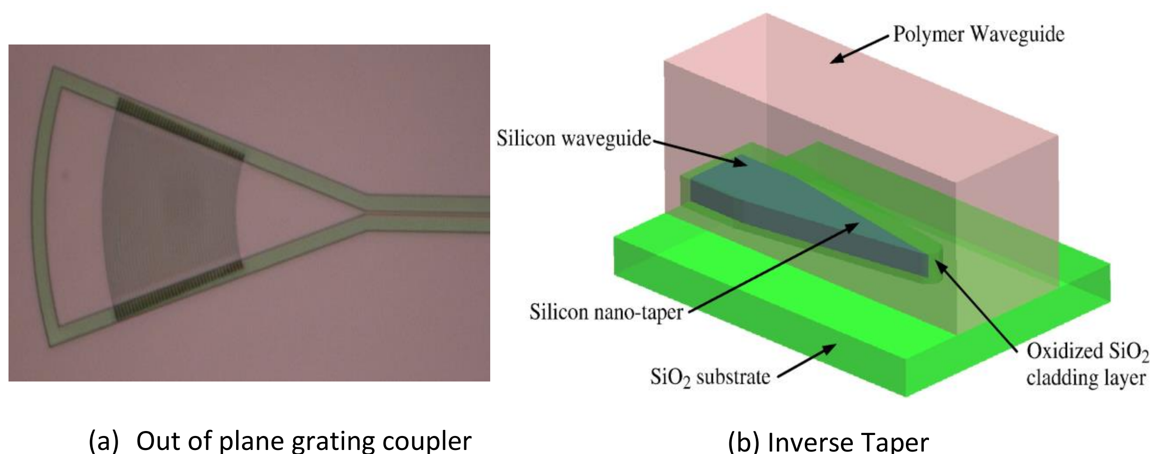

(a) Out of plane grating coupler (b) Inverse Taper

Figure 2-3 Grating couplers used for coupling light between a single mode fibre and Si waveguide on photonics chip. (a) Out of plane coupling (top view), (b) Inverse taper grating coupler (Image reproduced from [42]).

2.2 Modulators

Optical modulators perform the important function of controlling/varying the characteristics of light in relation to a control signal which can be in the form of an electrical, optical signal or other forms such as vibrations etc. For performance evaluation various factors are to be considered such as modulation depth, modulation speed, bandwidth, insertion loss, size, and power consumption which are explained in the following chapter. Usually, trade-offs are made between these parameters and devices are designed to be used in specific applications. In the following section, the fundamentals of optical modulation in group IV based materials are explained with briefs on their design and implementation.

2.2.1 Group IV based optical modulators

Optical modulators can be classified into 2 different categories, namely, electro-refraction and electro-absorption. Electro-refraction refers to the change in the real part of the refractive index, and electro- absorption refers to the change in the imaginary part of the refractive index in response to an electric field.

Due to the centro-symmetric crystal structure of Silicon, it does not exhibit strong electro optical effect [45]. Hence the main modulation mechanisms are thermo-optic effect, Franz-Keldysh

effect, Quantum Confined Stark effect, Plasma Dispersion effect, Pockels effect, introducing strain in the crystal, etc [2].

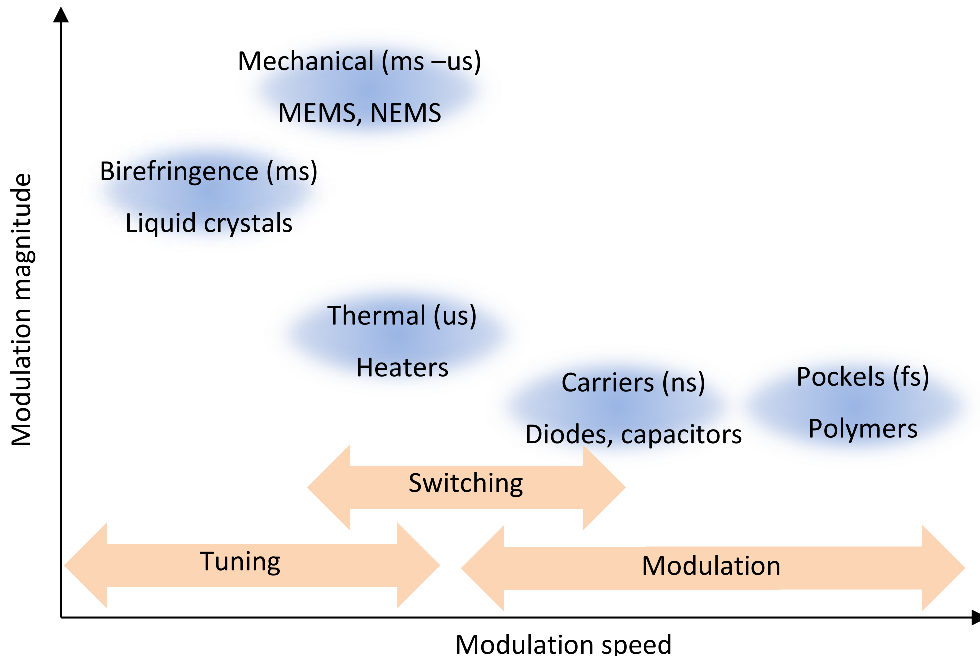

Figure 2-4 Various modulation mechanisms compared w.r.t. their speed and magnitude of modulation.

A basic outline for the application of various modulation mechanisms is shown in Figure 2-4 on the basis of their modulation speed and magnitude which usually decides the target applications. The following section describes the fundamental working physics and literature for these modulation mechanisms.

2.2.1.1 Plasma Dispersion Effect

Plasma Dispersion effect involves changing the concentration of free carriers in silicon, which in turn changes both the real and the imaginary part of the refractive index. These changes have been defined at 2 different telecommunication wavelengths [45], at $\lambda_0 = 1300$ nm.

$$\Delta n = \Delta n_e + \Delta n_h$$

$$= -[6.2 \times 10^{-22} \Delta N_e + 6.0 \times 10^{-18} (\Delta N_h)^{0.8}]$$

$$\Delta \alpha = \Delta \alpha_e + \Delta \alpha_h$$

$$= 6.0 \times 10^{-18} \Delta N_e + 4.0 \times 10^{-18} \Delta N_h$$

Where, Δn_e and Δn_h represent the changes in real part of refractive index resulting from changes in free electron and free hole carrier concentration, respectively and $\Delta\alpha_e$ and $\Delta\alpha_h$ represent the change in imaginary part of the refractive index (absorption).

For λ_0 = 1550 nm, the relations are

$$\Delta n = \Delta n_e + \Delta n_h$$

$$= -[8.8 \times 10^{-22}\Delta N_e + 8.5 \times 10^{-18}(\Delta N_h)^{0.8}]$$

$$\Delta\alpha = \Delta\alpha_e + \Delta\alpha_h$$

$$= 8.5 \times 10^{-18}\Delta N_e + 6.0 \times 10^{-18}(\Delta N_h)$$

Different structures (as shown in Figure 2-5) like carrier injection, carrier accumulation and carrier depletion have been implemented to achieve this change in free carrier concentration in silicon. All three structures use doping of Silicon to fabricate some form of PN junction along the cross section of the optical path.

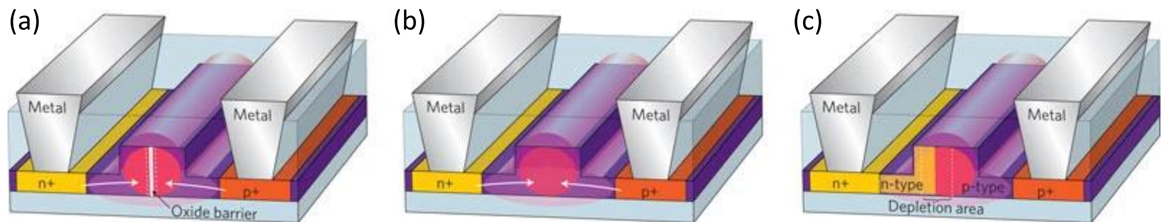

Figure 2-5 P-i-N Modulators based on (a) Carrier accumulation, (b) Carrier Injection, and (c) Carrier depletion. Image reproduced from [46]

Carrier injection structure utilizes a P-I-N junction structure with heavily doped P+ and N+ regions to inject electrons and holes in the intrinsic region on application of forward bias voltage. The resultant change in the carriers inside the intrinsic region interacts/overlaps with the optical mode to produce modulation. These types of devices benefit from high modulation efficiency when implemented on a strongly confining, small waveguide cross section due to their large diffusion capacitance (~10 pF). Devices using lateral and vertical PIN configuration have been reported[47].

One drawback of these devices is the temperature rise when large injection current and power is consumed, which causes heat and results in opposite modulation effect due to thermo-optic effect [48, 49]. The speed of such modulators is limited to around 1 GHz [50] and defined by the slower of the two factors which are (a) the injected electron-hole pair recombination time, (b) the sum of electrical driver output resistance and the bulk resistance of the doped regions [51].

Total capacitance of the p-n junction diode is given by the sum of depletion capacitance and diffusion capacitance as shown in Figure 2-6. Diffusion capacitance of the diode dominates in the forward bias regime defining the maximum switching speed (around few GHz) of carrier injection modulator devices. Whereas, in reverse bias operation (as in the case of depletion modulators explained next), depletion capacitance dominates leading to higher switching speeds.

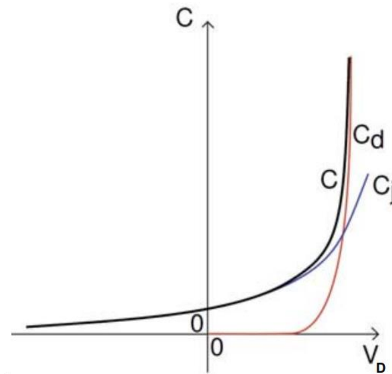

Figure 2-6 Diffusion capacitance (C_d) and depletion capacitance (C_j) of the p-n junction diode w.r.t. drive voltage V_D. Image reproduce from [52]

Using pre-emphasis the device speed (and power consumption) can be improved to 12.5 Gb/s [53]. Recently passive equalization techniques have been developed to increase the high speed operation of these modulator type with current state of the art injection modulators demonstrating > 20 Gb/s operation [51, 54]. Using passive RC equalization, modulator with 0.25 mm phase shifter, ~28 dB/cm loss, 37 GHz 3 dB bandwidth and V_π·L of 2 V·cm have reported [51]. The best modulation efficiencies of 0.274 V·cm has been reported for a 250 µm long phase shifter with corrugated side wall in a MZ configuration operating at 25 Gb/s and exhibited a propagation loss of 5.3 dB/mm [55].

Carrier depletion devices operate the P-N junction in reverse bias [56] and is the most widely implemented scheme utilizing the plasma dispersion effect. It depletes the junction of free carriers to produce change in the free carrier concentration. These are based on majority carriers offering much higher speeds (> 50 Gb/s) [57] and the present highest reported data rates of 100 Gb/s On-Off keying (OOK) were demonstrated using this modulation scheme. Their modulation efficiency is limited by the capacitance (0.2 - 0.8 pF/mm [58, 59]) which can be increased by shrinking the waveguide geometry or, by reducing the width of the depletion region, which requires higher doping concentrations leading to higher free carrier absorption loss. They offer comparatively low modulation efficiency, thereby increasing the device power consumption and footprint.

Carrier accumulation devices have a thin dielectric layer between the P-N junction forming a metal-oxide-semiconductor (MOS) capacitive structure. Typical implementations of these type of modulators (also called silicon-insulator-silicon capacitor or SISCAP) consists of a vertical slot waveguide where positively doped poly-silicon and negatively doped crystalline silicon surrounds a few nanometers thick gate oxide (<20nm) in the middle from top and bottom respectively. Under accumulation conditions, majority carriers are responsible for change in the refractive index [60, 61] and are hence free from the carrier generation and recombination speed limitation on the injection type device. On application of a positive bias to the structure, the optical mode overlap with the capacitive gate section enables modulation efficiency of <1 V.cm [62] with the best values published under 0.2 V.cm [63, 64] . The thickness of the gate oxide layer decides the trade-off between the modulation efficiency (higher capacitance) and modulation speed (lower capacitance) [65, 66]. Due to the high modulation efficiency, the phase shifters with lumped electrical driving and short lengths are typically used.

A performance summary of above discussed modulation mechanisms is presented in Table 1.

Table 1 Typical performance for plasma dispersion based modulators (partially reproduced from [47]).

Mechanism	**Modulation efficiency $V_{\pi}\cdot L$**	**Phase shifter length (mm)**	**Data rate (Gb/s)**
Carrier Injection	<0.5	0.1<l<0.3	~1
Carrier accumulation	<0.3	<0.5	~40
Carrier depletion	~2	>1	>40

2.2.1.2 Franz- Keldysh Effect and Quantum Confined Stark effect

Tilting of band edge upon application of electric field occurs in GeSi bulk material (Franz-Keldysh effect -FKE [67, 68]) or Ge/SiGe quantum well structures (Quantum Confined Stark effect -QCSE [69] [70]) as shown in Figure 2-7. This leads to enhancing the absorption coefficient of the respective structures in which photon with energy $E<E_g$ can allow tunnelling of valence band electrons to conduction band. Here E refers to the band gap energy of bulk material or quantum well without any applied electric field. This result in a change in the absorption properties of the

material around the bandgap. Both the effects can be implemented in compact, low power, high speed EAM modulators.

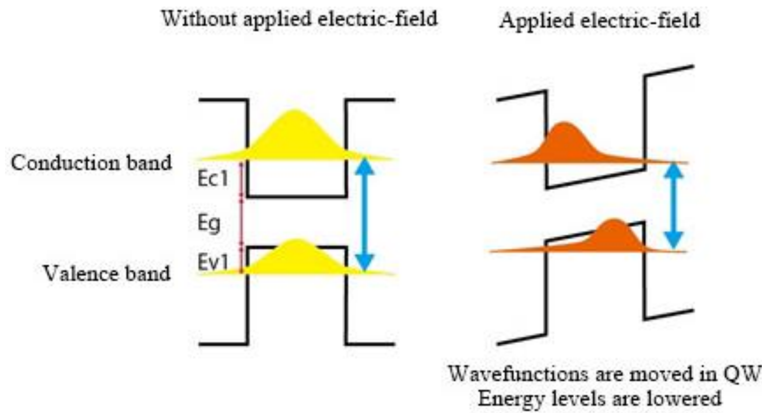

Figure 2-7 QCSE - Tilting of energy bands and wavefunction allowing photons with energy less than the band gap to be absorbed, in the presence of applied electric field. Image taken from [71].

The speed of both these effects is intrinsically fast with sub-picosecond response but QCSE is stronger than FKE [72] due to the strong exciton effect and discretized density of states. They both rely on bang gap engineering and hance have a limited optical bandwidth of ~30 nm for FKE and ~20 nm for QCSE.

Because of direct bandgap of Germanium around 1550 nm, it is a good candidate for FKE while also allowing for integrated active silicon devices. Various schemes for maximizing the modulation efficiency for the required wavelength band have been reported such as growing GeSi alloy and by engineering the strain while growing the alloy[73, 74].

Stark effect is the splitting of atomic spectra upon the application of electric field. Quantum wells are periodic structures of nm thickness, surrounded by barrier layers of different material or composition, which can be engineered using epitaxial growth techniques. Example of this is a thin Germanium layer stacked between SiGe alloys with low silicon concentration (~0.2) which causes the motion of electrons and holes to one direction when germanium layer thickness is of the order of de-Broglie wavelength of the electron wave function. In quantum well structure, the confinement energy is inversely proportional to the square of the well thickness, hence the band gap energy increases with decrease in Germanium well thickness[75].

2.2.1.3 Pockels Effect and Kerr Effect

Pockels effect is a linear electro-optic effect, but due to the centro-symmetric crystal structure of silicon, it does not exhibit strong electro optical effect. However, strain can be introduced by depositing silicon nitride at top of the silicon waveguide and allow for modulation based on this effect to be used in silicon. Asymmetrical crystal structure material like Lithium niobate ($LiNbO_3$) based modulators have been used for amplitude and polarization modulation. Other modulators include polymers and other compounds deposited on silicon waveguides to achieve compact design and fast modulation speeds.

In Kerr effect the refractive index change is proportional to the second order of the applied electric field and is relatively week in silicon. Silicon slot waveguides filled with silicon nanocrystal embedded in silica has been used to realize a Kerr effect based modulator [76].

2.2.1.4 Thermo Optic effect

The Thermo optic coefficient of Si can be used to change its refractive index and utilized in devices performing as tuneable switches for lossless optical networks [77, 78] and modulators [46]. The speed response of these devices are of the order of tens of milliseconds [79] too slow for high frequency signal transmission for modern telecommunication applications as they suffer from slow heat dissipation [80] due to the heat conductivity of silicon, which is about 1.4 W/(cm K).

$$\frac{dn}{dt} = 1.86 \times 10^{-4} K^{-1}$$

Primarily, two main types of Thermo optic phase shifters (TOPS) have been reported in the literature as shown in Figure 2-8 . One utilizes a metal heating bar on top of the waveguide and the other uses doped Si strips on both sides of the waveguide to produce temperature change.

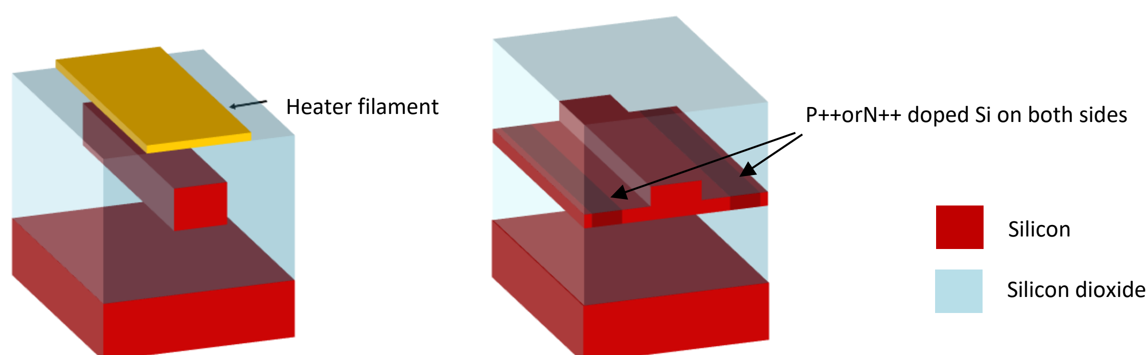

Figure 2-8 Typical implementations of TOPS (a) Metal bar on top of waveguide, (b) doped silicon on both sides of the waveguide.

SOI structures are largely beneficial for the power consumption of the TOPS as the heat conductivity of silicon dioxide is about one percent of that of silicon. However, much of the heat still leaks on to the surrounding due to the small thickness of the buried oxide layer which is around 2 µm [81]. To overcome this, thermal insulation of the waveguide from the substrate using an undercut has been performed previously giving a huge reduction (about 1/10th compared to conventional designs) in the phase shift power requirements but at the cost of fabrication complexity, increased production cost and difficulty, and slower response time (~ hundreds of microseconds). Typical power consumption of metal bar and doped silicon based heaters are of the order of 20 mW/π, and the undercut devices power consumption are of the order of 1-2 mW/π or lower[82] with response time of upwards of 100 µsec.

The first thermal switching device using single mode waveguide and Cr/Au heater filament were demonstrated in 260 nm SOI having a switching power of 50 mW and rise time < 3.5 us [83]. Extending the concept compactly packed waveguides in a spiral (Figure 2-9(c)) have been demonstrated to reduce the switching power to 6.5 mW with a rise time of 14 us [80]. Similar folded waveguide designs has been demonstrated to further improved the switching power to 3.8 mW/π [84] with 9 folded waveguides and 2.56 mW using 14 folded waveguides (Figure 2-9(b)) [81]. Another interesting approach has been demonstrated recently by recycling the light through a bus waveguide by using directional couplers and mode upshifting [85] with reported switching power of 1.7 mW using 7 passes.

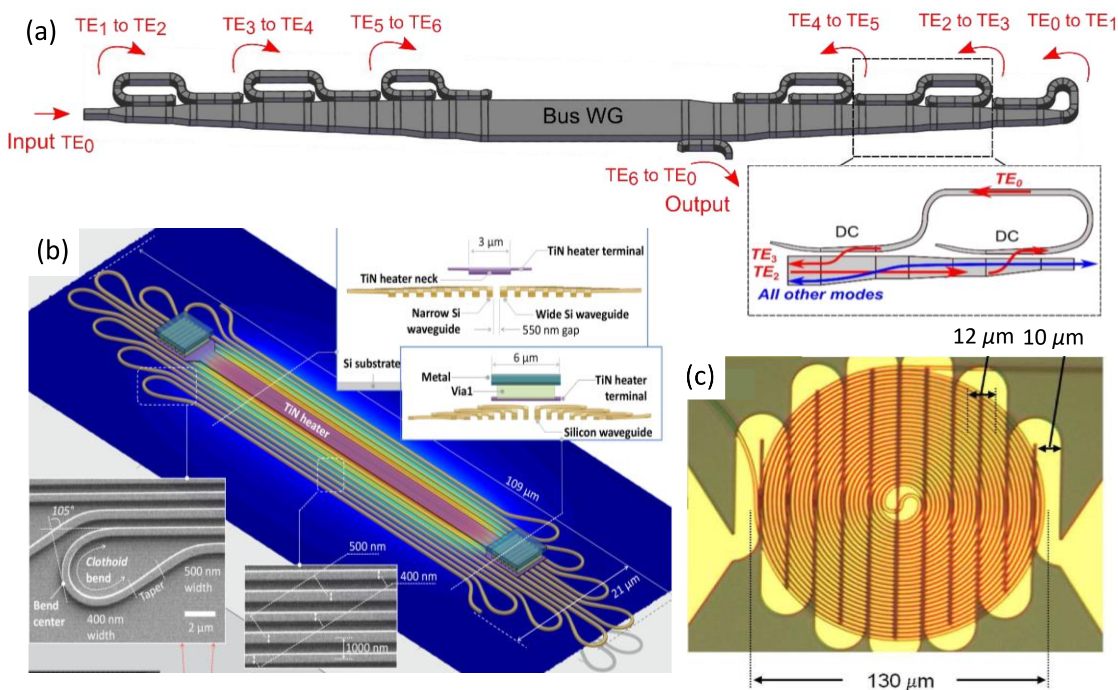

Figure 2-9 Thermal switch using (a) light recycling (Image reproduced from [85]), and densely packed waveguides using (b) 14 folded waveguides (Image reproduced from [81]), and (c) folded waveguide in a spiral structure (Image reproduced from [80]).

Thermal isolation of the waveguide and heater from the Si substrate has been reported [86] [87] [88] [89] to reduce the power consumption to about 0.5 mW [90] and 95 μW [84].

2.2.2 MEMS/NEMS photonic modulators

Another interesting mechanism commonly used for light switching utilizes Micro-electronic-mechanic-systems (MEMS) sometimes also referred to as Micro-opto-electronic-mechanic-systems (MOEMS). MOEMS devices for optical switching can be broadly classified into two different categories. The first utilizes reflection or refraction of light for intensity or directional variation for example MARS attenuator [91] , while the other uses mechanical motion to couple light or for changing the phase of light combined with diffraction or interference effects to obtain switching.

An example of first type was demonstrated by [92] using micro mirrors of size 300 µm x 600 µm supported by torsion polysilicon beams in a 2x2 configuration. The switching time and crosstalk reported were greater than 5 ms, 60 dB respectively with voltage of 100 ~ 150 V for actuating the mirror and 50 V holding voltage. Another 2x2 switch configuration is shown in Figure 2-10 (a). It consists of a sliding vertical mirror placed between 4 fibres and uses motion of a mirror (reflecting on both sides) to move the beam to desired output [93, 94]. Switching time of 0.2 ms was reported.

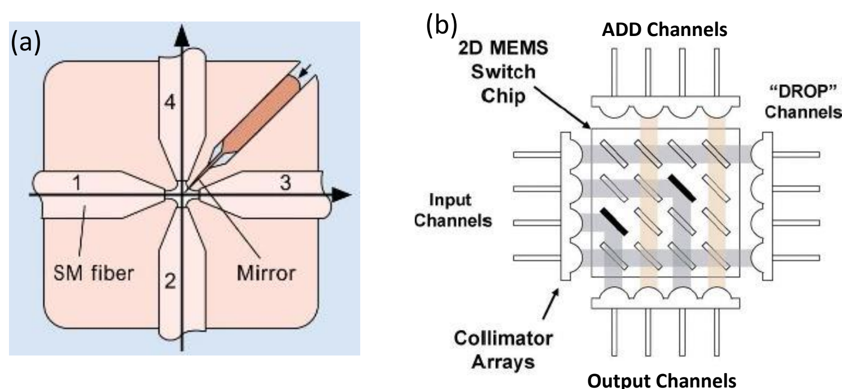

Figure 2-10 (a) 2x2 micro machined bypass switch denoting motion of the mirror, (b) 2D MEMS Add-Drop optics switches. Image reproduced from [93] and [95].

[96] Demonstrated a 4x4 switch configuration using free rotating hinged mirror with dimensions 150 x 140 µm^2. They reported an OFF to ON time of 500 µs, ON to OFF time of 560 µs with a extinction ratio and crosstalk between the channels greater than 60 dB and a coupling loss of around 15 dB The higher port version of this, utilizing similar switching methods is shown in Figure 2-10 (b).

Other approaches [93, 94, 97] have been used to successfully push the technology but to low impact. The main drawbacks of these free space optic devices are the scalability, gaussian beam optics and drift issue due to temperature and vibration which requires active feedback control for precise alignment of the mirrors arrays.

The second type discusses the quest for on chip switches which utilize segmented, coupled waveguides or their derivatives, and use electrostatic forces for their mechanical movement.

2.2.2.1 Electrostatic mechanism

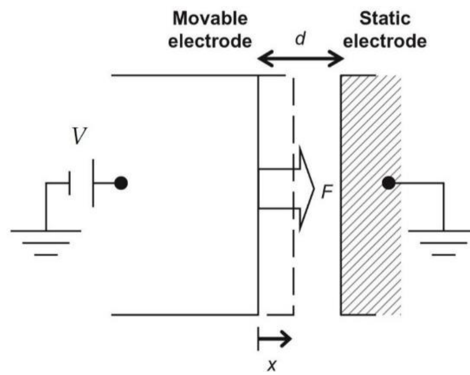

Figure 2-11 Parallel plate capacitor model for electrostatic forces. Image reproduced from [98].

The basics of electrostatic force are explained using a parallel plate capacitor model as shown in Figure 2-11 [99].The model consists of 2 electrodes separated by a distance d from each other filled with non-conducting material. One of the electrode is free to move but other is fixed. A voltage V is applied between the electrodes which stores energy in the form of

$$E = \frac{1}{2} C_0 V^2 \qquad 2.1$$

Where ε is the permittivity of the dielectric material and C_0 is the capacitance given by

$$C_0 = \varepsilon \frac{A}{d} \qquad 2.2$$

And ε is the permittivity of the dielectric material, A denotes the effective area of the electrode. If the gap is reduced by x, the capacitance changes to

$$C = \varepsilon \frac{A}{d - x} \qquad 2.3$$

The electrostatic force in this case can be written as negative gradient of energy.

$$F = -\frac{V^2}{2} \frac{\partial C}{\partial x} \qquad 2.4$$

Which can be expanded in Taylor series to give

$$\vec{F} = -\frac{V^2}{2d}C_o\left[1 + 2\left(\frac{x}{d}\right) + 3\left(\frac{x}{d}\right)^2 + 4\left(\frac{x}{d}\right)^3 + \cdots\right] \quad 2.5$$

The above equation infers that the force is dependent on square of the applied voltage. Considering that the applied voltage is a combination of ac + dc bias voltage of the form

$$V = V_{\{dc\}} + V_{\{ac\}}\cos(wt) \quad 2.6$$

Which gives dependence of force as following

$$F \propto V_{dc}^2 + \frac{V_{ac}^2}{2} + (V_{ac}^2)\, 2\cos(2wt) + 2\, V_{dc}\, V_{ac}\cos(wt) \quad 2.7$$

This mechanism has been extended to yield further actuation mechanisms such as comb drive actuator [100, 101].

Figure 2-12(a) shows two early proposed MOEMS modulators. Applied voltage between the substrate and the waveguide (formed by beam/cantilever) causes the deflection due to electrostatic force and couples the light out of the waveguide. [2] reported fabricated device with a 4780 µm cantilever and 12 dB contrast ratio between the on and off state for applied 10 V.

Also, coupler configurations have been used to demonstrate routing of light by changing the distance between the waveguides [102, 103]. Figure 2-12(b) shows one of the configuration. The reported response time are 2.5 µs for on state and 3.8 µs for off state. Similar coupled waveguide structures have been reported in [104-106].

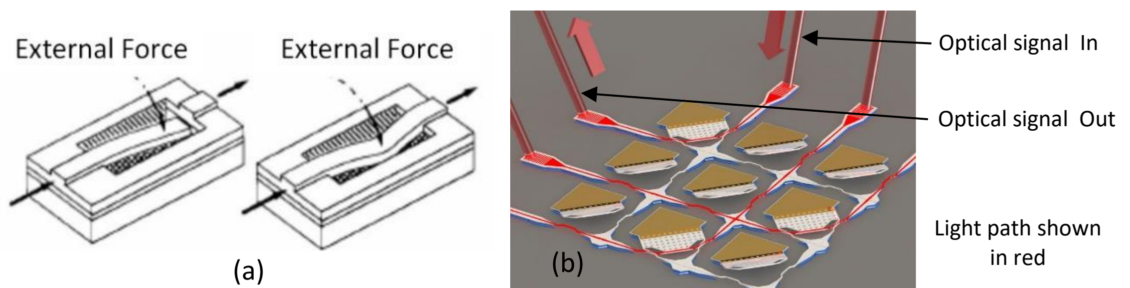

Figure 2-12 (a)Initial MOEMS devices proposed for optical modulation, (b)Light coupling based optical routing methods using MEMS/NEMS. Image reproduced from [2] and [102].

Phase modulation can also be achieved by deformation of free standing silicon waveguides (silicon wires). As shown in Figure 2-13(a), upon application of bias voltage, the deformation of optical waveguide causes stress on the material and optical path to be extended resulting in a phase change. For such structures, 0.18π phase shift has been reported [107] for a 150 µm long silicon wire with a bias of 35 V and a rise time of 1.5 ms. A cascaded configuration of 6 of such deformable structures was demonstrated [108] to achieve a phase change of 0.4 π with applied

voltage of 200 V. The reported power consumption was smaller than 0.2 mW, due to the leakage current of 1 μA with a rise time of 88 μsec.

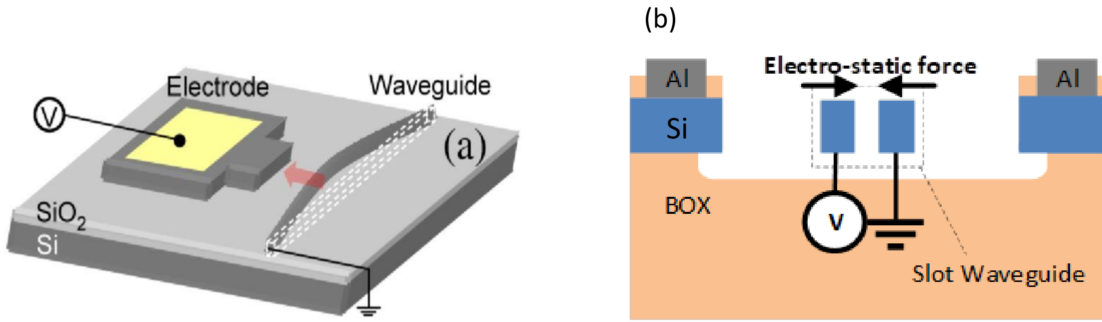

Figure 2-13 (a)Deformable silicon wire phase modulator. Image reproduced form [92]. (b)Cross section of under-etched slot waveguide used as modulator.

As shown in Figure 2-13(b), electrostatic forces can be used to move free standing slot waveguide structures for phase modulation [109]. The response speed is limited by the factors such as damping of the mechanical resonance by gasses, intrinsic losses due to defects, and clamping losses.

[110] Demonstrated the devices fabricated on 220 nm SOI waveguides having 2 μm BOX. The slot waveguides were 9 μm long free-standing waveguide, 230 nm wide beams and a slot gap of 100 nm. A phase change of 0.33π was reported for an applied voltage of 15 V and the dynamic characteristics were not reported. A cascaded configuration of three 5.8 μm length of free standing slot waveguides was demonstrated by [111] with reported phase change of 0.22π for an applied voltage of 13 V. The reported air damping time for the structure was 37 ns leading to MHz operation.

Wavelength selective on/off switching has been demonstrated using a movable aluminium membrane around the evanescent field of a silicon nitride ring resonator [112]. Wavelength tuning by changing the refractive index around the evanescent field (i.e. modal propagation) of a ring resonator using a MEMS cantilever has also been demonstrated [113].

A reconfigurable optical network using slot waveguide based photonic ring resonator has been demonstrated [114]. Out of plane electrostatic actuation was used to achieve 10 selectable channels in the range of 1 nm with static power dissipation less than 0.1 μW, and a bandwidth of 0.1 nm (Figure 2-14). The reported power performance is orders of magnitude below the reported values for thermally tuned rings and they also do not suffer from thermal crosstalk, allowing dense integration. Resonance wavelength tuning improvements were reported in [115].

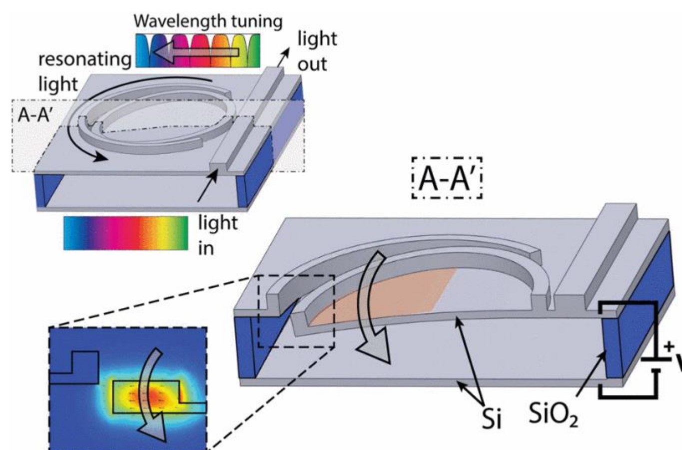

Figure 2-14 Schematic of MEMS tuneable ring resonator. Actuation of free standing cantilever forming part of the slot waveguide ring resonator changes the refractive index, resulting in resonance wavelength shift. Image reproduced from [114].

In this work, the attention is focussed on two different pathways for low power optical phase shifter devices. In the first approach, light recycling in the multimode region of an MMI have been utilized to increase the modulation efficiency. Although, similar light recycling approaches have been outlined previously, all of them work with single mode transmission. The light recycling based reported device in this work utilize multimode operation in the modulation region which can be advantageous in specific cases such as the thermal phase shifters. In such cases, width of the heating component smaller than the waveguide is preferred but is limited to micro-meter range due to fabrication constrains. For applications requiring speeds greater than offered by thermal devices, carrier injection devices have been investigated with comparable switching times to standard single mode modulator structures.

The second approach utilizes the MEMS/NEMS approach of utilizing free standing slot waveguides as reported in section 2.2.2 with study/integration of passive components and modulator devices incorporated in a MZI. Various passive components such mode converters to-and-from the slot waveguides, modulator designs, electrical isolation from other reported works have been absorbed and utilized as a starting point for delivering a platform for MEMS/NEMS optical phase modulators.

In summary, throughout this chapter we have reviewed various commonly used modulation mechanisms and their performance parameters. An exhaustive list of such devices can be found in [47, 79, 116, 117]. These optical modulators are implemented in various interference devices such as MZI, Michaelson interferometers, ring resonator, photonic crystal resonator, Fabry-Perot resonator etc, some of which are covered in the following chapter.

Chapter 3 Modulator device configurations, Simulation and Experimental tools

Electro-optical modulator devices modulate the optical signal (phase, power, polarization) in response to applied external electrical signal. The requirement for the performance of the modulators are high modulation efficiency and CMOS complaint drive signal circuitry [118]. For optical phase modulators, these are integrated on interferometric structures such as MZI, resonant optical cavities like ring resonator, Michelson and Fabry-Perot cavity which convert the optical phase modulation to amplitude modulation.

Ring resonators provide compact and low power modulation schemes but are limited by their temperature and fabrication tolerances, and narrow operation wavelength range. Other approach using slow light modulator structures provide reduced footprint/power consumption, but also suffer small wavelength bandwidth and fabrication and temperature sensitivity [119]. In comparison, the Mach-Zehnder Interferometer offers a broadband response (due to the broadband components that make up the MZI) and high thermal stability. Any ambient/unwanted temperature change is cancelled due to the presence of two arms. They require considerably large dynamic power compared to others. The basic working principle is discussed in the following section.

3.1 Mach-Zehnder Interferometer (MZI)

Mach Zehnder Interferometer is widely used to convert an optical phase shift into an optical intensity change which can be recorded by a photodetector. The schematic layout of a 1x2 MZI is shown in Figure 3-1. The input light is split evenly into two separate paths (also called the arms of the MZI), often realized using Y junctions or 1x2 MMI. The path lengths can be chosen to be different from each other (called imbalanced MZI), giving rise to a phase difference between the two traversed paths where they can also be manipulated by an active component for example PIN injection, depletion modulators etc. After traversing, light from both these arms is recombined and results in intensity variation at the output depending on the phase difference between the two arms, due to their coherence.

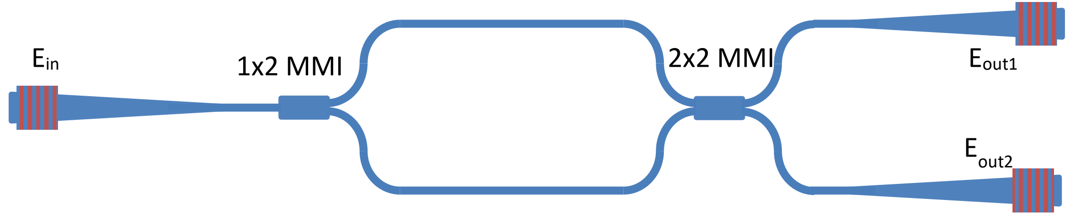

Figure 3-1 Schematic diagram of a 1x2 balanced MZI.

The transfer function of a 1x2 MZI response is defined as,

$$\begin{bmatrix} E_{OUT1} \\ E_{OUT2} \end{bmatrix} = M_{1X2\ MZI} \,.\, E_{IN}$$

$$= \begin{bmatrix} \frac{1}{\sqrt{2}} & -\frac{1}{\sqrt{2}} \\ \frac{1}{\sqrt{2}} & \frac{1}{\sqrt{2}} \end{bmatrix} \begin{bmatrix} \tau_1\, e^{j(\omega t - \phi_1)} & 0 \\ 0 & \tau_2\, e^{j(\omega t - \phi_2)} \end{bmatrix} \begin{bmatrix} \frac{1}{\sqrt{2}} \\ \frac{1}{\sqrt{2}} \end{bmatrix}$$

$$= \frac{1}{2} \begin{bmatrix} \tau_1\, e^{j(\omega t - \phi_1)} & -\tau_2\, e^{j(\omega t - \phi_2)} \\ \tau_1\, e^{j(\omega t - \phi_1)} & \tau_2\, e^{j(\omega t - \phi_2)} \end{bmatrix}$$

Here $\tau_n\, e^{j(\omega t - \phi_n)}$ represents the wavefunction with τ being the amplitude and ϕ the phase of the light signal.

Therefore, the relation between the two output arms can be written as,

$$\begin{bmatrix} E_{OUT1} \\ E_{OUT2} \end{bmatrix} = \begin{bmatrix} \frac{1}{2}\left(\tau_1\, e^{j(\omega t - \phi_1)} - \tau_2\, e^{j(\omega t - \phi_2)}\right) \\ \frac{1}{2}\left(\tau_1\, e^{j(\omega t - \phi_1)} + \tau_2\, e^{j(\omega t - \phi_2)}\right) \end{bmatrix}$$

$$\left[\frac{I_{OUT\,1}}{I_{IN}}\right] = \left(\frac{E_{OUT1}}{E_{IN}}\right)^2$$

$$= \frac{1}{4}\left[\tau_1\, e^{j(\omega t - \phi_1)} - \tau_2\, e^{j(\omega t - \phi_2)}\right].\left[\tau_1\, e^{j(\omega t - \phi_1)} - \tau_2\, e^{j(\omega t - \phi_2)}\right]^*$$

$$= \frac{1}{4}\left[\tau_1\, e^{j(\omega t - \phi_1)} - \tau_2\, e^{j(\omega t - \phi_2)}\right].\left[\tau_1\, e^{-j(\omega t - \phi_1)} - \tau_2\, e^{-j(\omega t - \phi_2)}\right]^*$$

$$= \frac{1}{4}\left[\tau_1{}^2 + \tau_2{}^2 - \tau_1\tau_2\, e^{j(\phi_1 - \phi_2)} + \tau_2{}^2 - \tau_1\tau_2\, e^{j(\phi_2 - \phi_1)}\right]$$

$$= \frac{1}{4}\left[\tau_1{}^2 + \tau_2{}^2 - 2\tau_1\tau_2 \cos(\phi_1 - \phi_2)\right]$$

Similarly, for output 2,

$$\frac{I_{OUT2}}{I_{IN}} = \left(\frac{E_{OUT2}}{E_{IN}}\right)^2$$

$$= \frac{1}{4}[\tau_1{}^2 + \tau_2{}^2 + 2\tau_1\tau_2 \cos(\phi_1 - \phi_2)]$$

Assuming that there is no loss while light propagates in both the arms, $\tau_1 = \tau_2 = 1$

$$\frac{I_{OUT1}}{I_{IN}} = \frac{1}{2}[1 - \cos(\phi_1 - \phi_2)]$$

$$= \sin^2(\frac{\phi_1 - \phi_2}{2})$$

$$= \sin^2(\frac{\Delta\phi}{2})$$

$$\frac{I_{OUT2}}{I_{IN}} = \frac{1}{2}[1 + \cos(\phi_1 - \phi_2)]$$

$$= \cos^2(\frac{\phi_1 - \phi_2}{2})$$

$$= \cos^2(\frac{\Delta\phi}{2})$$

The transfer function of the MZI can be represented by sinusoidal function with dependence on the phase difference between two arms which can be represented by Figure 3-2. The phase difference due to the electro optic modulator (present in one or both the arms) is hence converted into intensity variation detected by the photodetectors at the output.

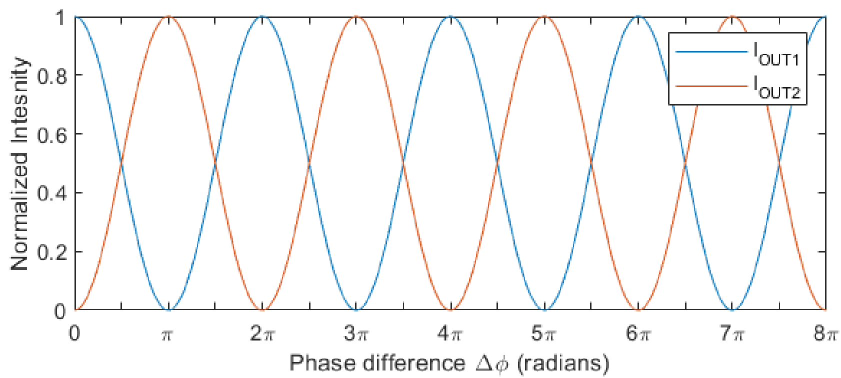

Figure 3-2 Normalized intensity response of an ideal MZI with changing phase.

3.1.1 MZI Free Spectral Range (FSR)

In the case of an unbalanced MZI, the two arms have different optical path length which is achieved by varying the effective refractive index or the dimensions (length etc). This results in

$$E = E_0 e^{j(\omega t - \beta' z)}$$

Where the complex propagation constant $\beta' = \frac{2\,\pi\, n_{eff}(\lambda)}{\lambda} - i.\frac{\alpha}{2}$

For the propagation velocity, only the real part needs to be investigated.

$$E = E_0 e^{j(\omega t - \beta z)}$$

And the propagation constant is defined as, $\beta = \frac{2\,\pi\, n_{eff}(\lambda)}{\lambda}$

$$\omega = 2\pi f = 2\pi\,\frac{c}{\lambda}$$

Phase velocity is defined as the propagation velocity of the carrier wave,

$$v_{ph}(\lambda) = \frac{\omega}{\beta} = \frac{c}{n_{eff}(\lambda)}$$

Group velocity of the signal is defined as,

$$v_g(\lambda) = \frac{d\omega}{d\beta} = \left(\frac{d\beta}{d\omega}\right)^{-1}$$

$$= c\left[\frac{d}{d\,\frac{1}{\lambda}}\,\frac{n_{eff}(\lambda)}{\lambda}\,.(-\lambda^2)\right]^{-1}$$

$$= c\left[\frac{d}{d\lambda}\,n_{eff}(\lambda)\,.(-\lambda^2)\right]^{-1}$$

$$= c\left[\,n_{eff}(\lambda) - \lambda\left(\frac{d}{d\lambda}\,n_{eff}(\lambda)\right)\right]^{-1}$$

$$= \frac{c}{n_g}$$

Where, $n_g = n_{eff}(\lambda) - \lambda\left(\frac{d}{d\lambda}\,n_{eff}(\lambda)\right)$

The FSR is the wavelength difference between adjacent transfer function peaks. For an imbalanced MZI with an arm difference of ΔL, assuming no other phase modulation,

$$FSR = \lambda_{m+1} - \lambda_m$$

The adjacent peaks are spaced 2π phase apart.

$$\frac{\pi}{FSR} = \frac{\frac{\phi(\lambda_{m+1})}{2} - \frac{\phi(\lambda_m)}{2}}{\lambda_{m+1} - \lambda_m}$$

$$\frac{1}{FSR} = \frac{\Delta L}{2\pi}\frac{\beta(\lambda_{m+1}) - \beta(\lambda_m)}{\lambda_{m+1} - \lambda_m}$$

$$\cong \frac{\Delta L}{2\pi}\frac{d\beta}{d\lambda}$$

$$= \frac{\Delta L}{2\pi} . 2\pi \left[\frac{1}{\lambda}\frac{d}{d\lambda}n_{eff}(\lambda) - \frac{1}{\lambda^2}n_{eff}(\lambda)\right]$$

$$= \frac{\Delta L}{\lambda^2}\, n_g$$

$$FSR = \frac{\lambda^2}{\Delta L \,.\, n_g}$$

3.2 Ring Resonators

The ring resonator consists of a cavity or ring shaped waveguide in close proximity of an input bus waveguide to facilitate evanescent coupling. An example of carrier injection optical phase modulator utilizing a ring resonator is shown in . Light propagating with integer multiple of wavelength over a round trip inside the ring and builds up in amplitude. This gives rise to a notch filter response, and changing the refractive index of the cavity causes a change in the resonance condition. A phase shifter is incorporated in the ring waveguide structure which upon actuation results in intensity changes at the output at a particular wavelength.

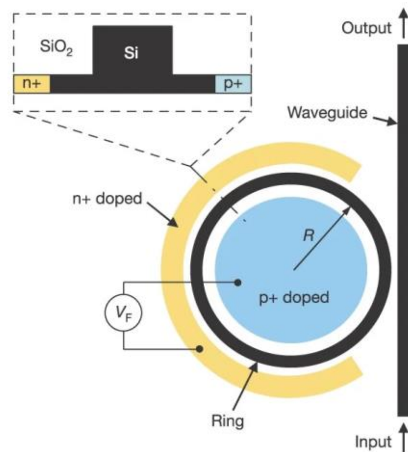

Figure 3-3 Schematic layout of a ring resonator based modulator (waveguide cross section on the top left). Image reproduced from [120].

Ring resonators are promising candidates in integrated optical systems due to their compactness, fabrication ease, high Q factor and their potential for dense integration. Their disadvantages being narrow operational bandwidth (~100pm) and need for active tuning of resonant wavelength for compensation against fabrication errors, temperature variations.

3.3 Standard Metrics

The following section describes some common performance metrics used widely to define the performance of devices with varying design and operation. The fundamental electro-optic metrics are modulation efficiency, insertion loss, modulation depth, power consumption, 3dB bandwidth, and rise and fall time.

3.3.1 Modulation Efficiency

The modulation efficiency is defined as the $V_\pi \cdot L_\pi$ product, where V_π and L_π are the voltage and length required for π phase shift of the light signal. Generally, the modulator design optimizes the power requirements by reducing the V_π and/or the footprint by reducing the L_π. A typical way to increase the efficiency is by increasing the mode overlap within the optical modulator element.

3.3.2 Insertion Loss (IL) and Extinction Ratio (ER)

Insertion loss refers to the optical transmission loss due to the device/component. It comprises of material absorption, scattering loss, coupling loss, propagation loss and interface loss within the device. It is defined mathematically as the ratio of the output signal power (P_o) to the input signal power (P_i)

$$IL\ (dB) = 10\log(\frac{P_o}{P_i})$$

The optical modulation properties are measured by driving the modulator with an external electric signal. Extinction ratio is defined as the ratio between highest (P_h) and lowest (P_l) power of the optical signal.

$$ER\ (dB) = 10\log(\frac{P_h}{P_l})$$

3.3.3 Dynamic Extinction Ratio

An eye diagram is used to measure the dynamic extinction ratio and working speed of a device [121]. Larger separation between the low and high signal levels is required for a better bit error

rate (BER) and permits a longer transmission path. Other factors such as jitter, rise time (10 to 90 % of signal peak), fall time (90 to 10 % of the peak signal) also contribute to the device performance.

3.3.4 Dark Current

Dark current increases the static power consumption and thereby reduces the performance and reliability of modulator devices. Various contributors to this are bulk diffusion current, surface currents flowing along the surface paths of the device and current due to the recombination of minority carriers in the depletion layer [122, 123]

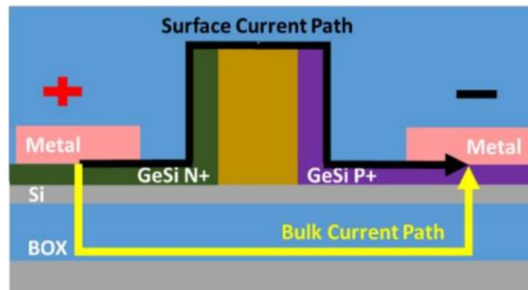

Figure 3-4 GeSi electro absorption modulator based on Franz-Keldysh effect showing dark current pathways in the device [124]. Image reproduced from [125] .

Power consumption is usually measured in energy per bit. In the case where thermal stabilization or tuning is required, such as in ring resonators, this power should also be taken into account. The highest operating speed of the device is defined by the frequency at which the response is reduced by 3dB.

3.4 Characterization setup

Figure 3-5 gives a basic block layout of the lab setup used for device characterization.

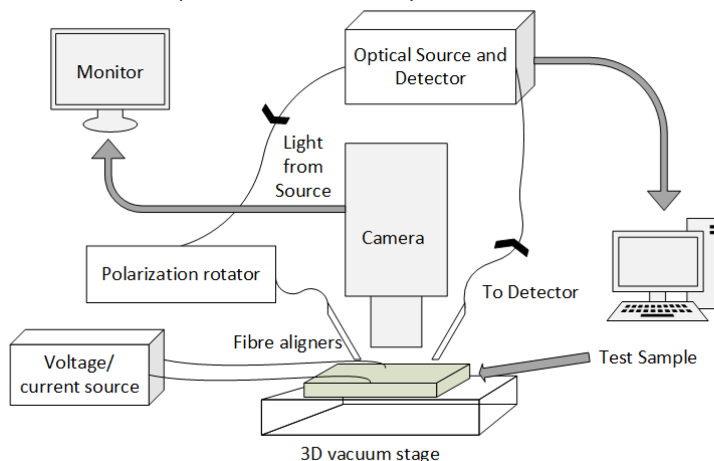

Figure 3-5 Lab setup for characterizing samples.

The setup consists of a Keysight 8163B lightwave multimeter connected to a computer for controlling the laser source, detector, and accessing and saving the data. The source is an InGaAsP EC tuneable laser working in wavelength range of 1520 nm to 1630 nm with maximum CW output power of 20 mW. The detector operational power range is from +10 to -110 dBm. A Keithley power supply (Keithley 6487 Picoammeter/Voltage source) is used to drive the modulators in DC. An optical fibre couples the light from the source to the sample, passing through a polarization rotator. The light is then coupled to the grating couplers on the sample using fibre holders placed on 3-dimensional stage 'nanomax-TS-Thorlabs MAX 302'. The sample is held firmly on vacuum stage with thermal control. On top of the sample stage is a camera connected to a screen used for alignment of the fibre. The light signal is then coupled out through a fibre which connects it to the detector.

3.5 Cutback method

The cutback method is usually utilized for characterizing waveguide or component loss. The transmission measurements for incremental lengths of waveguide are taken and then plotted to give the loss per unit length of the waveguide. Similar approach is applicable on a device level, where transmission from an array with increasing number of devices is used to calculate loss per device. Figure 3-6 shows the array configuration used to calculate loss per device in future chapters of this work.

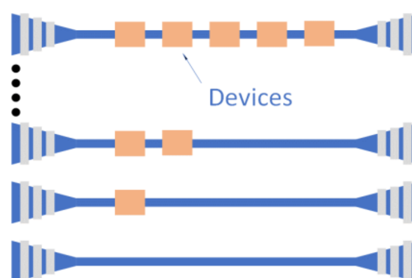

Figure 3-6 Illustration of cutback method to calculate the loss per device.

3.6 Device modelling and mask design tools and software

This section gives a brief overview of various methodologies, simulation tools and software packages and their applicability in device simulation, parameter extraction and mask designing used throughout the latter chapters in this work.

Eigenmode solvers provide time harmonic solutions to Maxwell's equation at a particular frequency for any waveguide geometry to give the transverse field distribution, also called the optical mode, that propagates along any given waveguide geometry. For generating the

wavelength response across a wavelength spectrum, various simulations are combined in approaches such as Finite Element Method (FEM), Finite Difference (FD), Effective Index Method [126] etc. Since silicon photonics structures consist of high index contrast waveguides, leading to a highly confined optical mode, fully vectorial techniques such as FEM and FD are particularly suitable. Various tools such as MATLAB Waveguide Mode Solver [127, 128], Lumerical MODE (now ANSYS) [129], COMSOL Multiphysics [130], Synopsys FemSIM [131], Photon Design FIMMWAVE [132] etc offer these capabilities.

The Finite Difference Time Domain (FDTD) method performs calculation of Maxwell equations by simulating a pulse of light (of ~ femtoseconds length), containing a broad wavelength spectrum, for a three dimensional (3D) structure [133]. The main disadvantage of this technique is its intensive computational resource requirement, but is particularly useful for studying light interaction in complex structures with sub wavelength scale features. In structures where one of the dimensions is not varying, two dimensional (2D) FDTD can be used to yield the solution using a comparatively short simulation time and less computational resources. For complex geometries such as photonic crystals and ring resonators, 2.5D FDTD approach can be used which combines 2D FDTD with the effective index method to model such devices with minimal errors and a quick simulation time [126].

The Eigenmode Expansion Method (EME) decomposes local fields at a particular point as a superposition of various modes, called as a super-modes and is particularly helpful in simulating long uniform cross section devices such as waveguides, MMI, couplers etc. Individual modes are propagated using the complex propagation constant and scattering parameters are used to calculate various coefficients between adjacent sections. Methods such as the Beam Propagation Method (BPM), Coupled Mode Theory (CMT), Transfer Matrix Method (TMM) [126] are also available but are not discussed here.

Mask layout is needed for transferring the required pattern onto the wafer. Usually lithographic tools such as electron beam, optical lithography, UV lithography are used depending on the minimum feature size needed. L-Edit [134] and K Layout [135] were used throughout this work to generate optical masks.

In this chapter we have reviewed the common optical modulator structures and standard metrics. Various testing and characterization tools have also been introduced along with the computational tools required for device simulation, design and mask patterning.

Chapter 4 Thermal optical modulators

This chapter details the extracting of additional phase change in thermal optical phase shift devices and improve the efficiency of such devices (compared to modulators with single pass through the modulating region). Usual approaches comprise of tightly packing waveguides [80] around the area where thermal change is generated using a heating element such as a metal strip. Other approaches involving light recycling utilizing mode upconverters and single mode guiding (different modes for each recycle) have also been demonstrated [85]. Both previously mentioned approaches usually consume large device areas which come at the price of device cost. Ring resonator based structures also utilize light recycling but suffer from a narrow operating bandwidth as well as fabrication and temperature variations and active tuning requirements.

Typical thermal devices constrains are width of the thermal heating element, which is restricted to ~ 2 µm because of the repeatability in fabrication. Since most devices in this scheme utilize single mode transmission waveguides (with width of ~ 0.5 um in SOI platforms), much of the thermal gradient generated by the heating element is not utilized in generating phase change. In other words the thermal gradient overlap with the optical guided mode is low. Our approach differs in the way that it uses multimode guiding of light in the modulation region (greater in width than the heating component) and utilizes the self-imaging property of MMI for light recycling. The multimode region of the MMI acts as the phase modulating region, where light circulates for two passes, and accumulates additional phase change without dissipating additional energy for thermal change (in the second pass through the modulation region). The advantage is in terms of small footprint of the device, increased thermal overlap and fabrication, ambient temperature tolerance (compared to above mentioned devices).

Extending this study in Chapter 6, the effect of thermal gradient generated on the unperturbed arm of the MZI is studied in common available SOI platforms.

Firstly, the light guiding principles of MMI are reviewed and in the following sections device design, simulation and characterization results to achieve power savings of 29.5% (compared to a 0.45 µm waveguide width) are demonstrated.

4.1 Review of fundamental Science of an MMI

Light guiding using Total Internal Reflection (TIR) with higher index core and lower index cladding waveguides is a well explained phenomenon [136, 137]. The number of transverse modes

supported by a waveguide can be obtained using the eigenvalue equation which involves the physical structure of the waveguide and its material properties.

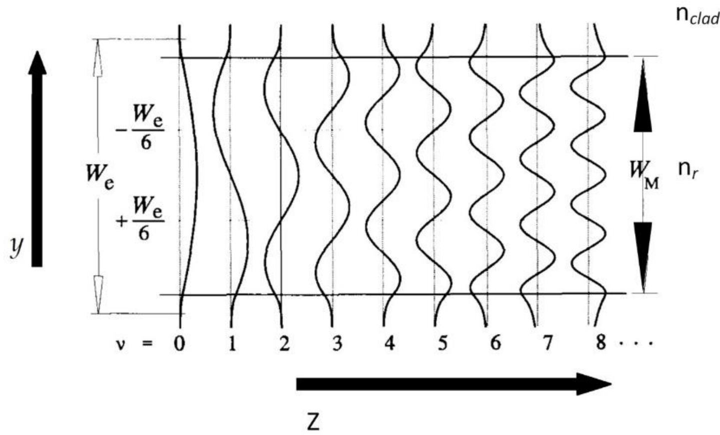

Figure 4-1 Modes of the multimode region [136]. W_e represents the effective width of the mode including the lateral penetration depth for each mode. Image recreated from [136].

Light from a single mode input waveguide couples into higher order modes of the multimode waveguide with different amplitudes. This is called the field excitation coefficient and is given by the overlap integrals (equation 4.1). Here $\Psi(y,0)$ represents the input field profile, and $\psi_v(y)$ the field distribution of different modes in the multi-mode region given by different v values as shown in Figure 4-1.

$$c_v = \frac{\int \Psi(y,0)\, \psi v(y)\, dy}{\sqrt{\int \psi_v^2(y)\, dy}} \qquad 4.1$$

The field profile at any distance z in the multimode region can be written as sum of the excited modes. Here the exponential j ωt and β_v z represent the time dependence and phase of the excited mode respectively.

$$\Psi(y,z) = \sum_{v=0}^{m-1} c_v\, \psi_v(y) \exp\left[j\,(\omega t - \beta_v z)\, \right] \qquad 4.2$$

The field profile at a distance L in the multimode region can be written by extracting the common time dependent term. Here L π is the beat length between the first 2 modes as defined in section 3 of [94, 136].

$$\Psi(y,L) = \sum_{v=0}^{m-1} c_v\, \psi_v(y) \exp\left[j\, \frac{v(v+2)\pi}{3L_\pi}\, L \right] \qquad 4.3$$

The field will be a reproduction of the input field when one of the following conditions are met.

$$\exp\left[j \frac{v(v+2)\pi}{3L_\pi} L \right] = 1 \ \text{or} \ (-1)^v \qquad 4.4$$

Satisfying the first condition gives a direct image of the input. Here the phase of all modes have gained additional 2π phase with reference to the starting position of multimode region. Satisfying the second condition gives a mirrored image of the input and happens when phases are an even multiple of π for even modes, and odd multiple of π for odd modes.

Tapering of the MMI region has been reported [138] to reduce the imaging length compared to straight MMI regions.

4.2 Thermo- optic phase shift modulator - 2x2 MMI (2 pass)

The 2x2 MMI is designed to have two passes through the multimode region as shown in Figure 4-2. Light from a single mode waveguide (Port A) is tapered and excites higher order modes in the multimode region. The length of the MMI region is chosen to be equal to a multiple of the self-imaging length. The output light after the first pass is tapered to a single mode waveguide (Port B) and then recirculated back to the multimode region (through Port C) using a 180-degree bend. As the multimode region length remains the same, light after the second pass (through the multimode region) is then collected and tapered to the output single mode waveguide (Port D).

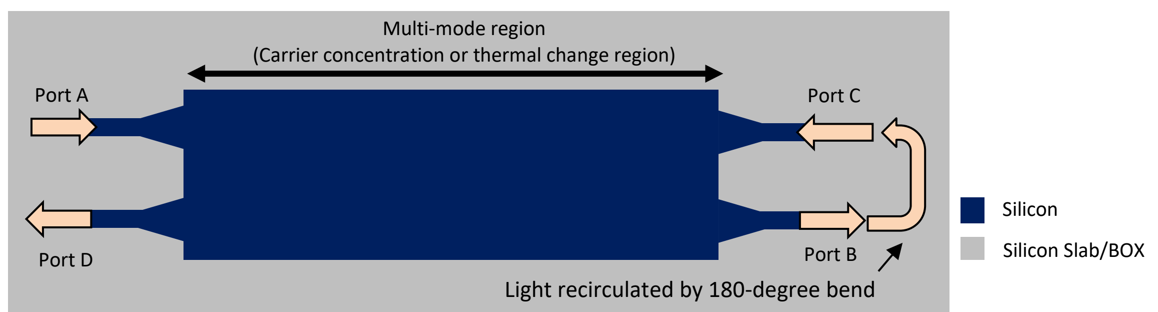

Figure 4-2 Top view of the two pass 2x2 MMI device used as a phase modulator in the arms of an imbalanced MZI (not shown here). The regions drawn in blue and grey are implemented in 220 nm thick silicon on a 2000nm BOX.

The multi-mode region is utilized as the optical phase modulator region and gives additional phase change compared to a single pass through this structure. Since the light circulates twice through the modulation region, the interaction length is effectively doubled and/or the device length halved.

4.2.1 Simulation parameters

For application of the two pass 2x2 MMI devices in thermal modulators, the first step was to study the thermal gradient created across a waveguide by a commonly used metal strip based heating element of fixed dimension using Lumerical HEAT solver. The heater width was set to 2um and placed 1um above the optical waveguide. The waveguide width was varied across 0.45 µm to 9 µm and the generated heat profile was recorded. Figure 4-3 shows the cross section of the structure used for simulation in Lumerical HEAT solver.

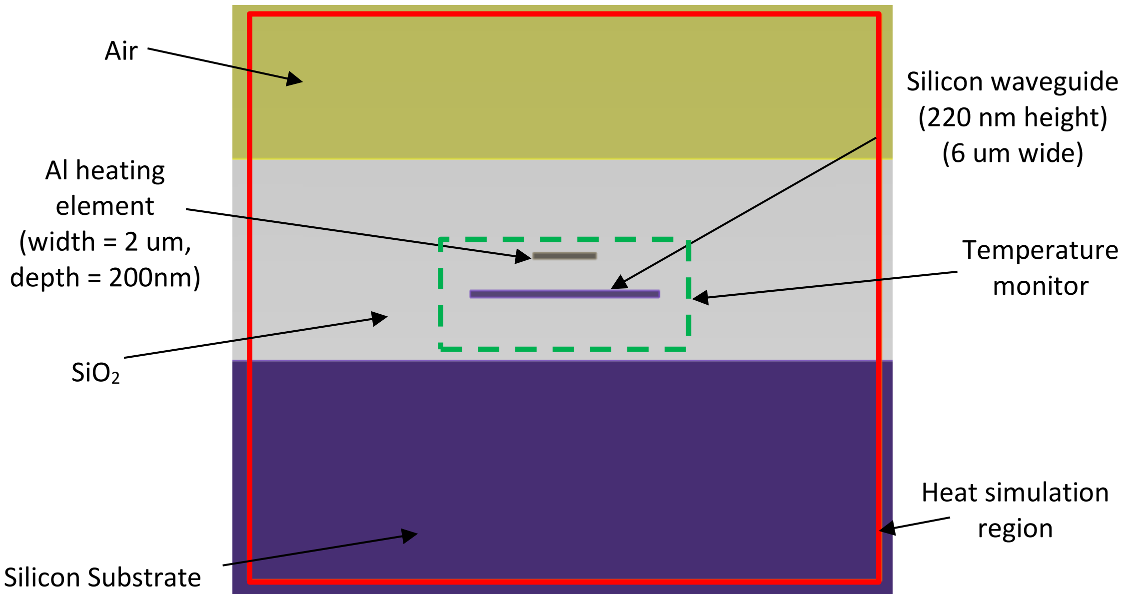

Figure 4-3 Simulation model cross section for the study of heat gradient across various waveguides for a fixed heater width of 0.2 µm.

A STRIP waveguide geometry was created using 220 nm silicon core with 2 µm of SiO_2 (BOX) at the bottom, followed by silicon substrate underneath the BOX. A thicker than usual top oxide of 4 µm was used to simplify the heat convection modelling of the Air-SiO_2 interface and minimise its effect on the generated thermal gradient. An aluminium heating element of width 2 µm was positioned centrally w.r.t the waveguide core and placed 1 µm over the waveguides top surface. The bottom surface of the silicon substrate was fixed at a temperature of 300K and the top Air-SiO_2 surface was modelled with constant convection model with 10 $W/m^2.K$.

The heat simulation region with dimensions 20 x 18 μm^2 (width x height) and maximum mesh edge length of 50 nm was created to study the steady state thermal response of the device with normalized length of 87.67 µm. 87.67 µm length was for compatibility with the MMI length used in the simulation analysis.

4.2.2 Simulated temperature and Δn_{eff} change

The heat profile across the waveguide width (centre of the waveguide, 110 nm height) was extracted from the simulation and the results are shown in Figure 4-4. The results show that as the waveguide width increases, the maximum temperature to which the waveguide core is heated decreases.

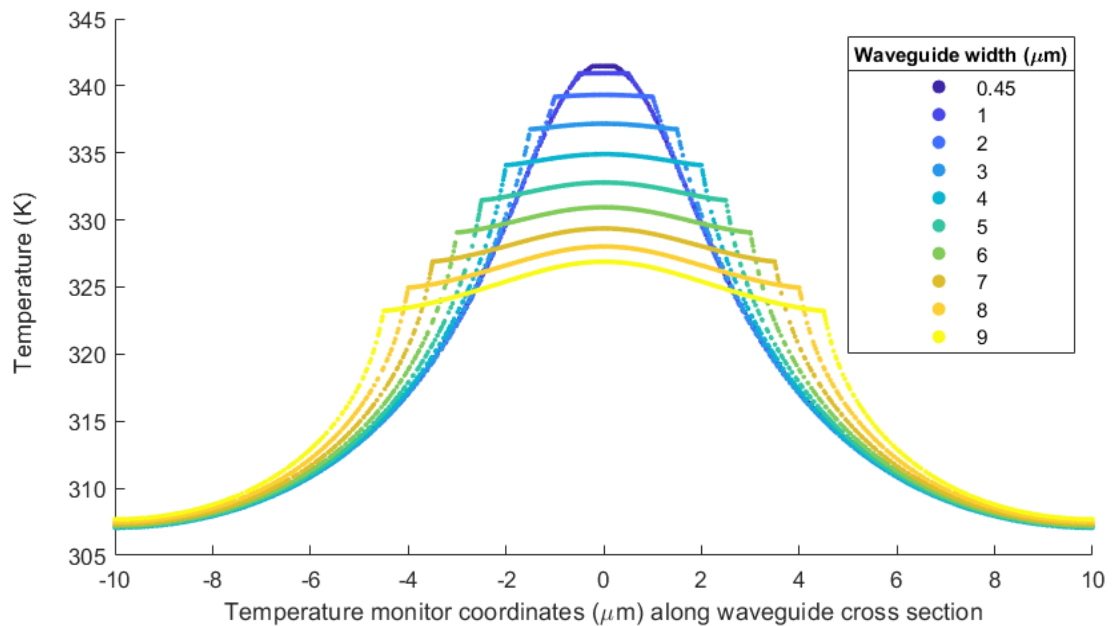

Figure 4-4 Thermal profile across the centre of waveguide for varying waveguide widths. Applied heater power is 20 mW for a heater filament width of 2 µm and length 86.67 µm .

Figure 4-4 displays the heat diffusion in silicon. A wider waveguide width causes heat to diffuse across the silicon waveguide which decreases the peak temperature at the centre of the waveguide (as shown in Figure 4-5). In simpler words, the heat is more spread out across the waveguide core as the waveguide width increases. The peak temperature at the centre of the waveguide was then extracted for different waveguide widths and is plotted in Figure 4-5.

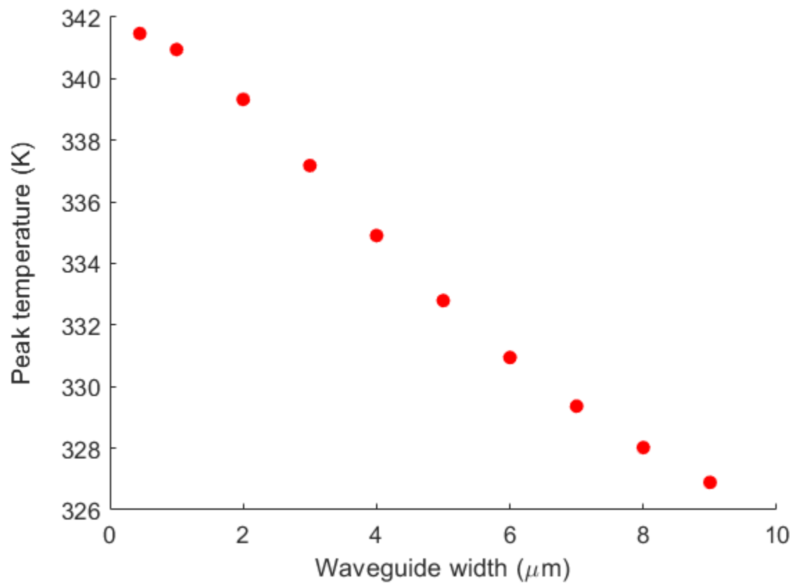

Figure 4-5 Peak waveguide temperature at the centre of waveguide for various waveguide widths (0.45 to 9um) with constant heater dimensions of 0.2 x 2 μm^2 (height x width), length 86.67 µm and 20 mW applied power to the heating element.

The thermal profile generated by Lumerical HEAT solver was then imported into Lumerical MODE solutions where it was used to define the refractive index perturbation for silicon (dn/dt = 1.8 e^{-4} K^{-1}) and simulate the effective index (N_{eff}) for varying waveguides widths and power. The change in effective index (ΔN_{eff}) was then calculated using MATLAB by subtracting the calculated N_{eff} with applied heater power by N_{eff} when no heater power is applied.

The results for change in effective index of the fundamental mode for waveguide widths ranging from 0.45 to 9um in plotted in Figure 4-6 for an applied heater power of 20 mW.

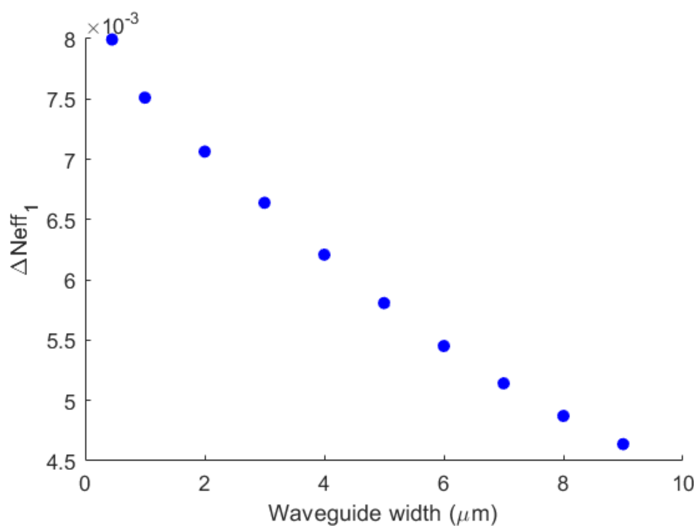

Figure 4-6 Change in the effective index of the fundamental mode for various waveguide widths with constant heater element dimensions (0.2 µm wide) and power 20 mW.

In the case of narrow width, tightly confined waveguides, we see a large change in effective index for the fundamental mode with applied heater power due to the higher temperature of the waveguide core. With increasing waveguide widths, the change in effective index for the fundamental mode decreases as the waveguide core temperature is reduced.

The simulated effective index change for the first ten modes for various waveguide widths (0.45 to 9 µm) are plotted in Figure 4-7.

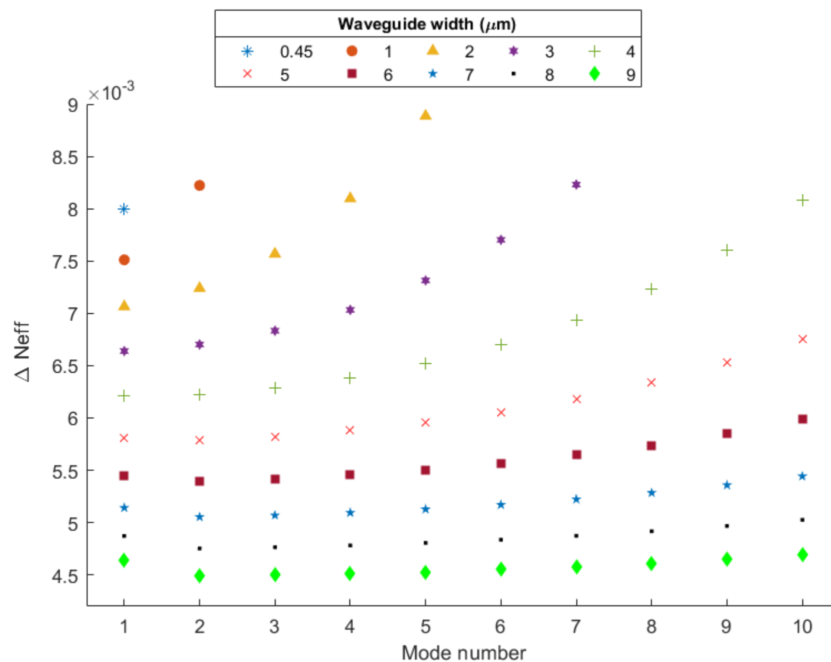

Figure 4-7 Change in the effective index for modes 1 to 10 for various waveguide widths (0.45 to 9 µm). The heater filament dimensions are fixed at 2um, 0.2um, 86.67 µm width, height and length with 20 mW of applied power.

Upon application of heater power, the thermal gradient generated along the waveguide width (from the centre towards the sidewalls and beyond) causes a change in the optical confinement of every mode. The higher order modes are less confined (more spread out along the width of the waveguide), however due to thermal gradient their overlap with the heated silicon waveguide region is increased and they show an increased ΔN_{eff} compared to the fundamental mode (or lower order modes).

The electric field intensity distribution for the first 5 modes of a 6 µm 220 nm STRIP waveguide surrounded by SiO_2 is shown are Figure 4-10.

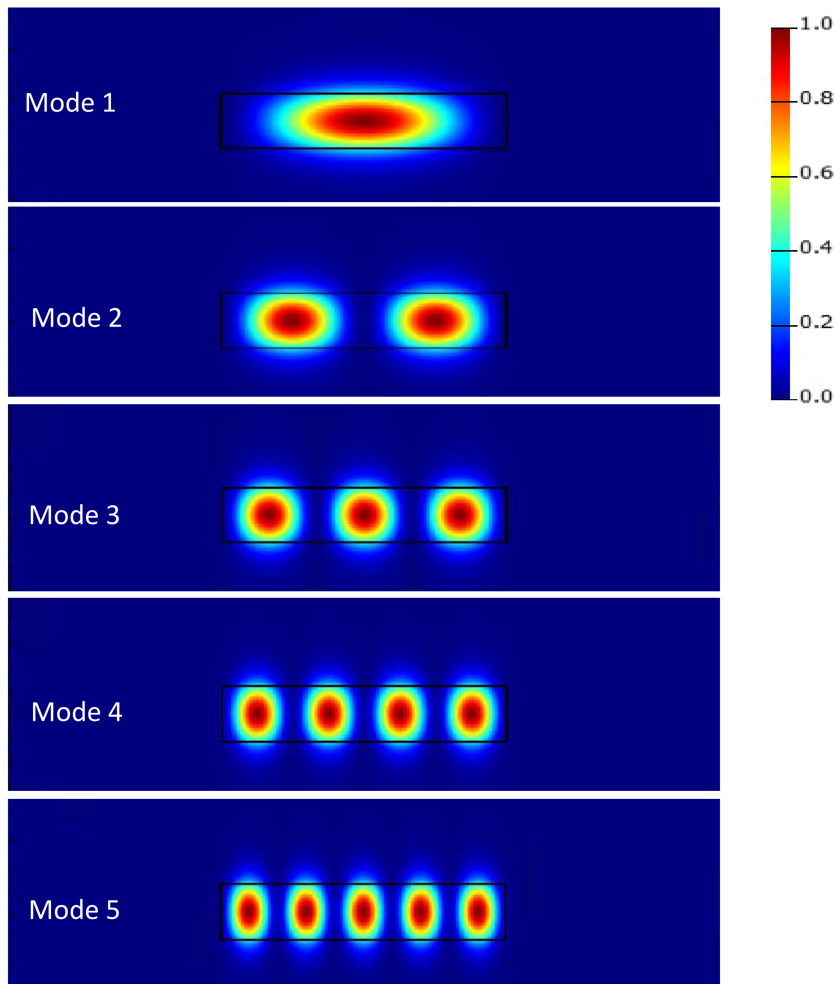

Figure 4-10 Simulated electric field intensity profile of a STRIP waveguide with width 6 µm, 220 nm height surrounded by silicon dioxide at the top and the bottom with no applied heater power.

The modal area [139] is a quantitative measure for the effective optical mode area and is defined as

$$Modal\ area = \frac{(\int |H|^2\, dx\, dy)^2}{\int |H|^4\, dx\, dy}$$

for a transverse mode propagating defined in directions x and y and propagating in z.

The modal area for a 2 µm and 6 µm wide waveguide on application of 20 mW heater power is presented in Table 2 and verifies the increase in confinement of optical mode when heater power is applied.

Table 2 Simulated modal area for modes of 2 µm and 6 µm width waveguide for applied heater power of 0 and 20 mW.

Mode number	Modal area (um^2)			
	Applied power = 0 mW		Applied power = 20 mW	
	2 µm waveguide	6 µm waveguide	2 µm waveguide	6 µm waveguide
1	0.477415	1.41586	0.47647	1.4079
2	0.483131	1.41765	0.482152	1.41553
3	0.492899	1.42064	0.491829	1.41858
4	0.507532	1.4248	0.506305	1.42274
5	0.529787	1.43015	0.528234	1.42806
6	-	1.43668	-	1.43455

4.2.3 Simulated phase change

Figure 4-11 shows the thermal profile for a STRIP waveguide with fixed height (220 nm) and various widths (0.45, 1, 2, 4, 6 µm) for a fixed heater power of 20 mW simulated using the HEAT solver in Lumerical. The generated heat profile is then imported into Lumerical MODE and utilized to calculate the change in the material refractive index and eventually phase change using EME solver.

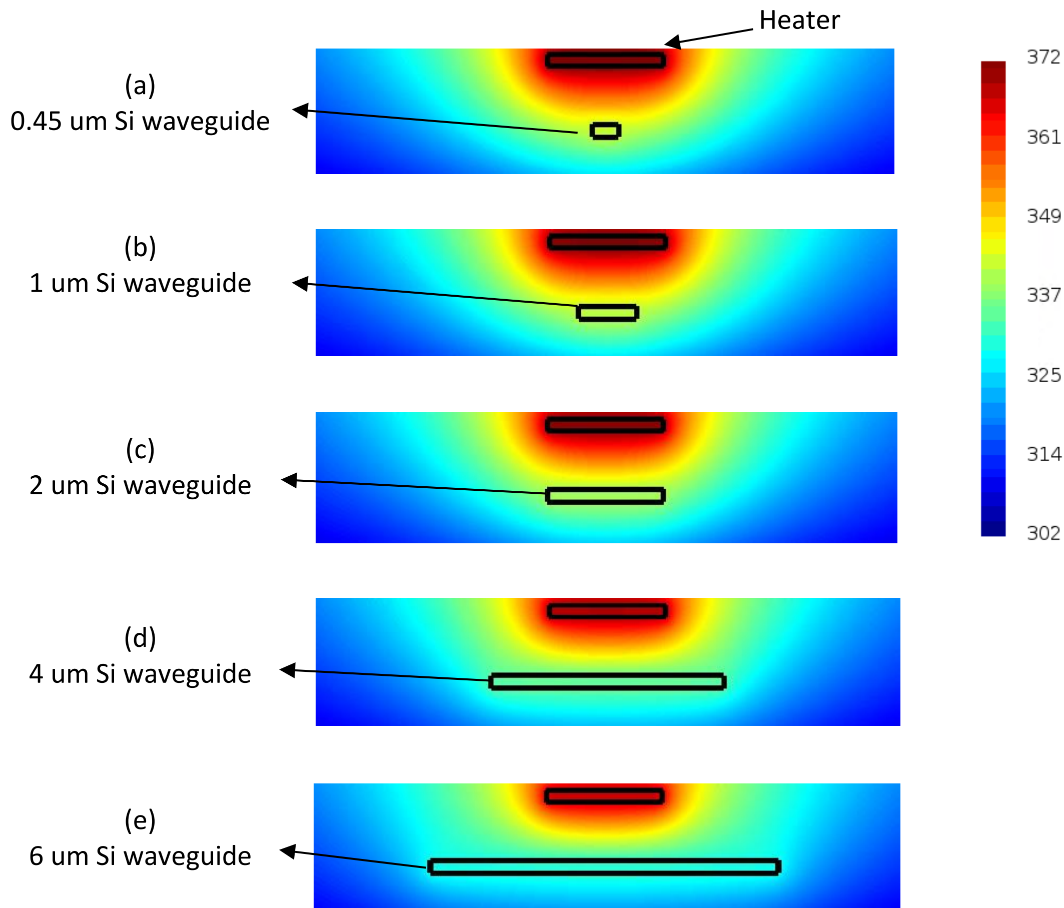

Figure 4-11 Simulated thermal profile for STRIP waveguide of height 220 nm and width (a) 0.45 µm, (b) 1 µm, (c) 2 µm, (d) 4 µm (e) 6 µm.

The phase change power efficiencies for the fundamental mode travelling through 0.45, 1, 2, 4 and 6 µm waveguide widths and 86.67 µm length were then simulated. A 6 µm MMI structure with access port parameters defined in section 4.2.4 and multimode region length of 86.67 µm (corresponding to the self-imaging length) with single pass through the structure was also simulated for its phase change efficiency. The results are presented in Table 3.

Table 3 Simulated phase change efficiencies for various waveguide widths for a heated section length of 86.67 µm.

Waveguide width (um)	Efficiency (mW/π)	
	Single mode propagation	Multimode propagation
0.45	22.35	-
1	23.79	-
2	25.30	-
4	28.78	-
6	32.78	32.77 (1 pass)

As expected from the results of section 4.2.2 the phase shift efficiency of the single mode propagation structures decrease with increase in waveguide width. For the 6 µm multimode region width MMI (with a single pass), the phase shift efficiency is worse than the 0.45 µm single mode waveguide phase shifter. However, using light recycling approach, light can travel twice through the same region modulation and effectively half the power required for π phase shift compared to a single pass structure through the MMI structure. That means the phase efficiency of two passes through a 2x2 6 µm MMI would be 16.38 mW/π which is better than efficiency with 0.45 µm waveguide as the phase shifter element and translates to power savings of 26.70%.

4.2.4 Device parameters

We chose to study the standard 6 µm width MMI, commonly used for power splitting and combining applications for our 2x2 MMI phase modulator device. Lumerical mode solution EME solver was used for simulating and extracting the passive device parameters having 220 nm silicon waveguide core with 100 nm silicon slab.

The input and output ports of width 1.5 µm were placed asymmetrically at a distance of 1.015 µm (centre to centre) from the centre of the multimode region in a cross MMI configuration. The length of the multimode region was swept using the EME solver with finite-difference algorithm, simulation temperature of 300K, and maximum mesh edge length of 20 nm at 1.55 µm wavelength. Figure 4-12 and Figure 4-13 show the simulated device dimensions and normalized output transmission of the multimode region length sweep used to calculate the MMI parameters.

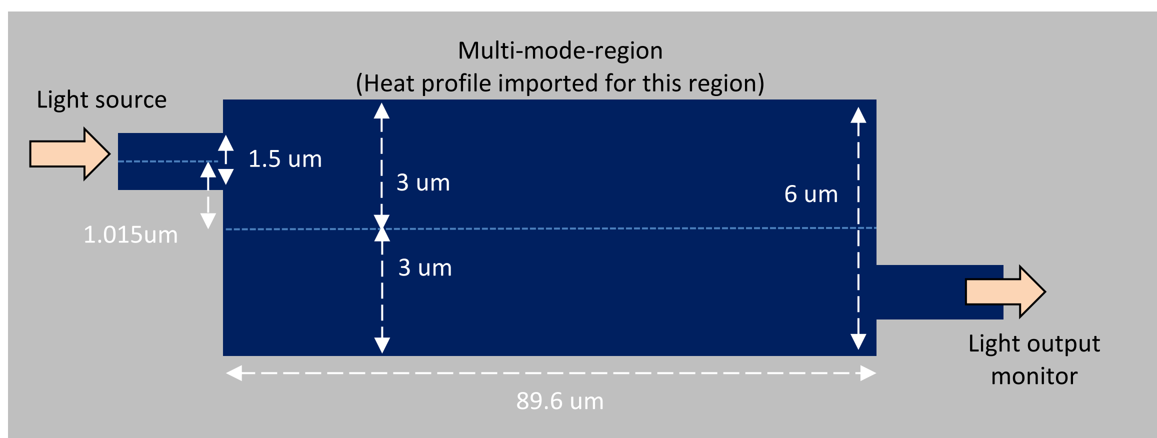

Figure 4-12 Top view of the 2x2 MMI modulator device and dimensions.

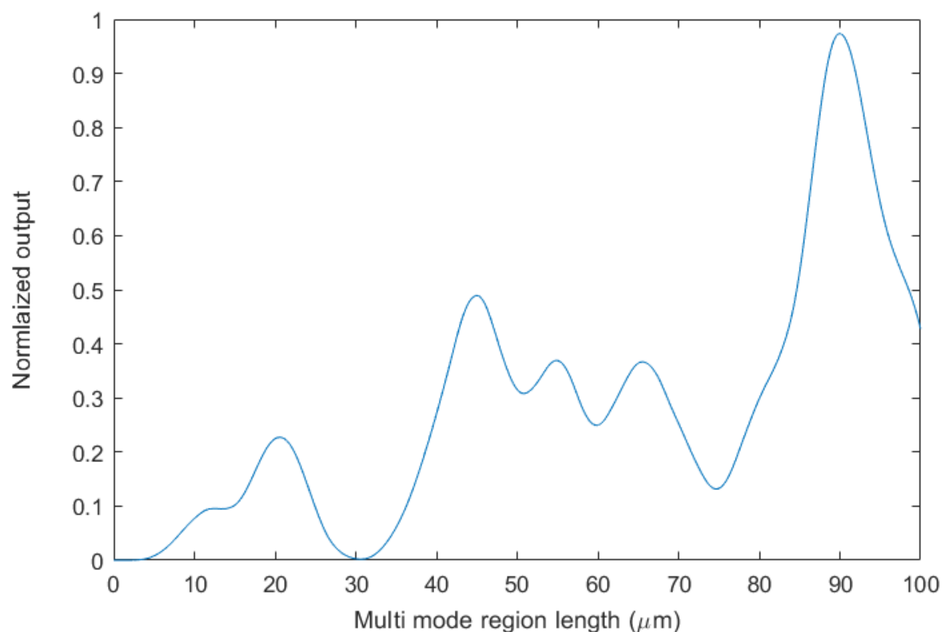

Figure 4-13 Normalized transmission vs multimode region length for the simulated 6 µm 2x2 MMI modulator device using the EME solver.

The simulated intensity profile (plane slice at 80 nm from the bottom of the slab region) for the multimode region length of 89.6 µm for MMI device in cross configuration is shown in Figure 4-14.

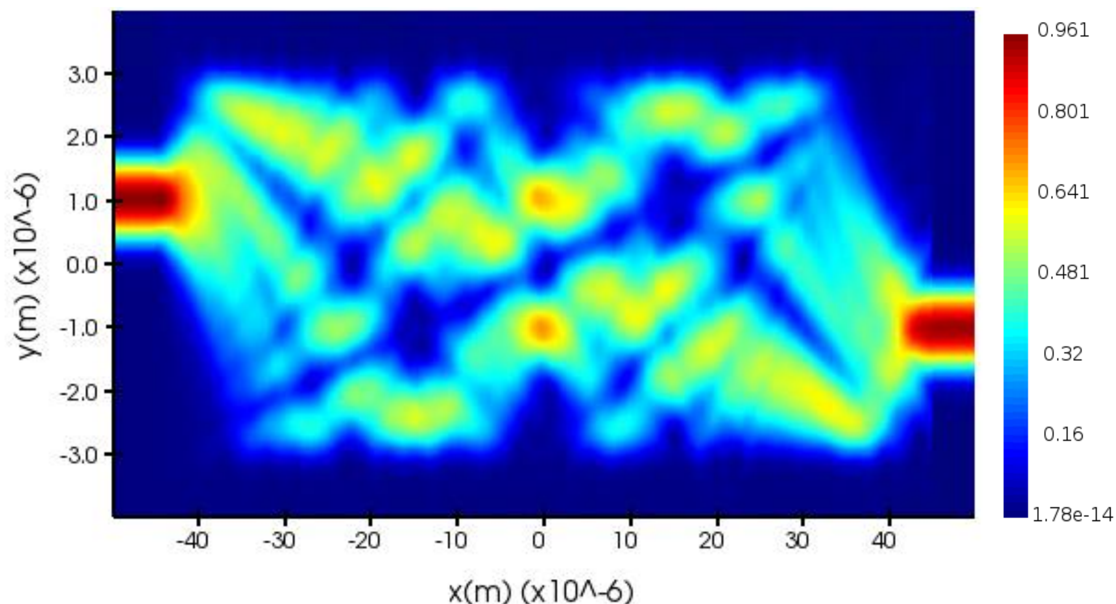

Figure 4-14 Intensity profile for the simulated MMI phase shifter device with multimode region length 89.6 µm at 1.55 µm wavelength.

4.2.5 Mask design and device Fabrication

2x2 MMI devices with various heater lengths were fabricated along with normalization structures with a waveguide width of 0.45 µm for comparison. A summary is presented in Table 4.

Table 4 Fabricated devices with various heater geometries.

Waveguide width (µm)	Heater dimensions		MMI length (µm)
	Width (µm)	Length (µm)	
0.45	2	80	-
0.45	2	160	-
6 (MMI)	2	80	89.6
6 (MMI)	2	160	179.2

A schematic top view of the fabricated 2x2 MMI phase shifter device with an MMI length of 89.6 µm is shown in Figure 4-15.

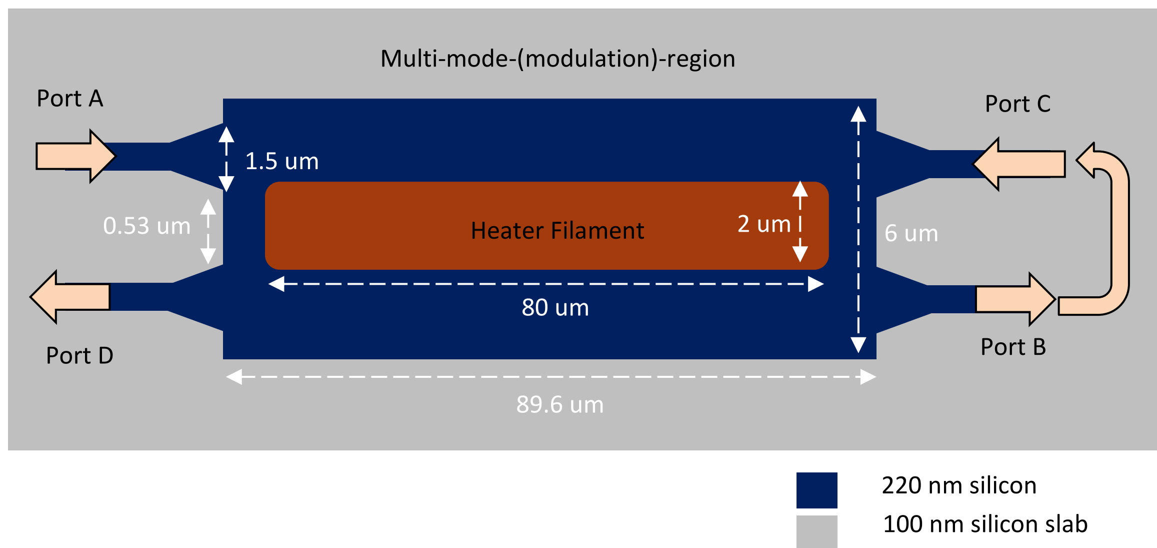

Figure 4-15 Schematic top view of the 2x2 MMI thermal phase shifter with dimensions.

The 180 degree bend was taken from the standard library and consisted of 45 degree S bends and 90 degree bends both of 25 µm radius as shown in Figure 4-16.

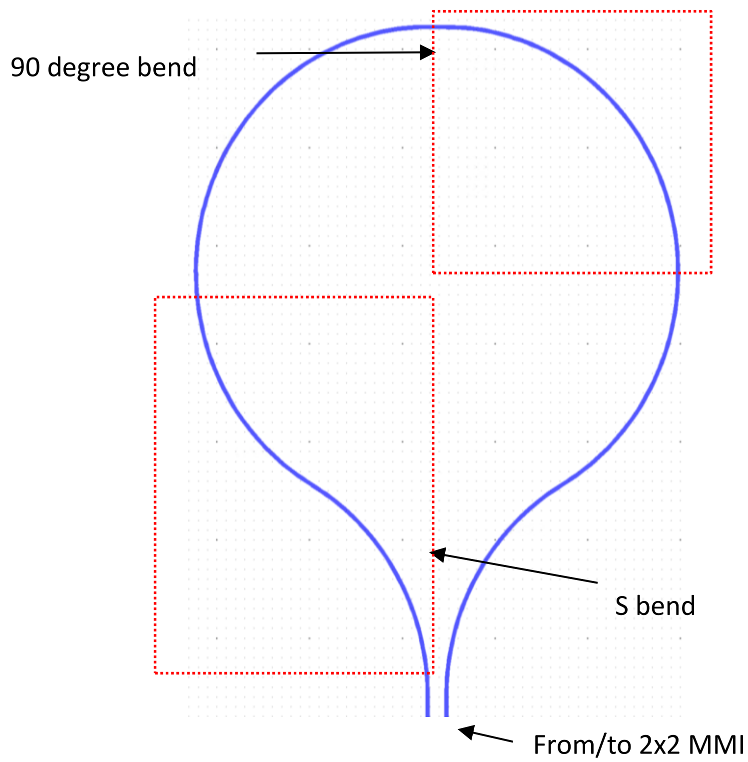

Figure 4-16 180 degree bend used for light recirculation in the 2x2 MMI.

The mask layout for the devices was then generated using L-edit. Figure 4-17 shows the generated layout for the 2x2 MMI thermo optic phase shifter in an imbalanced MZI configuration. Four different lithography layers were utilized to the fabricate the device which were used to define the waveguides, grating couplers, heater filament and the electrodes.

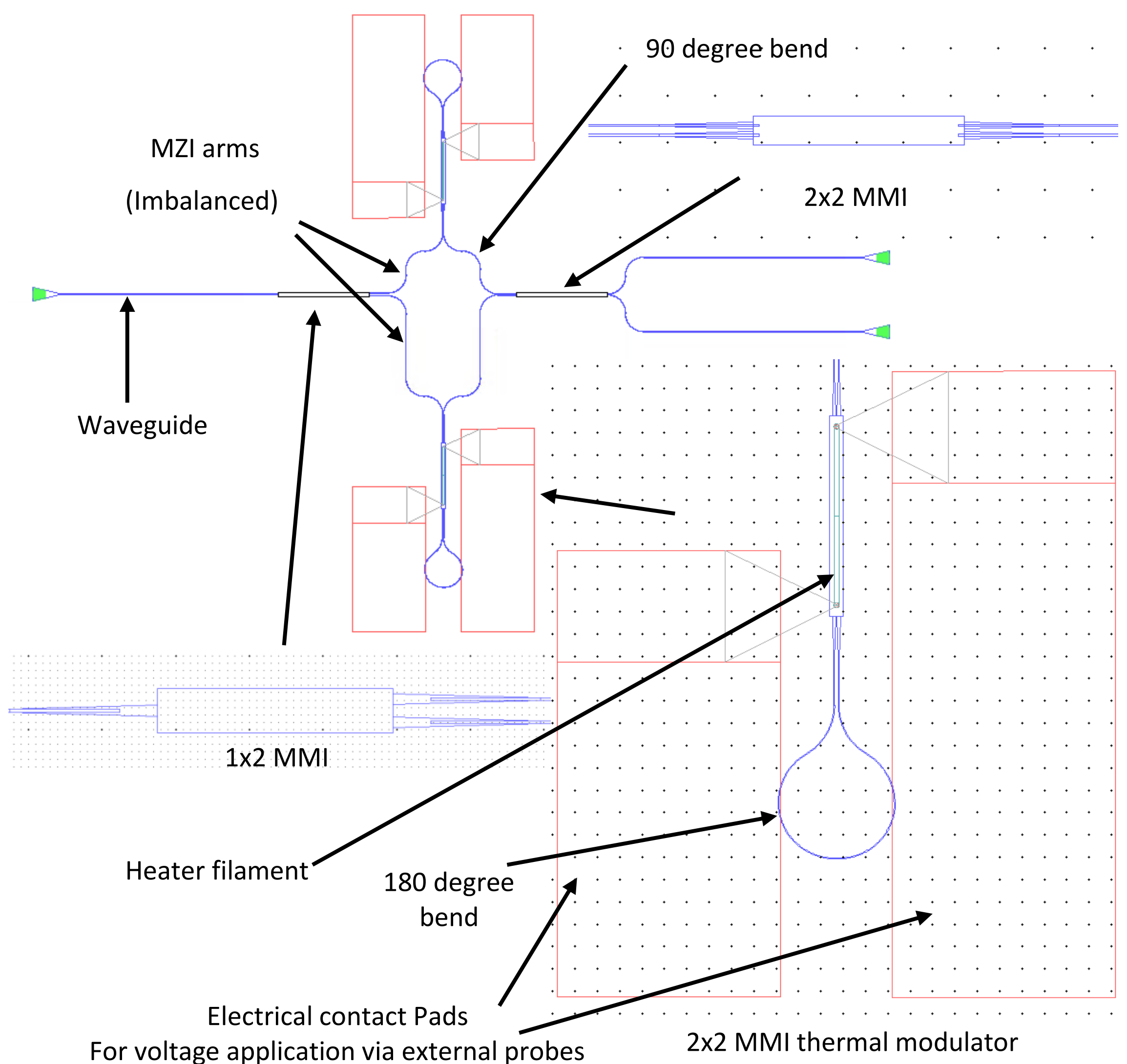

Figure 4-17 L-edit mask layout for 2x2 MMI modulator in an imbalanced MZI.

Fabrication was performed using a CORNERSTONE MPW run on 220nm SOI, within the nanofabrication cleanroom facilities at the University of Southampton. Figure 4-18 displays the flow chart for the process and the final cross section for a waveguide of width 0.45 µm (bottom). The first two steps involved defining the grating couplers (70 nm silicon etch) and RIB waveguides (120 nm silicon etch) by DUV lithography and inductively coupled plasma (ICP) etching. This was followed by depositing a 1µm thick PECVD SiO_2 cladding followed by two lift-off steps for the heater filament and contacts pads. The heater filament is made of TiN and has a thickness of 150 nm and the contact pads consist of a stack of Ti (30 nm) and Au (200 nm).

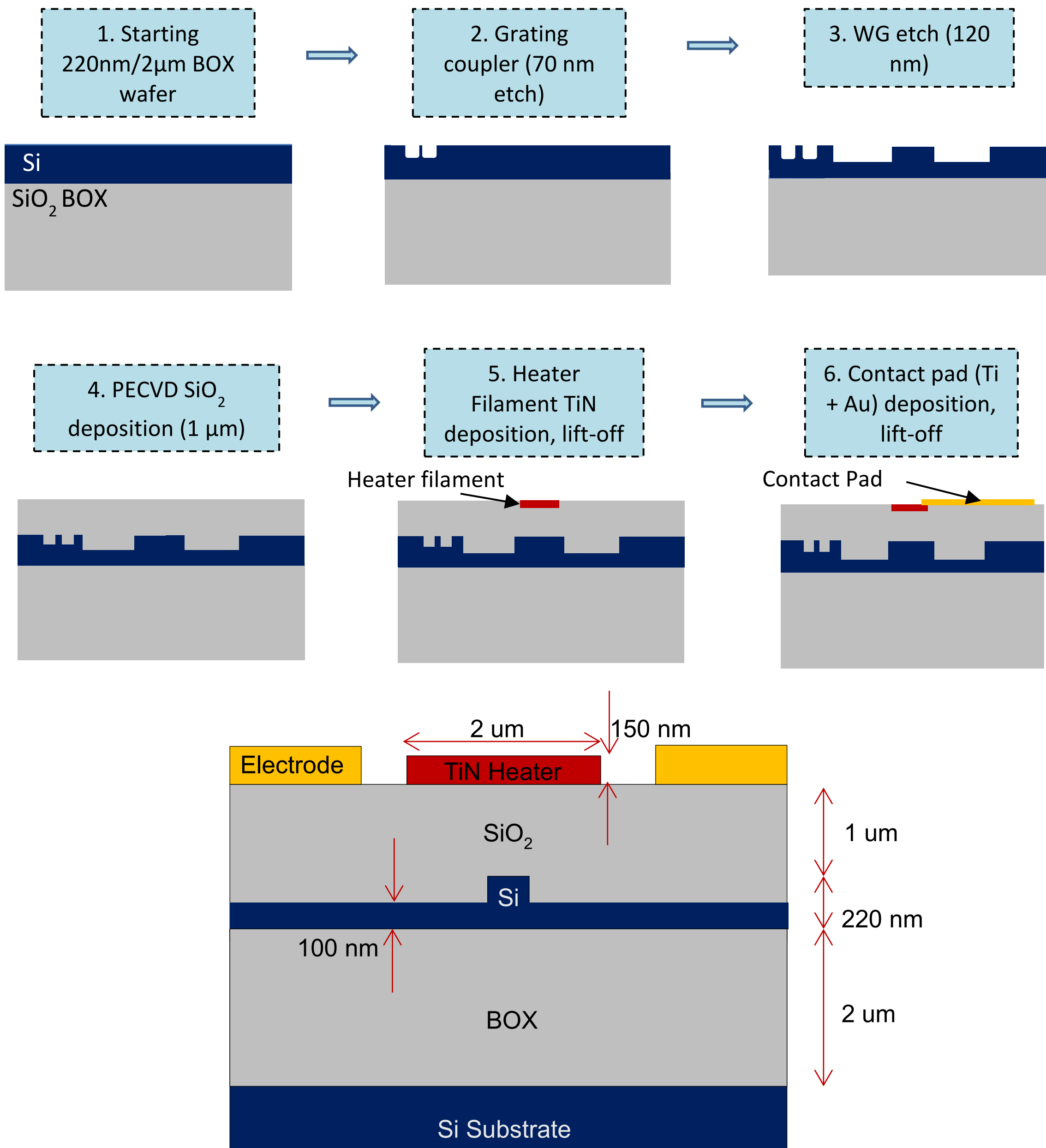

Figure 4-18 Fabrication flow (top) and schematic cross section (below) of the fabricated thermo-optic device (0.45 µm waveguide width).

4.2.6 Experimental Results

No cutback type test structures were fabricated for the 6 µm 2x2 MMI structures and additional insertion loss of less than 0.5 dB was recorded compared to normalization MZI device. The normalized wavelength spectrum for various applied heater power is shown in Figure 4-19.

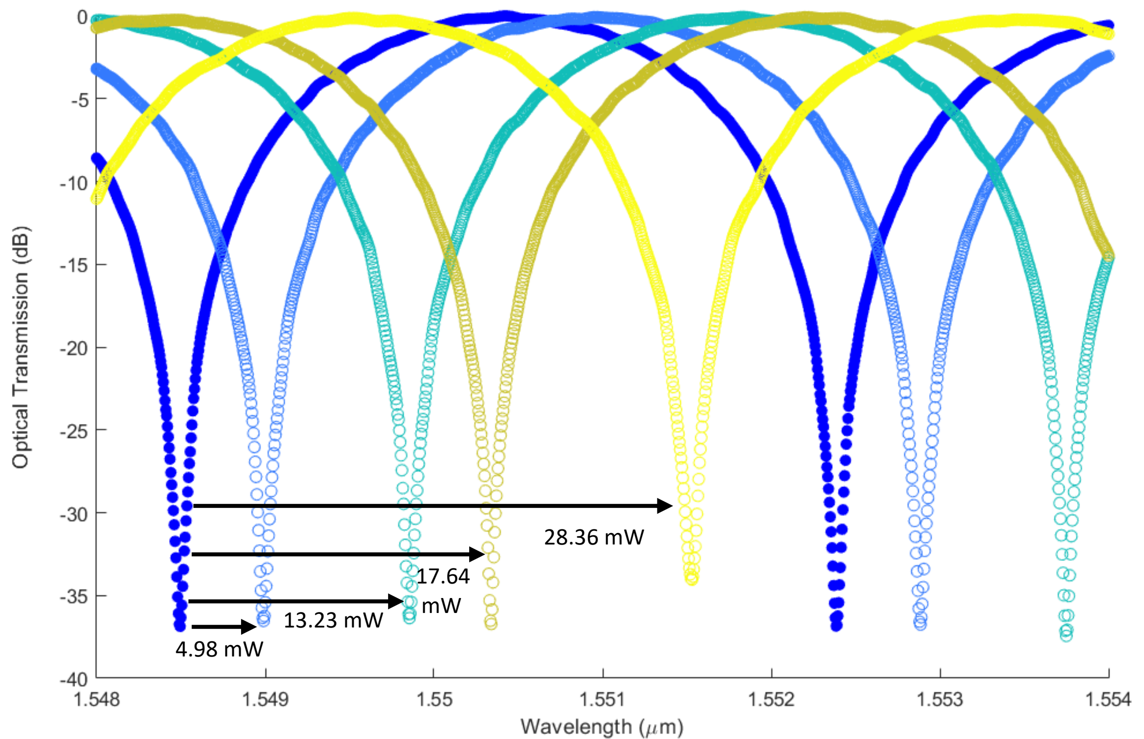

Figure 4-19 Normalized wavelength spectrum response of the MZI comprising 2x2 MMI phase shifter devices for various applied heater power. Filled blue dots represents wavelength spectrum when no voltage is applied.

The phase shift was extracted using a minima tracking code written in MATLAB with flow chart of the process shown in Figure 4-19. The computing code calculates the FSR by grabbing all the wavelength transmission minimums. It then looks for the nearest minima peak around the desired wavelength value, which was set to 1.55 µm in this case, and then tracks its shift as a small increments of power is applied to the heating element. Transmission wavelength spectrum for an increasing applied heater power is recorded and the results are post processed in MATLAB.

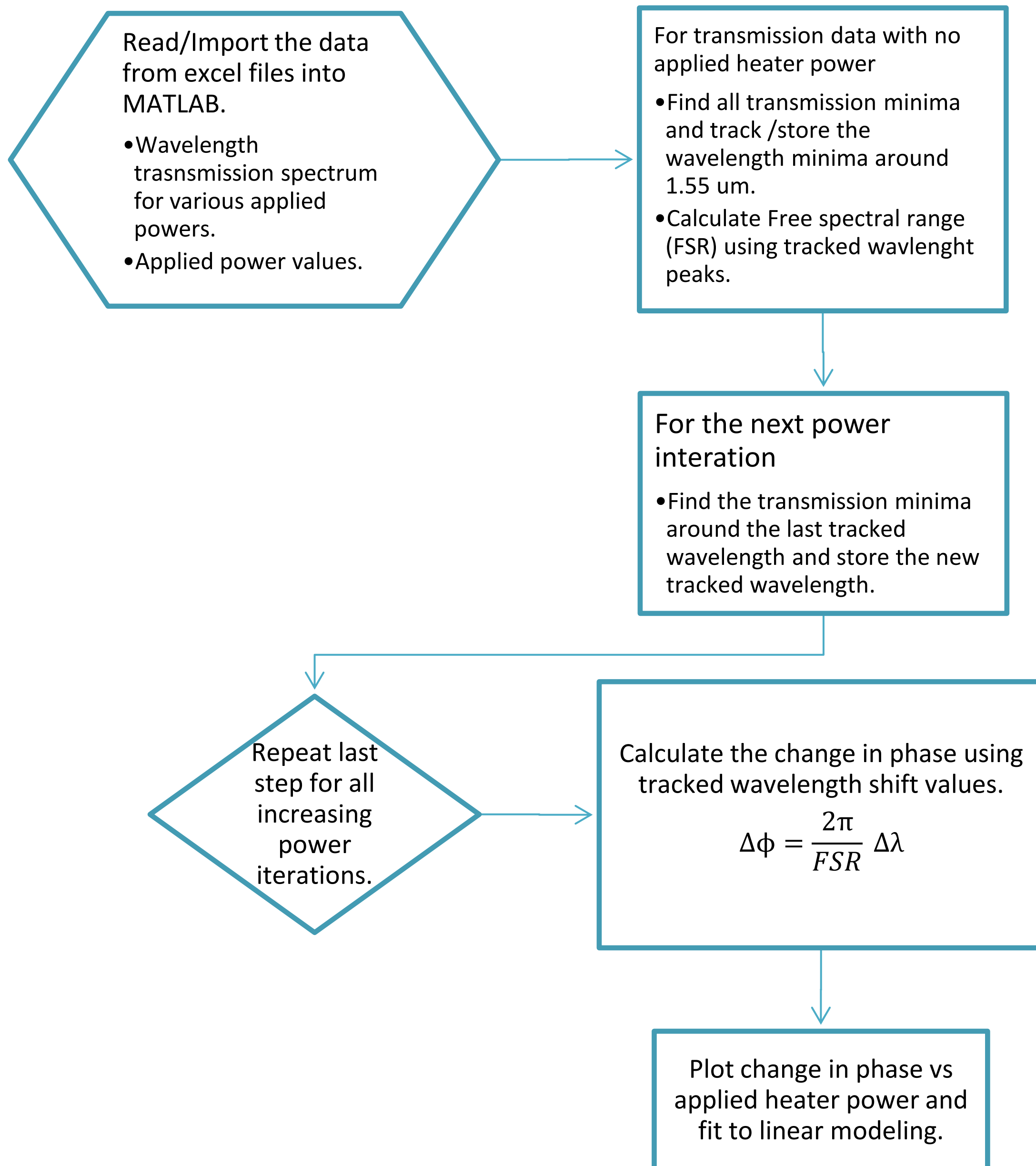

Figure 4-20 Flow chart representation of the MATLAB code used to calculate phase shift.

Using the MATLAB code, the change in phase vs applied heater power for various fabricated devices around 1550 nm are plotted in Figure 4-21.

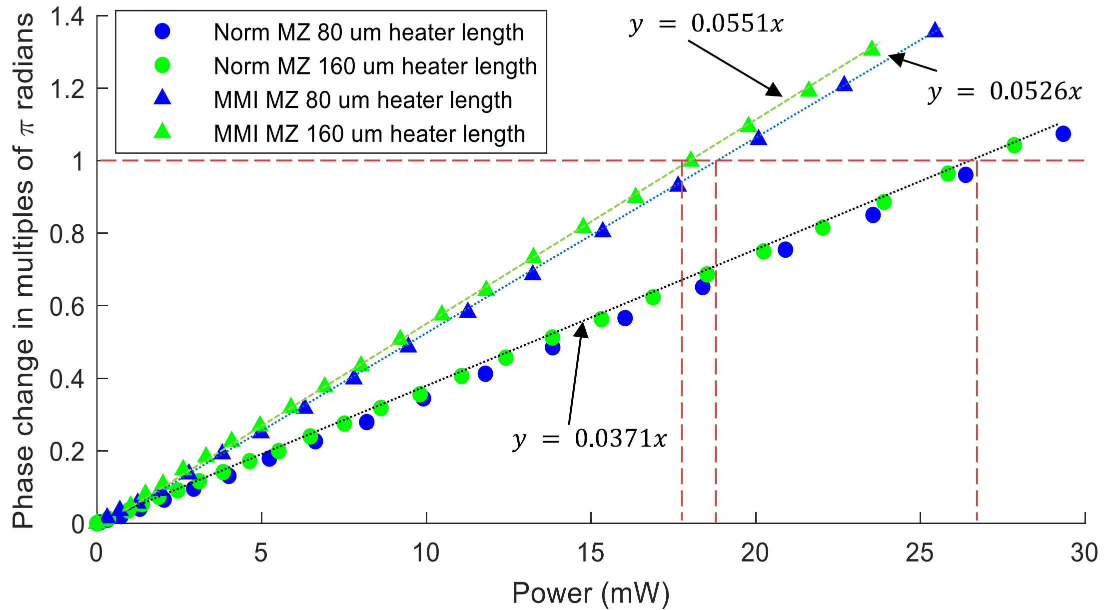

Figure 4-21 Phase shift vs applied heater power for devices with a heater width of 2 µm and lengths of 80 µm (blue) and 160 µm (green). Normalization MZI are represented by circles, and MMI based MZI devices are represented by triangles.

Normalization devices based on single mode waveguides (0.45 µm waveguide width) required 26.95 mW/π phase shift whereas, the two pass MMI based devices with multimode region length 80 µm and 160 µm needed only 19.01 and 18.145 mW/π respectively. This translates to power savings of 7.94 mW (29.46% reduction) and 8.81 mW (32.67% reduction) respectively for π phase shift compared to single mode waveguide based structures, which are in reasonably close agreement to the simulation modelling produced earlier in the chapter. The slight difference in the efficiency enhancement of 80 µm and 160 µm devices can be related to the fabrication tolerances between devices.

Table 5 Heater dimensions and efficiency results for fabricated thermo-optic devices.

Waveguide width (um)	Heater dimensions		Phase change (mW/ π)
	Width (um)	Length (um)	
0.45	2	80	27.62
0.45	2	160	26.95
6 (MMI)	2	80	19.01
6 (MMI)	2	160	18.15

4.3 Summary

In this chapter, light recirculation (two passes) using a 2x2 MMI with multimode region width of 6 μm has been demonstrated via simulation and experimental methods to achieve an enhancement in phase change efficiency and power savings of 29.46% compared to commonly used structures which have 0.45 μm waveguides.

Chapter 5 Carrier injection modulator

Similar to the previous chapter on thermo-optic phase modulators, this chapter explains the design procedure, simulation analysis, and experimental results for carrier injection based optical phase modulators utilizing the self-imaging property of MMI devices to get two passes through the multimode region and enhance the phase shift efficiency resulting in modulation power savings.

Carrier injection based devices can perform at ~GHz speed and device speed is an important consideration for these devices. Since the carriers are injected into the junction, the device speed is limited by the carrier lifetime (minority carriers) which scales increasingly with increasing waveguide geometry. Hence MMI with large multimode region width (6 µm multimode region width MMI as considered in last chapter) are not suitable and the design idea is to keep the multimode region width as small as possible to minimise the size of the electrical structure and maximise the operating speed while still keeping the multimode region large enough to work as an MMI (supporting at least 2 modes). For this purpose tapering of the multimode region into narrower width is considered in the chapter. Figure 5-1(a) shows top view of the 2x2 MMI phase modulator and Figure 5-1 (b) shows the 2x2 MMI devices with linear tapering of the multimode region.

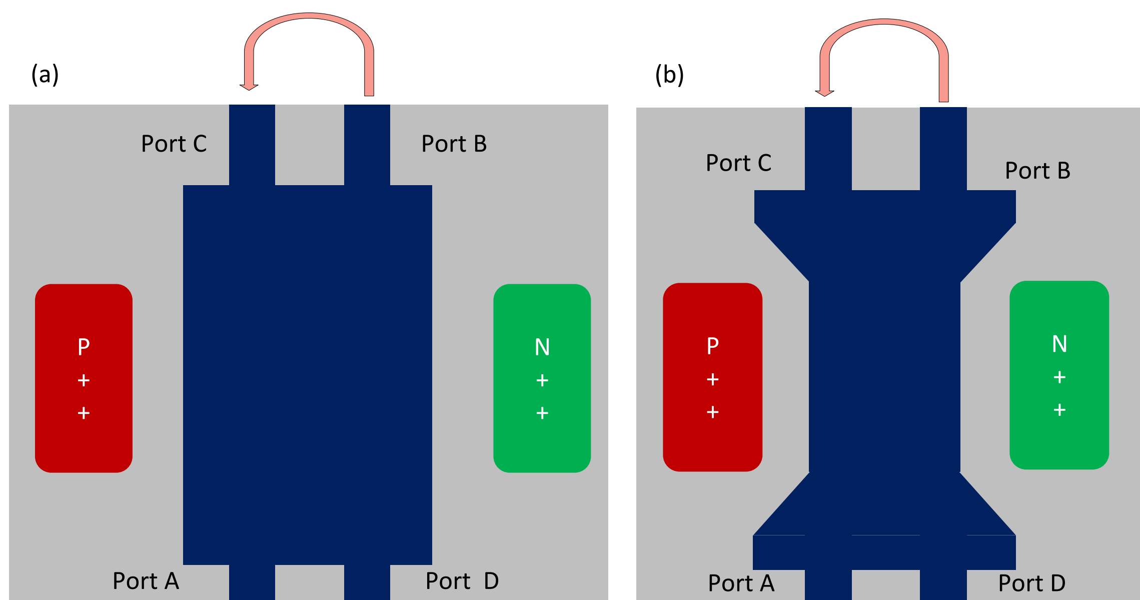

Figure 5-1 Schematic top view of the PIN junction based injection current modulators (a) 2x2 multiple pass MMI modulator, (b) tapered 2x2 multiple pass MMI modulator.

5.1 Simulation Analysis

To study the effect of waveguide width on modulation efficiency in carrier injection based devices, the following steps were undertaken to create functioning device geometry.

1. A waveguide geometry with 400 nm width silicon core of height 220nm, a 100 nm silicon slab was created in CHARGE solver within Lumerical DEVICE package with bottom and top region of the waveguide covered by 2 µm silicon dioxide.
2. N++ and P++ doped regions with doping concentration $1e^{20}$, separated by 0.8 µm from the waveguide sidewall on either side were added to form the p-i-n junction.
3. Aluminium metal electrodes geometries were placed on top of the doping region such that the closest waveguide sidewall edge and metal edge are separated by 1.8 µm.
4. Device length of 100 µm was used for generated cross section in step 1-3.
5. A 2-dimensional and linear charge monitor was placed midway along the silicon waveguide core (device cross-section) to record the change in carriers as voltage was applied across the electrodes.
6. This change in carriers was imported in Lumerical MODE to calculate the change in the refractive index of silicon waveguide and the eventually the change in mode effective index.

Lumerical and MATLAB scripting was used to sweep the applied power for various waveguide geometries (as mentioned in step 1-3), record and export the simulated carrier concentration.

A graphical image (cross section) of the generated geometry in the software is shown in Figure 5-2.

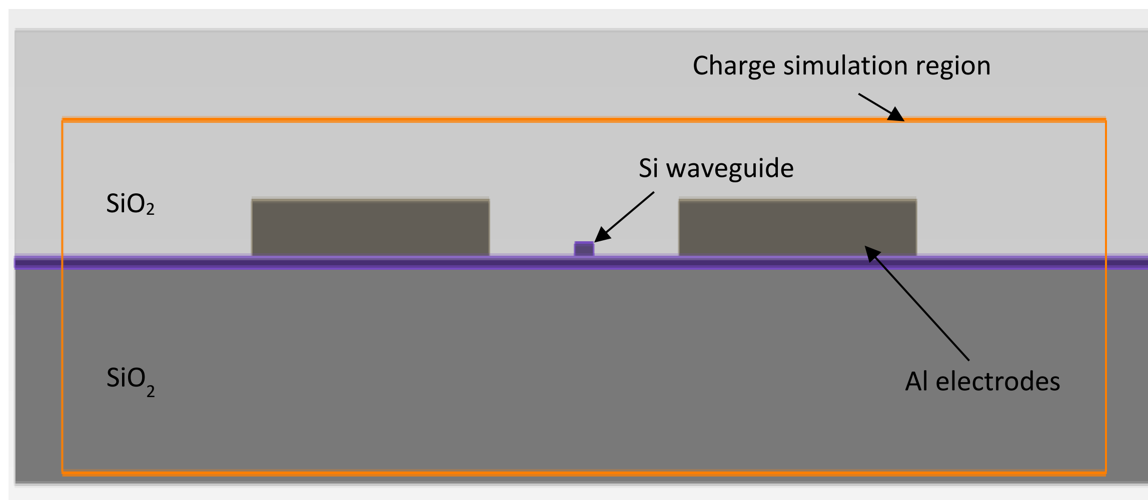

Figure 5-2 Device geometry used in Lumerical DEVICE with CHARGE solver to calculate the carrier concentration change.

5.1.1 Optical mode confinement and carrier density induced ΔN_{eff}

Phase modulation for carrier based modulation mechanisms is dependent on the mode overlap with the generated carrier concentration change and is desirable characteristic for obtaining high efficiency of modulation.

Firstly, the optical confinement factor (in silicon) for initial four modes was simulated in Lumerical MODE using FDE solver with maximum mesh edge length of 20 nm for various waveguide widths. The results are plotted in Figure 5-3 and clearly show the increase in silicon confinement (for individual modes) as the waveguide width is increased.

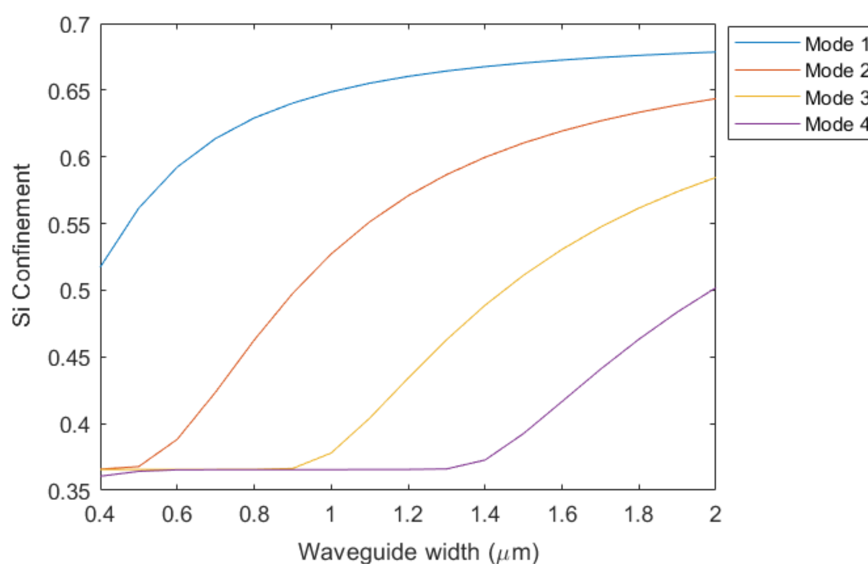

Figure 5-3 Mode 1, 2, 3, 4 silicon confinement factor for waveguide widths from 0.4 µm to 2 µm.

The carrier density for applied power across the junction was simulated for varying waveguide widths, from 0.4 µm to 2 µm, using charge simulation package in Lumerical. While sweeping the waveguide width the separation between the waveguide sidewall and the doping regions (and electrodes) was kept constant at 0.8 µm. The electron density (with applied power of 21.24 mW) for various simulated waveguide widths is plotted in Figure 5-5. From the image it can be inferred that, for a constant applied power, increase in the waveguide width reduces the amount of generated carriers. Similar trend can also be plotted for hole density.

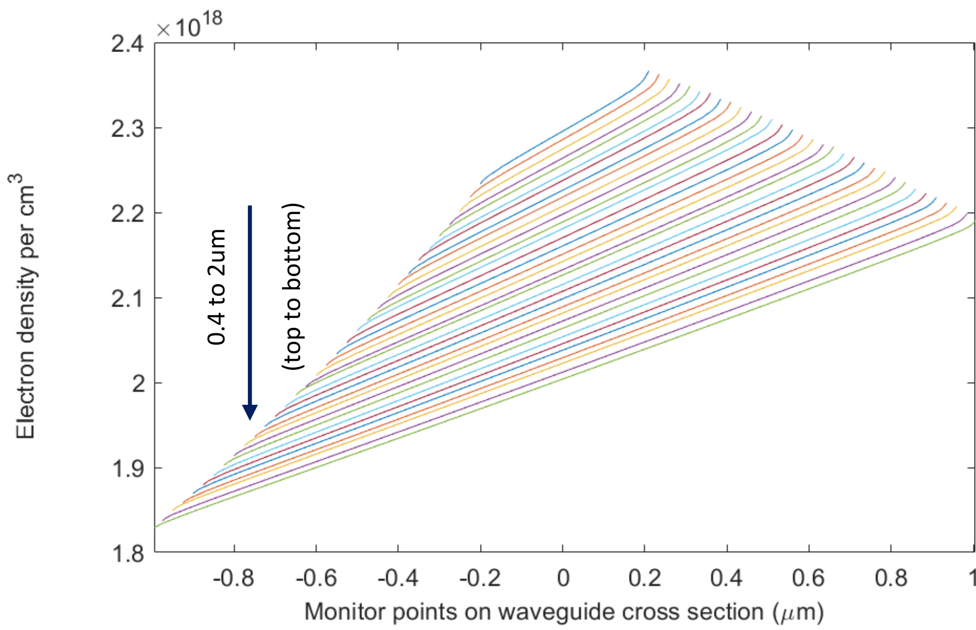

Figure 5-4 Electron density for various waveguide widths with an applied power of 21.24 mW.

The optical mode confinement (in silicon) and charge carrier density are both desirable factors for high efficiency modulation, but they show opposite trends. For increasing waveguide widths, the confinement factor increases while the carrier density generated decreases for a constant applied power.

The simulated carrier density profiles (2D) were then imported in Lumerical MODE to calculate the effective index, N_{eff}, for the first four optical modes. The change in effective index, ΔN_{eff}, was calculated using MATLAB by subtracting the N_{eff} with generated carriers from when no power is applied across the junction. The process was repeated for waveguide widths increasing from 0.4 µm to 2 µm in 0.05 µm steps for a fixed power. Using MATLAB the change in the effective index of the modes for various waveguide widths was extracted and the results are plotted in Figure 5-5 for input power of 21.24 mW.

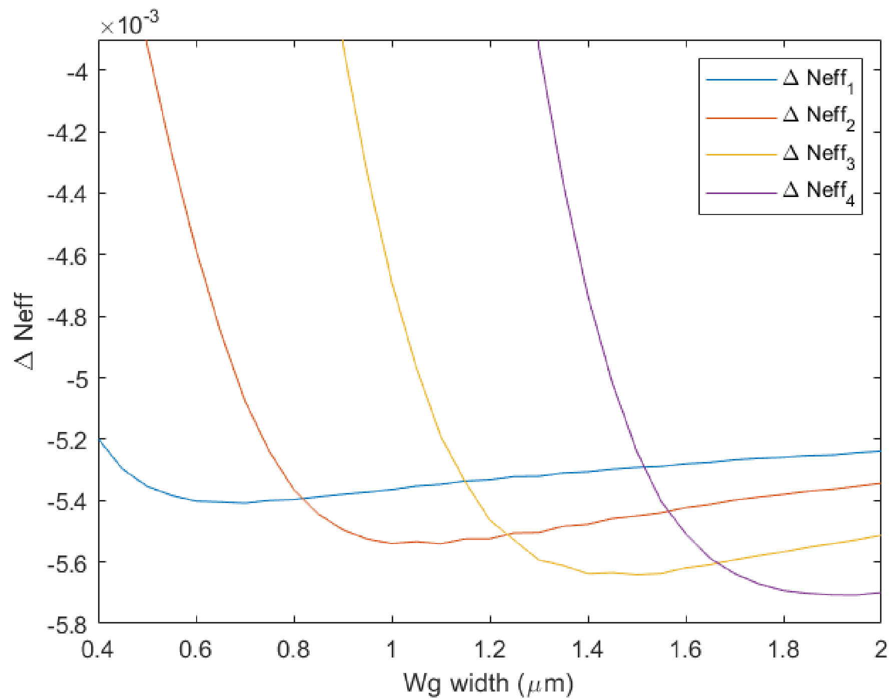

Figure 5-5 Variation in Delta Neff vs waveguide geometry for the first 4 guided modes relating to injection modulators with power of 21.24 mW.

The study revealed the optimum waveguide dimensions to achieve most efficient effective index modulation for the each mode. For mode 1, 2, 3, 4 it was found to be 0.7 µm, 1.1 µm, 1.5 µm, 1.95 µm respectively.

5.1.2 Design motivation for two pass 2x2 MMI injection phase modulator

Techniques such as light recycling in a 6 µm width 2x2 MMI (as in chapter 4) would worsen the device response time. Hence the focus of investigation was narrowed down to multimode region with minimum width which can support at least two guided modes to facilitate the working of a MMI.

Using the extracted ΔN_{eff}, change in phase of the optical mode travelling in an arbitrary 100 µm waveguide of widths 0.4 µm to 2 µm can be generated using the following equation.

$$\nabla\phi_{1,2} = \frac{2\pi L}{\lambda_0}\, \Delta N_{eff1,2}$$

5.2 Device design strategy

In order to successfully maximize the use of carrier concentration change and keep the multimode operation of the multimode region, the width of the multimode modulation region was chosen to be around 0.8 µm which supports two optical guided modes. To make sure no power is lost while tapering the MMI, the design constrain was set to have a combination of multimode region and access waveguides which allow maximum power to be coupled into the first two modes of the multimode region.

The first step was to calculate the power overlap of the access waveguide with the multimode region. For this FDE analysis in Lumerical (with maximum mesh edge length of 5 nm) was performed by sweeping three different parameters.

1. Width of the multimode region (0.8um to 2um)
2. Width of the access waveguide (0.4um to 0.8 µm)
3. Position of the access waveguide w.r.t the multimode region.

Some restrictions were imposed while sweeping the parameters such as separation between the access waveguides which was limited by the minimum lithography resolution (320 nm).

The overlap of the access waveguide fundamental mode with the first two modes of the multimode region was then recorded. The resultant parameters of the best result is shown in Table 6.

Table 6 Simulated (highest) FDE power overlap for mode 1 and mode 2 for access waveguide dimensions (position and width) w.r.t. multimode region width.

MMI input port width	MMI port position	Multimode region width	Power overlap with first 4 modes using FDE	Power overlap with first 2 modes using FDE
0.47 µm	0.395 µm	1.76 µm	0.95 (-0.22 dB)	0.90 (-0.45 dB)

The electric field intensity profile for the first four modes of the multimode region with width 1.76 µm are shown in Figure 5-6. The corresponding effective index and power coupling with the fundamental mode of access waveguide are presented in Table 7 and Table 8 respectively.

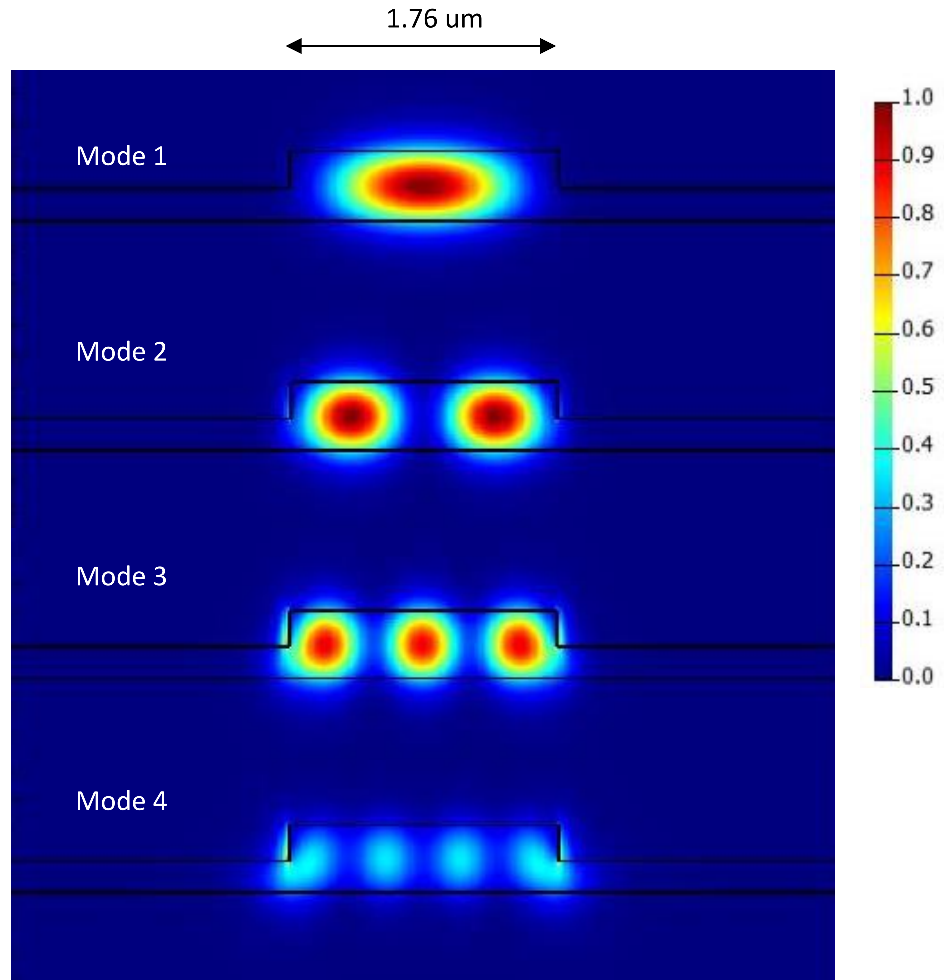

Figure 5-6 Simulated mode profiles of the multimode region with width 1.76 µm on 220 nm Silicon with 100 nm Silicon slab.

Table 7 Real part of effective index of guided modes of a 1.76 µm wide waveguide.

	Mode 1	Mode 2	Mode 3	Mode 4
Effective index (real)	2.818249	2.727719	2.575593	2.368905

Table 8 Simulated mode overlap and power coupling of access waveguide fundamental mode with multimode region (1.76 µm) guided modes.

Multimode region modes →	Mode 1	Mode 2	Mode 3	Mode 4
Overlap with access waveguide mode	0.482726	0.418307	0.0342077	0.016636
Power coupling	0.481807	0.418222	0.0341907	0.0163392

For simulating the MMI length, device geometry with multimode region and access waveguide (as quoted in Table 6) was created in Lumerical MODE with maximum mesh edge length of 5 nm. Power monitors were placed at the two output ports and their output recorded as the length of the multimode region was swept.

Figure 5-7 shows the variation of the normalized output transmission, for top and bottom output port, recorded using the power monitors.

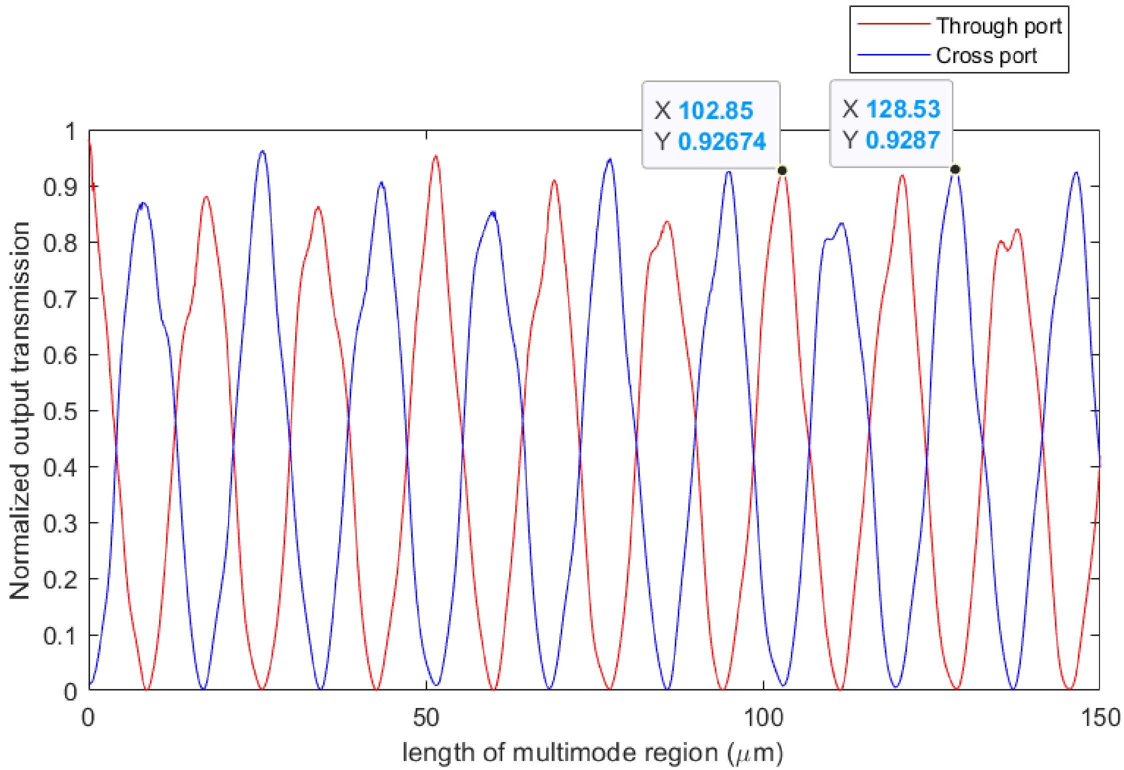

Figure 5-7 Simulated length sweep for non-tapered MMI (through port and cross port for single pass) usign EME solver.

The beat length L_π for the first two modes of the multimode region is defined by ,

$$L_\pi = \frac{\pi}{\beta_0 - \beta_1} = 8.56\ um$$

β_0 and β_m are the propagation constants for the fundamental and the mth higher order mode. And the MMI self-imaging length is defined as

$$L_{MMI} = p(3L_\pi)$$

Where p is an integer value, and even and odd values represent non mirrored (through) and mirrored image (cross) reproduction length of the MMI respectively.

There can be instances where the input field is not perfectly imaged at the self-imaging length, and lead to a degradation of the final image. Δ_m defines the propagation constant error of the m-the mode [140]. Closer the value of $|\Delta_m|$ is to zero, the better is the image reproduction in the MMI (in our case $|\Delta_m|$ = 0.03652).

$$\Delta_m = \frac{\beta_0 - \beta_m}{\beta_0 - \beta_1} - \frac{m(m+2)}{3}$$

The through port transmission response of the MMI device shows a self-imaging length of 51.46 µm which agrees with the above analysis. The intensity profile across the plane placed at a height of 100 nm (towards the top) from the bottom of the silicon slab is shown in Figure 5-8.

Table 9 Simulated multimode region length and transmission for MMI defined by parameters in Table 6.

Parameters	1.76 µm multimode region
MMI length	102.85 µm
Normalized Transmission	0.9287
Loss (dB) – 1 Pass	0.32

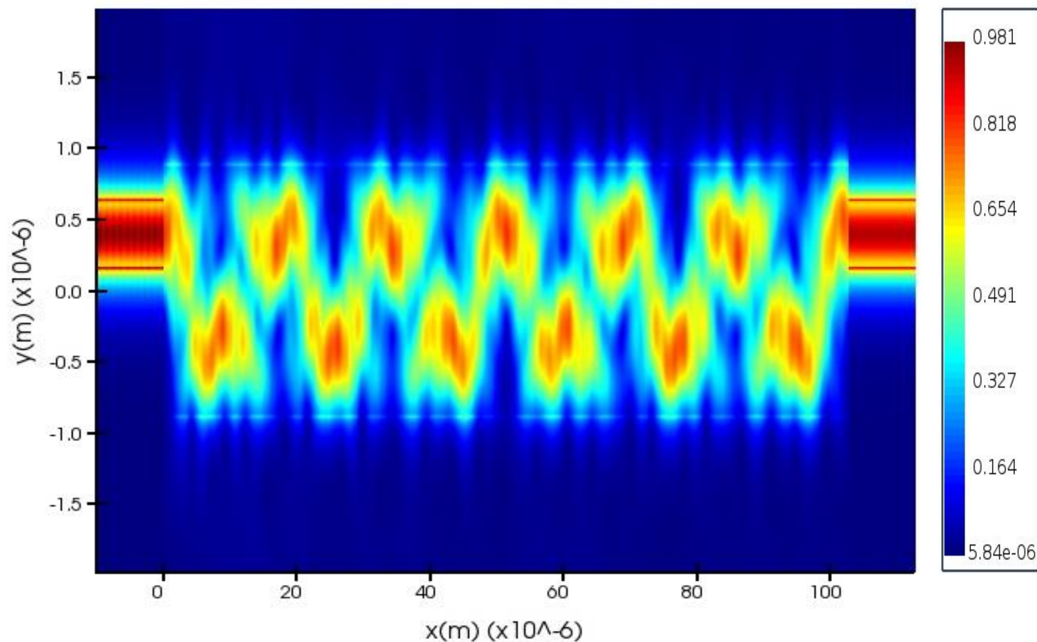

Figure 5-8 Simulated intensity profile of the MMI defined by parametrs in Table 6 and Table 9.

Due to the design procedure, most of the power is coupled into the first two modes of the MMI, hence the multimode region can be tapered to width of 0.8 µm, which supports only two guided modes, using linear adiabatic tapers. The taper length was simulated for mode tapering from 1.76 to 0.8 µm waveguide as shown in Figure 5-9 and was chosen to be 20 µm.

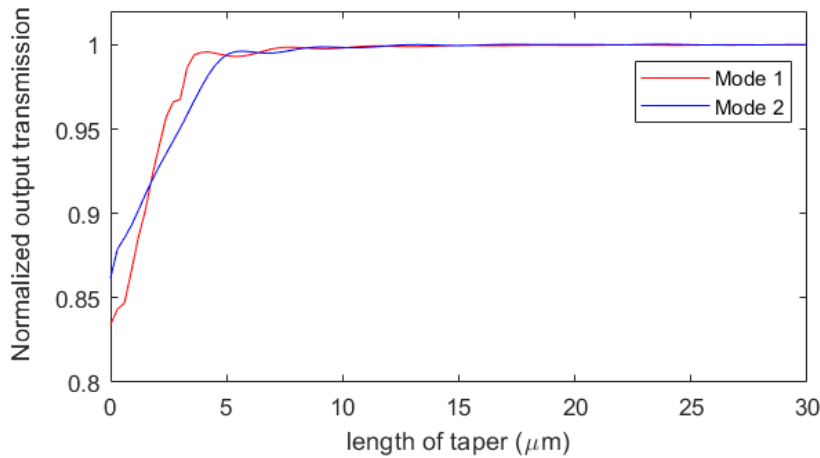

Figure 5-9 Linear adiabatic taper length sweep for mode conversion from 1.76 µm to 0.8 µm waveguide.

Various other parameters along the length of the MMI were chosen in the following manner and top view is shown in Figure 5-10.

1. Initial multimode region length of 5um to allow the modes of 1.76 µm waveguide to settle.
2. The tapered multimode region of width 0.8 µm was set to a length of 100 µm to allow for doping region length (90 µm) to be consistent with non-tapered devices.
3. External length sweep (of multimode region width 1.76 µm) was performed to give the final MMI length dimension.

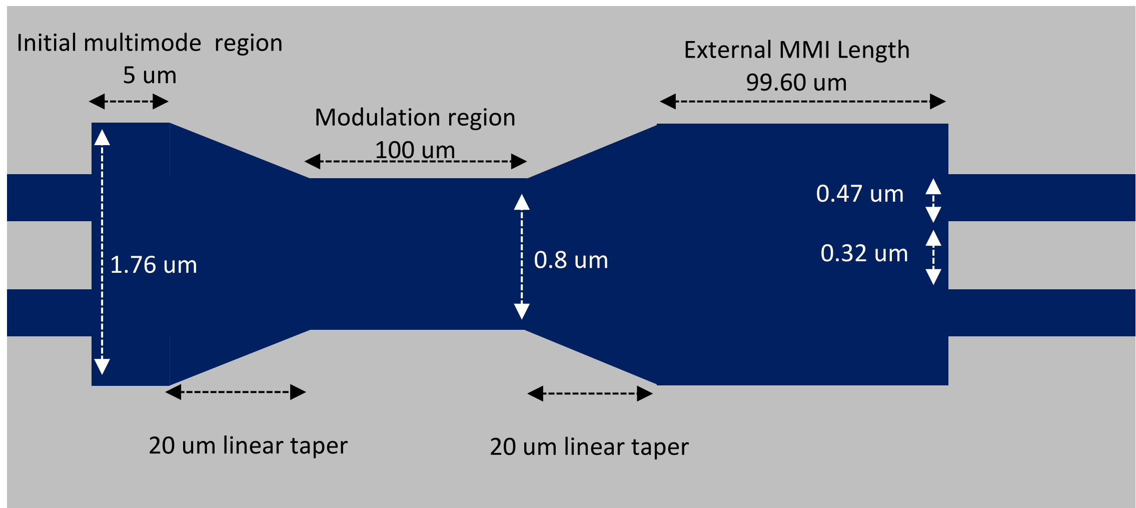

Figure 5-10 Simulation device parameters for tapered MMI device.

The simulated external MMI length is shown in Figure 5-11

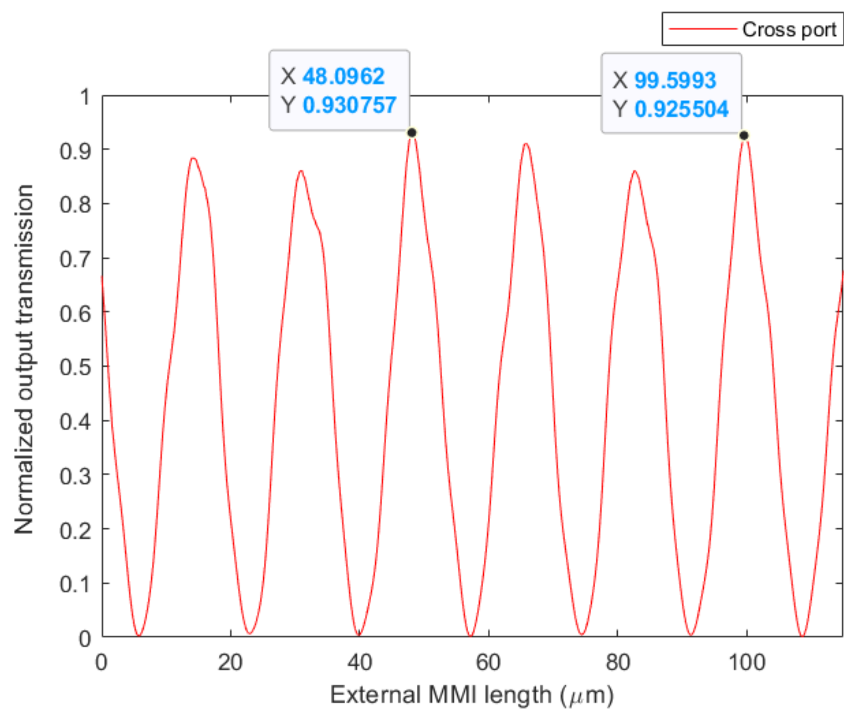

Figure 5-11 Simulated external MMI length (1.76 μm width) for tapered MMI device.

The simulated tapered device parameters are repeated in Table 10. The simulated device intensity profile is displayed in Figure 5-12.

Table 10 Simulated device dimensions for tapered 2x2 MMI device.

Parameters	Dimensions
Access waveguide width	0.47 µm
Access waveguide position w.r.t centre of multimode region	0.395 µm
Initial multimode region	Width = 1.76 µm, length = 5 µm
Adiabatic multimode taper length	20 µm
Multimode region for modulation	Width = 0.8 µm, length = 100um
External multimode region	Width = 1.76 µm, length =99.60 µm
Normalized transmission	0.9255
Loss – 1 Pass	0.33 dB

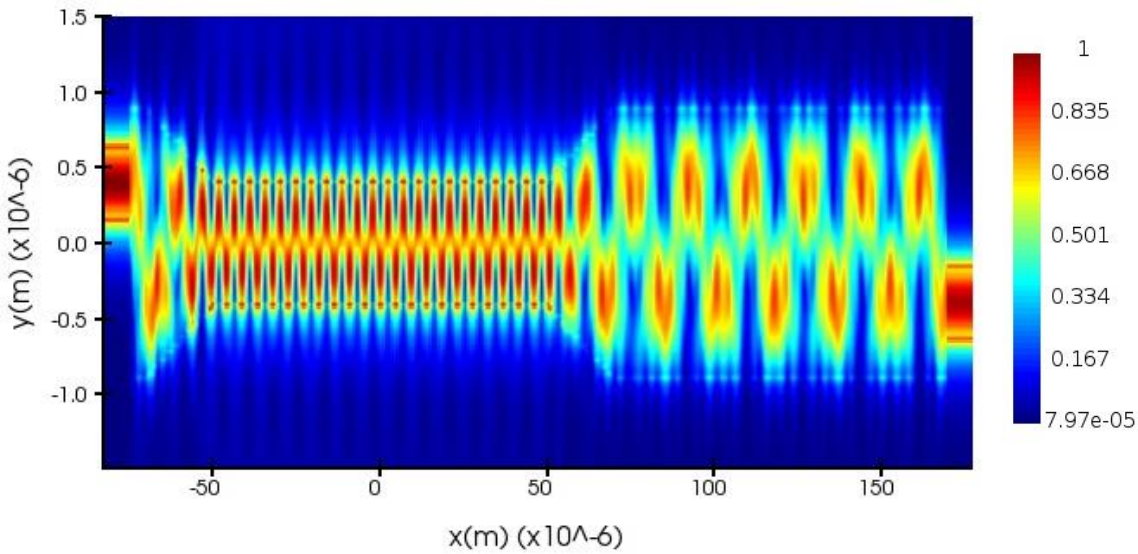

Figure 5-12 Intensity profile for simulated device dimensions as quoted in Table 10 .

5.2.1 Simulation errors and multimode region length of fabricated devices

Unfortunately the initial simulations produced at the Cornerstone MPW mask submission deadline were found to be slightly inaccurate. Different lengths were therefore fabricated to those found to be optimal in the above section. All other parameters were kept the same in the new analysis (as demonstrated in previous section) and only the MMI lengths corrected. Table 11 shows the fabricated device lengths for the respective cases.

Table 11 Fabricated device lengths (different than presented in simulation work).

Device Identifier	Simulated multimode region length (corrected)	Fabricated multimode region length
Non tapered MMI	102.85 µm	100 µm
Tapered MMI (External MMI length)	99.60 µm	106.53 µm

Cutback structures with increasing number of devices connected in series (1 to 5) were fabricated to obtain the insertion loss of the devices. Length iterations with Multimode region length of -4 µm, -2 µm, +2 µm, +4 µm from the fabricated multimode region length were also fabricated to account for any fabrication tolerance.

Cutback devices with single pass of all the above mentioned variations were also fabricated. In a single pass structure the light is not recycled and light coming out of the through port of the MMI is coupled out of the chip using grating coupler.

Due to limited writing area available on the CORNERSTONE platform, most of the space was taken up by the test device structures and no length iterations were fabricated for the active devices in imbalanced MZI configuration.

Normalization structures consisting of 0.4 µm single mode waveguide as the phase shifting element were fabricated alongside the MMI phase shifter devices for comparison.

The doping region separation for all fabricated devices was set to 0.8 µm from the edge of the waveguide sidewall.

5.3 Layout and Fabrication

Layout masks were generated using L-edit and fabricated via CORNERSTONE platform on 220 nm SOI. A 70nm shallow etch was used to define the grating couplers followed by a 120 nm etch to define the waveguide layer using DUV lithography and ICP etching tools. P++ and N++ doped regions were then defined through DUV lithography and high dose ion implantation of BF_2 and Phosphorus. This was followed by depositing a 1µm thick PECVD SiO_2 cladding. Vias were then etched through this top cladding layer down to the high doped regions. The electrodes consisting of Ti, TiN and Al stack were then formed through sputter deposition, lithography and ICP etching. Figure 5-13 shows the fabrication flow for the CORNERTONE active run.

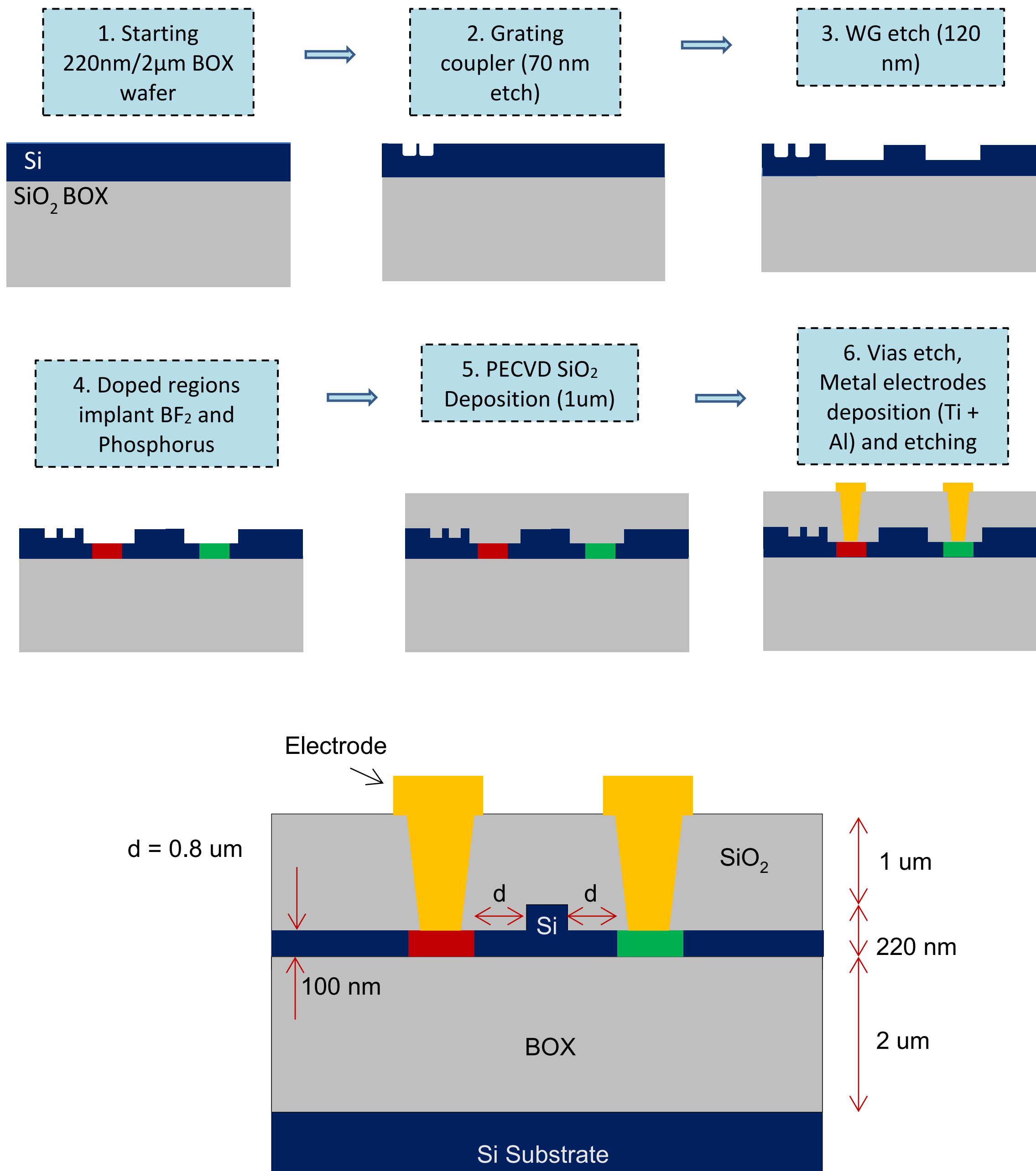

Figure 5-13 Fabrication flow (top) and schematic cross section (below) of the fabricated carrier injection phase shift devices.

The layout mask for carrier injection based devices followed a similar procedure to that used in the case thermal optical devices as shown in Figure 4-17 with the lithographic parameters shown in the image above.

5.4 Experimental results

The wavelength transmission response of the fabricated MMI devices (cutback and phase shifter MZI) were normalised to a single mode waveguide (width = 0.4 µm) to remove the grating coupler

spectral response, coupling loss and the testing set up loss. The response after normalization of the test structures is shown in Figure 5-14.

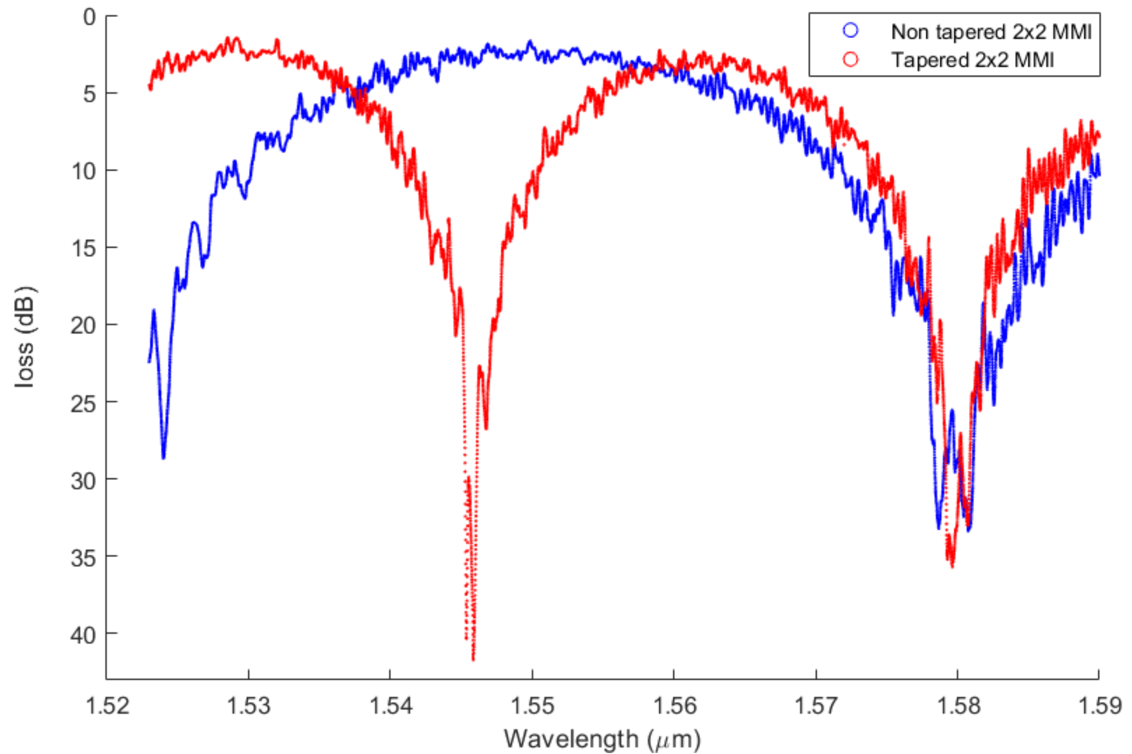

Figure 5-14 Transmission wavelength spectrum of the fabricated non tapered and tapered 2x2 MMI device with MMI length = 100 µm and external length = 106.53 µm repectively (wihtout MZI).

The transmission response of the fabricated tapered and non-tapered MMI devices (Figure 5-14) showcase a different FSR due the difference in the effective index (or propagation constant represented by β_n for n^{th} mode) of the first two modes. This is related to the difference in the beat length, $L_\pi = \frac{\pi}{\beta_0 - \beta_1}$ for the tapered and non-tapered MMI devices and the self-image length for the through port of the MMI device which is defined by $(m \times L_\pi) + 1$, where $m = 0,6,12$ ... and so on.

Ripples were observed in the transmission spectrum. Post processing to the data was performed in MATLAB. The smoothing function averaged +/-100 wavelength data points around the central wavelength (201 points in total) to give the "filtered data" used for loss calculations. Figure 5-15 displays the filtered data and verifies that it closely replicates the transmission spectrum trend of the device without the ripples.

The non-tapered and tapered 2x2 MMI devices recorded minimum insertion loss of 1.58 dB (at 1.55 µm) and 1.64 dB (at 1.53 µm) respectively. Wavelength 3 dB spectrum response of around 24 nm and 15 nm respectively for non-tapered and tapered cases was also observed. Since only the

MMI lengths of 100 µm and 106.53 µm were fabricated in the phase modulator MZI configuration, only those results are considered in the remaining of this chapter. Minimum loss wavelength and loss value are reported in Table 12 for non-tapered 2x2 MMI devices and in Table 13 for tapered 2x2 MMI devices. The transmission spectrum for non-tapered and tapered 2x2 MMI devices used for cutback measurements are displayed in Figure 5-15 and Figure 5-16 respectively.

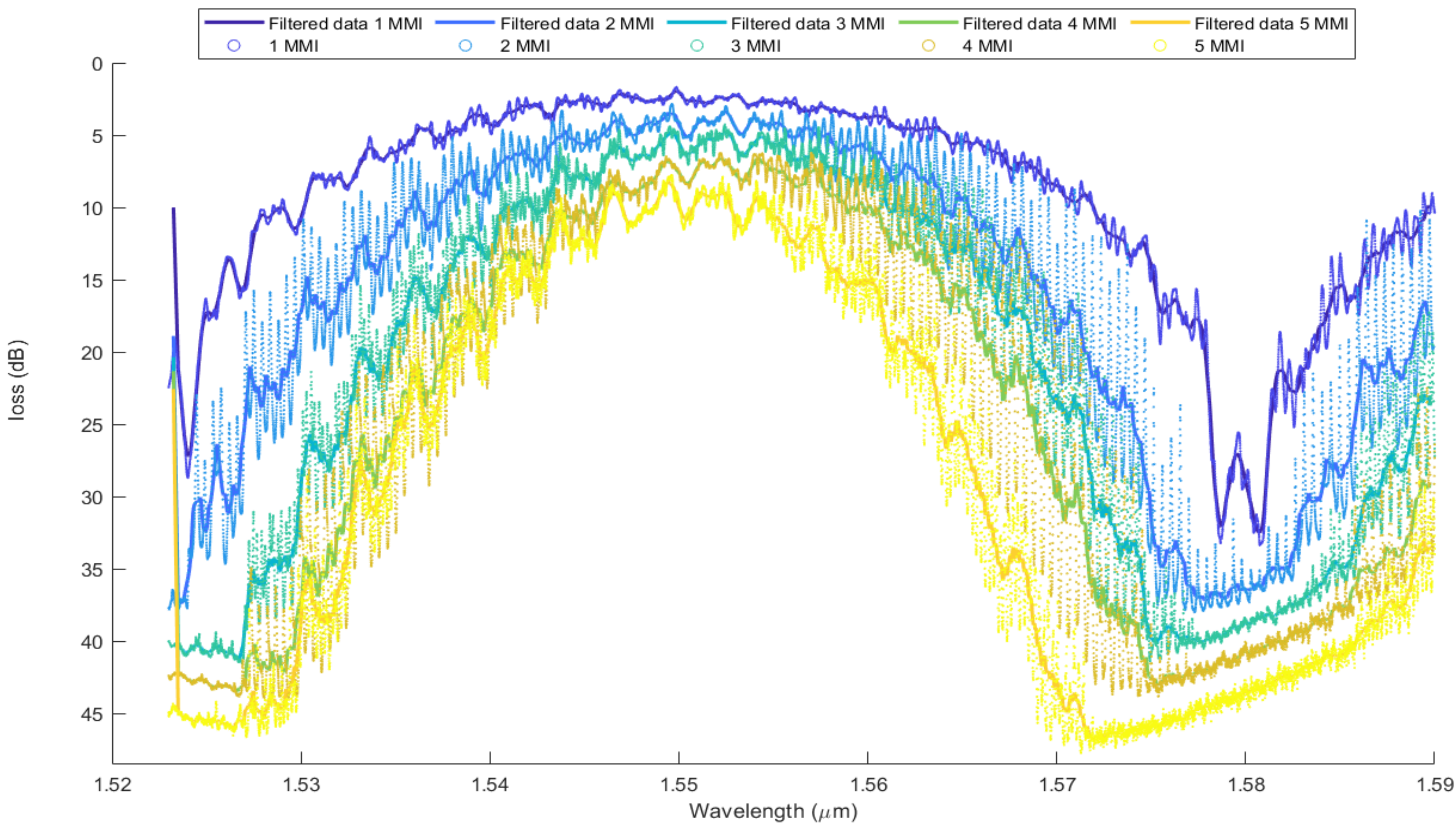

Figure 5-15 Transmission wavelength spectrum of the fabricated cutback type non- tapered 2x2 MMI devices with external MMI length = 100 um (1, 2, 4, 5 two pass MMI devices in series) and averaging function giving the ' filtered data' used for calculations.

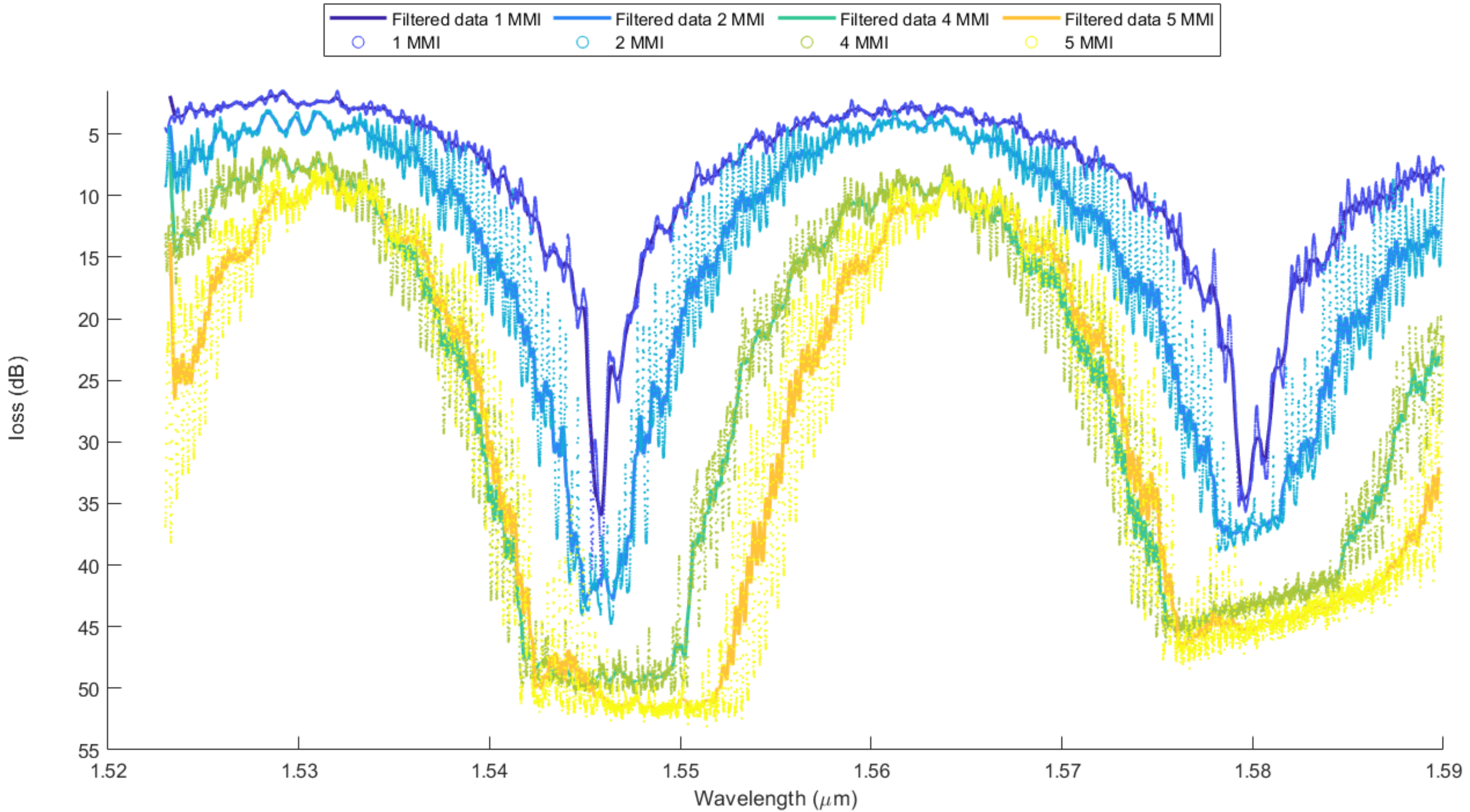

Figure 5-16 Transmission wavelength spectrum of the cutback type fabricated tapered 2x2 MMI devices with external MMI length = 106.53 um (1, 2, 4, 5 two pass MMI devices in series) and averaging function giving the ‘ filtered data’ used for calculations.

MATLAB was again utilized to calculate the loss per device and the results are portrayed in Table 13.

Table 12 Minimum loss and wavelength for non-tapered 2x2 MMI device.

MMI length (um)	Wavelength (um)	Minimum loss (dB/ MMI)
96	1.5776	Out of wavelength spectrum
98	1.5634	1.67
100	1.5509	1.58
102	1.5372	1.39
104	1.5781	1.74

Table 13 Minimum loss and wavelength for tapered 2x2 MMI device.

External MMI length (um)	Wavelength (um)	Minimum loss (dB/ MMI)
102.53	1.5876	1.38
104.53	1.5720	1.12
106.53	1.5308	1.64
108.53	1.5857	1.83
110.53	1.5732	2.46

As mentioned in section 5.2.1, the length of the fabricated MMI devices was incorrect. From simulation results (Figure 5-18), it is clear that the device length is not equal to self-imaging and the minimum loss recorded in experimental devices is comparable to the simulated loss at multimode length of $(m \times L_{\pi}) + 1$, where $m = 0,6,12 \ldots$ and so on and defines the self-image length for the through port of the MMI device. Since, due to design constrains majorly two modes are excited in the multimode region, each port (cross and through) displays a maximum value every $2L_{\pi}$ multimode region length apart (as shown in Figure 5-17). Fabricated MMI devices must be operating on one such wavelength maxima defined by MMI length of $(m \times L_{\pi}) + 1$, where $m = 0,6,12 \ldots$ Possible reasons for this could be silicon waveguide height and fabrication tolerances which lie in the range of +/-20 nm. Similar analysis is true for the tapered designs as well as they recorded a loss of around 1.64 dB.

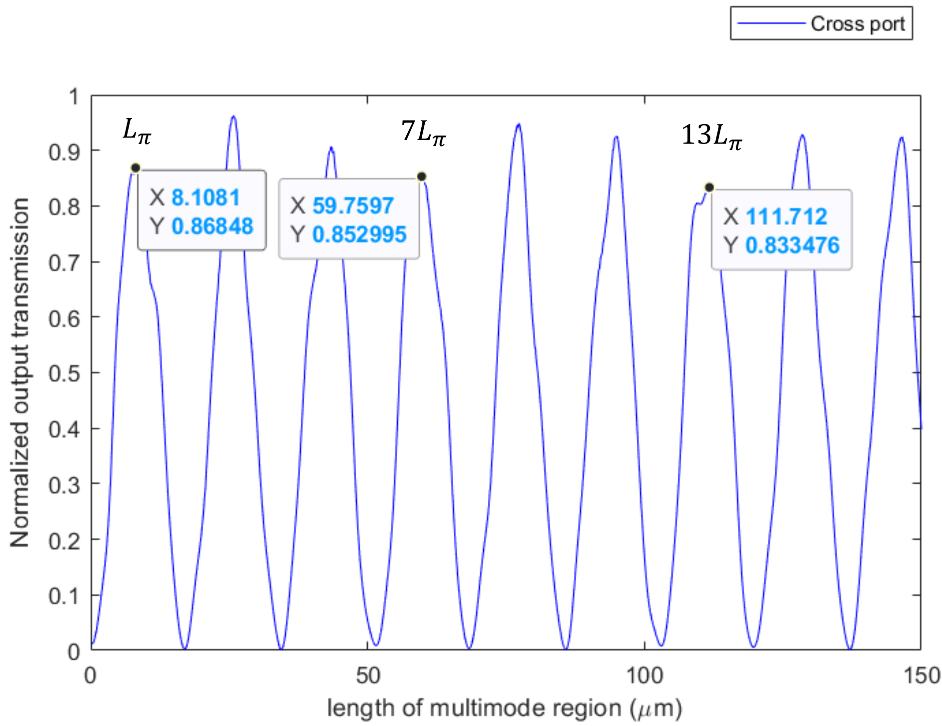

Figure 5-17 2x2 non-tapered MMI cross port output transmission as a function of multimode region length.

The simulated non tapered device shows a (2 pass) loss of 1.58 dB for a multimode region length of 111.712 µm which is in good agreement with the experimental device loss of 1.58 dB for fabricated multimode length of 100 µm.

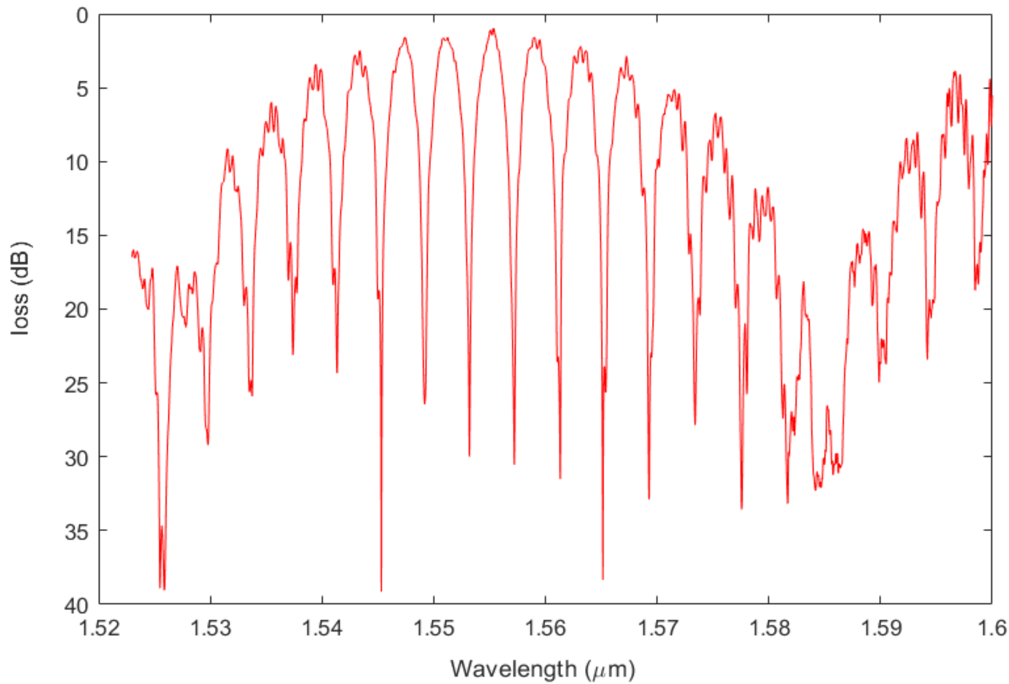

Figure 5-18 Normalized MZI response with 2x2 non-tapered MMI as phase shifter elements in both arms.

The MZI response is enveloped by the wavelength response of the 2x2 MMI devices as shown in Figure 5-18.

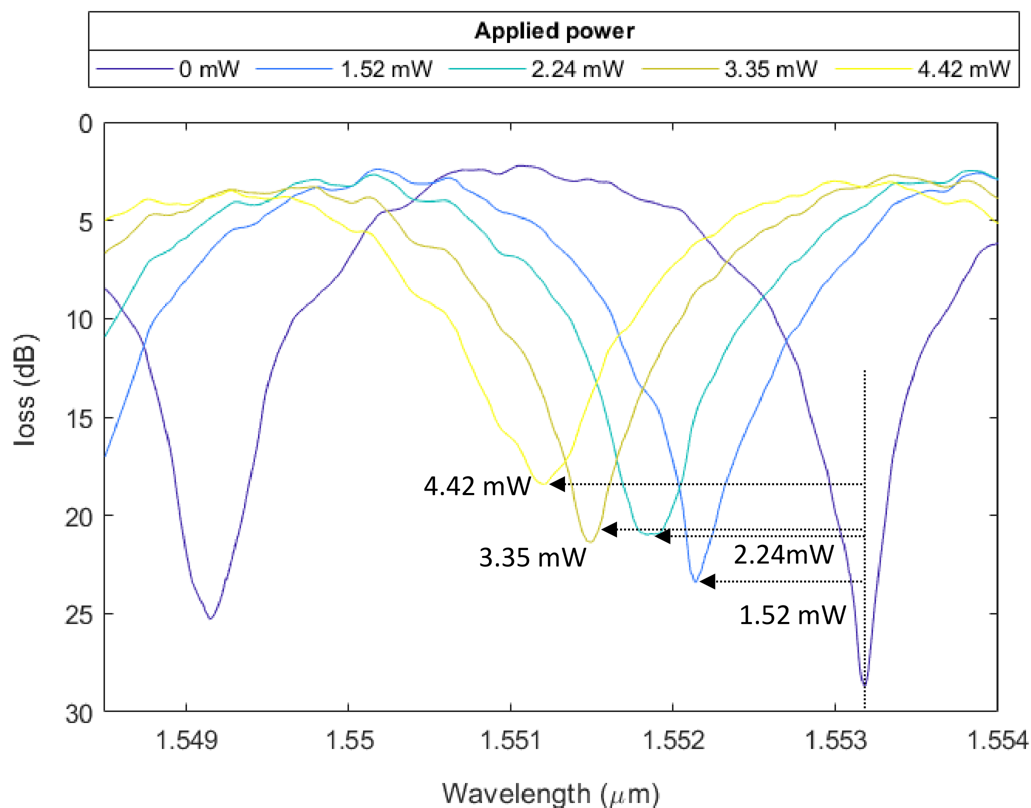

Figure 5-19 Wavelength spectrum shift with applied power for MZI with 2x2 non-tapered MMI as phase shifter element.

Figure 5-19 shows the recorded optical wavelength spectrum for various applied powers for MZI with non-tapered 2x2 MMI as the phase shifter element. A spectral minima nearest to the 1.55 µm wavelength in the transmission spectrum is tracked in the MATLAB analysis as the input power is swept through. Next, the phase shift from the recorded spectrum is extracted using minima tracking techniques similar to section 4.2.6. Similarly the recorded optical transmission spectrum for tapered 2x2 MMI devices is plotted in Figure 5-20.

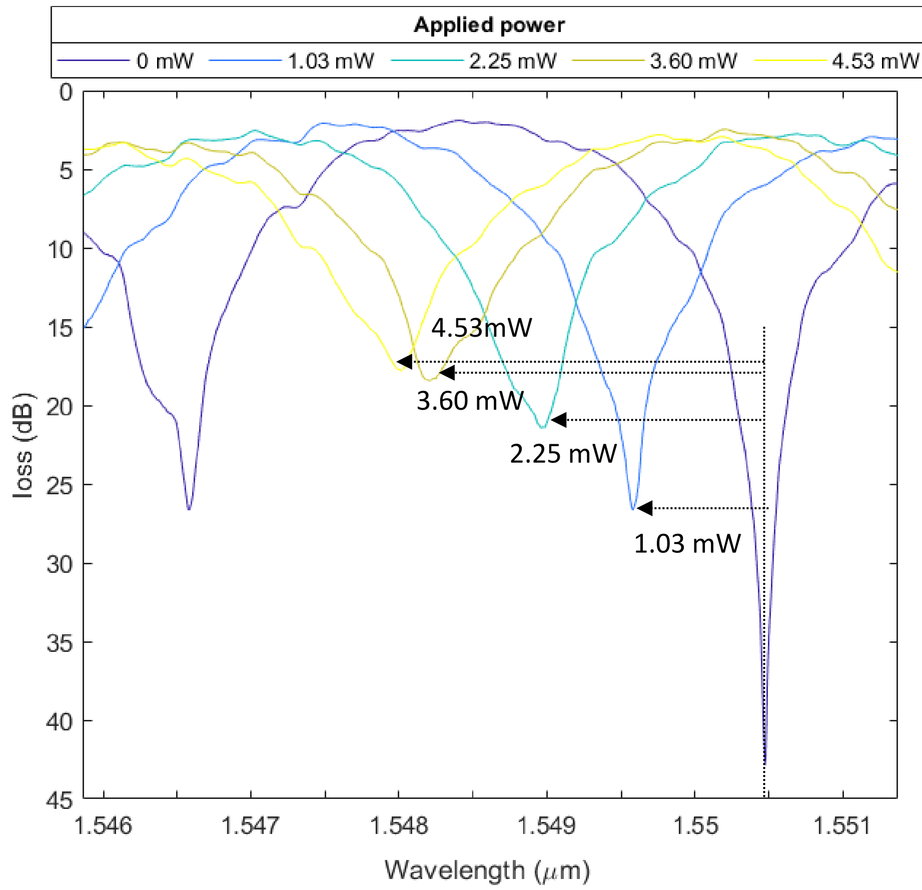

Figure 5-20 Wavelength spectrum shift with applied power for MZI with 2x2 tapered MMI as phase shifter element.

Figure 5-21 displays the extracted phase shift w.r.t applied power for the fabricated devices at wavelengths around 1.55 µm.

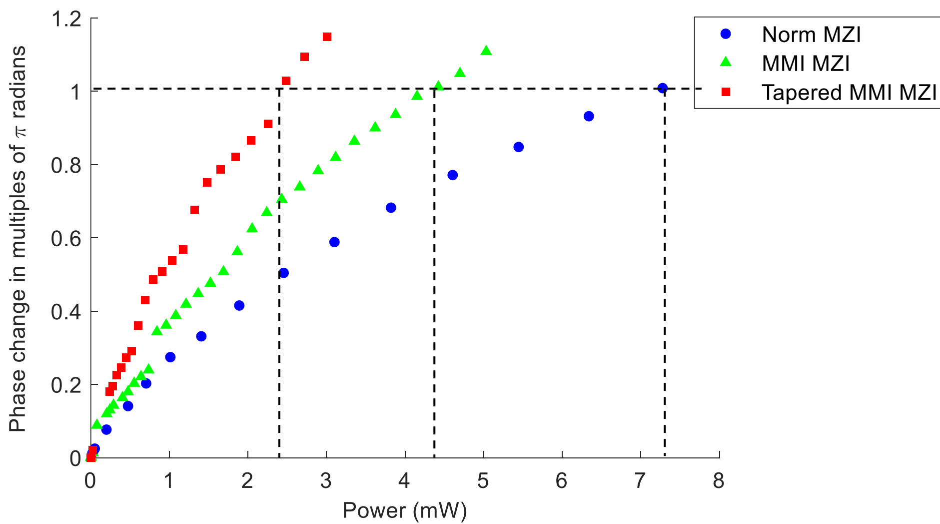

Figure 5-21 Phase shift vs applied power for fabricated normalization MZI and MZI with 2x2 MMI devices at 1.55 µm.

The phase shift curves for the MMI based devices are not smooth like that obtained for normalization device due to the minima tracing mechanism used in phase extraction and ripples in the measured device spectrum.

The Non-tapered and tapered MMI phase shifter based MZI devices achieved a π phase shift for 4.30 mW and 2.43 mW respectively compared to 7.28 mW required by the conventional single mode waveguide (waveguide width = 0.4 µm) based normalization MZI structures. This justifies the simulation work presented earlier in this chapter and translates to power savings of 40.9 % and 66.6 % respectively.

Table 14: π phase shift current and power requirements for fabricated devices around 1.55 µm wavelength.

Device	Wavelength (um)	Modulation efficiency	
		I (mA)	Power (mW)
Norm MZI	1.5498	6.19	7.28
2x2 Non-tapered MMI MZI	1.5492	3.69	4.30
2x2 Tapered MMI MZI	1.5505	2.32	2.43

5.4.1 AC characterization

For AC response, the devices were actuated with a peak-to-peak AC voltage of V_{ac} = 0.19 mV around a DC Bias of Vdc = 0.9 V at 1550 nm to be in the operating range of the devices. All of the devices were operated at a modulation rate of 31.25 MHz. The optical output responses are shown in Figure 5-22 and the rise time (90 %) and fall time (10%) of different devices are plotted in Table 15.

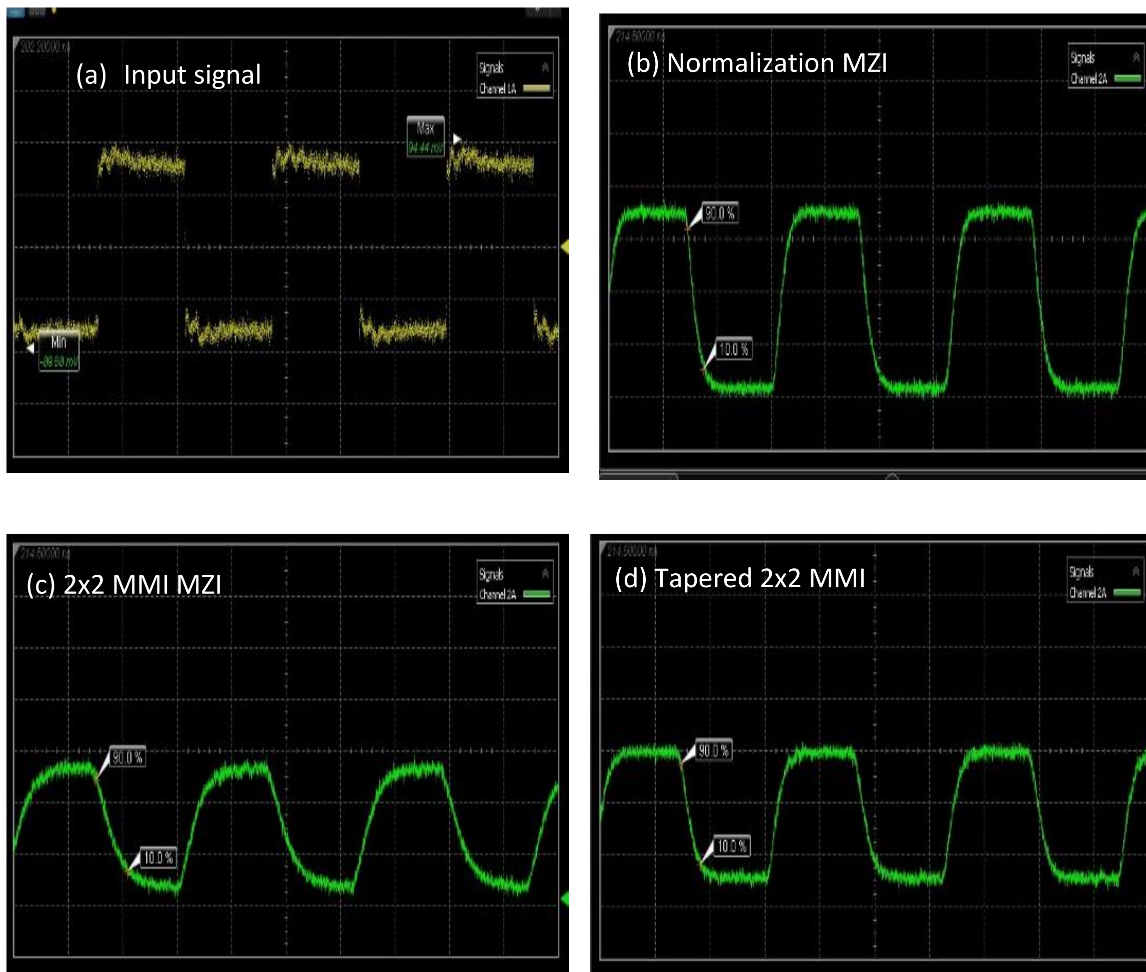

Figure 5-22 AC measurements for various devices (a) the input signal 31.25 MHz, (b) Normalization MZI, (c) 2x2 MMI MZI, (d) Tapered 2x2 MMI MZI.

Table 15: Time response of the fabricated MZI devices at 1.55 µm wavelength.

Device	AC characteristics	
	Rise time (ns)	Fall time (ns)
Norm MZI	2.81	3.07
2x2 Non-tapered MMI MZI	5.20	5.35
2x2 Tapered MMI MZI	3.29	3.32

As expected, the Rise/fall time increases with the increase in the separation between the doping regions, which is a characteristic of the P-i-N junction injection modulator devices. For the tapered MMI devices, the On-off time is within close range to the single mode waveguide based normalization MZI devices.

5.5 Summary

In this chapter power reduction and efficiency enhancement of carrier injection based phase modulation devices using a 2x2 MMI with modulation region consisting of 1.76 µm width waveguide and 0.8 µm waveguide have been studied. Power reduction of 40% and 66% have been experimentally demonstrated with 2x2 non-tapered and tapered MMI devices having with light recycled twice through them.

The MMI length of 251.53 µm and 100 µm for the tapered and non-tapered 2x2 MMI were utilized to achieve this efficiency enhancement. The devices length can be further reduced by shortening the external MMI length for the tapered MMI case to the 1st self-imaging length and using smaller linear tapers (or logarithmic tapers) for mode conversion to and from 1.76 µm and 0.8 µm waveguides. The device insertion loss can also be reduced to less than 1 dB by using the correct self-imaging length for the multi-mode region.

Chapter 6 Spread of heat from Thermo optic elements

As the density of photonic integrated circuits increases, the thermal crosstalk between nearby photonic elements becomes a considerable issue to tackle ensuring that the circuit works efficiently. Designers usually seek to make the overall footprint of the circuit as small as possible in order to make efficient use the silicon real estate, allowing a lower fabrication cost per chip. Understanding the lateral heat spread from a thermo-optic element of a device is therefore a very important consideration, limiting the compactness of closely packed components before thermal crosstalk becomes an issue, ultimately dictating how small the overall chip can be.

Nowadays, many different platforms (defined by silicon and buried oxide layer thickness) are used to fabricate devices on SOI (Silicon-over-insulator) wafers in silicon photonics. Some of the common platforms are offered by CORNERSTONE [141], and are displayed in Table 16.

Table 16 Common SOI platforms offered by CORNERSTONE MPW service.

Si Overlayer thickness	BOX thickness	RIB waveguide slab height	Top cladding layer thickness
220 nm	2 µm	-	1 µm
220 nm	2 µm	100 nm	1 µm
340 nm	2 µm	-	1 µm
340 nm	2 µm	100 nm	1 µm
500 nm	3 µm	-	2 µm
500 nm	3 µm	200 nm	2 µm

In this chapter, simulation and experimental results have been presented to study the heat spread from a commonly used metal bar strip based thermal element used in the CORNERSTONE MPW.

6.1 Simulation and fabrication test structure

Lumerical's HEAT solver was used to simulate the steady state thermal response of the area around the thermo optic element. Two basic types of device geometry were created in Lumerical as shown in Figure 6-1. Type A study device consisted of single STRIP (and RIB for other platforms) waveguide defined by 5 µm trenches around it and with centre of the heater placed at ΔS_{offset} - from the centre of the waveguide.

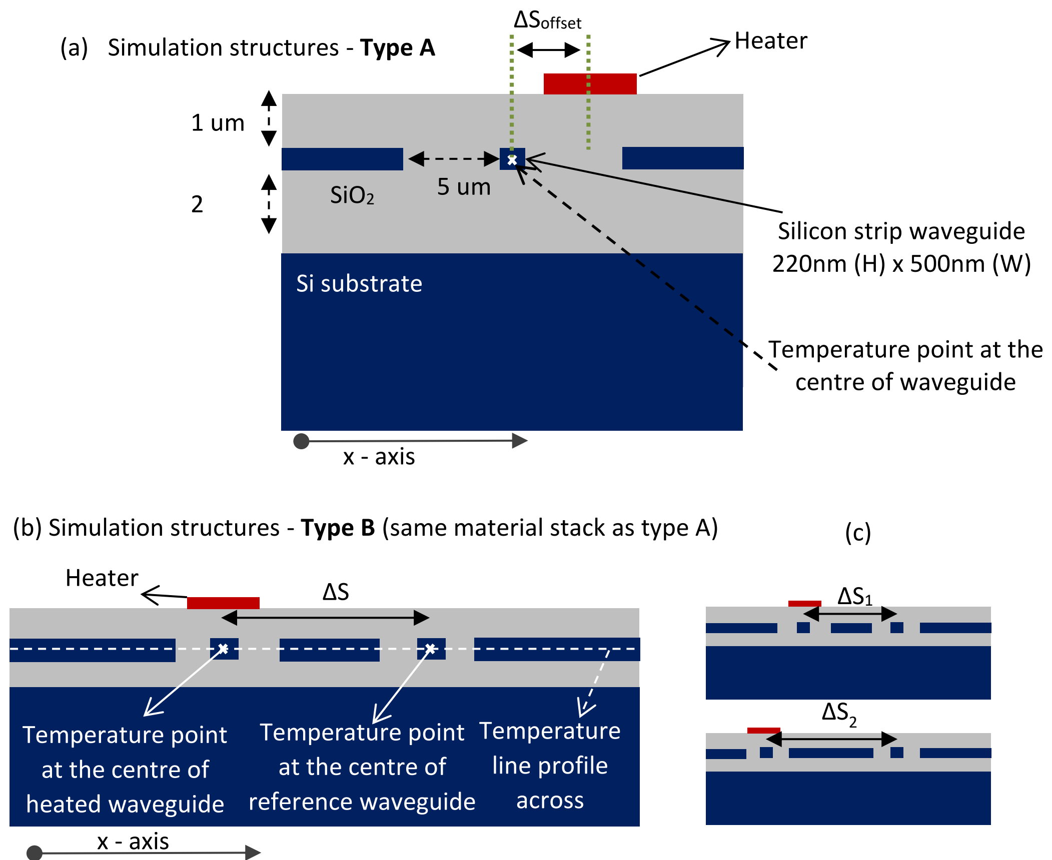

Figure 6-1 Cross-section of the simulated structures with 220nm x 500 nm (height x width) STRIP waveguides. (a) Represent the study structure for change in heater offset (ΔS_{offset}) w.r.t. the waveguide centre. (b) Represents the study structure for thermal crosstalk between two waveguides separated by ΔS (c) Cross-section for two different waveguide separations (Type B), ΔS2>ΔS1.

For heat simulation, the silicon substrate height was chosen to be 725um thick and the bottom of the substrate set to a fixed temperature of 300 K. A uniform heat source object made of aluminium with dimensions of 150 nm x 2 µm (height, width), placed 1 µm over the waveguide, and surrounded at the top by air was used in conjunction with temperature monitors placed around the waveguide to capture the temperature profile.

Figure 6-2 shows the two different type of test structures fabricated to study the effect of heat spread from the thermal element in 220 nm SOI STRIP platform. The first (Figure 6-2(a)) corresponds to type A of the simulated structures and consisted of various heating elements placed along the one arm of a MZI with large separation (>220 µm) between both the arms, so as to avoid any crosstalk from the heated arm. The offset of the heating elements from the centre of the waveguide were 0 µm, 2 µm, 4 µm, 6 µm and 8 µm. The second type of test structures

corresponds to type B of the simulated structures and had a varying separation of the two MZI arms to study the thermal crosstalk between the adjacent arms.

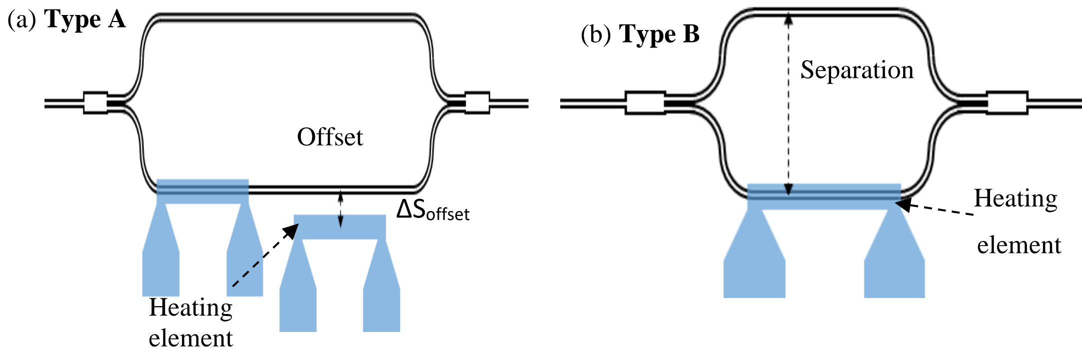

Figure 6-2 Fabricated test structures for characterization of the lateral spread of heat. (a) Type A- Consists of multiple heating elements along one arm of MZI, each with a different positional offset from normal position (ΔS_{offset}=0, where centre of the waveguide and the centre of the heating element are placed on top of each other). (b) Type B - Consists of a set of MZI, each with a different waveguide arm separation to study the thermal crosstalk.

6.2 Fabrication

Fabrication of the test phase modulators was performed using the Cornerstone MPW service [141] in 220nm overlayer silicon on insulator. First, 248nm deep ultraviolet (DUV) lithography is used to expose the grating couplers in photoresist before inductively coupled plasma (ICP) etching of 70nm into the silicon overlayer. DUV lithography and 220nm ICP silicon etching was then used to define strip waveguides. One micron of silicon dioxide was then deposited as a top cladding of the waveguide using plasma enhanced chemical vapor deposition (PECVD). Two DUV lithography, metal deposition and lift-off steps were then used to define first the titanium nitride heater filaments and then gold pads for electrical connection to the filament. An optical microscope image of one of the fabricated thermo-optic MZI is shown in Figure 6-3.

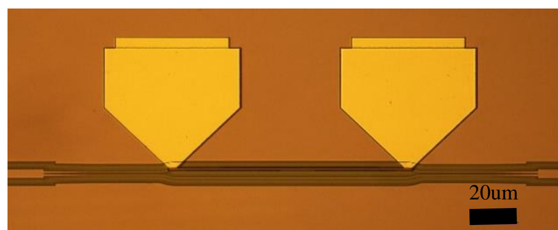

Figure 6-3 Microscope image (top view) of the fabricated devices (Type B).

6.3 Simulation and experimental results

The applied electrical power to the heater and the respective wavelength spectrum was then recorded using characterization techniques mentioned in chapter 3. The MZI output optical power versus electrical power data was then fitted to sinusoidal functions to extract the switching power (or power required to produce a π radian phase shift).

6.3.1 Type A structures (with heater element and waveguide displacement)

The normalised optical transmission against electrical drive power on the heater for the Type A test structure is shown in Figure 6-4(a). The different colour plots represent the optical power measured for the heater elements with different offset positions. Figure 6-4(b), shows the extracted switching power (2π) for each heating element offset. A switching power (2π) of 26mW is required for the zero-offset case. 2π phase shift was not reached over the range of electrical power applied to the heating element for offsets of 6um or larger. It can be seen that the switching power required to achieve a 2π phase shift rises dramatically at ΔS_{offset} of 6um and beyond.

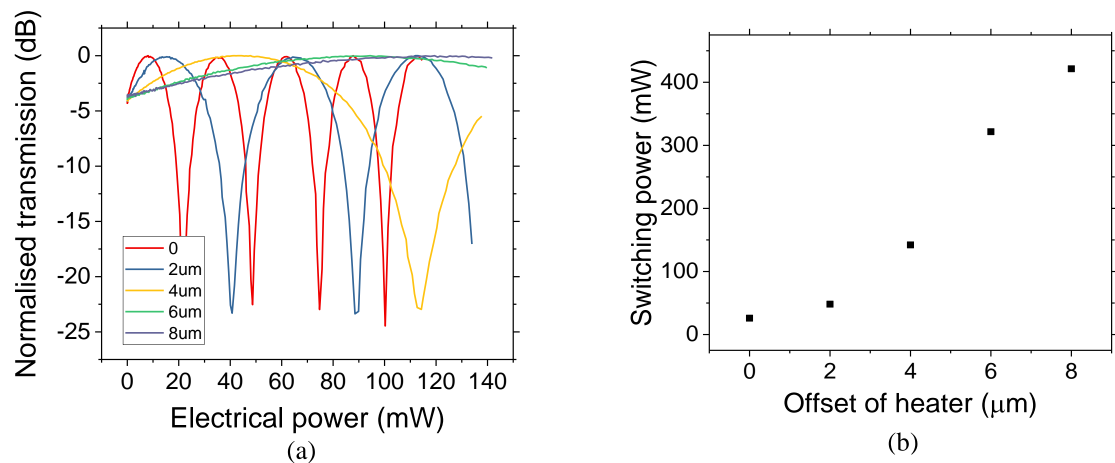

Figure 6-4 (a) MZI normalised transmission against electrical drive power for the different heating element offset positions. (b) Electrical power required for switching (2π phase shift) with the heater off-set from the waveguide by different amounts.

Since the thermo-optic effect in silicon is well known [142], it is possible to calculate the rise in temperature in the waveguide with the switching power required for a 2π phase shift. This data is plotted in the graph shown in Figure 6-5. Although, the propagating mode would be affected by temperature profile overlapping the mode area, temperature data at the centre of the waveguide was used for comparison with the experimental results (displayed by the white cross on Figure 6-1 (a)).

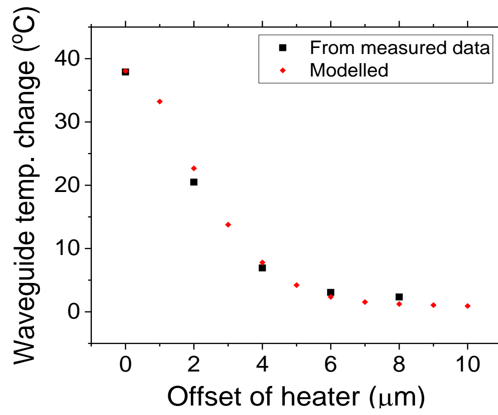

Figure 6-5 Temperature change in the waveguide for different heater element position offsets (ΔS_{offset}) with the electrical power required for 2π switching in the zero offset case.

A good agreement between simulation and experimental results can be observed. As can be seen the temperature change in the waveguide drops from approximately 38°C with $\Delta S_{offset} = 0$, to around 2°C with $\Delta S_{offset} = 8$um. According to the simulations the temperature change in the waveguide drops to around 0.6°C with a 10um ΔS_{offset}.

6.3.2 Type B structures (with separation between the MZI arms)

The simulated temperature profile for type B structures (along the white dotted line passing through the middle across the height, as shown in Figure 6-1(b)) are plotted in Figure 6-6.

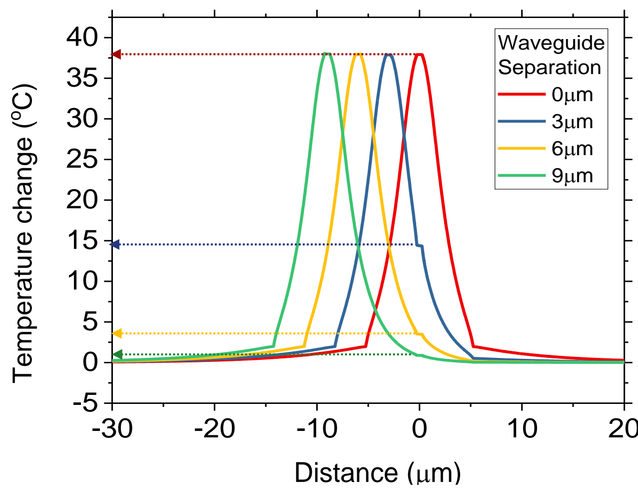

Figure 6-6 Simulated temperature line profile across the centre of waveguide cross section (as shown in Figure 6-1(b)) for different MZI arm separations. Red line (ΔS=0) represents the heated and reference waveguide without separation (i.e. they are the same waveguide), and blue, orange, green line represents heated waveguides at position -3, -6, -9um distance with reference waveguide placed at 0 μm.

It is clearly visible that for different ΔS, the reference waveguide is also heated to an extent which causes the lowering of the effective phase shift between the two arms. It can also be seen that the temperature of reference waveguide reduces as the heated arm and filament moves further away from it.

Next, the type B fabricated test structures consisting of the 3 separate MZI with ΔS = 2um, 4um and 6um (separation between the two MZI arms) were measured. The normalised optical transmission against the heater electrical drive power for each MZI arm separation is shown in Figure 6-7 (a). As with the type A test structure the switching power required for each of the MZI was then extracted using a fitting method and the data plotted in Figure 6-7(b).

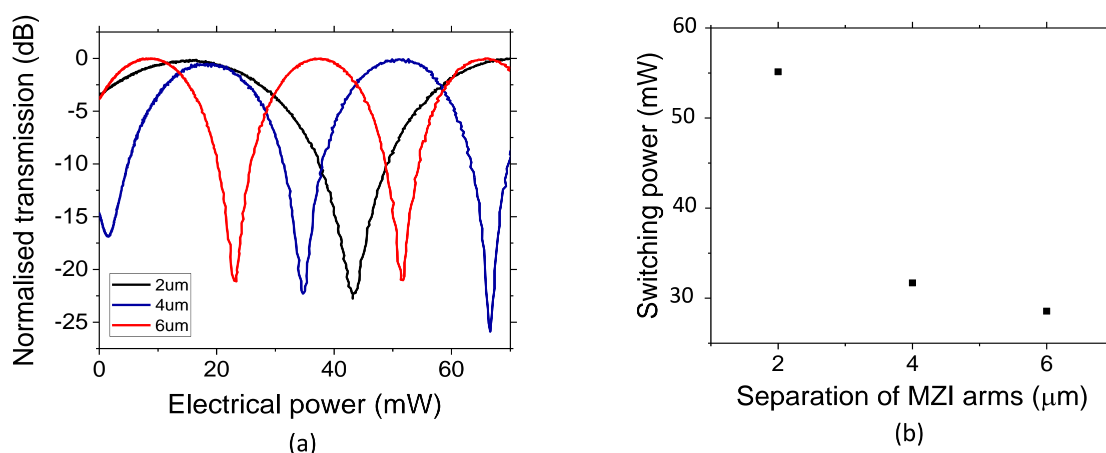

Figure 6-7 (a)Normalised transmission against electrical drive power for the three MZI with waveguide arm separations of 2um, 4um and 6um. (b) Electrical power required for switching (2π phase shift) for the 3 different MZI with different arm separation.

As the MZI arm separation (ΔS) is reduced, the electrical drive power required for switching (2π) is increased due to the thermal crosstalk from the heater on one arm to the other, meaning that the phase shift in the intentionally heated arm is partially cancelled out and therefore needs to be driven harder. At a separation of 6um the electrical power required for switching is 28.6mW which is just slightly higher than the 26mW required in the first test structure where a very large MZI arm separation >220um was used. This indicates that thermal crosstalk is minimal when a separation of 6um or greater is used.

6.3.3 Other platforms

The simulation techniques utilized above can be extended for analysing other SOI platforms for example those offered by CORNERSTONE and in general use as well. Three different silicon overlayer thicknesses as the starting wafer have been considered as shown in Table 16.

From the experimental analysis in section 6.3.2, we can conclude that there would be minimal thermal crosstalk effects from one arm of the MZ to the other when the distance between the waveguides is more than 6 µm. This calculates to a percentage change of 90%, compared to the peak temp of the reference waveguide undergoing phase transition. This threshold number has been used to analyse the other platforms and the data is plotted in Figure 6-8.

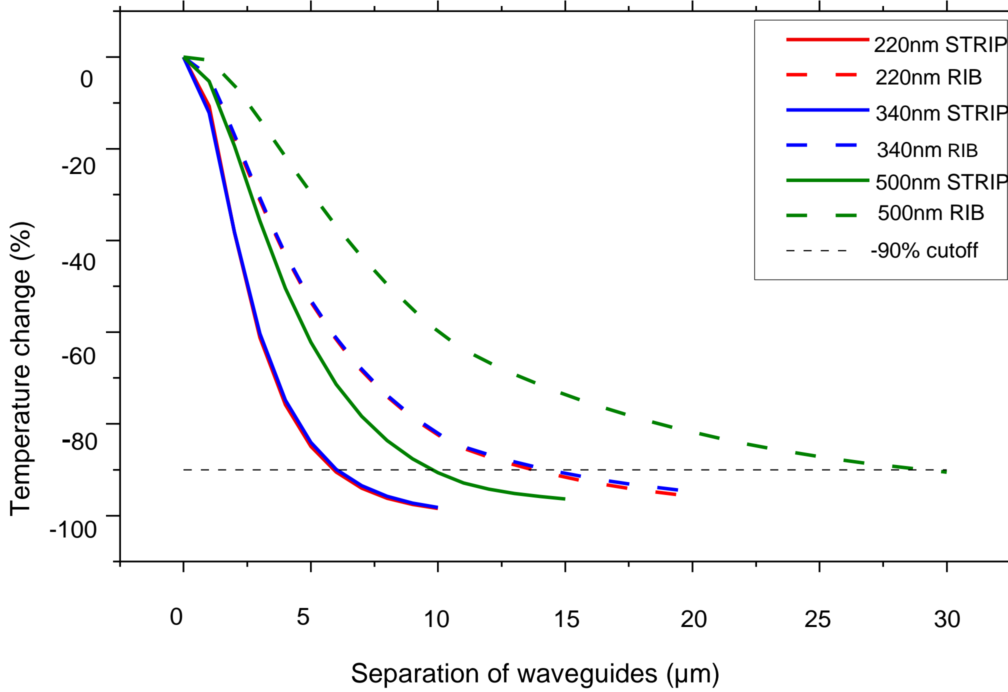

Figure 6-8 Percentage temperature change in the reference waveguide for different waveguide separations (ΔS) in various SOI platforms.

From Figure 6-8, the following guidelines for minimal crosstalk (-90% temperature) can be inferred.

Table 17 Guidelines for waveguide separation with minimal thermal crosstalk for various SOI platforms.

Si overlayer thickness	STRIP	RIB
220nm	6um	14um
340nm	6um	14um
500nm	10um	28um

The data in Table 17 shows that the RIB waveguide-based platforms require a larger separation to achieve minimal crosstalk due to the presence of the silicon slab layer which is comparatively more conductive of heat than SiO_2. The relatively high lateral spread of heat in the 500nm SOI platform which utilizes a greater silicon slab height (200nm) is also clearly noticeable in the results.

6.4 Summary

In this chapter guidelines for dense packing of PIC using metal strip bar thermal element have been presented for various SOI platforms via simulation and experimental demonstration. The results from this chapter have also been published [143].

Chapter 7 MOEMS Phase modulator

Strong confinement and guiding of light in nanometer wide low index structures has been demonstrated by [99, 144, 145]. This chapter firstly introduces the fundamentals and simulation results for using electrostatic force to displace free standing silicon beams of a fully-etched slot waveguides. This displacement results in a change of the effective index of the slot mode and corresponding phase variation which can be used in phase tuning or in an interferometric configuration such as MZI for switching.

After the initial investigation, the later part of the chapter introduces the challenges in fabrication of freestanding MOEMS devices and various fabrication procedures and corresponding device designs proposed and utilized in this work.

7.1 Slot waveguide mode

The slot waveguide structure consists of sub-micron slot (gap) region of lower refractive index material (such as air) between two silicon beams. According to Maxwell's equations, the normal component of Electric flux density should be continuous at a high index contrast interface. For quasi-TE mode of a slot waveguide, this translates to the Electric field component having discontinuity at the interface which is proportional to the ratio of squares of refractive indices between the low index slot region and silicon [146]. Thus, the electric field ends up having a larger magnitude in the lower index slot region than in the silicon beams. When the width of the slot region is much smaller than the decay length of the field (defined as length where electric field drops to 1/e), the electric field remains high throughout the slot region. With such high confinement of light, slot waveguides have been proposed for applications in sensing and high density optical integration.

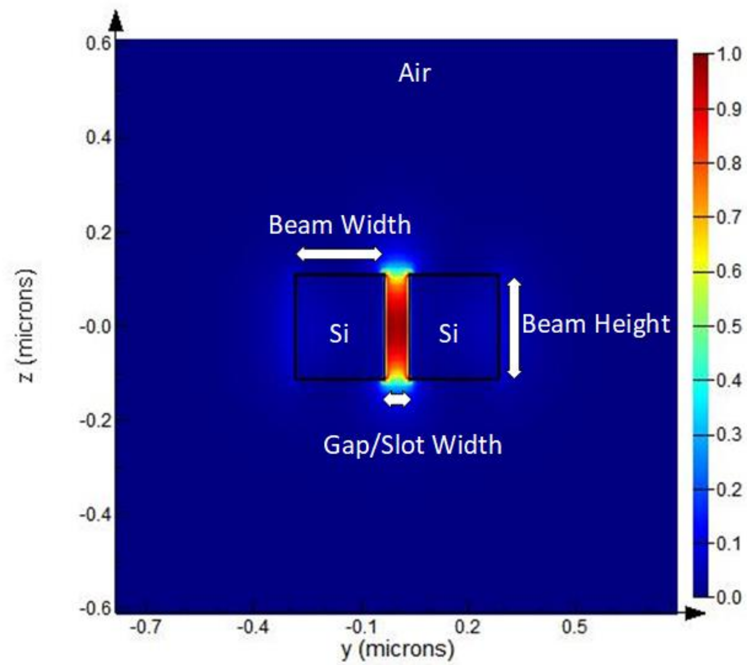

Figure 7-1 Slot mode intensity profile (TE) for a waveguide cross section having beam width 250 nm, height 220 nm, and air gap of 70 nm.

The slot mode intensity profile (Figure 7-1) and normalized electric field for the quasi-TE mode (Figure 7-2) with beam width, height and gap width of 250 nm, 220 nm, 70 nm respectively are simulated using the FDE solver in Lumerical.

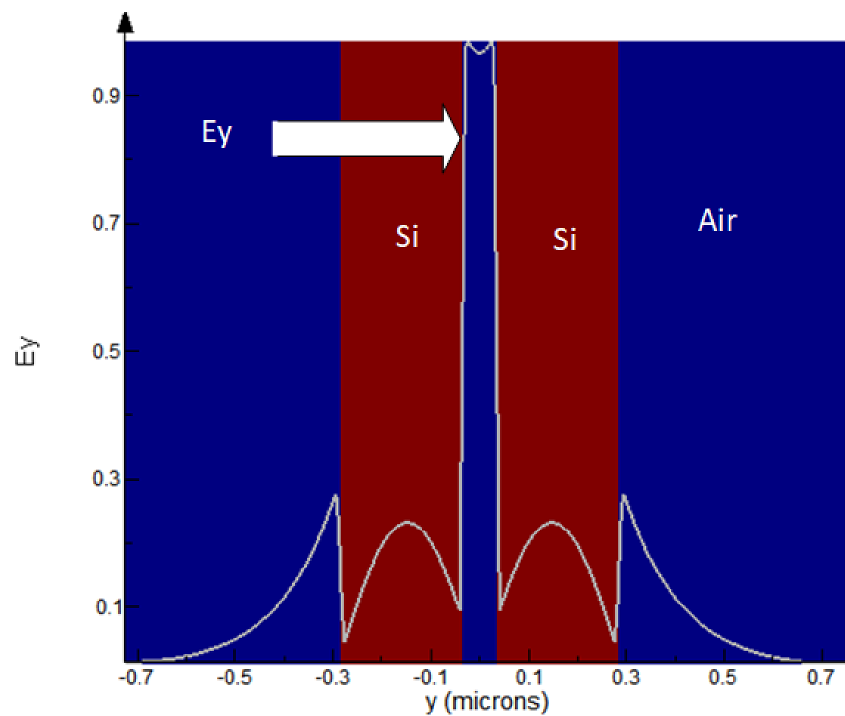

Figure 7-2 Normalized Electric field profile of the slot mode (TE) for a beam width 250 nm, height 220 nm, and gap 70 nm.

7.2 Simulation Analysis

This section details the principle for using freestanding slot waveguides as a phase modulators. The silicon beam displacement due to electrostatic actuation and the change in effective index of the slot waveguide mode with the variation in air gap between them is discussed.

7.2.1 Effective index variation

The TE mode for a slot waveguide consisting of varying silicon beam widths (with height 220 nm) and air gap region between them were simulated using the FDE solver in Lumerical. The effective index extracted from the simulated mode profiles are plotted in the Figure 7-3.

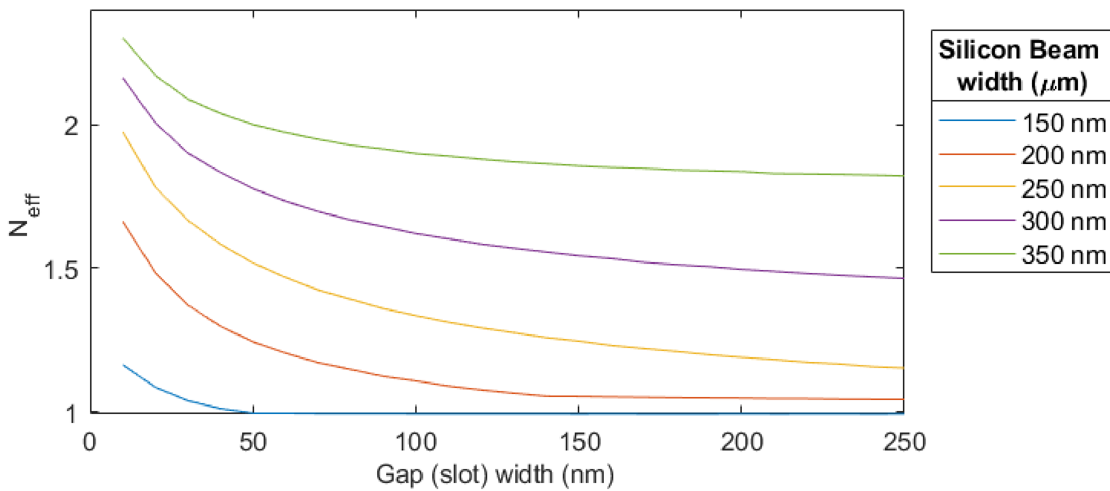

Figure 7-3 Effective index variation of slot waveguide mode with air gap for different silicon beam widths and varying air gap between them.

From Figure 7-3 it can be inferred that (for fixed height of silicon beam 220 nm) changing both the parameters i.e. air gap width and silicon beam width, have an impact on the effective index of slot waveguide mode. Table 18 illustrates the change in the effective index for variations in beam width and the air gap between them.

Table 18 Change in effective index vs slot gap size.

Air gap change (from - to)	ΔN_{eff}			
	200 nm	250 nm	300 nm	350 nm
60 to 50 nm	0.03935	0.05051	0.04361	0.02759
70 to 60 nm	0.03301	0.04393	0.03608	0.02329
80 to 70 nm	0.02349	0.03211	0.02959	0.02076

For the propagating slot mode, this change in air gap separation, and therefore the effective index (N_{eff}), will result in a phase shift. A silicon beam height of 220 nm, width of 250nm and gap variation from 70 to 60 nm gives effective change in index (ΔN_{eff}) of 0.04393. For the given effective index change (ΔN_{eff}), length required to get a phase change of π can be calculated using equation 7.1.

$$\Delta\varphi = \frac{2\,\pi}{\lambda}\,\Delta N_{eff}\;\cdot L \qquad 7.1$$

$$=> L \sim 20\;um$$

In a practical device this length would be much greater than 20 µm due to the bending nature of the silicon rails which is discussed in the following section.

7.2.2 Displacement of beam under electrostatic forces

In this section, the displacement of the silicon beam due to electrostatic force, upon application of an electrical potential between two silicon beams is studied using COMSOL. An electrostatic model was created to replicate two silicon beams of width 250 nm, height 220 nm and air gap of 500 nm. One of the beam was fixed throughout its length while the other was fixed only at the two outside edge surfaces (short edges) and free to move under electrostatic force. The model approximates two suspended silicon beams surrounded by air which is the same as a slot waveguide detailed in section 7.1. A voltage potential of 5 V was applied between the two beams, causing electrostatic force and the results for deformation of the beam (fixed only at the edges) are plotted in Figure 7-4.

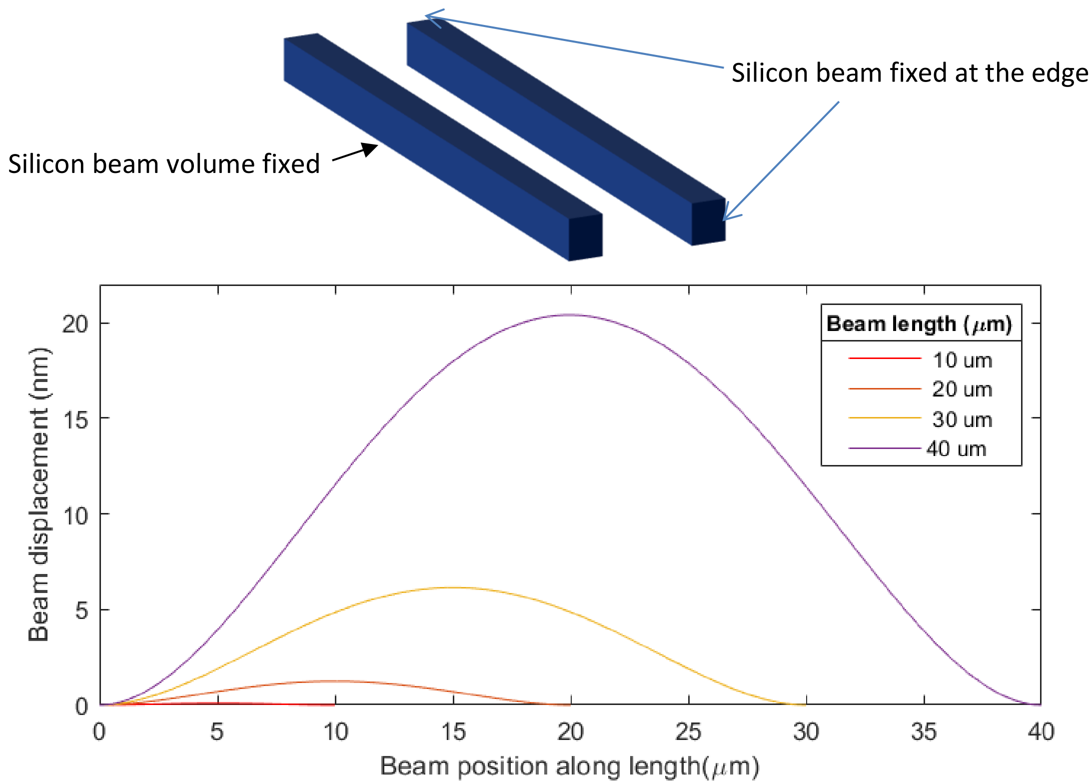

Figure 7-4 Deformation of different lengths of silicon beams (width= 250 nm, height =220 nm) for an applied potential of 5 V between them.

It can be seen that for longer silicon beam lengths, the displacement at the centre of the beam is larger compared to beams of shorter lengths (for same applied voltage). The beam deformation along the length of the beam can also be inferred from Figure 7-4. This varying beam displacement will lead to varying ΔN_{eff} along the length of the slot waveguide.

The response time of the device is limited by the resonance frequency of the silicon beam used in the slot waveguides. The resonance frequency is inversely proportional to the square of the length of the free standing silicon beam. Hence, shorter freestanding silicon regions are better suited for a faster time response. On the contrary, shorter free standing silicon beams provide less displacement for a given voltage, corresponding to smaller phase change. To achieve a large phase shift using shorter length free standing silicon beams, a cascaded configuration of such smaller sections can be used to achieve an accumulated π phase change.

7.3 Device configuration

In the previous sections, the idea of using free standing slot waveguides as phase modulators has been introduced. Figure 7-5 shows the schematic layout for slot waveguide modulators incorporated in MZI. Light propagation in the MZI (except for the phase modulator) can be achieved using standard RIB/STRIP waveguides without the under-etch of the BOX. The incoming

light is split equally into two arms of the MZI containing RIB/STRIP waveguides by 1x2 MMI. The transition from RIB/STRIP waveguides to free standing slot waveguide is made in two steps. First from the RIB/STRIP waveguide to partially etched slot waveguide (supported by either a thin silicon slab or the BOX) followed by partially etched slot waveguide to fully suspended slot waveguide. Similar transitions are made after the modulator region to convert the light back into RIB/STRIP waveguide and light is fed to a 2x2 MMI at the output end of the MZI.

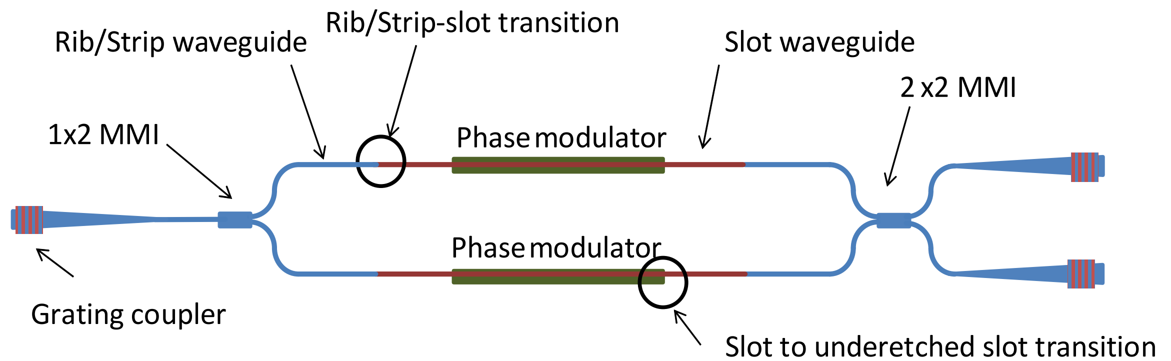

Figure 7-5 Schematic layout of the phase modulators incorporated in an MZI.

Figure 7-6 details the modulators regions where electrostatic force causing the silicon beam deviation in two different ways which were fabricated before the start of this work. The single beam modulator has one fully under etched silicon beam which deflects away from the other fixed silicon beam, and is attracted towards the silicon slab by electrostatic force as shown in Figure 7-6(a). In the case of the double beam modulator, both beams are under etched and applied voltage causes the beams to be deflected away from each other and attracted towards nearest silicon slab.

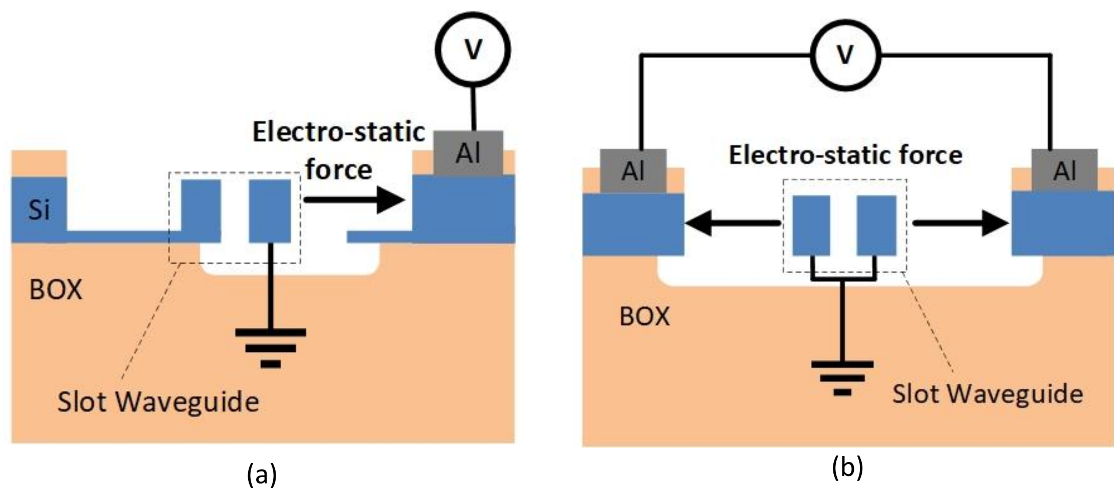

Figure 7-6 Designs of modulators using (a) Single beam modulator, (b) Double beam modulator.

Figure 7-7 shows the top view for the fabricated single beam and double beam slot waveguide modulator devices. The final under-etch of the BOX to make the free standing silicon beams was performed by dipping the samples in wet HF which caused the freestanding beams to collapse under surface tension of the evaporating rinsing liquid (usually water).

The non-suspended slot waveguide loss was measured using the cutback method and was recorded to be 1.13 dB/mm. In the rib-slot mode converter design [147], the input strip waveguide was approximately tapered down to the air gap in the slot waveguide, while simultaneously two conductor beams were tapered up to width of the beams in slot waveguide (as explained in section 7.7) . Simulated loss results for a pair of transitions was 4.62 dB. In comparison with a normalization MZI, Single beam modulator devices recorded an additional loss of ~ 6 dB which can be attributed to the pair of rib-partial slot transitions and presence of debris on the devices causing scattering and absorption.

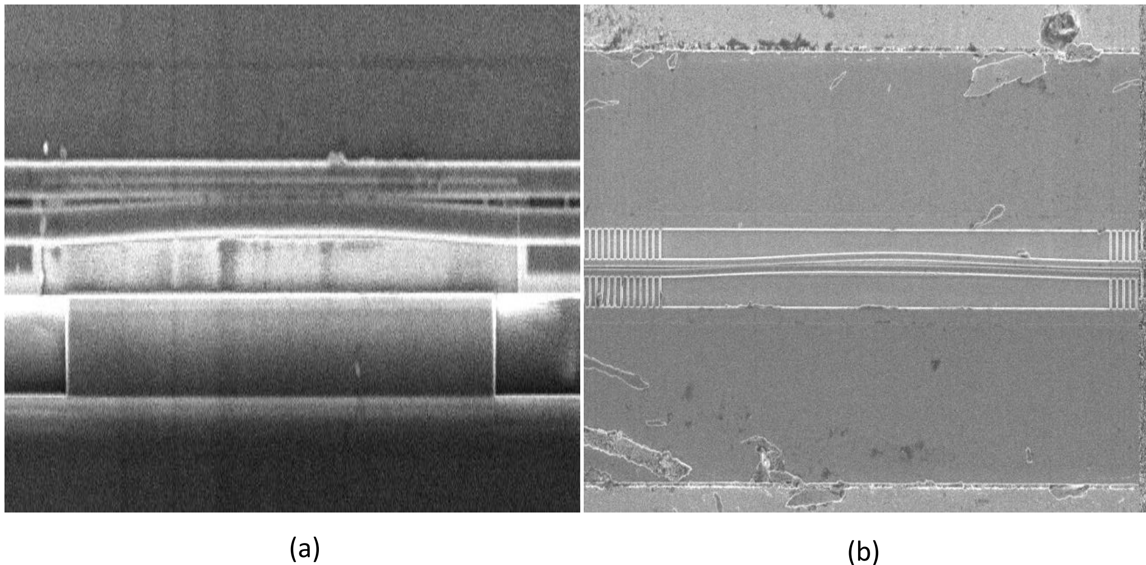

(a) (b)

Figure 7-7 SEM images (top view) of the fabricated (a) Single beam and (b) double beam slot waveguide modulator devices in the initial run.

In the proposed designs for this work (Figure 7-8), the voltage is applied between the beams and electrostatic force causes attraction of the beams towards each other. As the applied voltage appears across the two free standing silicon beams (which are separated by a small distance compared to the designs in Figure 7-6) , it yields a greater force and displacement of the beams which is beneficial.

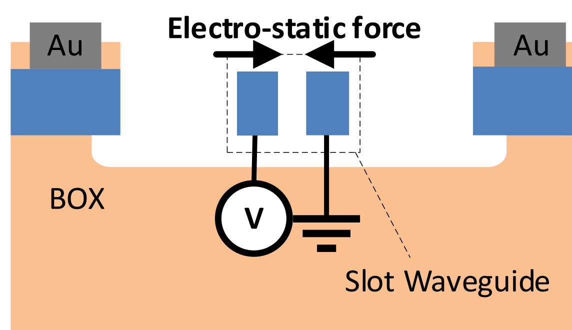

Figure 7-8 Proposed device with electrostatic forces causing attraction between the beams of slot waveguide.

Two fabrication approaches have been explored (section 7.6) to overcome the stiction issues observed in the previous run. The first method utilizes HF vapour-based etching and the second uses Critical point drying for the etching of the BOX to make free standing slot waveguide structures. Each process calls for a unique design procedure and process flow. The equipment and setup for the individual fabrication processes are detailed in following sections. Mode converters and other passive elements have been described towards the later part of this chapter.

7.4 Fabrication

The fabrication process for MEMS based devices can be categorised into bulk micromachining and surface micromachining. Surface micromachining is preferred due to its flexibility in material selection and high-resolution pattering. Photolithography is a widely used method for defining features of submicron scale. For even smaller resolution, electron beam lithography (EBL), focused ion beam (FIB) [148], optical projection lithography, extreme UV lithography and X-ray lithography are available [149]. EBL and FIB have ultra-high resolution of few nanometers and do not require a physical mask. Instead, the respective beam is focussed over a small region and the process is repeated to form the whole feature, making it time consuming.

After the required feature is defined using EBL, etching and deposition of materials is performed to realise required structure. For deposition, various techniques such as chemical [150] and physical vapour deposition [151, 152] and sputtering (for metal) are available for dielectric materials. The final step in MEMS fabrication is chemical etching of sacrificial layers to form suspended structures. For this, in SOI, the buried oxide is etched away by Hydrofluoric (HF) acid to release silicon structures forming a freestanding MEMS/NEMS device.

7.5 Issues with Stiction

Stiction is a commonly encountered issue with MEMS fabrication which occurs when part of the released device such as a cantilever arm or beams become fused with another surface. Surface tension of the final rinse solution (usually water) damages the released structures due to tangential forces during evaporation. This impacts the yield and profitability of the fabrication process and causes devices to fail. Stiction can also occur due to bad packaging, surface moisture and handling of the devices.

Stiction is referred to as a two-phase phenomenon. First, it causes one silicon surface to come in contact with another and secondly, it allows the silicon-silicon contact to bond. Initially, the device is separated from other surfaces by sacrificial layers. These sacrificial layers are then removed in the final step by wet etching followed by rinsing and drying. During this process, the rinsing liquid can get trapped in the narrow gaps between the suspended structures and other surfaces. When the liquid dries, interfacial forces can cause the structures to collapse and permanently stick to each other. Electrostatic charge can also cause stiction of successfully released freestanding structures. Figure 7-9 shows some failed devices due to Stiction.

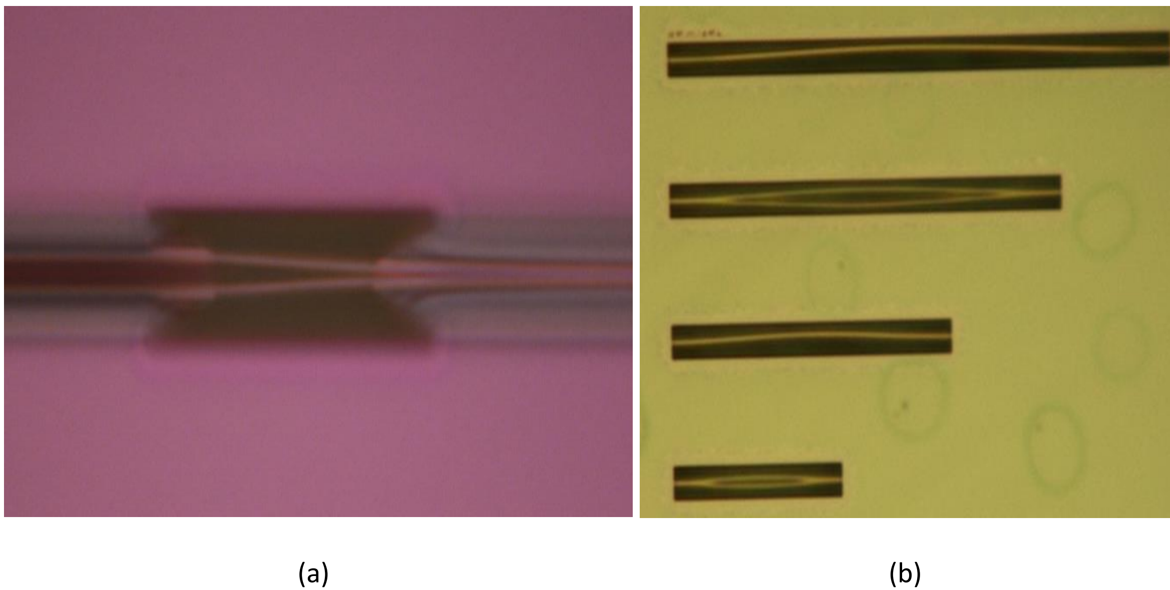

(a) (b)

Figure 7-9 Failed devices due to Stiction. Stiction due to (a) capillary forces while drying, (b) electrostatic charge.

7.6 Stiction removal approach

7.6.1 HF vapour etch

Vapour phase etching of SiO_2 with HF is regarded as a two-step reaction [98]. The water gets adsorbed to the silicon oxide surface forming silanol groups. The silanol groups are then attacked by HF creating water and SiF_4 as by-products which are then removed from the surface by desorption.

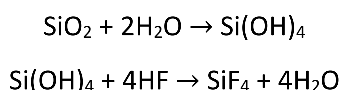

$$SiO_2 + 2H_2O \rightarrow Si(OH)_4$$
$$Si(OH)_4 + 4HF \rightarrow SiF_4 + 4H_2O$$

It is important to note that water acts as a catalyst for the reaction. If the rate of water production during the reaction and removal via desorption is controlled, there is no residual liquid in the process eliminating stiction issues.

The etch rate can also vary due to parameters such as chamber pressure, substrate and HF temperature etc. The Silicon oxide etch rate varies inversely with temperature and etching at an elevated temperature (30-50^oC) has benefits of improved etch rate control, which is linked to water production as a by-product.

The choice of materials for use as a mask for HF vapour is selective as photoresists are porous, and HF vapour can penetrate through. The usual practise is to use thin slab of silicon as a hard mask for defining the etch area. Metal electrode materials such as aluminium places a limit on the silicon oxide etch rate before they risk damaging the metal surface hence gold (Au) is usually used for metal contacts to avoid this issue.

Test structures with varying silicon beam lengths, widths and gap were fabricated on the 220 nm SOI platform to study the maximum length of freestanding slot waveguide that can be fabricated without deformation. Figure 7-10 shows the layout of fabricated test structures with 2 µm etch window.

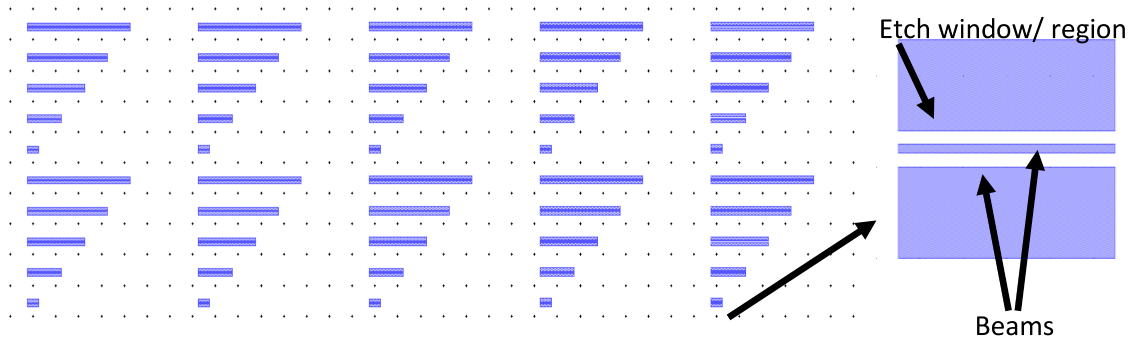

Figure 7-10 L-Edit layout of fabricated test structures to get the maximum fabrication length of the freestanding slot waveguides.

Figure 7-11 shows the successfully released test structures of different length with a beam width of 250 nm and gap of 70 nm using 49% HF in the chamber. The sample was etched for 2 hours with a substrate temperature of 45°C and HF temperature of 25°C. Trenches of ~ 70 nm height were observed due to HF penetrating through the e-beam resist which was erroneously left on top of the sample. The maximum length of successfully suspended silicon beams with a gap of 70 nm was 45 µm.

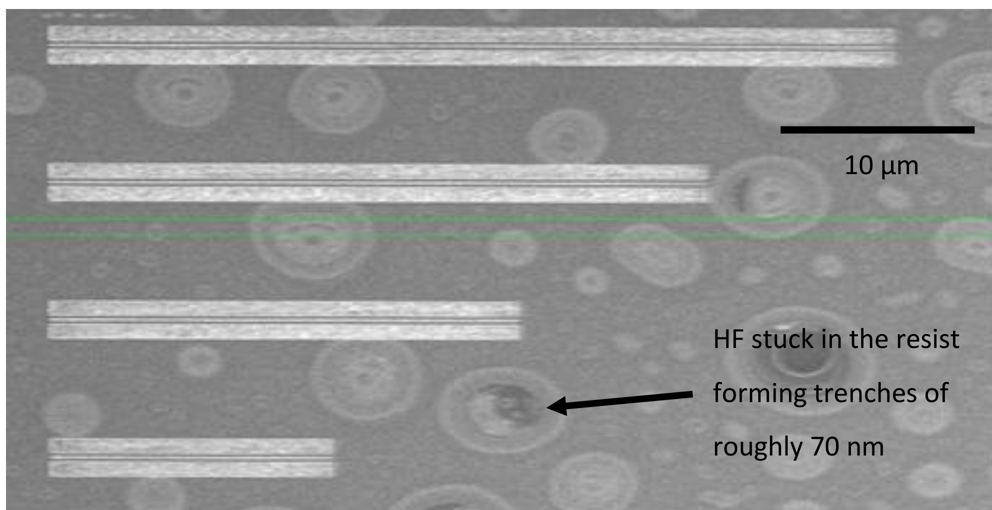

Figure 7-11 Sample etched in vapour HF with ZEP as a mask. 70 nm gap and 250 nm beams of length 15, 25, 35, and 45 µm from bottom to top.

7.6.1.1 Fabrication flow

Figure 7-12 shows the proposed device using HF vapour to release the modulator region in the final step. The input RIB waveguide is converted into a STRIP waveguide using linear tapering of the silicon slab region. The STRIP waveguide is converted to a STRIP-loaded -SLOT waveguide, in which a second silicon beam is introduced and its width is increasingly tapered up while reducing

the distance between the two silicon beams. The other silicon beam is tapered down in width as the light propagates along the length of the converter. This is called a STRIP-loaded-SLOT waveguide which is then converted into a fully suspended slot waveguide acting as the modulator region. The inverse transitions are done afterwards to convert back to a RIB waveguide.

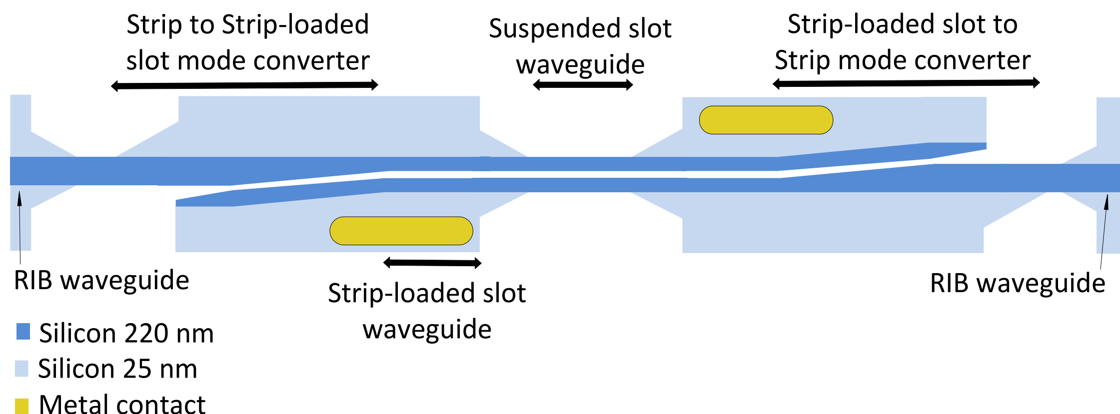

Figure 7-12 Pictorial representation of the modulator waveguide transition using HF vapour for release.

Figure 7-13 shows the fabrication flow for the proposed design on the 220 nm SOI platform using a 25 nm slab for the passive components. First 40 nm of oxide is deposited using PECVD. The first mask is written using e-beam lithography with an ultrafine beam (5 nm spot size) for defining the waveguides. For this e-beam resist ZEP was spun on the sample at 5000 rpm to give a thickness of 256 nm. 195 nm of silicon was etched leaving a 25 nm slab. Also, trenches for electrical isolation are defined in the same step.

A second e-beam mask protects the slab region and defines the silicon etch region (etch to the BOX) in the modulator region, isolation trenches and in the slot waveguides. The third e-beam mask writes the grating couplers which are etched 70 nm leaving 150 nm silicon. A fourth e-beam step is used to define a lift-off mask, used to deposit gold for the electrical connections while actuating the modulator. The final step is the release of the structures using HF vapour etching to fully suspend the slot waveguides in modulator region.

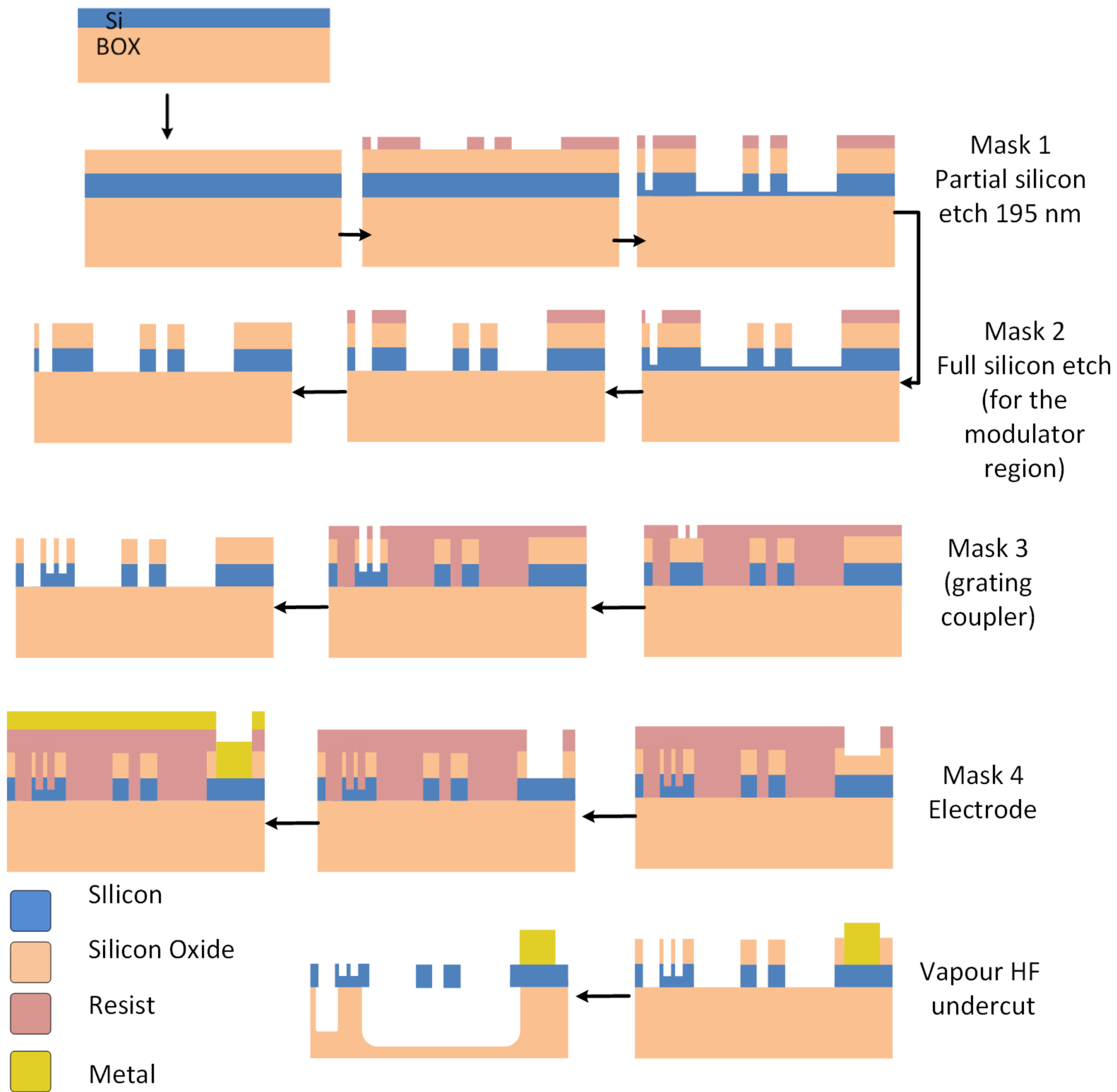

Figure 7-13 Fabrication flow using vapour HF for the freestanding slot waveguide modulators.

7.6.2 Critical point drying (CPD)

Another way to stop stiction from happening is to displace the water in the final rinse solution with methanol which has a lower surface tension. A unique way to accomplish safe devices is to use supercritical CO_2 drying also called critical point drying. At critical point, the characteristics of liquid and gases are similar and surface tension effects can be avoided.

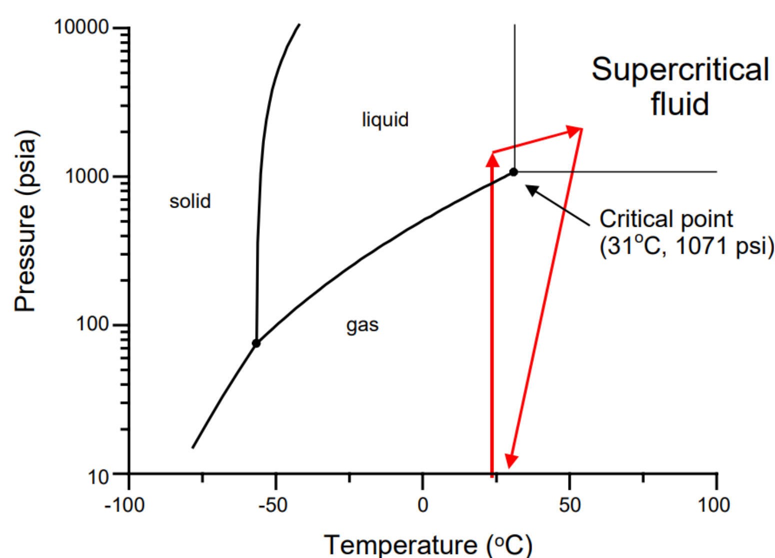

Figure 7-14 CO_2 Pressure temperature phase diagram with process trajectory. Image reproduced from [153].

The critical point of water is 374 °C and 3321 psia. On the other hand, the critical point of liquid CO_2 lies at 31°C and 1014 psia [153] which is relatively easy to maintain. But CO_2 is not miscible with water and a transitional fluid such as methanol or acetone is used which each have good solubility with water and liquid CO_2 , to replace the water over several mixing iterations[154]. Once all the water is displaced, the liquid CO_2 is heated up to critical point and converted into gaseous phase by decreasing the pressure at constant critical point temperature (Figure 7-14). The procedure for using the CPD setup is explained next.

The sample is placed in a basket for easy handling and transferred to a beaker containing HF. After the desired etch time, water is gently poured to overflow the beaker for five minutes. After that the PH level of the water is checked using litmus paper. When all of the HF is displaced by water, the beaker is filled with transitional fluids to displace water over a few iterations as shown in Figure 7-15.

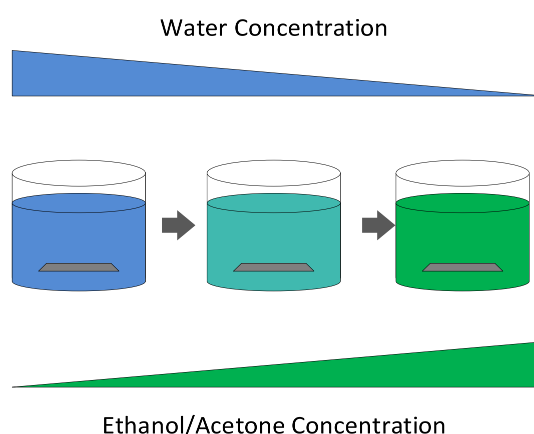

Figure 7-15 Concentration of water and transitional fluid after etching.

The sample immersed in the transitional fluid is then ready to be loaded into the CPD tool. During the CPD process, the transitional fluid is removed with CO_2 using the steps described by the process flow in Figure 7-16.

Step 1 - Fill - Fill the chamber with liquid CO_2 and carefully transfer the sample.

Step 2 - Purge - Transition fluid replaced by liquid carbon dioxide.

Step 3 - Critical point - Chamber is heated above the critical point temp and pressure of CO_2.

Step 4 - Bleed - Gaseous CO_2 is released slowly (100 psia /min) from the process chamber.

Step 5 - Vent - Accelerates decomposition of exhaust CO_2 from process chamber.

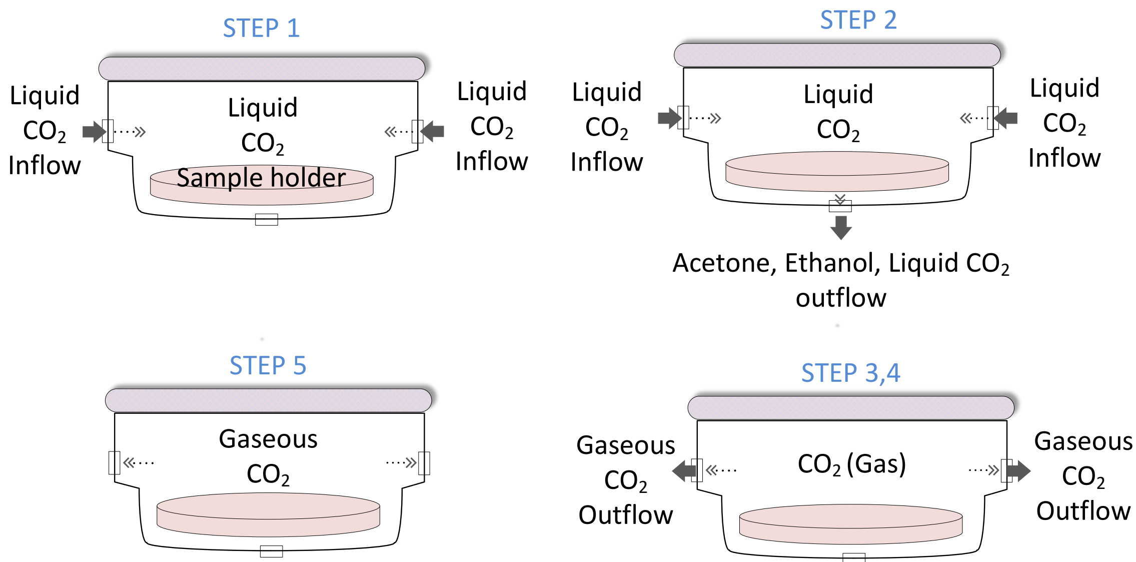

Figure 7-16 CPD process flow.

For test runs, two different transitional fluids, acetone and methanol were used. While opening the process chamber after completion of the CPD process, the transitional fluid evaporating from the sample surface was observed and the test sample displayed stiction issues. Different purge cycle times were also experimented with to remove the transitional fluid but to no success.

In all experimental iterations with the tool, the samples were found to be displaced during the process from the initial position with some transitional fluid remaining at the bottom of the chamber which explains the cause for process failure. The possible reason for this could be the design of chamber optimized only for wafer scale processing with a maximum wafer size of six inch.

7.6.2.1 Fabrication flow

Figure 7-17 shows the schematic top view of the fabricated devices using CPD after using wet HF to etch the BOX and create freestanding slot waveguides in a 220 nm STRIP waveguide based platform.

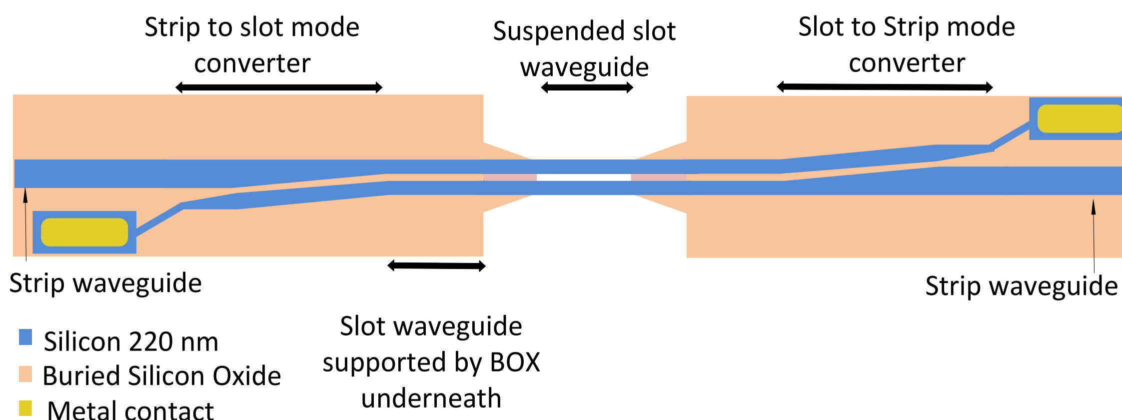

Figure 7-17 Pictorial representation (top view) of the free standing slot waveguide modulator using CPD after etching of the BOX.

Figure 7-18 shows the fabrication steps used to fabricate free standing slot waveguides utilizing CPD after wet HF for the final BOX etching to create freestanding structures. A Silicon-on-Insulator (SOI) wafer with 220 nm thick silicon on top of 2 µm silicon oxide was used for fabricating the samples. 40 nm of oxide is deposited on top of the samples. The first mask is written with e-beam lithography with 265 nm of ZEP as resist. 220 nm of silicon is etched to define the waveguide regions. A second mask uses e-beam to define the grating couplers. The third mask is used to define a lift-off mask upon which to deposit metal for the contacts. The final mask is used to expose only the modulator region during wet etching which is followed by CPD to eliminate any stiction issues.

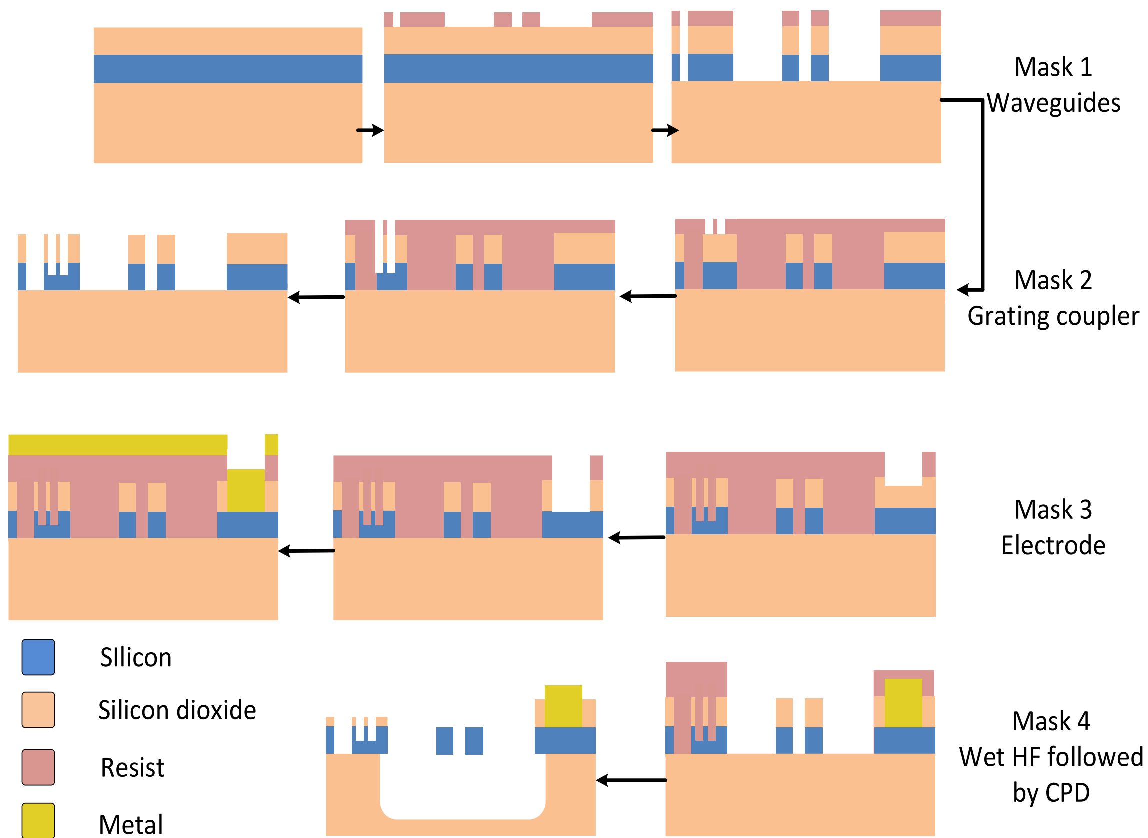

Figure 7-18 Fabrication layout for Strip and strip-loaded based designs.

Until now in this chapter, two different approaches to tackle stiction issues in the MEMS devices have been described. The device geometry for both approaches have been introduced and the fabrication flow is detailed.

Both fabrication approaches require different passive components to convert to and from the slot waveguide modulator, the designs for which are explained in the following sections.

Due to time restrictions and difficulties encountered during fabrication no working device from both the approaches could be fabricated. However, a passive device run (without the under-etch) involving STRIP waveguide based designs was fabricated and its results are presented in this chapter along with the simulation work to support both the fabrication approaches.

7.7 Mode converter design

STRIP/RIB waveguides are widely used in silicon photonics because of their low transmission losses for small bend radii. With increasing effort of sub wavelength confinement in slot waveguides, the STRIP/RIB to slot mode converter becomes a key component in utilizing slot waveguide-based devices. Owing to the huge modal mismatch between STRIP/RIB waveguides

and slot waveguides, direct coupling is very inefficient. A few different types of mode converters for this purpose have been proposed in the literature [147, 155-159].

Figure 7-19 explains the Y Shape mode converter [157] utilizing two complementary tapers together. The input strip waveguide is tapered down directing the mode to the slot waveguide. The high index regions of the slot are also tapered to tips for avoiding reflections. Very high efficiency coupling can be achieved for optimal lengths.

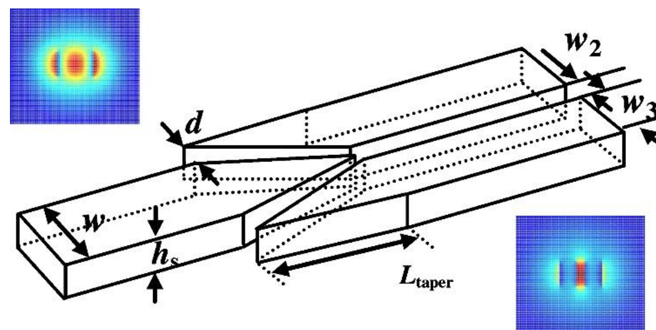

Figure 7-19 Schematic diagram of the Y shaped strip to slot mode converter w=400 nm, d=60 nm, w2=100 nm, w3= 260 nm, h_s=250 nm. Image reproduced from [157].

Other type of converters utilize tapering down of the strip waveguide to the rail of the slot waveguide and introducing another rail with gradual up tapering for efficient mode conversion [155, 159]. The tapering of the strip waveguide delocalizes the input mode which is funnelled into a slot mode (Figure 7-20).

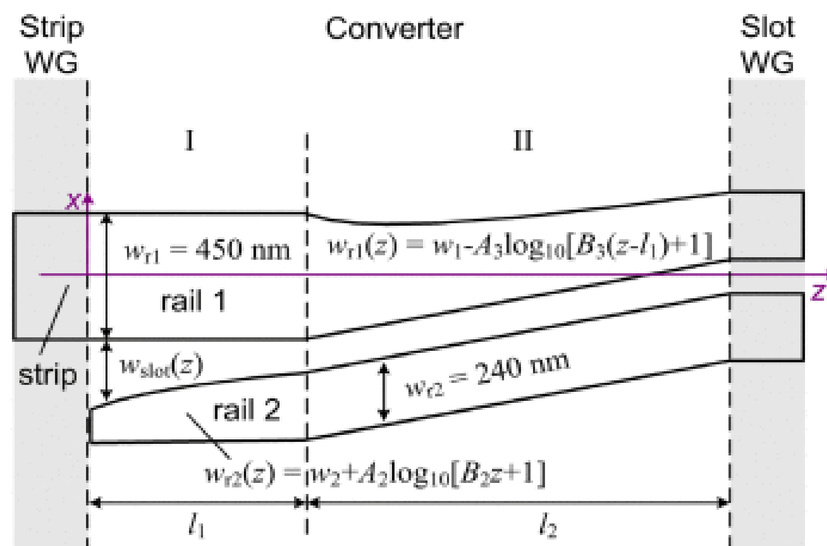

Figure 7-20 Schematic of the strip to slot mode converter. Image reproduced from [159].

Two different platforms for the mode converters (based on the release process in the previous chapter) are studied in this chapter. Section 7.8.1 describes the design parameters, simulation results and the experimental results obtained for the STRIP-to-SLOT mode converter that are compatible with the CPD process. Section 7.9.1 gives the design review for the STRIP to STRIP-loaded-SLOT based design which were used to implement the final devices using HF vapour.

7.8 STRIP waveguide based platform for CPD

Section 7.8.1 describes the design, fabrication, simulation and experimental results for the strip to slot converter followed by the 1x2 and 2x2 MMI results. A simulation analysis of the strip to strip-loaded slot transition is given in section 7.9.1.

7.8.1 Strip to Slot mode converter

The design (shown in Figure 7-21) converts a 450 nm strip waveguide to a slot waveguide with gap of 70 nm and beam (rail) width of 250 nm. The 220 nm SOI platform with 40 nm oxide on top was chosen to improve the transition from the slot mode to fully suspended slot mode with design parameters similar to [159].

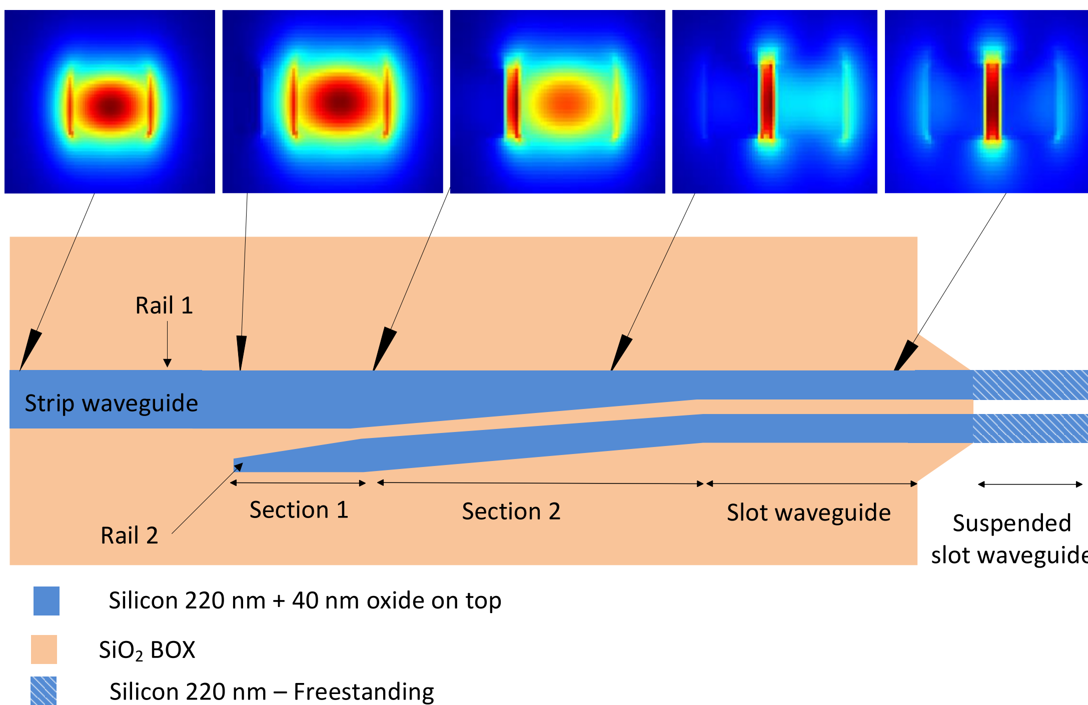

Figure 7-21 Top view of the strip to slot mode converter with mode profiles (cross section) along the length of the converter as the mode is transformed.

For the purpose of explanation, the converter is split into 3 sections. Section 1 consists of the input strip waveguide of width 450 nm and rail 2 which is linearly tapered in width from 120 nm to 250 nm. The separation between the two rails reduces from 200 nm (at the start) to 70 nm (at the end of section 1) across the length of this section. The rail 2 taper is used to reduce the reflections caused by any modal mismatch due to its introduction.

In section 2, the separation between the two silicon rails/beams is kept constant (70 nm) while the rail 1 width is tapered linearly from 450 nm to 250 nm. The width of rail 2 is also kept constant in this section. The tapering of rail 1 is done to achieve mode matching between the strip waveguide and the slot waveguide. Finally, section 3 is a slot waveguide with desired parameters.

7.8.2 Fabrication

Two 30 x 40 mm^2 chips with design variations and test structures were fabricated to compare the simulated and experimental devices (for passive devices only without under-etch). Figure 7-22 and Figure 7-23 show SEM images of fabricated strip to slot converter test structures (as detailed in section 7.8.1) with length of section 1 and 2 equalling to 0.5 µm and 20 µm, and some contamination that was found on the first chip respectively.

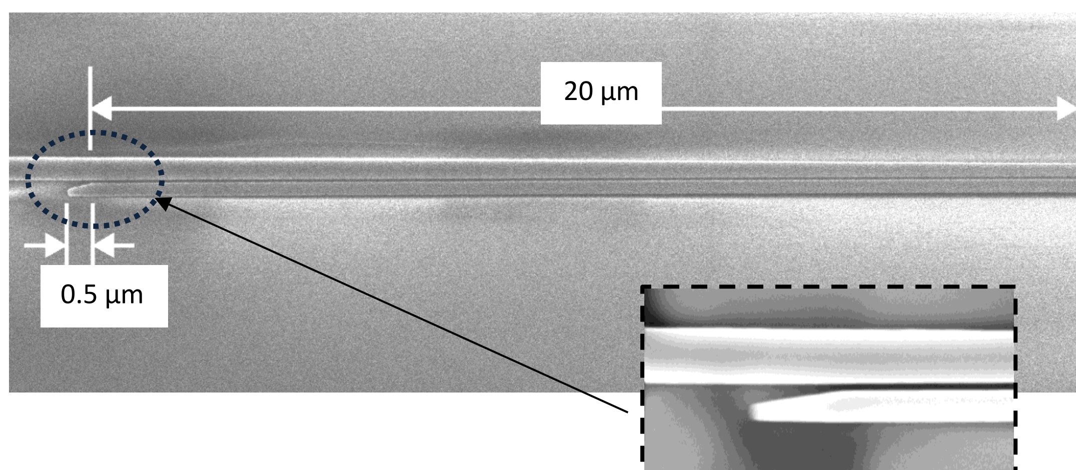

Figure 7-22 SEM image (top view) of the fabricated Strip to slot converter with section 1 length 0.5 µm and section 2 length 20 µm.

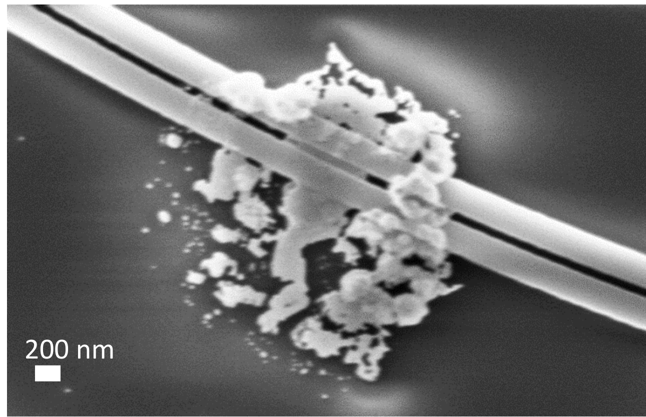

Figure 7-23 Contamination after ICP etch.

Figure 7-24 shows e-beam stitching error and development issues rendering some of the MZI devices unusable. The complementary silicon waveguide rails that were supposed to be increasingly tapering up in width (from bottom to top in Figure 7-24(a)) were observed to be different from the designed mask (shown in green sub image). One possible reason for that is suspected to be the shot/dose adjustment while writing patterns in an area by the ebeam. Usually a few iterations are needed to define the dose adjustment, correct resist thickness and resist development strategies in order to achieve the required features. In our case we utilized 256 nm thick ZEP as the resist, and a 5 nm spot ultrafine beam with the suggested dose by the ebeam engineer. The unwanted features seem to be overdeveloped, leading to wider features of the rails than designed.

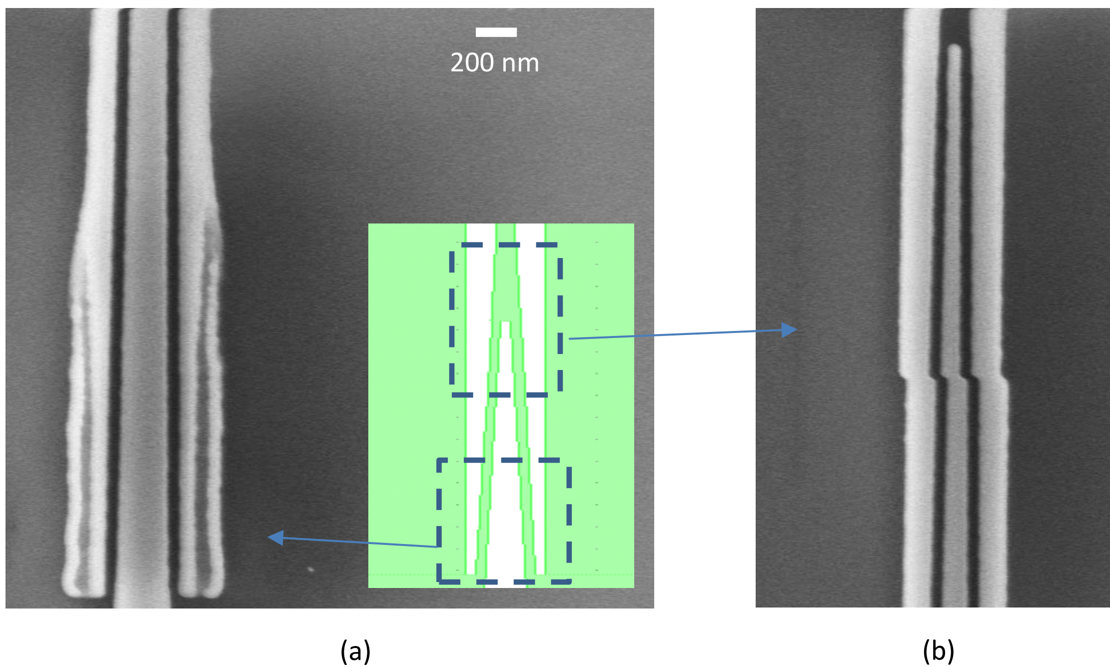

Figure 7-24 Fabrication issues on chip 1 (a) Unexpected features due to ebeam writing and development (b) E-beam stitching error.

The Ebeam stitching error was also observed on the patterned MZI devices which degraded the performance of the slot mode converters leading to a very high loss of the MZI device which could not be measured during the experimental characterization.

The second chip was contaminated while etching in the ICP tool (Figure 7-25). After trying different dry and wet cleaning methods [160], the contamination was still found on small features throughout the chip and no usable data was obtained from the second chip.

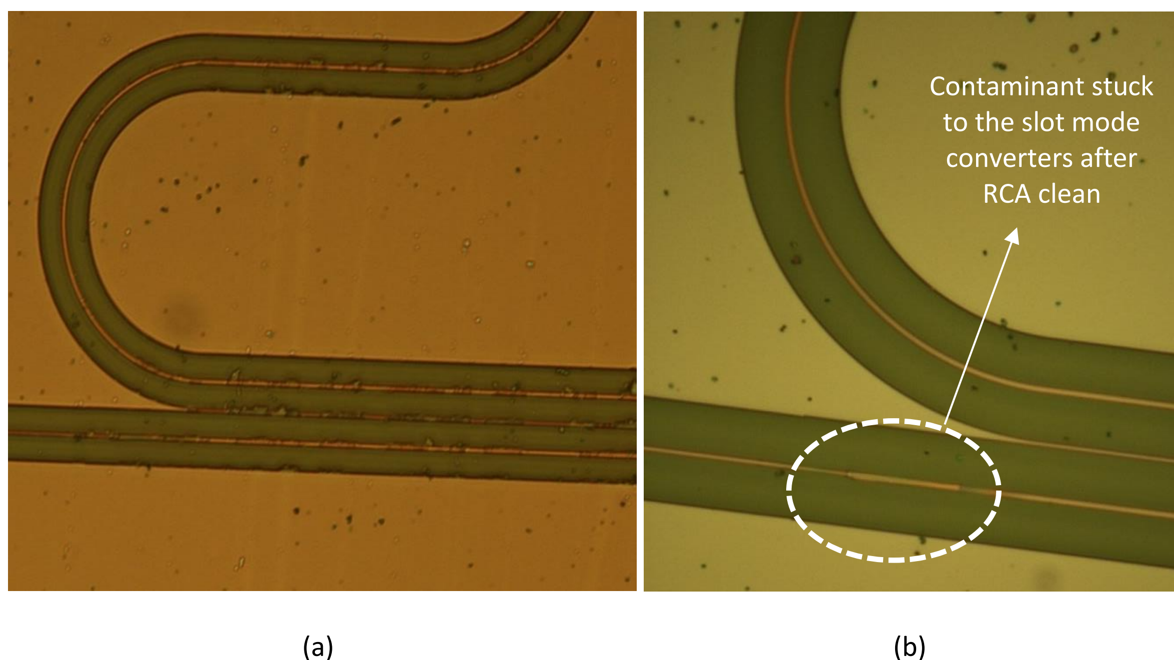

Figure 7-25 The sample contaminated from ICP (a) Before RCA clean (b) after RCA clean

7.8.3 Simulation and experimental results

7.8.3.1 Length section 1 variation

This section explains the effect of varying length of section 1 on the transmission properties of the STRIP-to-SLOT mode converter. For cutback style test devices, the length of section 1 was varied from 0.5 to 2.3 µm in steps of 0.2 µm while keeping the length of section 2 at 20 µm and other parameters also kept constant. The transmission (blue circle), reflections (orange circle) at the output slot waveguide and input waveguide respectively are plotted in Figure 7-26 from the device simulation performed in Lumerical using the EME solver. Also plotted is the experimental transmission data.

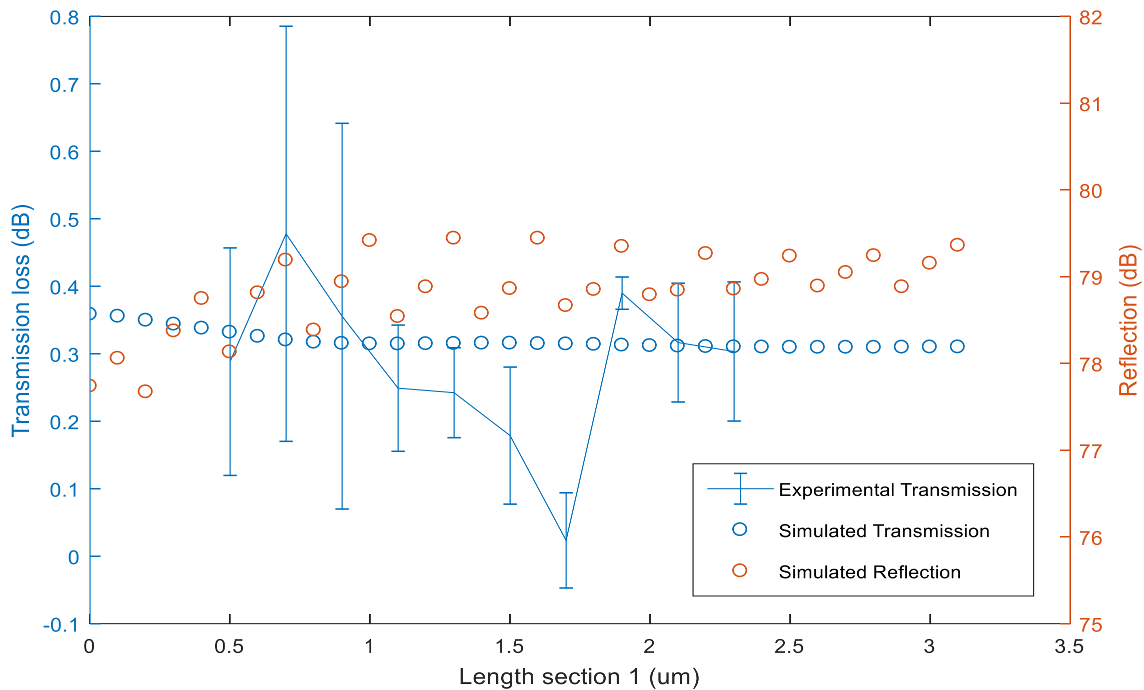

Figure 7-26 Experimental transmission data for pair of mode converters fabricated with variation in length section 1 compared to simulation results.

For each section 1 length, an array containing 1 to 9 devices were fabricated as explained in Chapter 3.5. The data was then fitted to a straight line with the slope of the fit giving the loss per converter for each particular length. The error for each length was calculated by taking the standard deviation of the residuals in the fit as explained in Appendix (section - Data points selection and fitting).

The experimental results for a pair of converters with the longest section 1 lengths (2.3 µm) was 0.30 dB with an error of 0.20 dB. Most of the results fall within an acceptable range of the simulated data. The array of devices for length 1.7 µm was affected the by e-beam stitching error and show a large deviation from the simulated values. For the other experimental data showing lower loss than simulated values, this might be due to excessive loss of the normalization waveguide owing from issues reported in previous section. The error values are large compared to the transmission loss which could possibly be explained by the low loss of the devices combined with contamination issues reported previously.

7.8.4 Effect of section 2 length variation

Figure 7-27 shows the simulation and experimental results of fabricated devices investigating the length of section 2 within the strip-to-slot converter varying from 5 µm to 14 µm in 1 µm steps. The data analysis is performed in a similar manner as with the previous section.

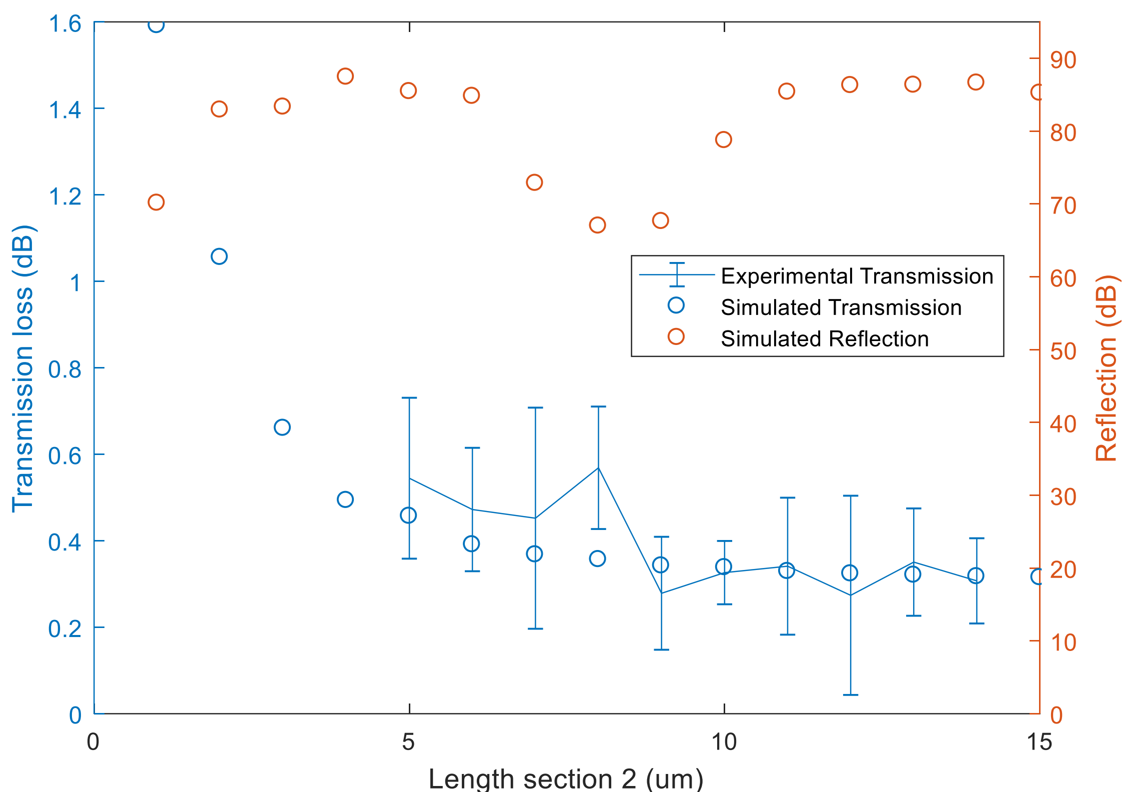

Figure 7-27 Experimental, simulated transmission and reflection data for a pair of mode converters fabricated with variations in length of section 2 compared to the simulation results.

The experimental results closely follow the simulated data. The transmission loss begins to saturate around a length of 10 µm which agrees with the simulation results. The experimental data for a pair of converters with section 2 length equal to 14 µm was calculated to be 0.31 +/- 0.20 dB.

7.8.5 1x2 MMI

The input and output waveguides at the MMI are tapered in width from 450 nm to 1.5 µm over a length of 20 µm. The input port position was at the centre of the width of multimode region and output port at +-1.5 µm from the centre of the multimode region of width 6 µm. Figure 7-28 shows the simulated device without tapers using EME solver in Lumerical. The transmission for individual output ports was 0.489 with a multimode region length of 32.04 µm.

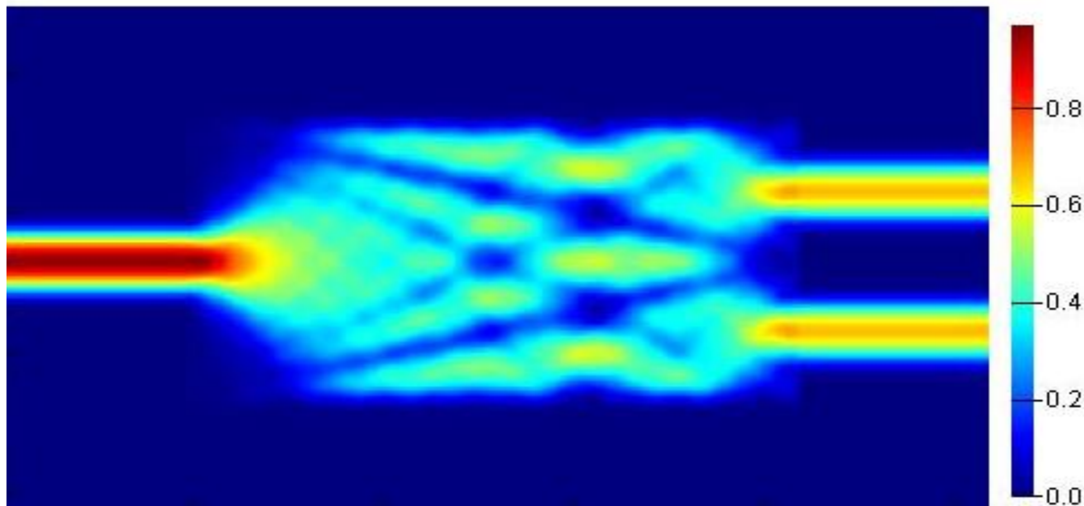

Figure 7-28 Simulated 1x2 MMI intensity profile with a 32.04 µm MMI length using the EME solver in Lumerical.

Figure 7-29 shows the layout for an array of MMI that was fabricated for a particular length. Length variations of the MMI array were fabricated ranging from 30.04 µm to 34.04 µm in 0.5 µm steps. Figure 7-30 shows the SEM of the fabricated MMI.

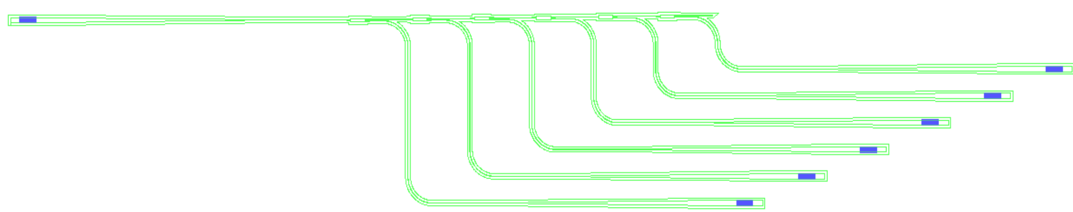

Figure 7-29 L-edit layout mask for array fabricated to characterize the 1x2 MMI loss.

Figure 7-30 SEM image (top view) of fabricated 1x2 MMI of length 32.04 µm.

Figure 7-31 shows the experimental results for the 1x2 MMI for different fabricated multimode region length variations. The experimental data for each array is fitted to a linear curve giving the loss per device and errors calculated as with the previous sections. The experimental data follows the trend of the simulated data closely. The fabricated length of 32.54 µm shows a splitting ratio of 3.23 +- 0.20 dB.

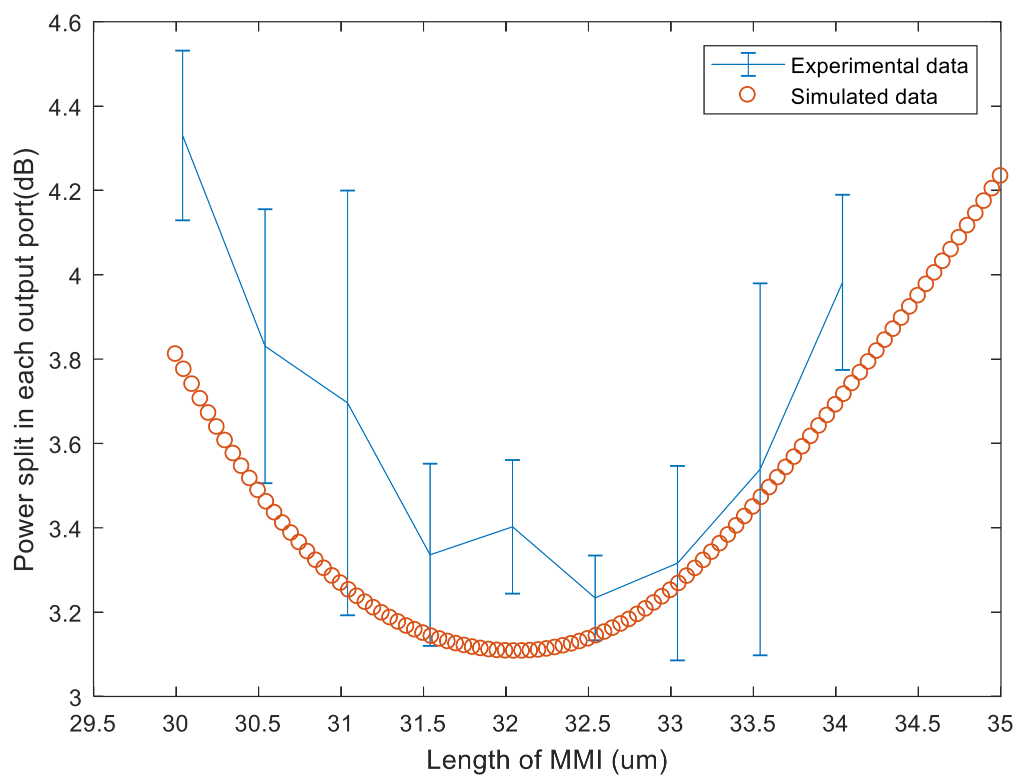

Figure 7-31 Experimental data for the fabricated 1x2 MMI lengths compared with the simulation results.

7.8.6 2x2 MMI

The input and output waveguides at the MMI are tapered in width from 450 nm to 1.5 µm over a length of 20 µm. The input and output port positions were chosen to be +-1 µm from the centre of the multimode region of width 6 µm. The length of multimode region was simulated to be 42.56 µm with a total transmission of 0.97. Figure 7-32 shows the simulated field profile using the EME solver without input and output tapers. Figure 7-33 shows SEM image of fabricated device.

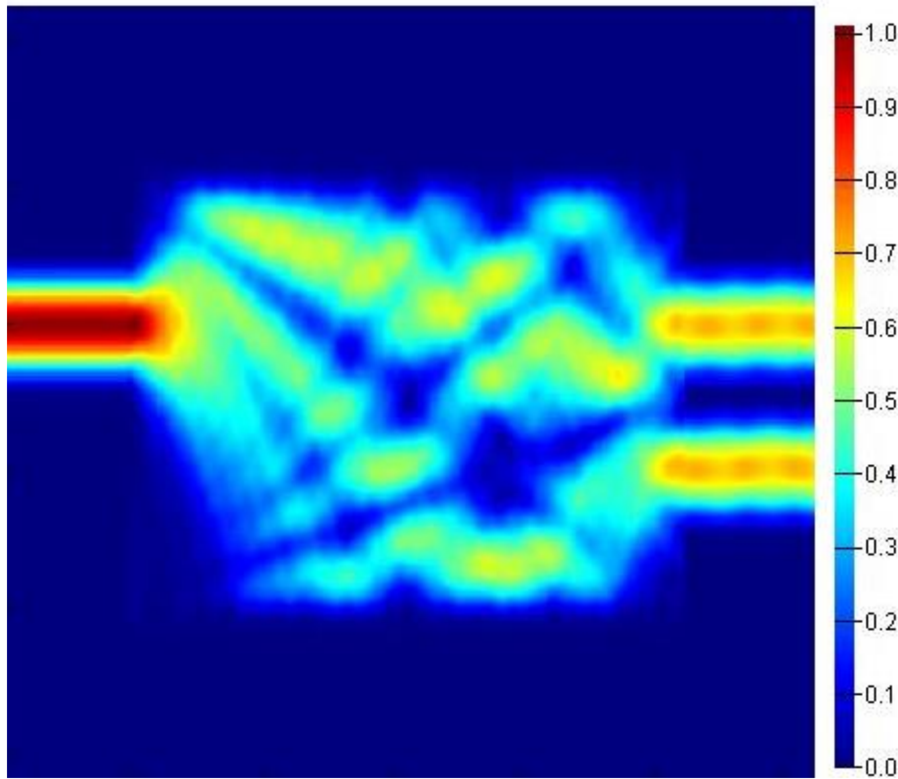

Figure 7-32 2x2 MMI simulated field profile.

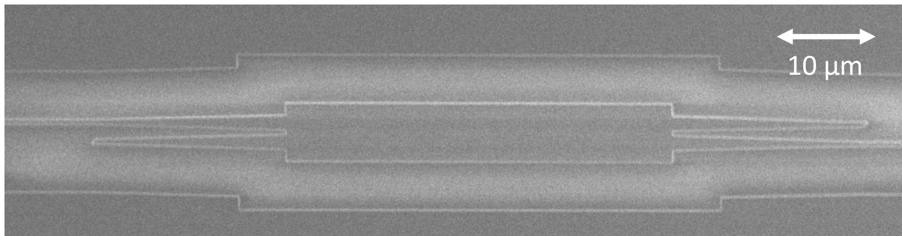

Figure 7-33 SEM image of a fabricated 2x2 MMI with multimode region with a length of 42.56 µm.

Figure 7-34 shows an array of one to seven 2x2 MMI with outputs from the lower port used to test the transmission response. The length where the transmission from both ports is equal would give the optimum length for the multimode region. The loss for individual lengths and the errors are calculated as with the 1x2 MMI. Figure 7-35 shows the comparison between the simulated and experimental results.

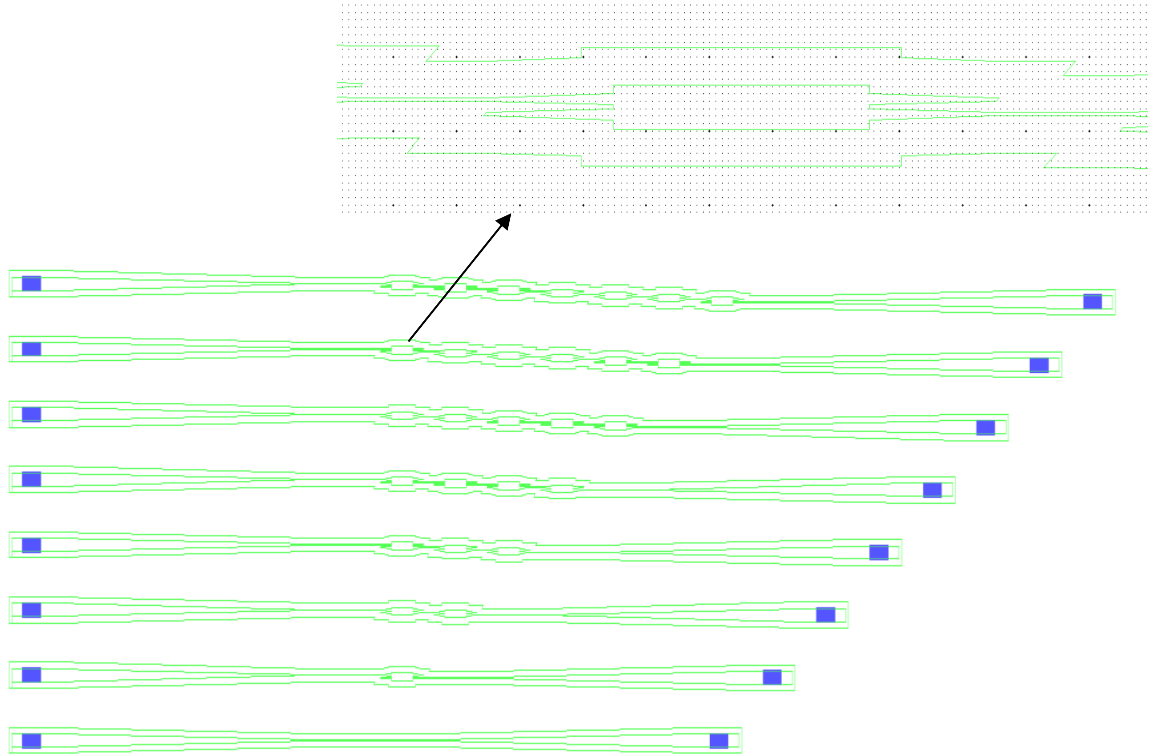

Figure 7-34 L-Edit layout of the MMI array for the 2x2 MMI with the output from the lower port.

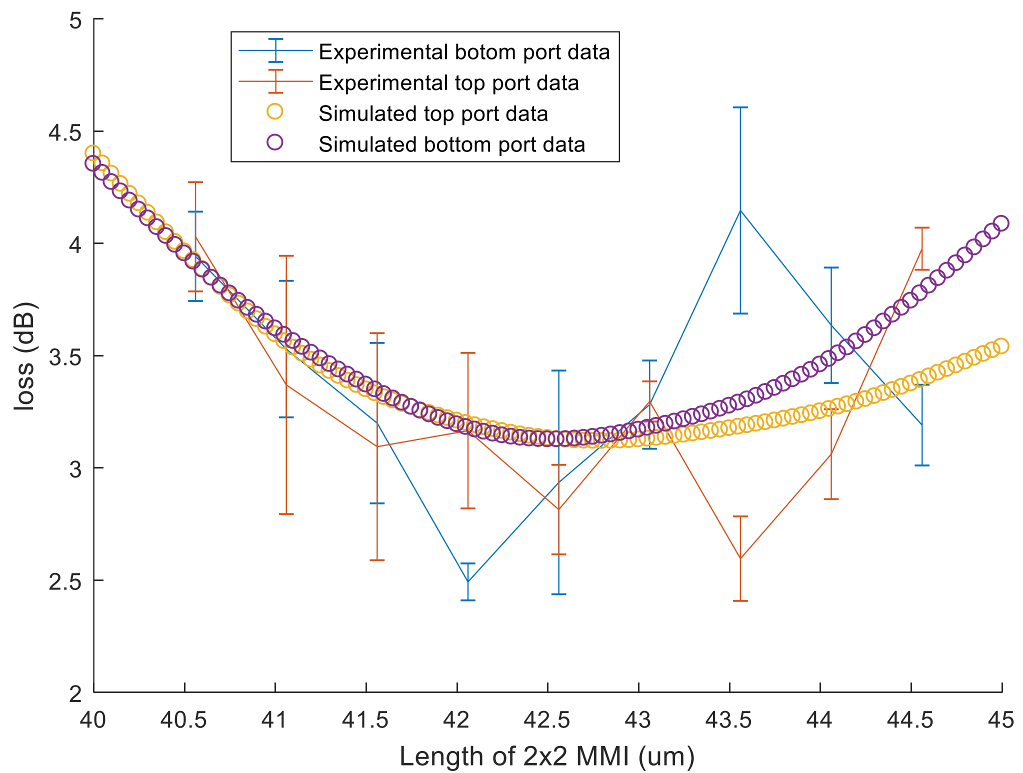

Figure 7-35 Experimental data for different fabricated 2x2 MMI lengths.

The experimental results show similar behaviour compared to simulated data but is too noisy to make any conclusive remarks about the optimum length of the device. The optimum length though looks to be around the simulated value of 42.56 µm with comparable loss values. Figure 7-36 shows the wavelength scan for the transmission through the lower port of the MMI with a multimode region length of 42.06 µm. Ripples were observed for all of the fabricated 2x2 MMI devices with increasing extinction as the number of MMI in the array increased. A possible cause for this could be reflections from the other output port which was not terminated with a grating coupler.

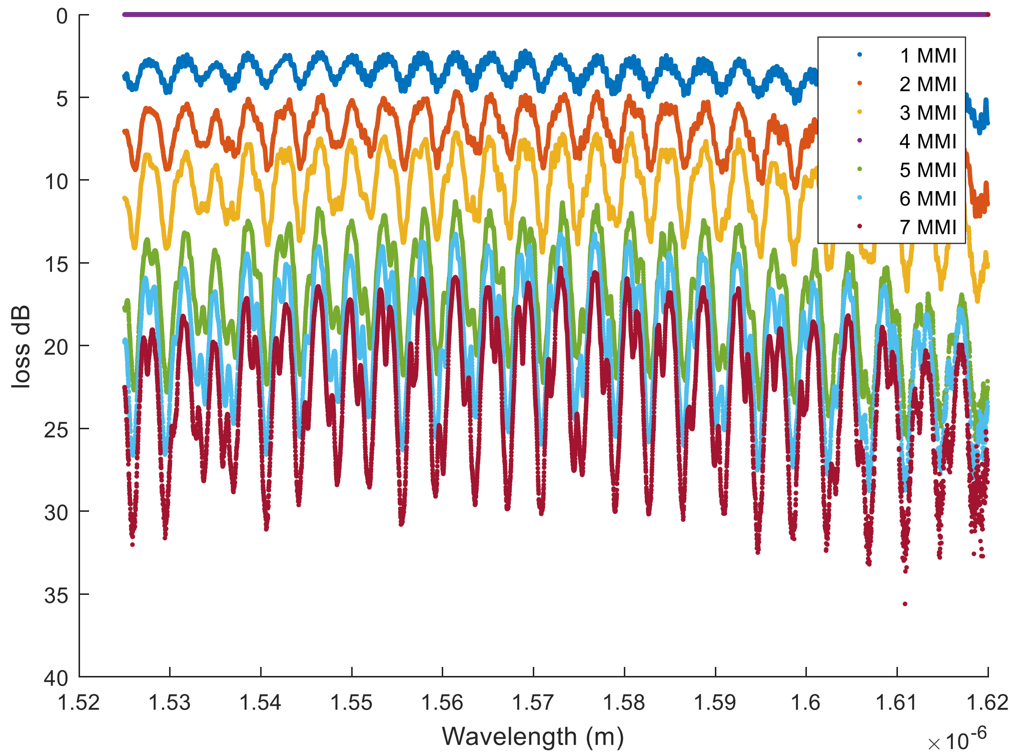

Figure 7-36 Wavelength scans for transmission through the lower port of the 2x2 MMI with a multimode region length of 42.56 µm.

The length of input and output taper was 20 µm each and the length of multimode region ~40 µm giving a total length of 80 µm. Using this length in the formulae for the Free-spectral-range (FSR) with a group index (n_g) ~3.75 (simulated for a 6 µm waveguide) gives an FSR of 8 nm which is close to the observed value supporting the reflection explanation.

$$\Delta\lambda = \frac{\lambda^2}{n_g.L} = \frac{(1.55 * 10^{-6})^2}{3.75 * 80 * 10^{-6}} = 8.008\ nm$$

7.8.7 Slot waveguide losses

Figure 7-37 shows an SEM image of a fabricated slot waveguide with a beam width of 250 nm and gap of 70 nm.

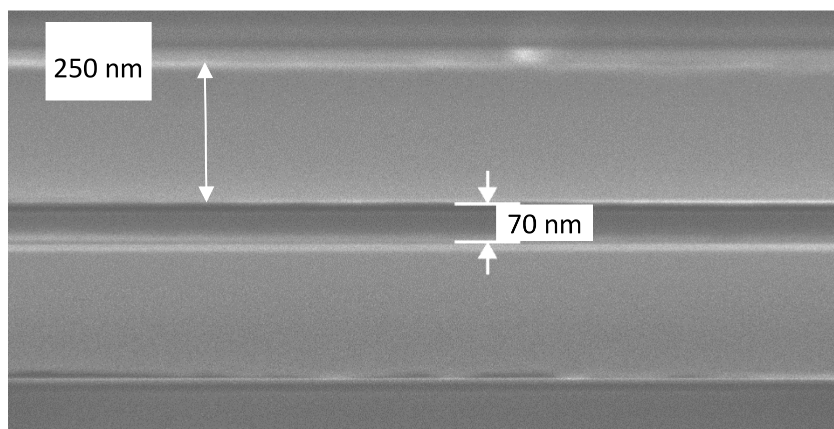

Figure 7-37 SEM image of a fabricated slot waveguide with a 70nm gap and 250 nm beam width.

The obtained data for the slot waveguide cutback losses was inconsistent with the transmission loss being over 80 dB due to contamination and e-beam stitching error issues (shown in Figure 7-24) and therefore, the slot waveguide loss could not be verified with this chip.

Remarks: The fabrication of devices using CPD was forfeited due to the tool not being able to process on chip level.

7.9 RIB waveguide based platform for vapor phase HF

This section reviews the strip-loaded based design which can be fabricated using the HF vapour-based fabrication techniques. The design parameters are similar to the strip to slot-based design except for the 25 nm silicon slab around the waveguide regions to allow the final release to be performed using silicon as a hard mask.

7.9.1 STRIP to STRIP-loaded SLOT mode converter

The dimensions for STRIP to STRIP-loaded-SLOT waveguide mode converter used to convert a 450 nm silicon STRIP waveguide mode to the SLOT mode with 250 nm silicon beams/rails and a 70 nm air gap is displayed in Figure 7-39.

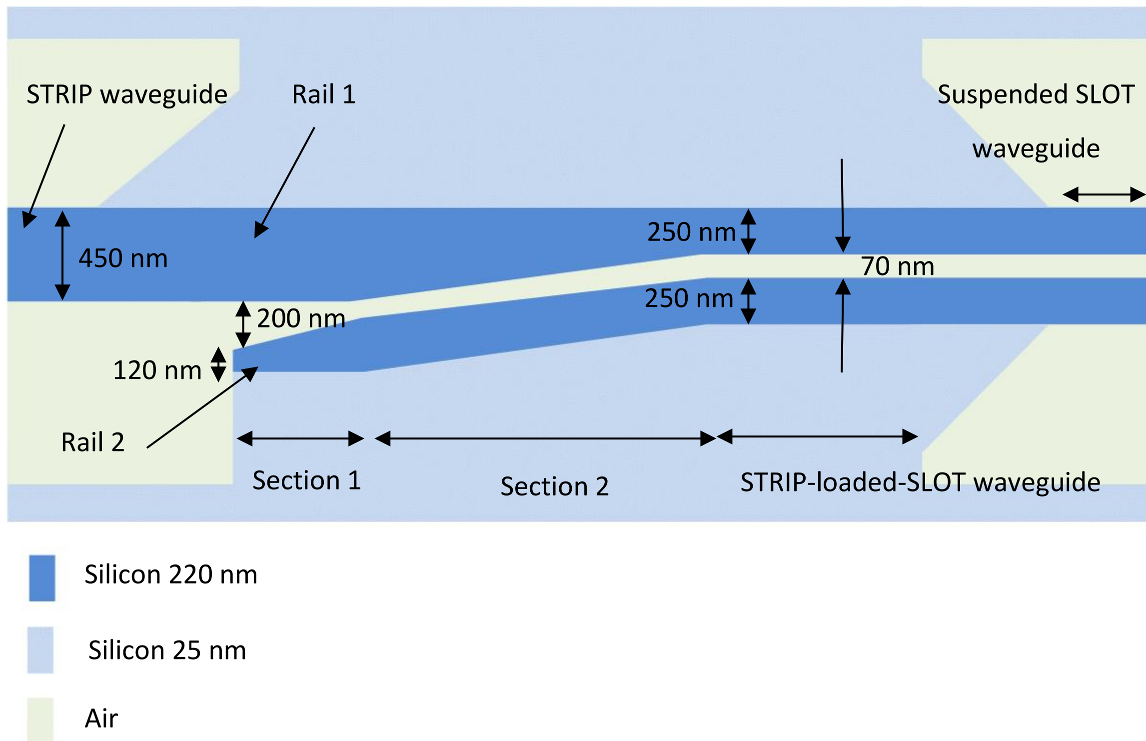

Figure 7-39 Schematic representation of the STRIP to STRIP-loaded-SLOT wavegudie mode converter for 250 nm silicon rails and an air gap of 70 nm.

Similar to section 7.9.1 the converter is split into 3 sections. Section 1 consists of the input strip waveguide of width 450 nm and rail 2 which is linearly tapered in width from 120 nm to 250 nm. The separation between the two rails reduces from 200 nm (at the start) to 70 nm (at the end of section 1) across the length of this section.

In section 2, the separation between the two silicon rails/beams is kept constant (70 nm) while the width of rail 1 is tapered linearly from 450 nm to 250 nm. The width of rail 2 is kept constant in this section. The tapering of rail 1 is done to achieve mode matching between the strip waveguide and slot waveguide. Finally, section 3 is a slot waveguide with a 25 nm silicon slab – referred to as a STRIP-loaded-SLOT waveguide after which the slab sections are tapered down to achieve the fully suspended SLOT waveguide mode.

The lengths of section 1 and section 2 are set to be 5 µm, and 50 µm in MZI devices respectively while cutback type test structures with varying lengths of section 1 (from 0.5 µm to 5 µm in 0.5 µm increments) were fabricated with the length of section 2 fixed at 100 µm to the verify optimum length of section 1. Similarly, cutback type test structures with varying lengths of section 2 (from 4 µm to 20 µm in 2 µm increments) were fabricated with length of section 1 fixed at 50 µm.

Silicon slab thicknesses of 25nm, 50 nm, and 100nm, were simulated to test the mode converter performance and the 25 nm thick silicon slab layer was chosen to act as a hard mask for selective under-etch of the BOX. Also, in the simulation analysis a small under etch of the BOX (width < 0.5 µm) under the beams in the slot mode converter region was considered to be close to the fabricated device.

Figure 7-40 shows the top view of the STRIP to STRIP-loaded-SLOT waveguide mode converter with mode profiles (cross section) as it propagates along its length. Cross section A, B, and C in Figure 7-40 represent the under-etched STRIP waveguide mode, the STRIP-loaded-SLOT waveguide mode, and the fully etched SLOT waveguide mode respectively.

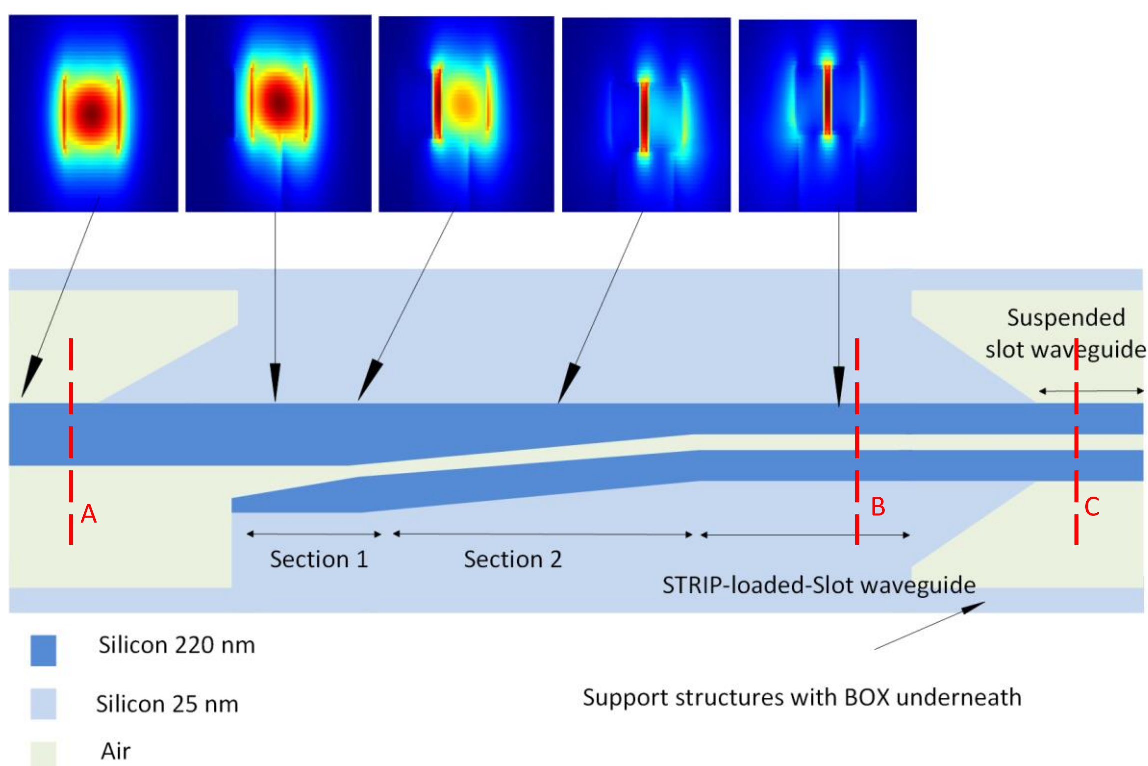

Figure 7-40 Top view of the STRIP to strip-loaded slot mode converter with mode profiles (cross section) along the length of the converter as the mode is transformed. A represents the under-etched STRIP waveguide mode, B represents the Strip-loaded-SLOT waveguide mode, and C represents fully etched SLOT waveguide mode.

Figure 7-40 shows the cross section of the mode as it propagates along the converter. The length of section 1 and section 2 were chosen to be 5 µm and 20 µm respectively. The transmission for wavelengths ranging from 1.5 µm and 1.6 µm was averaged and found to be 0.25 dB per converter using FDTD simulations.

The results for the RIB to under-etched STRIP transition utilized before the STRIP waveguide to slot mode converter are plotted in Figure 7-41.

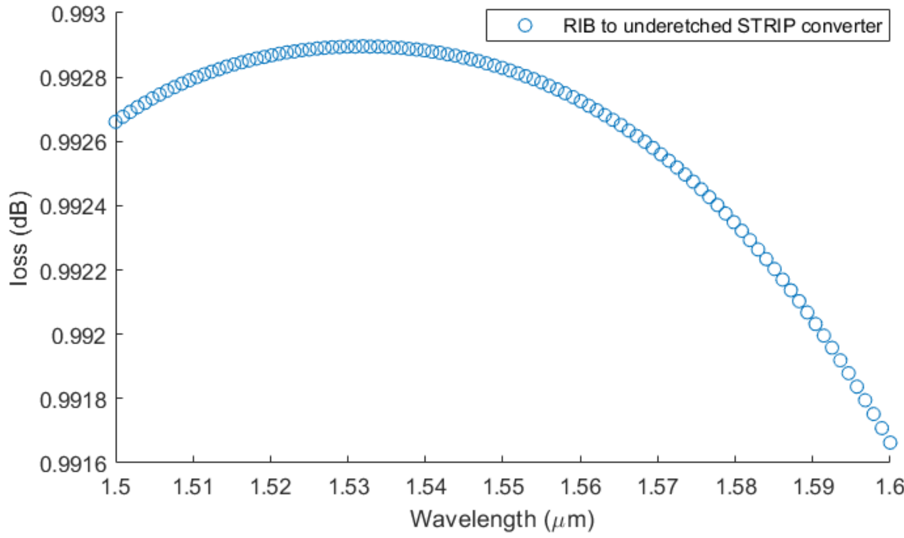

Figure 7-41 Simulated transmission for RIB to under-etched STRIP waveguide using the FDTD solver.

Next the transition from the under-etched STRIP waveguide to STRIP-loaded-SLOT waveguide mode is considered. The transmission results using FDTD solver are plotted in Figure 7-42.

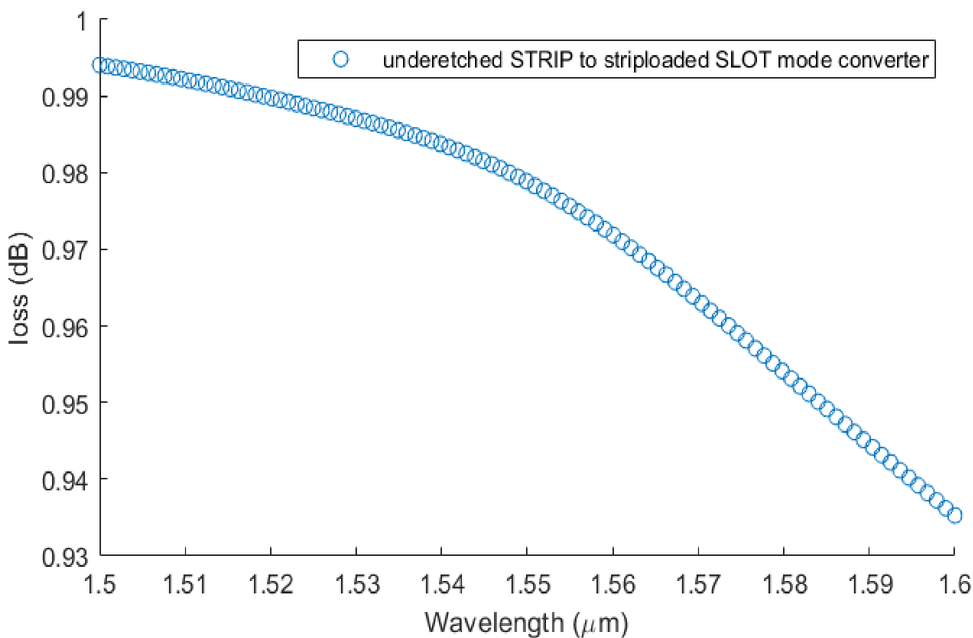

Figure 7-42 Simulated transmission for under-etched STRIP waveguide to STRIP-loaded-SLOT waveguide using the FDTD solver.

And finally the STRIP-loaded-SLOT to fully suspended SLOT waveguide mode transition is simulated and the results are plotted in Figure 7-43.

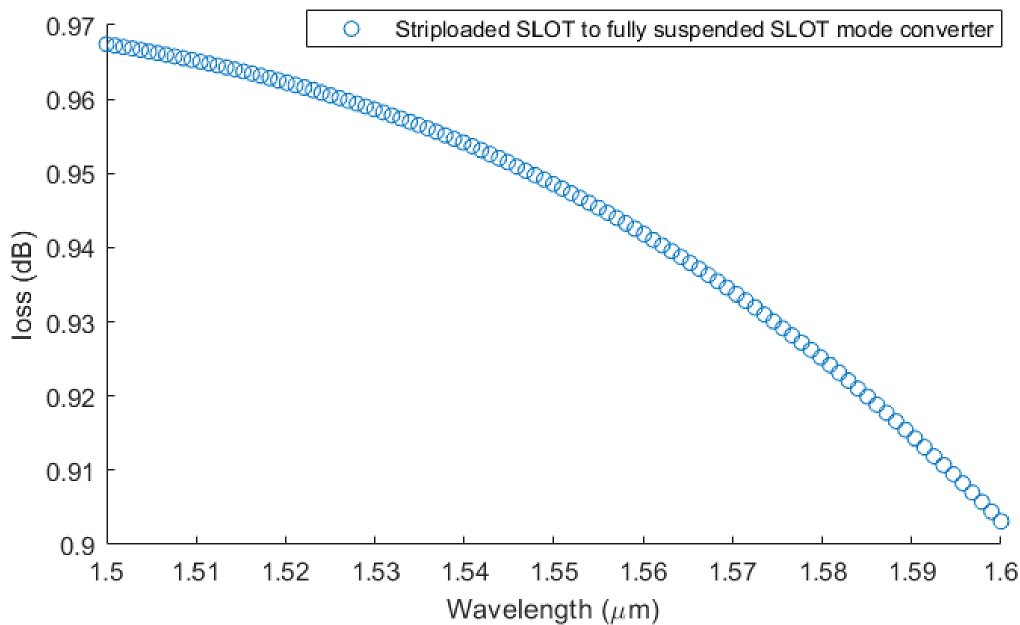

Figure 7-43 Simulated transmission for the STRIP-loaded SLOT mode to fully suspended SLOT mode using FDTD.

From simulation results we can clearly see that the designed 25 nm slab waveguide based mode converter is fairly low loss producing 0.5 dB per pair of mode conversions

7.9.2 1x2 MMI

The input and output waveguides at the MMI are tapered in width from 450 nm to 1.5 µm over a length of 20 µm. The input port position was at the centre of the width of multimode region and output port at +-1.5 µm from the centre of the multimode region which was chosen to be 6 µm in width. The simulation results for the length sweep of the multimode region is plotted in Figure 7-44.

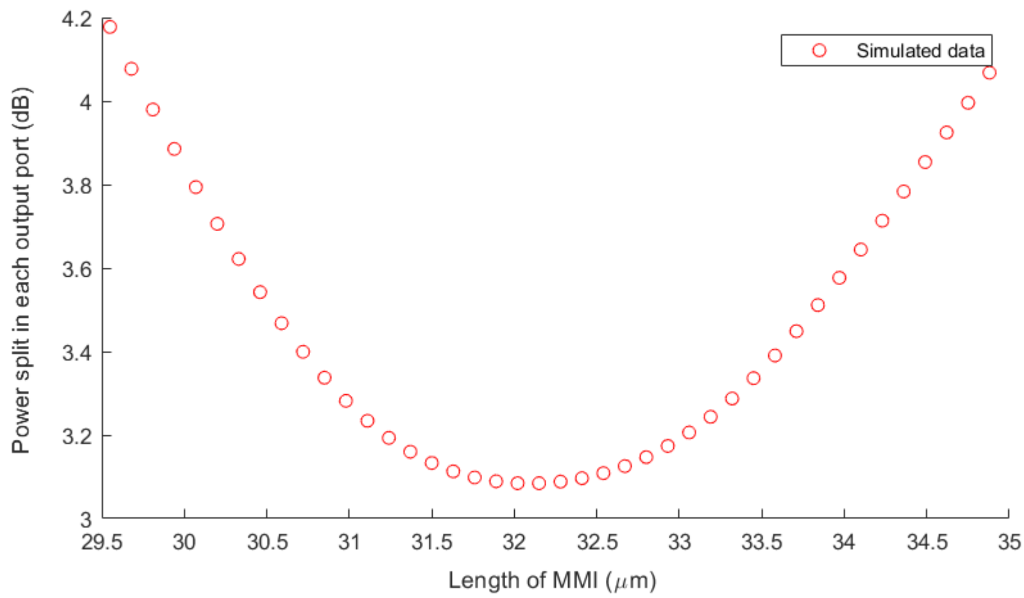

Figure 7-44 Simulation results for 1x2 MMI for various MMI lengths.

The transmission for individual output ports was 0.49 at multimode region length of 32.1 µm. Figure 7-45 shows the simulated device without tapers using the EME solver in Lumerical.

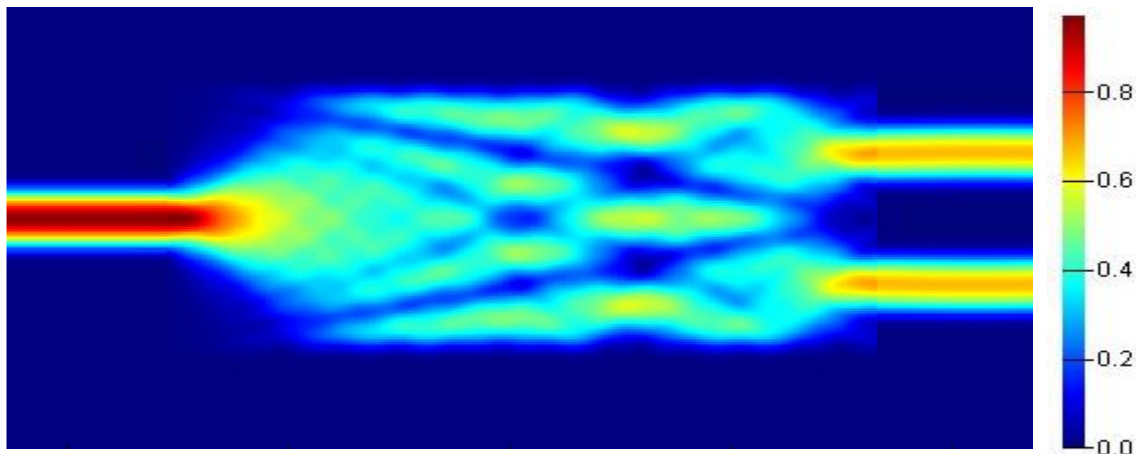

Figure 7-45 Simulated 1x2 MMI intensity profile at 32.1 µm MMI length using the EME solver in Lumerical.

The results for the MMI length do not deviate much from what was observed for the STRIP platform which is reasonable since there is only a 25 nm thin slab present.

7.9.3 2x2 MMI

The simulation results for 2x2 MMI length with 25 nm slab region using EME are plotted in Figure 7-46

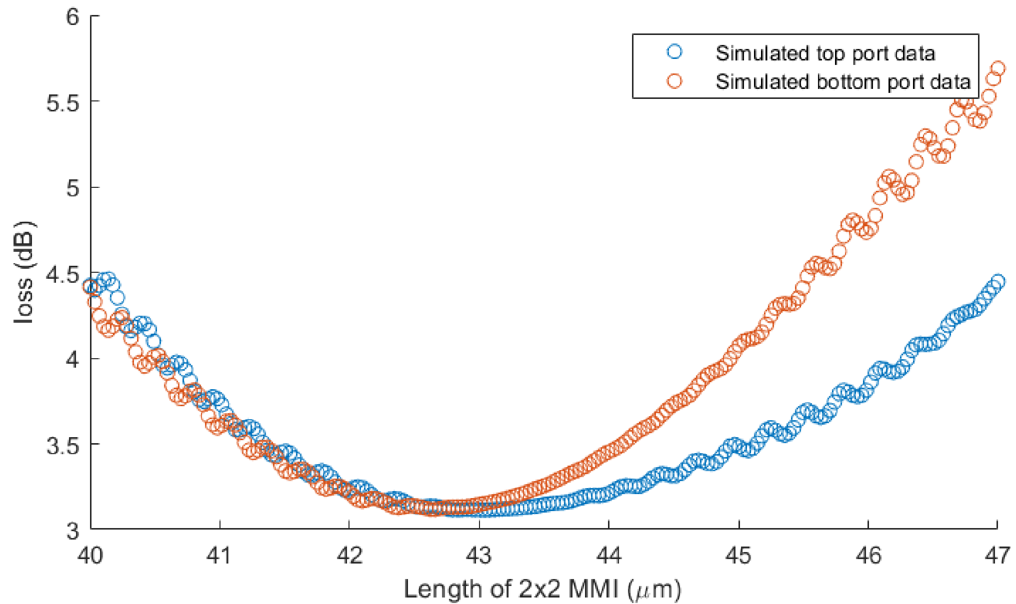

Figure 7-46 Simulation results for length of the multimode region of the 1x2 MMI.

The simulated length for the MMI region is 42.2 µm and the intensity profile is plotted in Figure 7-47.

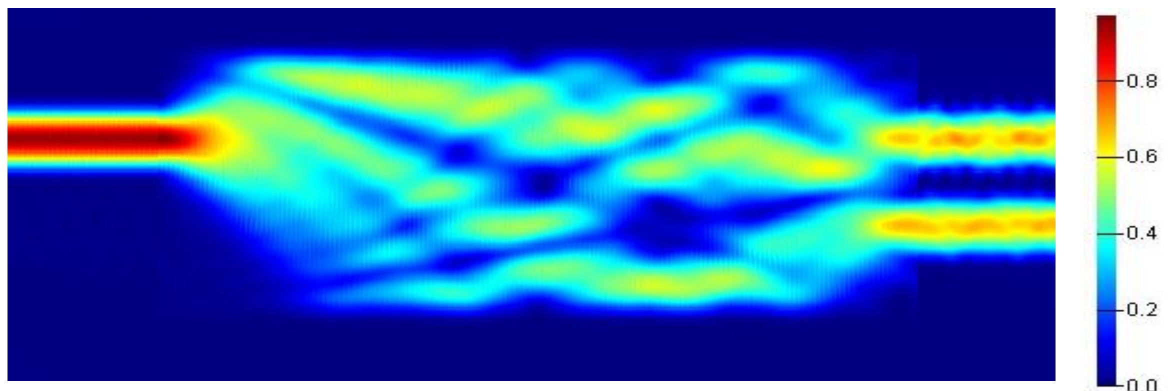

Figure 7-47 Simulated 2x2 MMI intensity profile at 42.2 µm MMI length using EME solver in Lumerical.

7.9.4 Fabrication

For the mask design some iteration of the silicon beam width and air gap were considered and are displayed in Table 19 . For all slot waveguide modulator dimensions under-etch length variations

of 2.5 µm to 12.5 µm were fabricated. Alongside the MZI with one modulator element in each arm, a cascaded configuration of 3, 5, 7 modulators in each arm were also fabricated. Three 30 x 40 mm^2 chips for each slot waveguide iteration (beam width and gap) were fabricated totalling to 12 chips on a 8 inch 220nm SOI wafer.

Table 19 Slot waveguide device iterations fabricated.

Silicon beam/rail width	Air gap width	Modulator under-etch length
250 nm	70 nm, 100 nm	2.5, 5, 7.5, 10, 12.5 µm
300 nm	70 nm, 100 nm	2.5, 5, 7.5, 10, 12.5 µm

Figure 7-48 displays the mask layout for the slot waveguide modulator with 1, 3, 5 and 7 cascaded modulators in each MZI arm for a 250 nm silicon beam width and 70 nm air gap.

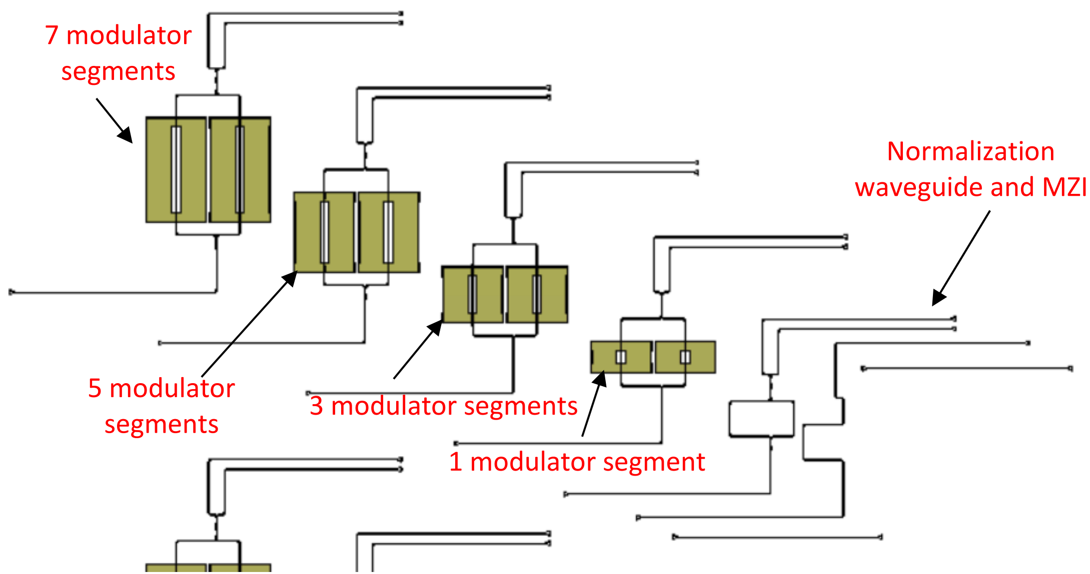

Figure 7-48 Mask layout of the slot waveguide modulator MZI (beam width = 250 nm, gap width =70 nm) with 1, 3, 5 and 7 modulator segments in each MZ arm.

7.9.4.1 Imaging before the modulator under-etch

This section presents the SEM imaging of the fabricated devices before the under-etch of the BOX was performed to make freestanding SLOT waveguide structures. Figure 7-49 displays the RIB waveguide to STRIP waveguide transition using a 10 µm long tapering of the slab region.

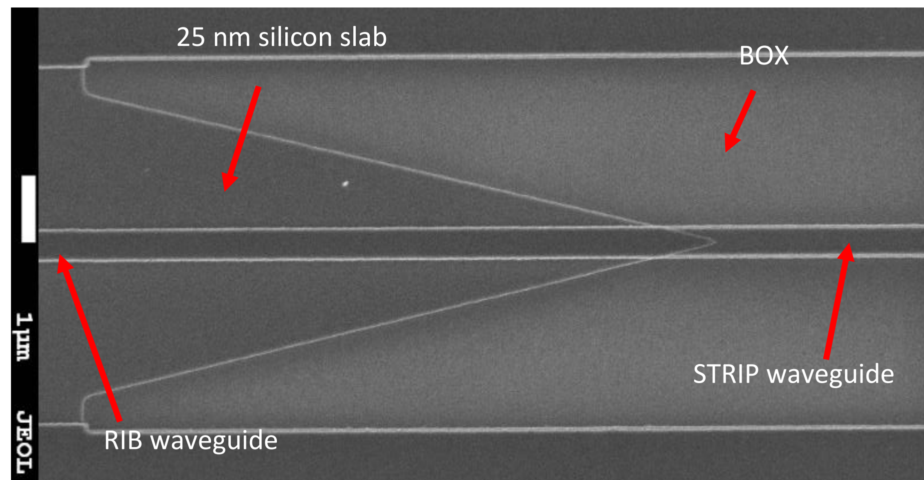

Figure 7-49 Fabricated RIB to STRIP mode converter before performing the under-etch.

Figure 7-50 displays the transition from STRIP waveguide to the start of the STRIP to STRIP-loaded mode converter and bits of section 1 for the mode converter.

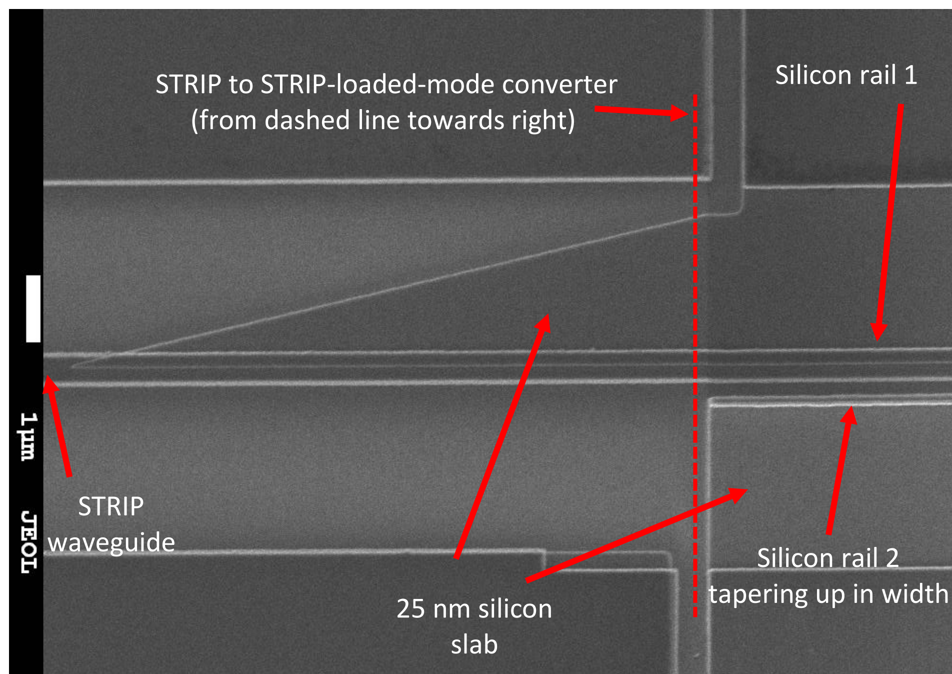

Figure 7-50 Fabricated STRIP to STRIP-loaded-SLOT mode converter before performing the under-etch for a silicon beam width of 250nm and gap width 70 nm.

Figure 7-51 displays a modulator region of 12.5 μm length transitioning to and from a STRIP-loaded-SLOT waveguide using 5 μm length linear tapering of the slab.

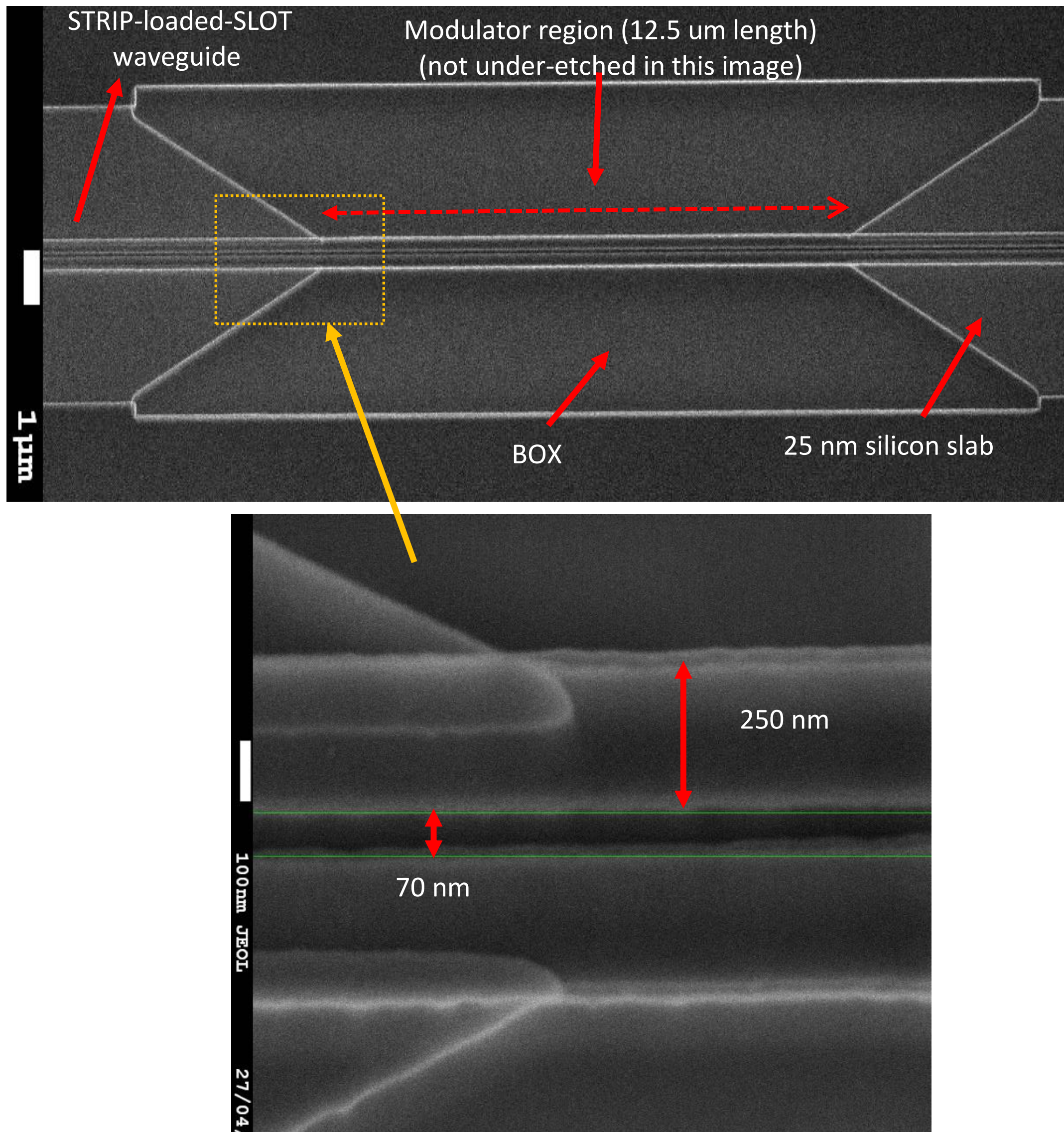

Figure 7-51 Fabricated modulator with a silicon beam width of 250nm, gap width of 70 nm and a length of 12.5 µm (before performing the underetch)

7.9.4.2 Imaging after HF vapour etching

Erroneously 30 nm of titanium was used as the adhesion layer for the metal electrodes. Titanium reacts with hydrofluoric acid producing hydrogen gas as a by-product [161].

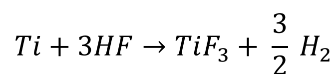

$$Ti + 3HF \rightarrow TiF_3 + \frac{3}{2}H_2$$

The trapped hydrogen gas forms tiny bubbles along the edges of the gold layer and in most cases made the electrode layer delaminate, damaging the whole chip. Figure 7-52 shows the microscope image of a sample with titanium used as the seed layer after being processed with vapor HF.

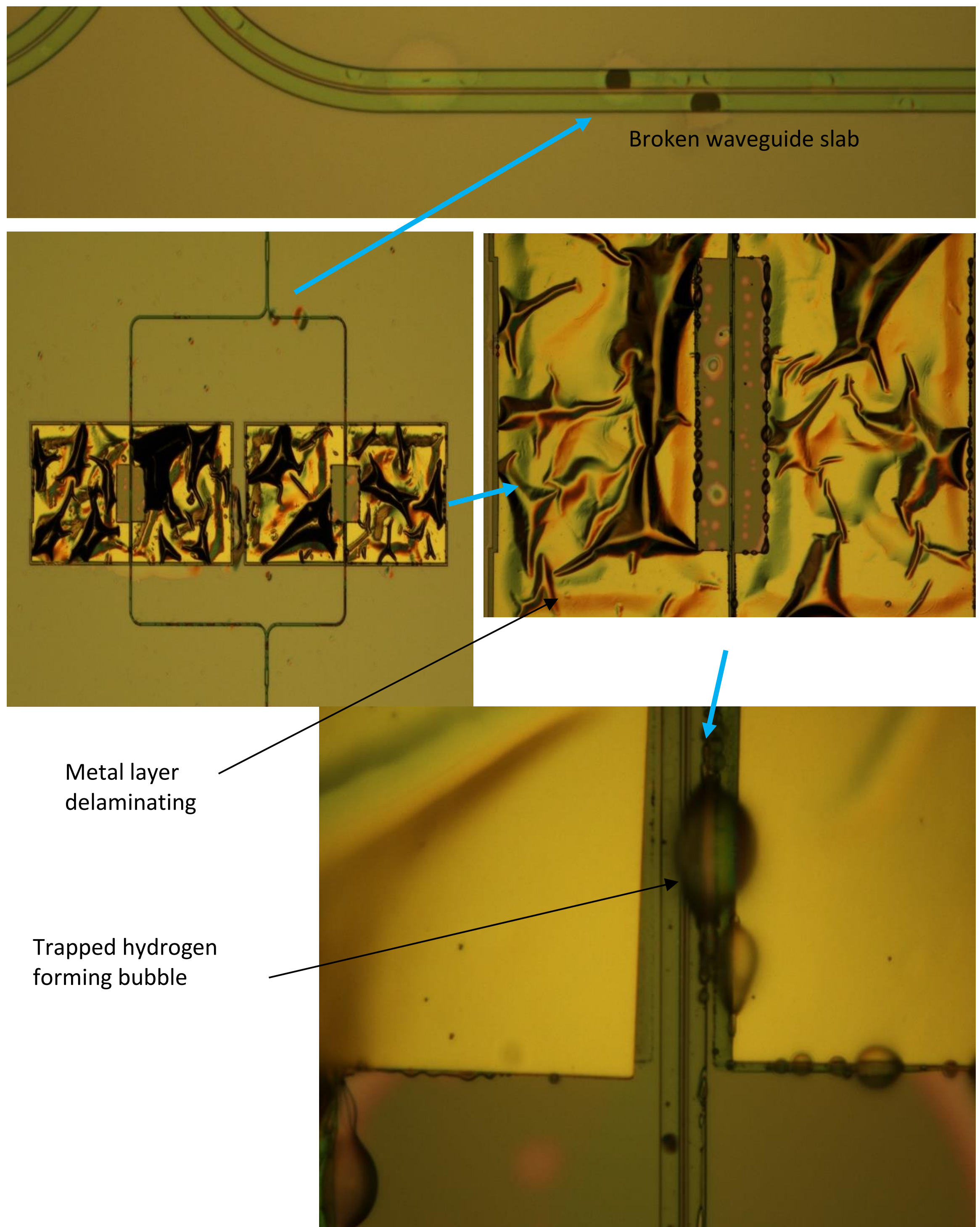

Figure 7-52 Sample with titanium as adhesion layer after being processed with vapour HF.

Clearly the delamination of the gold layer and the damage caused to the wavegudies is visible. Since the devices do not have any protecting oxide layer on top, these chips were abondoned.

For the remaining samples, the electrode layer was etched away using gold and titanium etchant. The remaining chips were then sent again for ebeam writing of the metal layer outside of the unversity facilities due to ebeam tool failure. This caused significant delays slong with the COVID

shutdown initially and restricted working conditions afterwards. After the ebeam patterning , Au was deposited with Cr as seed layer ready to be procesed in the HF vapour tool when unfortunately it was reported broken. Acquiring the parts from manufacturers overseas added long delays to the project. Once the tool was fixed, some calibration runs were performed on the tool when it broke down again and requred in depth investigation.

At this point, the decision to unfortnately abandon fabrication on remaining few chips was made due to unknwown down time period and reliability of the tool after repair and calibration.

7.10 Summary

In this chapter, the working principle and device designs for two different approaches to fabricate free standing slot waveguide based phase modulators have been explored. A STRIP waveguide based platform, requiring critical point drying using CO_2, and HF vapour based etching using a silicon slab as a hard mask to avoid stiction related issues with their fabrication have been detailed.

The mode converters for both platforms have been described via simulation work and experimentally demonstrated for the STRIP waveguide based platform with a low loss of < 0.5 dB per conversion.

A RIB waveguide based platform has been attempted, but unfortunately due to tool failures and COVID work restrictions, the fabrication of full devices for experimental characterization could not be completed.

Chapter 8 Conclusion

Since the advent of optical fibre, information transfer via light has grown manifold. Borrowing the facilities from CMOS fabrication, silicon photonics has already made a stronghold on the optical interconnect market with ever higher transmission and detection schemes while still delivering a cost effective solution.

Emerging applications with large numbers of optical components such as optical phased arrays for LIDAR, optical machine learning and quantum information processing are now on a look out for compact, low loss modulation mechanisms that can provide for the large number of integrated components with moderate modulation speeds and without overloading the power budget.

This project was set out to explore compact modulation mechanisms for slow/moderate speed switching to deliver for large scale integrated circuits. The three different types of modulation mechanisms studied during this work were thermo optic, carrier injection, NEMS optical phase shifters. The operating speeds of each type modulator was found to be similar to (or slightly higher) than the respective normalization devices (with single mode waveguide structures). The thermal and NEMS based devices being the slowest and operating at 100's of KHz, whereas the injection modulation scheme allows for up to GHz operational speed. When comparing the power consumption of the three modulation schemes, the lowest power requirement is for NEMS optical devices (owing to only leakage current) followed by free carrier injection based devices, and thermal modulation schemes being the most power hungry of them all. For dense optical integration, NEMS based devices are preferable compared to thermal devices as thermal devices also suffer from heat crosstalk between various closely spaced components.

The device footprint in all three modulation schemes need a deeper look. In the case of NEMS modulator, the suspended waveguide modulator itself might be 10 or 20 µm in length, but to achieve low insertion loss a large number of adiabatic passive mode converters need to be incorporated into the MZ design which increased the devices footprint by manifolds. The thermal and carrier injection based approaches utilizing MMI approaches similar device footprint compared to the typically used designs with an added 90 degree bend requiring an additional 60 x 50 μm^2 area.

Typical device configurations of thermal and carrier injection modulators were studied during this work for various waveguide widths on the 220 nm SOI platform, and utilized to investigate their respective optical phase shift. Mode overlap with the change in the carrier density and thermal gradient is utilized to study the change in mode effective index and guidelines for optimal device geometry can be inferred from the presented work in each case.

Light recycling through a waveguide cross section was presented with extensive FDE analysis to study the modal properties of the waveguide geometries. Compared to other light recycling approaches such as ring resonators, mode upconverters, and dense packing of waveguides which are either very sensitive to temperature, have a very narrow bandwidth (in the case of ring resonators), or need great design and fabrication complexity, our study focussed on commonly used, fabrication and temperature tolerant MMI structures in a MZI configuration. The self-imaging properties of the MMI device were utilized to cycle light twice through the multimode region of the MMI.

The thermal gradient from a commonly used metal strip heater element was discussed and the known thermo optic coefficient was utilized to study the change in the refractive index of silicon waveguides of various width using simulations. Then its effect on the optical modes propagating along the various waveguide widths was presented and the resultant phase change for selective waveguide widths, with fundamental mode propagation, and 6 µm multimode region width MMI were reported. Although simulation analysis using EME was utilized to study the resultant phase change, a computing program with parameters of effective index and intermodal coupling for various heater powers can be synthesised to yield agreeable results using only the FDE solver. Finally, a power saving of 29.26% was achieved with the light propagating twice through the 6 µm 2x2 MMI compared with one pass through the single mode waveguide.

Although the other works utilizing similar light recycling techniques [81, 85] show better efficiencies than what was reported in this work, our results should only be taken as a proof of concept for using a 2x2 MMI for phase modulation applications. The trends of effective index change (of various optical modes) for varying waveguide widths also point out that even greater power saving can be achieved for MMI with narrower multimode region than 6 µm. Increased power savings using this approach can therefore be expected with optimisation of the device geometry.

Guidelines for compact packaging of thermal photonic devices using metal strip heating element were presented for various commonly used SOI platforms. It was shown that to avoid thermal cross talk, a minimum 6 µm and 14 µm of heating component separation is necessary in the case of STRIP and RIB (100 nm silicon slab) waveguides respectively for silicon overlayer thickness of 220 nm. Similarly for silicon overlayer thickness of 500 nm, the minimum separation as found to be 10 µm and 28 µm for the case of STRIP and RIB (200 nm silicon slab) waveguides.

Carrier injection modulation schemes on a 220 nm height silicon waveguide core with 100 nm silicon slab were also considered in this work. Similar analysis (as thermal) was presented for the effective index change of various waveguide widths, for an applied power across the waveguide p-

i-n junction. Trends for the carrier concentration change across the waveguides of varying silicon core widths were reported. Smaller widths of the MMI multimode region (compared to 6 µm in the thermal case) were considered due to the larger carrier concentration change and faster switching time achievable which are both desirable characteristics in such devices.

Mode overlap studies using FDE analysis were used to excite specific modes in the multimode region of the MMI. Light recycling using the self-imaging properties for a 2x2 MMI with multimode region tapered to a waveguide of width 0.8 µm were then demonstrated experimentally to yield power savings of 66% compared to the normalization modulators which were based on a waveguide width of 0.4 µm. The device rise and fall time of 3.29 ns and 3.32 ns were also reported which were marginally higher than the normalization modulator structures.

Experimental characterization results for a 2x2 MMI device with an un-tapered multimode region width of 1.76 µm were also reported with a power saving (compared to normalization modulator) of 40.9% alongside rise and fall times of 5.20 ns and 5.35 ns respectively.

The light recycling approaches proposed in this work using a 2x2 MMI for thermal and carrier injection modulation schemes have been successful in reducing the phase modulation power requirements. Taking a step ahead from recycling light twice through the modulation region, similar self-imaging principles can be applied to a n x n MMI device to achieve manyfold efficiency increment in the case of thermal devices. Another interesting approach would be to utilize a polarization rotator [162] before re-entering the light in the MMI for second pass such that counter propagating modes have orthogonal polarization and hence reduce any interference based effects in the modulation output.

MEMS/NEMS based optical phase shifters made of free standing slot waveguides consisting of two silicon beams of width 250 nm and height 220 nm with an air gap of 70 nm between them were also studied extensively in this work. The phase modulation mechanism which uses the attractive electrostatic force between the two silicon beams to change the air gap width between them was detailed and two fabrication approaches were presented.

For the STRIP waveguide platform, the final freestanding structures were to be fabricated by etching away the supporting buried oxide layer using wet hydrofluoric acid. The rinsing liquid was then to be removed using critical point drying with $C0_2$ to eradicate any difficulties caused by stiction of the freestanding silicon beams which is a common problem in MEMS fabrication. On the other hand, the RIB waveguide platform with 25 nm of silicon slab acting as a hard mask was to be used for etching the sacrificial oxide layer underneath.

Unfortunately, due to repeated failures of the tools used in the final fabrication processing steps of both the approaches and substantial delays due to COVID related lab restrictions, no working devices could be fabricated. However, a passive fabrication run without the oxide under-etch for the STRIP waveguide based platform was successful. The results for mode converter designs from the passive run were reported to be < 0.5 dB per pair. The simulation results for the mode converter designs used to transition into and out of the free standing slot waveguide in the modulator devices on both STRIP and RIB platforms were presented.

Even though the fabrication run for full devices was not successful, simulation results for the passive components such as the mode converter loss and MMI loss for both platforms can be utilized as guidelines for future work involving similar devices.

If the loss of the slot waveguides and mode converters approaches considerably low values, the free standing slot waveguide modulator devices would be a good match to achieve low power static tuning for example for aligning the resonant wavelength for ring resonator based structures which currently require considerable power budget for active tuning of the resonant wavelength to counter temperature and fabrication variations. A schematic top view of such devices is shown in Figure 8-1. Similar work for refractive index sensing [163] and with electro optic polymer [164, 165] has been reported.

A slot waveguide based platform (instead of STRIP/RIB) can also be utilized in a similar manner as reported in [164, 166].

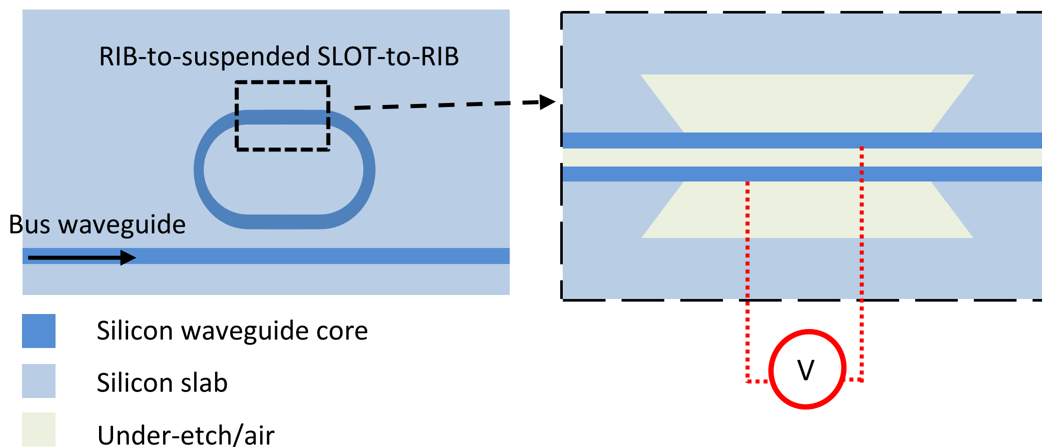

Figure 8-1 Freestanding SLOT waveguides as resonant wavelength tuning element in racetrack resonator.

The ring resonator wavelength tuning can be further extended by using a coupled ring approach, where one ring structure, containing a free standing slot waveguide modulator is used for tuning,

and the other ring is utilized for modulation using conventional carrier based schemes as shown in Figure 8-2.

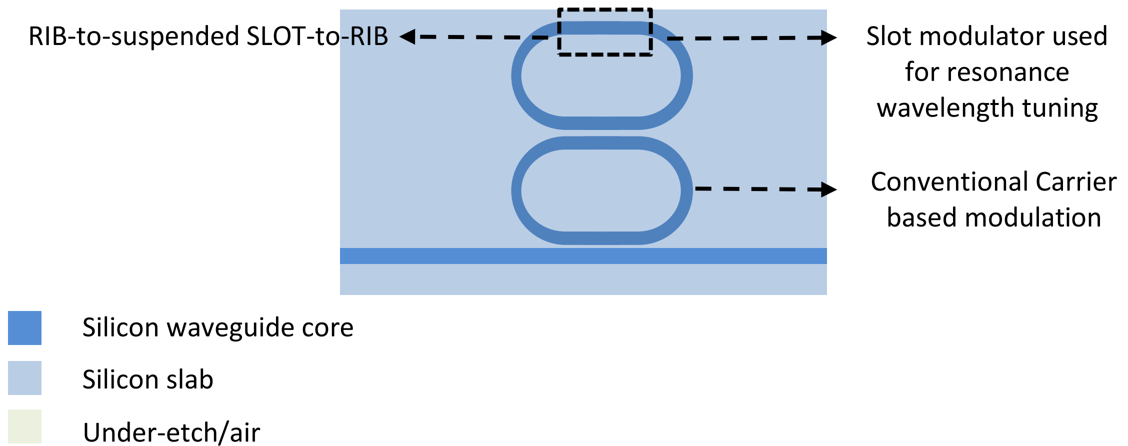

Figure 8-2 Coupled ring structures consisting of freestanding SLOT waveguides as resonant wavelength tuning element in racetrack resonator.

The use of coupled rings geometry provides electrical isolation in the ring resonator with freestanding SLOT waveguide modulator used for tuning.

To summarise, light recycling structures for thermal and carrier injection mechanisms, and MEMS based free standing slot waveguide optical phase modulators have been studied in this work and the simulation and experimental results were discussed along with some ideas for future work.

Appendix A

For optical simulations throughout this work, Lumerical MODE solutions was used. It incorporates different solvers utilizing specific techniques with varying computing and time resources. Here some comments about these solvers are provided with reasons as to why they were implemented for specific devices [126]. The Mode solver (also called Eigenmode solver) gives the optical mode profile of a given waveguide geometry by solving Maxwell's equations in the frequency domain. For a fixed cross section of waveguide, the mode profile does not change in the propagation direction. For accurate results in high confinement waveguides, fully vectorial techniques such as

the finite element and finite difference approaches should be used [126]. For mode calculations throughout this report the finite difference eigenmode solver (FDE) of Lumerical mode solutions was extensively used.

For the propagation of light in waveguides and MMI, the Eigenmode Expansion Method (EME) was used. In this, the local fields are decomposed into modes of cross section and propagated individually, adding up the phase as they propagate along the structure. Various sections can then be connected together using scattering parameters. This technique takes into account both forward and backward propagation of light and can take advantage of the symmetrical geometry in the structure, hence reducing the computational requirements for modelling long guided optical structures like MMI, directional couplers, gratings, etc. while providing accurate results.

A.1 Data points selection and fitting

The section explains the data fitting process for the strip to slot mode converters studied in chapter 9. The experimental data collected from the lab setup (plotted with blue circles in Figure A-8-3) is refined for fitting in 2 steps using MATLAB. The first step calculates the median of all collected data points and eliminates outliers outside of the standard deviation from it. The second step selects a moving window of 5 consecutive data points (along x axis) and checks for the outliers lying outside standard deviation of the median. The remaining data points (plotted with blue stars) are fitted to a linear curve to give the loss for two converters for a particular length. The standard deviation of residuals of the fitted data is then calculated and used as the error.

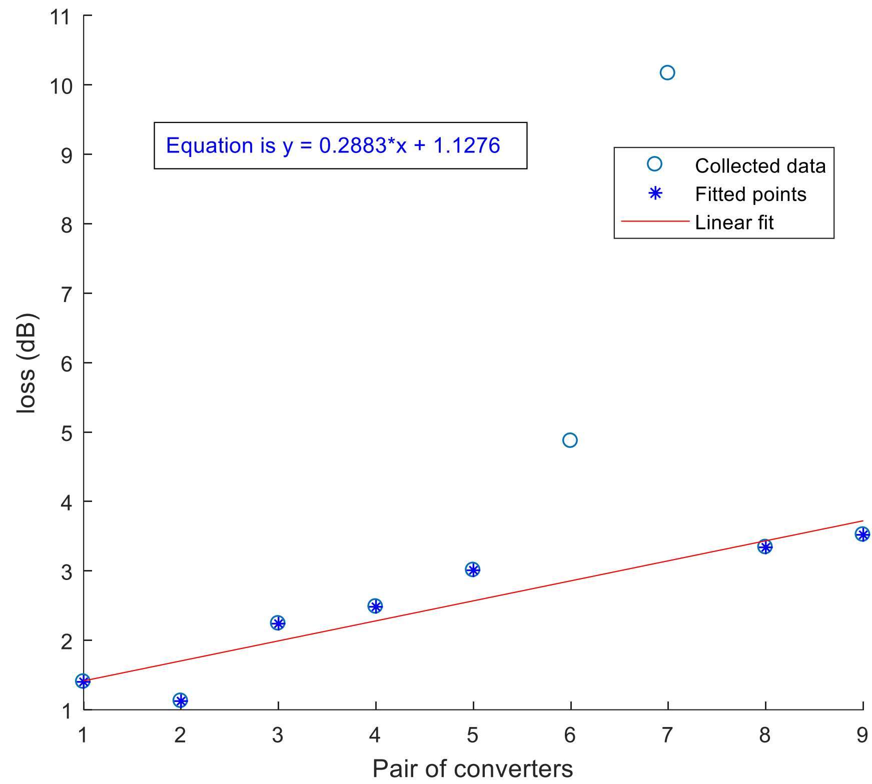

Figure A-8-3 Experimental and fitted data points for Strip to slot mode converter with length section 1=0.5 µm and length section 2 = 20µm.

Bibliography

1. Optica Industry, R., *Optics and Photonics: The Impact on a Global Economy*, in *Optica Industry Report*. 2022, Optica. p. 12.

2. Reed, G.T., W.R. Headley, and C.E.J. Png. *Silicon photonics: the early years*. in *Integrated Optoelectronic Devices 2005*. 2005. SPIE.

3. Soref, R. and J. Lorenzo, *Single-crystal silicon: a new material for 1.3 and 1.6 μm integrated-optical components.* Electronics Letters, 1985. **21**(21): p. 953-954.

4. Soref, R. and J. Larenzo, *All-silicon active and passive guided-wave components for λ= 1.3 and 1.6 μm.* IEEE Journal of Quantum Electronics, 1986. **22**(6): p. 873-879.

5. Rahim, A., et al., *Open-Access Silicon Photonics: Current Status and Emerging Initiatives.* Proceedings of the IEEE, 2018. **106**(12): p. 2313-2330.

6. IBM. *III–V on silicon photonics*. 2022 26/12/2022]; Available from: https://www.zurich.ibm.com/st/photonics/iii-v.html#:~:text=Silicon%20photonics%20is%20a%20versatile,cost%2C%20as%20known%20from%20microelectronics.

7. Zhang, J., et al., *III-V-on-Si photonic integrated circuits realized using micro-transfer-printing.* APL Photonics, 2019. **4**(11): p. 110803.

8. Hiraki, T., et al., *Heterogeneously integrated III–V/Si MOS capacitor Mach–Zehnder modulator.* Nature Photonics, 2017. **11**(8): p. 482-485.

9. Takenaka, M., et al. *High-efficiency, Low-loss Optical Phase Modulator based on III-V/Si Hybrid MOS Capacitor*. in *Optical Fiber Communication Conference*. 2018. San Diego, California: Optica Publishing Group.

10. Bu, H. *5 nanometer transistors inching their way into chips*. 2017 25/04/2022; Available from: https://www.ibm.com/blogs/think/2017/06/5-nanometer-transistors/.

11. Minasian, R.A., *Photonic signal processing of microwave signals.* IEEE Transactions on Microwave Theory and Techniques, 2006. **54**(2): p. 832-846.

12. Capmany, J., et al., *Microwave Photonic Signal Processing.* Journal of Lightwave Technology, 2013. **31**(4): p. 571-586.

13. Tsybeskov, L., D.J. Lockwood, and M. Ichikawa, *Silicon Photonics: CMOS Going Optical [Scanning the Issue].* Proceedings of the IEEE, 2009. **97**(7): p. 1161-1165.

14. *Silicon Photonics Market and Technology Report 2021*, Y. Developpement, Editor. 2021: https://www.i-micronews.com/products/silicon-photonics-2021/.

15. Thomson, D., et al., *Roadmap on silicon photonics.* Journal of Optics, 2016. **18**(7): p. 073003.

16. Khanna, A., et al. *Complexity Scaling in Silicon Photonics*. in *Optical Fiber Communication Conference*. 2017. Los Angeles, California: Optica Publishing Group.

17. Hochberg, M., et al., *Silicon Photonics: The Next Fabless Semiconductor Industry.* IEEE Solid-State Circuits Magazine, 2013. **5**(1): p. 48-58.

18. Pond, J., et al. *A simulation tool development roadmap to support a scalable silicon photonics design ecosystem*. in *2015 IEEE 12th International Conference on Group IV Photonics (GFP)*. 2015.

19. Lim, A.E., et al., *Review of Silicon Photonics Foundry Efforts.* IEEE Journal of Selected Topics in Quantum Electronics, 2014. **20**(4): p. 405-416.

20. Hochberg, M. and T. Baehr-Jones, *Towards fabless silicon photonics.* Nature Photonics, 2010. **4**(8): p. 492-494.

21. Baets, R., et al. *Silicon Photonics*. in *2007 International Symposium on VLSI Technology, Systems and Applications (VLSI-TSA)*. 2007.

22. Sun, J., et al., *Large-scale nanophotonic phased array.* Nature, 2013. **493**(7431): p. 195-199.

23. Abediasl, H. and H. Hashemi, *Monolithic optical phased-array transceiver in a standard SOI CMOS process.* Optics Express, 2015. **23**(5): p. 6509-6519.

24. Chung, S., H. Abediasl, and H. Hashemi, *A Monolithically Integrated Large-Scale Optical Phased Array in Silicon-on-Insulator CMOS.* IEEE Journal of Solid-State Circuits, 2018. **53**(1): p. 275-296.

25. O'Brien, J.L., A. Furusawa, and J. Vučković, *Photonic quantum technologies.* Nature Photonics, 2009. **3**(12): p. 687-695.

26. Harris, N.C., et al., *Quantum transport simulations in a programmable nanophotonic processor.* Nature Photonics, 2017. **11**(7): p. 447-452.

27. Shen, Y., et al., *Deep learning with coherent nanophotonic circuits.* Nature Photonics, 2017. **11**(7): p. 441-446.

28. Vandoorne, K., et al., *Experimental demonstration of reservoir computing on a silicon photonics chip.* Nature Communications, 2014. **5**(1): p. 3541.

29. Dumais, P., et al., *Silicon Photonic Switch Subsystem With 900 Monolithically Integrated Calibration Photodiodes and 64-Fiber Package.* Journal of Lightwave Technology, 2018. **36**(2): p. 233-238.

30. Bogaerts, W. and A. Rahim, *Programmable Photonics: An Opportunity for an Accessible Large-Volume PIC Ecosystem.* IEEE Journal of Selected Topics in Quantum Electronics, 2020. **PP**: p. 1-1.

31. Pavesi, L., *Will silicon be the photonic material of the third millenium? *.* Journal of Physics: Condensed Matter, 2003. **15**(26): p. R1169-R1196.

32. Jalali, B., et al., *Advances in silicon-on-insulator optoelectronics.* IEEE Journal of Selected Topics in Quantum Electronics, 1998. **4**(6): p. 938-947.

33. Yap, K.P., et al., *Correlation of Scattering Loss, Sidewall Roughness and Waveguide Width in Silicon-on-Insulator (SOI) Ridge Waveguides.* Journal of Lightwave Technology, 2009. **27**: p. 3999-4008.

34. Thomson, D.J., et al., *Silicon Photonics*, in *Wiley Encyclopedia of Electrical and Electronics Engineering*. p. 1-22.

35. Cheung, S., et al., *Ultra-Compact Silicon Photonic 512 × 512 25 GHz Arrayed Waveguide Grating Router.* IEEE Journal of Selected Topics in Quantum Electronics, 2014. **20**(4): p. 310-316.

36. Mashanovich, G.Z., et al., *Silicon Photonic Waveguides and Devices for Near- and Mid-IR Applications.* IEEE Journal of Selected Topics in Quantum Electronics, 2015. **21**(4): p. 407-418.

37. Headley, W.R., et al., *Polarization-independent optical racetrack resonators using rib waveguides on silicon-on-insulator.* Applied Physics Letters, 2004. **85**(23): p. 5523-5525.

38. Hu, Y., et al., *Wavelength division (de)multiplexing based on dispersive self-imaging.* Optics Letters, 2011. **36**(23): p. 4488-4490.

39. Loiacono, R., et al., *Laser erasable implanted gratings for integrated silicon photonics.* Optics Express, 2011. **19**(11): p. 10728-10734.

40. Taillaert, D., et al., *Grating Couplers for Coupling between Optical Fibers and Nanophotonic Waveguides.* Japanese Journal of Applied Physics, 2006. **45**(8A): p. 6071-6077.

41. Yu, Z., et al., *High efficiency and broad bandwidth grating coupler between nanophotonic waveguide and fibre.* Chinese Physics B, 2010. **19**(1): p. 014219-5.

42. Pu, M., et al., *Ultra-low-loss inverted taper coupler for silicon-on-insulator ridge waveguide.* Optics Communications, 2010. **283**(19): p. 3678-3682.

43. Zaoui, W.S., et al., *Bridging the gap between optical fibers and silicon photonic integrated circuits.* Optics Express, 2014. **22**(2): p. 1277-1286.

44. Bakir, B.B., et al., *Low-Loss (<1 dB) and Polarization-Insensitive Edge Fiber Couplers Fabricated on 200-mm Silicon-on-Insulator Wafers.* IEEE Photonics Technology Letters, 2010. **22**(11): p. 739-741.

45. Soref, R. and B. Bennett, *Electrooptical effects in silicon.* IEEE journal of quantum electronics, 1987. **23**(1): p. 123-129.

46. Reed, G.T., et al., *Silicon optical modulators.* Nature Photonics, 2010. **4**(8): p. 518-526.

47. Rahim, A., et al., *Taking silicon photonics modulators to a higher performance level: state-of-the-art and a review of new technologies.* Advanced Photonics, 2021. **3**(2): p. 024003.

48. Jiate, Z., et al., *Analysis of the thermo-optic effect in lateral-carrier-injection SOI ridge waveguide devices.* Journal of Semiconductors, 2010. **31**(6): p. 064009.

49. Zhao, Y., et al., *Influence of doping position on the extinction ratio of Mach—Zehnder-interference based silicon optical modulators.* Journal of Semiconductors, 2012. **33**(1): p. 014009.

50. Ching Eng, P., et al., *Optical phase modulators for MHz and GHz modulation in silicon-on-insulator (SOI).* Journal of Lightwave Technology, 2004. **22**(6): p. 1573-1582.

51. Sobu, Y., et al. *70 Gbaud Operation of All-Silicon Mach–Zehnder Modulator based on Forward-Biased PIN Diodes and Passive Equalizer*. in *2019 24th OptoElectronics and Communications Conference (OECC) and 2019 International Conference on Photonics in Switching and Computing (PSC)*. 2019.

52. Farhan Rana, C.U. [cited 2022 26/12]; Available from: https://courses.cit.cornell.edu/ece315/Lectures/handout7.pdf.

53. Xu, Q., et al., *12.5 Gbit/s carrier-injection-based silicon micro-ring silicon modulators.* Optics Express, 2007. **15**(2): p. 430-436.

54. Baba, T., et al., *25-Gb/s broadband silicon modulator with 0.31-V·cm VπL based on forward-biased PIN diodes embedded with passive equalizer.* Optics Express, 2015. **23**(26): p. 32950-32960.

55. Akiyama, S., et al. *High-performance silicon modulator for integrated transceivers fabricated on 300-mm wafer*. in *2014 The European Conference on Optical Communication (ECOC)*. 2014.

56. Thomson, D.J., et al., *High Performance Mach–Zehnder-Based Silicon Optical Modulators.* IEEE Journal of Selected Topics in Quantum Electronics, 2013. **19**(6): p. 85-94.

57. Xiao, X., et al. *High speed silicon photonic modulators*. in *2017 Optical Fiber Communications Conference and Exhibition (OFC)*. 2017.

58. Akiyama, S., et al., *Compact PIN-Diode-Based Silicon Modulator Using Side-Wall-Grating Waveguide.* IEEE Journal of Selected Topics in Quantum Electronics, 2013. **19**(6): p. 74-84.

59. Reed, G.T., et al., *Recent breakthroughs in carrier depletion based silicon optical modulators.* Nanophotonics, 2014. **3**(4-5): p. 229-245.

60. Liu, A., et al., *A high-speed silicon optical modulator based on a metal–oxide–semiconductor capacitor.* Nature, 2004. **427**(6975): p. 615-618.

61. Liao, L., et al., *High speed silicon Mach-Zehnder modulator.* Optics Express, 2005. **13**(8): p. 3129-3135.

62. Boeuf, F., et al., *Benchmarking Si, SiGe, and III–V/Si Hybrid SIS Optical Modulators for Datacenter Applications.* Journal of Lightwave Technology, 2017. **35**(18): p. 4047-4055.

63. Fujikata, J., et al., *High-performance MOS-capacitor-type Si optical modulator and surface-illumination-type Ge photodetector for optical interconnection.* Japanese Journal of Applied Physics, 2016. **55**(4S): p. 04EC01.

64. Webster, M., et al. *Low-power MOS-capacitor based silicon photonic modulators and CMOS drivers*. in *2015 Optical Fiber Communications Conference and Exhibition (OFC)*. 2015.

65. Gardes, F., G. Mashanovich, and G. Reed, *Evolution of optical modulation in silicon-on-insulator devices.* SPIE Newsroom, 2007. **27**.

66. Basak, J., et al., *Developments in Gigascale Silicon Optical Modulators Using Free Carrier Dispersion Mechanisms.* Advances in Optical Technologies, 2008. **2008**: p. 678948.

67. Keldysh, L., *Behavior of non-metallic crystals in strong electric fields.* Soviet Journal of Experimental and Theoretical Physics, 1958. **6**: p. 763.

68. Liu, J., et al., *Waveguide-integrated, ultralow-energy GeSi electro-absorption modulators.* Nature Photonics, 2008. **2**(7): p. 433-437.

69. Miller, D.A.B., et al., *Band-Edge Electroabsorption in Quantum Well Structures: The Quantum-Confined Stark Effect.* Physical Review Letters, 1984. **53**(22): p. 2173-2176.

70. Kuo, Y.-H., et al., *Quantum-confined Stark effect electroabsorption in Ge/SiGe quantum wells on silicon substrates*. Vol. 2005. 2005. 284-285.

71. Sophia University, J. [cited 2022 21/5]; Available from: https://pweb.cc.sophia.ac.jp/shimolab/html-e/qcse-e.html.

72. Gupta, S., et al. *50GHz Ge waveguide electro-absorption modulator integrated in a 220nm SOI photonics platform*. in *2015 Optical Fiber Communications Conference and Exhibition (OFC)*. 2015.

73. Kasper, E. and K. Lyutovich, *Properties of silicon germanium and sige:carbon.* The Institution of Electrical Engineers, 2000: p. 59-93.

74. Jongthammanurak, S., et al., *Large electro-optic effect in tensile strained Ge-on-Si films.* Applied Physics Letters, 2006. **89**(16): p. 161115.

75. Fox, M. and R. Ispasoiu, *Quantum Wells, Superlattices, and Band-Gap Engineering*, in *Springer Handbook of Electronic and Photonic Materials*, S. Kasap and P. Capper, Editors. 2007, Springer US: Boston, MA. p. 1021-1040.

76. Simili, D.V., M. Cada, and J. Pistora, *Silicon Slot Waveguide Electro-Optic Kerr Effect Modulator.* IEEE Photonics Technology Letters, 2018. **30**(9): p. 873-876.

77. Konoike, R., et al., *Ultra-compact silicon photonics switch with high-density thermo-optic heaters.* Optics Express, 2019. **27**(7): p. 10332-10342.

78. Chu, T., et al., *Compact 1 × N thermo-optic switches based on silicon photonic wire waveguides.* Optics Express, 2005. **13**(25): p. 10109-10114.

79. Liu, S., et al., *Comparison of thermo-optic phase-shifters implemented on CUMEC silicon photonics platform*. Seventh Symposium on Novel Photoelectronic Detection Technology and Application 2020. Vol. 11763. 2021: SPIE.

80. Densmore, A., et al., *Compact and low power thermo-optic switch using folded silicon waveguides.* Optics Express, 2009. **17**(13): p. 10457-10465.

81. Chung, S., M. Nakai, and H. Hashemi, *Low-power thermo-optic silicon modulator for large-scale photonic integrated systems.* Optics Express, 2019. **27**(9): p. 13430-13459.

82. Sun, H., et al., *Silicon Photonic Phase Shifters and Their Applications: A Review.* Micromachines (Basel), 2022. **13**(9).

83. Espinola, R.L., et al., *Fast and low-power thermooptic switch on thin silicon-on-insulator.* IEEE Photonics Technology Letters, 2003. **15**(10): p. 1366-1368.

84. Murray, K., et al., *Dense dissimilar waveguide routing for highly efficient thermo-optic switches on silicon.* Optics Express, 2015. **23**(15): p. 19575-19585.

85. Chang You-Chia, R.S.P., Stern Brian, Lipson Michal, *Resonance-Free Light Recycling.* https://doi.org/10.48550/arxiv.1710.02891, 2017.

86. Vlasov, Y., et al., *Vlasov, Y. A., O'Boyle, M., Hamann, H. F. & McNab, S. J. Active control of slow light on a chip with photonic crystal waveguides. Nature 438, 65-69.* Nature, 2005. **438**: p. 65-9.

87. Fang, Q., et al., *Ultralow Power Silicon Photonics Thermo-Optic Switch With Suspended Phase Arms.* IEEE Photonics Technology Letters, 2011. **23**(8): p. 525-527.

88. Hashizume, Y., et al. *Low-power silicon thermo-optic switch with folded waveguide arms and suspended ridge structures*. Electronics Letters, 2012. **48**, 1234-1235.

89. Lu, Z., et al., *Michelson Interferometer Thermo-Optic Switch on SOI With a 50-μW Power Consumption.* IEEE Photonics Technology Letters, 2015. **27**(22): p. 2319-2322.

90. Celo, D., et al. *Thermo-optic silicon photonics with low power and extreme resilience to over-drive*. in *2016 IEEE Optical Interconnects Conference (OI)*. 2016.

91. Walker, J.A., K.W. Goossen, and S.C. Arney, *Fabrication of a mechanical antireflection switch for fiber-to-the-home systems.* Journal of microelectromechanical systems, 1996. **5**(1): p. 45-51.

92. Toshiyoshi, H. and H. Fujita, *Electrostatic micro torsion mirrors for an optical switch matrix.* Journal of Microelectromechanical Systems, 1996. **5**(4): p. 231-237.

93. Neukermans, A. and R. Ramaswami, *MEMS technology for optical networking applications.* IEEE Communications Magazine, 2001. **39**(1): p. 62-69.

94. Syms, R.R.A. and D.F. Moore, *Optical MEMS for telecoms.* Materials Today, 2002. **5**(7): p. 26-35.

95. Wu, M.C., O. Solgaard, and J.E. Ford, *Optical MEMS for lightwave communication.* Journal of Lightwave Technology, 2006. **24**(12): p. 4433-4454.

96. Lin, L.Y., E.L. Goldstein, and R.W. Tkach, *Free-space micromachined optical switches with submillisecond switching time for large-scale optical crossconnects.* IEEE Photonics Technology Letters, 1998. **10**(4): p. 525-527.

97. Lee, C. and J.-L.A. Yeh, *Development and evolution of MOEMS technology in variable optical attenuators.* Journal of Micro/Nanolithography, MEMS, and MOEMS, 2008. **7**(2): p. 021003.

98. Lindroos, V., et al., *Handbook of Silicon Based MEMS Materials and Technologies, William Andrew Applied Science Publishers*. 2010: Oxford.

99. Feng, N.-N., J. Michel, and L.C. Kimerling, *Optical field concentration in low-index waveguides.* IEEE journal of Quantum Electronics, 2006. **42**(9): p. 885-890.

100. Tang, W.C., T.-C.H. Nguyen, and R.T. Howe, *Laterally Driven Polysilicon Resonant Microstructures.* Sensors and Actuators, 1989. **20**(1): p. 25-32.

101. Tang, W.C., et al., *Electrostatic-comb drive of lateral polysilicon resonators.* Sensors and Actuators A: Physical, 1990. **21**(1): p. 328-331.

102. Seok, T.J., et al., *Large-scale broadband digital silicon photonic switches with vertical adiabatic couplers.* Optica, 2016. **3**(1): p. 64-70.

103. Han, S., et al., *Large-scale silicon photonic switches with movable directional couplers.* Optica, 2015. **2**(4): p. 370-375.

104. Akihama, Y., Y. Kanamori, and K. Hane, *Ultra-small silicon waveguide coupler switch using gap-variable mechanism.* Optics Express, 2011. **19**(24): p. 23658-23663.

105. Abe, S., et al., *Time Response of a Microelectromechanical Silicon Photonic Waveguide Coupler Switch.* IEEE Photonics Technology Letters, 2014. **26**(15): p. 1553-1556.

106. Akihama, Y. and K. Hane, *Single and multiple optical switches that use freestanding silicon nanowire waveguide couplers.* Light: Science & Applications, 2012. **1**(6): p. e16-e16.

107. Chang, C.C., et al. *MEMS-actuated waveguide phase modulators*. in *2010 International Conference on Optical MEMS and Nanophotonics*. 2010.

108. Chiu, W.-C., et al., *Optical phase modulators using deformable waveguides actuated by micro-electro-mechanical systems.* Optics Letters, 2011. **36**(7): p. 1089-1091.

109. Almeida, V.R. and R.R. Panepucci. *NOEMS devices based on slot-waveguides*. in *2007 Quantum Electronics and Laser Science Conference*. 2007.

110. Acoleyen, K.V., et al. *NEMS-based optical phase modulator fabricated on Silicon-On-Insulator*. in *8th IEEE International Conference on Group IV Photonics*. 2011.

111. Van Acoleyen, K., et al., *Ultracompact Phase Modulator Based on a Cascade of NEMS-Operated Slot Waveguides Fabricated in Silicon-on-Insulator.* IEEE Photonics Journal, 2012. **4**(3): p. 779-788.

112. Nielson, G.N., et al., *Integrated wavelength-selective optical MEMS switching using ring resonator filters.* IEEE Photonics Technology Letters, 2005. **17**(6): p. 1190-1192.

113. Abdulla, S.M.C., et al., *Tuning a racetrack ring resonator by an integrated dielectric MEMS cantilever.* Optics Express, 2011. **19**(17): p. 15864-15878.

114. Errando-Herranz, C., et al. *A low-power MEMS tunable photonic ring resonator for reconfigurable optical networks*. in *2015 28th IEEE International Conference on Micro Electro Mechanical Systems (MEMS)*. 2015.

115. Errando-Herranz, C., et al., *Low-power microelectromechanically tunable silicon photonic ring resonator add-drop filter.* Optics Letters, 2015. **40**(15): p. 3556-3559.

116. Wang, B., et al., *MODULATION ON SILICON FOR DATACOM: PAST, PRESENT, AND FUTURE (INVITED REVIEW).* Progress In Electromagnetics Research, 2019.

117. Thomson, D.J., et al., *Silicon Photonics*, in *Wiley Encyclopedia of Electrical and Electronics Engineering*. 2015.

118. Narasimha, A., et al. *A 40-Gb/s QSFP Optoelectronic Transceiver in a 0.13µm CMOS Silicon-on-Insulator Technology*. in *Optical Fiber Communication Conference/National Fiber Optic Engineers Conference*. 2008. San Diego, California: Optica Publishing Group.

119. Brimont, A., et al., *High speed silicon electro-optical modulators enhanced via slow light propagation.* Optics Express, 2011. **19**(21): p. 20876-20885.

120. Xu, Q., et al., *Micrometre-scale silicon electro-optic modulator.* Nature, 2005. **435**(7040): p. 325-327.

121. Miller, C.M., *High-speed digital transmitter characterization using eye diagram analysis.* Hewlett Packard Journal, 1994. **45**: p. 29-29.

122. Wei, Y., et al., *Analysis of dark current dependent upon threading dislocations in Ge/Si heterojunction photodetectors.* Microelectronics International, 2012. **29**.

123. Chen, H., et al., *Dark current analysis in high-speed germanium p-i-n waveguide photodetectors.* Journal of Applied Physics, 2016. **119**(21): p. 213105.

124. Feng, D., et al., *High-speed GeSi electroabsorption modulator on the SOI waveguide platform.* IEEE Journal of Selected Topics in Quantum Electronics, 2013. **19**(6): p. 64-73.

125. Mastronardi, L., *GeSi Franz-Keldysh modulator for silicon photonic integrated circuits*. 2019, University of Southampton. p. 39.

126. Chrostowski, L. and M. Hochberg, *Silicon photonics design: from devices to systems*. 2015: Cambridge University Press.

127. *WGMODES*. Available from: https://photonics.umd.edu/software/wgmodes/.

128. Fallahkhair, A.B., K.S. Li, and T.E. Murphy, *Vector Finite Difference Modesolver for Anisotropic Dielectric Waveguides.* J. Lightw. Technol., 2008. **26**(11): p. 1423-1431.

129. Ansys/Lumerical. *MODE*. Available from: https://www.lumerical.com/products/mode/.

130. *COMSOL*. Available from: https://www.comsol.com/.

131. *Synopsys FemSIM*. Available from: https://www.synopsys.com/photonic-solutions/rsoft-photonic-device-tools/passive-device-femsim.html.

132. *Phton Design - FIMMWAVE*. Available from: https://www.photond.com/products/fimmwave.htm.

133. Hagness, S.C. and A. Taflove, *Computational electrodynamics: The finite-difference time-domain method.* Norwood, MA: Artech House, 2000.

134. solutions, E. *L-Edit, Phonics IC design*. Available from: https://www.eda-solutions.com/integrated-photonics/.

135. *K layout*. Available from: https://www.klayout.de/.

136. Soldano, L.B. and E.C. Pennings, *Optical multi-mode interference devices based on self-imaging: principles and applications.* Journal of lightwave technology, 1995. **13**(4): p. 615-627.

137. Reed, G.T. and A.P. Knights, *Silicon photonics: an introduction*. 2004: John Wiley & Sons.

138. Levy, D.S., et al., *Fabrication of ultracompact 3-dB 2 x 2 MMI power splitters.* IEEE Photonics Technology Letters, 1999. **11**(8): p. 1009-1011.

139. Ansys/Lumerical. [cited 2022 20/03]; Available from: https://optics.ansys.com/hc/en-us/articles/360034917453-Overlap-analysis-Modal-Analysis-Tab.

140. Yin, R., *Improving the self-imaging in multimode interference (MMI) couplers.* Optica Applicata, 2011. **41**: p. 679-685.

141. *CORNERSTONE*. 27/05/2022]; Available from: https://www.cornerstone.sotonfab.co.uk/.

142. Li, H.H., *Refractive index of silicon and germanium and its wavelength and temperature derivatives.* Journal of Physical and Chemical Reference Data, 1980. **9**(3): p. 561-658.

143. Pant, B., et al., *Study into the spread of heat from thermo-optic silicon photonic elements.* Optics Express, 2021. **29**(22): p. 36461-36468.

144. Xu, Q., et al., *Guiding and confining light in void nanostructures.* Opt. Lett, 2004. **29**(11): p. 1209-1211.

145. Xu, Q., et al., *Experimental demonstration of guiding and confining light in nanometer-size low-refractive-index material.* Optics letters, 2004. **29**(14): p. 1626-1628.

146. Liu, Y., M. Kong, and Y. Jiang, *Transverse magnetic modes in planar slot waveguides.* Journal of the Optical Society of America B, 2015. **32**(10): p. 2052-2060.

147. Penadés, J.S., et al., *Low-Loss Mid-Infrared SOI Slot Waveguides.* IEEE Photonics Technology Letters, 2015. **27**(11): p. 1197-1199.

148. Kowalski, Z.W. and I.W. Rangelow, *Microelectronic and medical applications of an ion beam milling system.* Journal of Materials Science, 1983. **18**(3): p. 741-752.

149. Chen, Y. and A. Pépin, *Nanofabrication: Conventional and nonconventional methods.* ELECTROPHORESIS, 2001. **22**(2): p. 187-207.

150. Choy, K.L., *Chemical vapour deposition of coatings.* Progress in Materials Science, 2003. **48**(2): p. 57-170.

151. Helmersson, U., et al., *Ionized physical vapor deposition (IPVD): A review of technology and applications.* Thin Solid Films, 2006. **513**(1): p. 1-24.

152. Singh, J. and D.E. Wolfe, *Review Nano and macro-structured component fabrication by electron beam-physical vapor deposition (EB-PVD).* Journal of Materials Science, 2005. **40**(1): p. 1-26.

153. Resnick, P.J. and P.J. Clews, *Whole wafer critical point drying of MEMS devices*. Micromachining and Microfabrication. Vol. 4558. 2001: SPIE.

154. microsystems, l. *Brief Introduction to Critical Point Drying*. 2019 [cited 2019 10 May]; Available from: https://www.leica-microsystems.com/science-lab/brief-introduction-to-critical-point-drying/.

155. Blasco, J. and C.A. Barrios. *Compact slot-waveguide/channel-waveguide mode-converter*. in *CLEO/Europe. 2005 Conference on Lasers and Electro-Optics Europe, 2005.* 2005.

156. Liu, Y., et al., *Efficient Strip to Strip-Loaded Slot Mode Converter in Silicon-on-Insulator.* IEEE Photonics Technology Letters, 2011. **23**(20): p. 1496-1498.

157. Wang, Z., et al., *Ultracompact low-loss coupler between strip and slot waveguides.* Optics Letters, 2009. **34**(10): p. 1498-1500.

158. Ruan, Z., et al., *Subwavelength grating slot (SWGS) waveguide on silicon platform.* Optics Express, 2017. **25**(15): p. 18250-18264.

159. Palmer, R., et al., *Low-Loss Silicon Strip-to-Slot Mode Converters.* IEEE Photonics Journal, 2013. **5**(1): p. 2200409-2200409.

160. Kern, W., *The Evolution of Silicon Wafer Cleaning Technology.* Journal of The Electrochemical Society, 1990. **137**(6): p. 1887-1892.

161. Markle, R., *Etching titanium with HF and nitric acid solutions part 1*. 2018, PA, USA Retrieved from http://www. chemcut. net/wp-content/uploads/2015/02 ….

162. Sacher, W.D., et al., *Polarization rotator-splitters in standard active silicon photonics platforms.* Optics Express, 2014. **22**(4): p. 3777-3786.

163. Steglich, P., et al., *CMOS-Compatible Silicon Photonic Sensor for Refractive Index Sensing Using Local Back-Side Release.* IEEE Photonics Technology Letters, 2020. **32**: p. 1241-1244.

164. Steglich, P., et al., *Partially slotted silicon ring resonator covered with electro-optical polymer*. SPIE Photonics Europe. Vol. 9891. 2016: SPIE.

165. Steglich, P., et al., *On-Chip Dispersion Measurement of the Quadratic Electro-Optic Effect in Nonlinear Optical Polymers Using a Photonic Integrated Circuit Technology.* IEEE Photonics Journal, 2019. **11**: p. 1-10.

166. Fu, P.-H., et al., *Microring resonator composed of vertical slot waveguides with minimum polarization mode dispersion over a wide spectral range.* Applied Optics, 2016. **55**(13): p. 3626-3631.